UNIVERSITÉ DE STRASBOURG

ÉCOLE DOCTORALE 269
Laboratoire des sciences de l'Ingénieur, de l'Informatique et de l'Imagerie (UMR 7357 ICube)

&

FACHHOCHSCHULE NORDWESTSCHWEIZ

Institut pour l'ingénierie Médicale et l'Informatique Médicale (IM²)

&

COMMISSARIAT A L'ENERGIE ATOMIQUE ET AUX ENERGIES ALTERNATIVES (CEA)

Laboratoire Spintec

THÈSE présentée par :

Hugo NICOLAS

soutenue le : **16 Décembre 2024**
pour obtenir le grade de : **Docteur de l'université de Strasbourg**

Discipline / Spécialité : **Electronique, Microélectronique, Photonique**

Développement de magnétomètres intégrés à base de jonctions tunnel magnétiques à couple de transfert de spin

THÈSE dirigée par :
Mr. KAMMERER Jean-Baptiste Maître de conférences, HDR, Université de Strasbourg
Co-dirigée par :
Mr. SOUSA Ricardo Directeur de recherche, HDR, Spintec
Co-encadrée par :
Mr. PASCAL Joris Professeur, Fachhochschule Nordwestschweiz, Suisse

RAPPORTEURS :
Mr. SAEZ Sébastien Professeur, Université de Caen
Mr. JACQUEMOD Gilles Professeur, Université Côte d'Azur

AUTRES MEMBRES DU JURY :
Mme. PANNETIER-LECOEUR Myriam Directrice de recherche, CEA Saclay
Mme. FISCHER Johanna Chargée de recherche, Spintec
Mr. FRICK Vincent Professeur, Université de Strasbourg

Université de Strasbourg

Fachhochschule Nordwestschweiz

msii ÉCOLE DOCTORALE

UNIVERSITY OF STRASBOURG

DOCTORAL SCHOOL 269
Laboratory of engineering science, computer science and imaging (UMR 7357 ICube)

&

FACHHOCHSCHULE NORDWESTSCHWEIZ

Institute for Medical Engineering and Medical Informatics (IM²)

&

FRENCH ALTERNATIVE ENERGIES AND ATOMIC ENERGY COMMISSION

Spintec Laboratory

THESIS presented by:

Hugo NICOLAS

defended on: **16 December 2024**
To obtain the degree of: **Ph. D., Doctor of the University of Strasbourg**

Discipline / Speciality: **Electronics, Microelectronics, Photonics**

Development of integrated magnetometers using spin transfer torque magnetic tunnel junctions

THESIS directed by:
Mr. KAMMERER Jean-Baptiste Associate Professor, HDR, University of Strasbourg
Co-directed by:
Mr. SOUSA Ricardo Research Director, HDR, Spintec
Co-supervised by:
Mr. PASCAL Joris Professor, Fachhochschule Nordwestschweiz, Switzerland

REFEREES:
Mr. SAEZ Sébastien Professor, University of Caen
Mr. JACQUEMOD Gilles Professor, Côte d'Azur University

INSPECTORS:
Ms. PANNETIER-LECOEUR Myriam Research Director, CEA Saclay
Ms. FISCHER Johanna Researcher, Spintec
Mr. FRICK Vincent Professor, University of Strasbourg

Abstract

This thesis presents the use of perpendicular STT-MTJs, originally developed for MRAMs, as integrated magnetic sensors. MRAMs based on MTJs are often using the STT effect to change the orientation of the magnetization of a soft ferromagnetic layer by applying a strong voltage across the junction. This leads to a change of resistance allowing the MTJ to be set in two different resistive states called parallel and antiparallel. However, the energy required to flip the magnetization of the free layer from one state to the other is not only related to the voltage applied to the junction but also to the external magnetic field. Using this property, this work investigates a new application of STT-MTJs, which consists of using it as a magnetic sensor. These sensing elements have significant advantages compared to currently available Hall effect and magnetoresistive sensors. Hence, their nanometric dimensions as well as high bandwidth allow the development of new applications.

Key-words: STT-MRAM, STT-MTJ, Magnetic sensor, Electronics, Spintronics.

Résumé

Cette thèse présente l'utilisation de STT-MTJs perpendiculaires, développées initialement pour les MRAMs, en tant que capteurs magnétiques intégrés. Les MRAMs basées sur des MTJs utilisent généralement l'effet STT pour modifier l'orientation de l'aimantation d'une couche ferromagnétique douce en appliquant une forte tension aux bornes de la MTJ. Cela conduit à un changement de résistance permettant de placer la MTJ dans deux états distincts, parallèle et antiparallèle. Cependant, la tension nécessaire pour provoquer le retournement de l'aimantation de la couche douce dépend du champ magnétique externe. En utilisant cette propriété, nous explorons une nouvelle application des STT-MTJs qui consiste à les utiliser comme capteurs magnétique présentant des avantages significatifs par rapport aux capteurs à effet Hall et magnétorésistifs. Leurs dimensions nanométriques ainsi que leurs bandes passantes élevées permettent le développement de nouvelles applications.

Mots-clés : STT-MRAM, STT-MTJ, Capteur magnétique, Electronique, Spintronique.

Acknowledgement

This thesis finally reaches its end, what a journey! I will finally complete this manuscript, by thanking all the people who supported me and my work over more than these three years.

First, I will express my deep gratitude for my Ph. D. director, Jean-Baptiste Kammerer, who positively accepted my application for this very interesting project a few years ago, and who helped me a lot over all these years of work, at so many different levels. Your expertise, advices and reviews were always very helpful to overcome many difficulties.

I want to also express my sincere gratitude for Ricardo Sousa, my Ph. D. co-director, who allowed me to understand, and explain me a lot about the physics of the junctions, and who helped me a lot to carry out all the measurements, especially at Spintec during my multiple stays. Your knowledge, support and advices were always greatly appreciated.

I can not continue further without also giving very strong gratitude for Joris Pascal, for supervising me, and helping me a lot also, at so many different aspects of this work over these multiple years. I have learned so much thanks to all your suggestions and advices. I am also incredibly grateful for all the opportunities you gave me to work on so many different side projects, helping me to learn a lot and progress on so many different aspects beside this thesis.

Thank you also to all the administrative personnel from ICube laboratory, Spintec laboratory and from the FHNW for all your help in all these administrative tasks over all these years.

I will continue by thanking also a lot Stefan Gorenflo, Adrian Graña, Markus Hufschmid and Amon Inderbitzin from the FHNW Brugg, for all these years working on these SNI projects, for all your advices and work, resulting in lots of very interesting and promising achievements.

I want to also thank the company Camille Bauer Metrawatt AG, with their CEO, Max Ulrich and previously Thomas Keusch, for accepting to be part of these SNI projects. This support was very important and allowed us to do a lot with these projects, as well as for the possibility to carry out our measurements in your facility.

I am also very grateful to Luc Hebrard and Lucian Prejbeanu for all your feedbacks and advices over these years. Your reviews, help and knowledge were always really great additions and very helpful at so many different levels.

Thanks a lot also to all the people who helped me during my different stays at Spintec over this last year, for the final measurements, especially Kosuke Komuro. Your help, knowledge and advices were very much appreciated, as well as all the very interesting discussions! :)

I want to also thanks a lot all the people at the FHNW Muttenz who took part directly or indirectly in this project, including Thomas Quirin, Céline Vergne, Corentin Féry, Guilherme Baumgarten, Simon Lemoigne, Dominic Jeker, and all the others.

I want to particularly thanks a lot Céline, Thomas and Corentin. Your help and support, technical - but also moral :) - were very much appreciated during all these years and this tough final year!

Finally, I will thank all my friends, my parents and all my family for their continuous support, from the beginning, and over all these years of the Ph. D. Thank you so much to everyone!

To all the junctions fallen during the measurements.

Contents

List of Figures

Glossary

Acronym	Definition
ADC	Analog to Digital Converter
AP	AntiParallel state
APP	AntiParallel to Parallel
AMR	Anisotropic MagnetoResistance
CMOS	Complementary Metal-Oxide Semiconductor
DDS	Direct Digital Synthesizer
DOS	Density Of State
FL	Free Layer
FM	Ferromagnetic
FS	Full Scale
GMR	Giant MagnetoResistance
HPF	High Pass Filter
HC	High Coercivity
IC	Integrated Circuit
LPF	Low Pass Filter
LC	Low Coercivity
MCU	MicroController Unit
MRAM	Magnetic Random-Access Memory
MTJ	Magnetic Tunnel Junction
NM	Non-Magnetic layer
NPSD	Noise Power Spectral Density
OpAmp	Operational Amplifier
P	Parallel state
PAP	Parallel to AntiParallel
PCB	Printed Circuit Board
PL	Pinned Layer
PWM	Pulse Width Modulated
PMA	Perpendicular Magnetic Anisotropy
RAM	Random Access Memory
RT	Room Temperature
SEM	Scanning Electron Microscope
STT	Spin Transfer Torque
SV	Spin Valve
TMR	Tunnel MagnetoResistance
TDC	Time to Digital Converter
$\uparrow$	Spin Up
$\downarrow$	Spin Down

Symbols

Symbol	Unit (SI)	Definition
$\mathbf{V}$	V ($m^2.kg.s^{-3}.A^{-1}$)	Voltage
$\mathbf{R}$	Ω ($m^2.kg.s^{-3}.A^{-2}$)	Resistance
$\mathbf{I}$	A	Electric current
$\mathbf{H}$	Oe ($A.m^{-1}$)	Magnetic field strength
$\mathbf{B}$	T ($kg.s^{-2}.A^{-1}$)	Magnetic field flux density
$\mathbf{M}$	Oe ($A.m^{-1}$)	Magnetization
$\mathbf{F}$	Hz (s^{-1})	Frequency
$\mathbf{L}$	H ($m^2.kg.s^{-2}.A^{-2}$)	Inductance
$\mathbf{C}$	F ($m^{-2}.kg^{-1}.s^4.A^2$)	Capacitance
$\boldsymbol{H_c}$	Oe ($A.m^{-1}$)	Coercive field
$\boldsymbol{H_0}$	Oe ($A.m^{-1}$)	Offset field
$\boldsymbol{V_0}$	V ($m^2.kg.s^{-3}.A^{-1}$)	Offset voltage
$\boldsymbol{M_r}$	T ($kg.s^{-2}.A^{-1}$)	Remanent field
$\mathbf{T}°$	°C (K)	Temperature
$\mathbf{t}$	s	Time
$\mathbf{T}$	s	Period
$\mathbf{q}$	$\approx 1.602 * 10^{-19} C$	Elementary charge
$\boldsymbol{\mu_0}$	$\approx 1.256 * 10^{-6} H.m^{-1}$	Vacuum permeability
$\boldsymbol{k_B}$	$\approx 1.380 * 10^{-23} J.K^{-1}$	Boltzmann constant
$\boldsymbol{V_T}$	$\approx 25.8 mV$@$300K$	Thermal voltage

Introduction

General introduction

Magnetic tunnel junctions (MTJs) represent a major progress in the field of spintronics, a scientific domain that has been rapidly expanding over the past years, using the electrons as main actors, and based on the combination of the electronic property of the electron with its magnetic property, through the spin, a quantum property with multiple applications. Among major technological progresses in this field, magnetic tunnel junctions represent one of the most promising, used in many scientific domains, with strong industrial potential.

MTJs are made of a nanometric layer of a non-magnetic and non-conductive material, often magnesium oxide (MgO), placed between two layers of conductive ferromagnetic materials, typically based on an alloy of iron, cobalt and boron (FeCoB). These devices are fabricated in the shape of vertical pillars (cylinders), with diameters in the order of 10 to 100 nm for a similar height and are manufactured using microelectronics and nanoelectronics processes in clean rooms. The magnetization of one of the two ferromagnetic layers is fixed (also called reference or pinned layer) in a unique direction while the other ferromagnetic layer has a magnetization free to be flipped. When this magnetization vector is in the plane of the junction, called in-plane junctions, the device is used mainly as a magnetic sensor. On the other hand, when this vector is perpendicular to the plane of the junction, the device, called perpendicular magnetic tunnel junction (pMTJ), is used almost exclusively in magnetic random-access memories (MRAMs), especially thanks to several physical advantages observed (e.g., dimensions, manufacturing, stability, etc.), compared to in-plane junctions. In both cases, the result is a device whose free magnetization vector has two stable states, one state called parallel (P), when it is in the same direction as the pinned layer, and one state called antiparallel (AP), when it has a direction opposite to the reference layer. The resistance of the junction in the two states is different, induced by the tunnel magnetoresistance (TMR) effect, with variation of which can easily reach 100 to 200 %. Through this bistable configuration, these devices are therefore perfectly suited to the storage of binary information and are used as magnetic random-access memories.

Magnetic memories, based on perpendicular junctions, are among the most promising applications of these devices, with a strong potential to compete with existing technologies in specific tasks. These MTJ-based magnetic memories offer very interesting power consumption performance, with very low write and read currents. In addition, they offer non-volatile storage capability, high read and write speeds, with nanometric dimensions, and therefore high storage density possibility. Finally, these devices remain compatible with CMOS manufacturing processes, allowing a large-scale production, embedded in more complex circuits. These memories are already produced at large scale at major foundries facilities (e.g., TSMC, Samsung or GF) despite still presenting different drawbacks. For instance, magnetic memories remain significantly more expensive than their competitors with standard technologies (e.g., Flash, SRAM or DRAM), and remain difficult to produce in a reproducible way.

Hence, controlling these junctions as memory cells comes down to the control of the P and AP state. To do this, two methods are possible. Since the free layer is made of a ferromagnetic material, applying a sufficiently strong enough external magnetic field in a specific direction allows its magnetization to be flipped. However, this method is not very practical. On the other hand, through another physical phenomenon, extremely important in the field of spintronics and called spin transfer torque (STT), the application of a sufficiently strong enough current (or voltage) through the device allows the junction to be placed in the P or AP state depending on the polarity used. To achieve this, a specific voltage (positive or negative) must be applied to exceed the reversal threshold, typically around (absolute) voltages of 0.5 to 1 V.

However, the switching voltage and the magnetic field can affect each other. Thus, the external magnetic field can change the effective field, and the energy required to flip the magnetization vector of the free layer such that the threshold voltage is affected. **This results in a reversal threshold proportional to the external magnetic field**. This phenomenon corresponds to the fundamental principle of a new generation of magnetic sensors, studied over this Ph. D. project.

Thesis objective

This thesis, entitled "**Development of integrated magnetometers based on spin transfer torque magnetic tunnel junctions**" aims to demonstrate the proof of principle of a new generation of integrated magnetic sensors, by using nanoscale devices, called magnetic tunnel junctions, in an unusual way, through the spin transfer torque effect, originally used for magnetic memories, to obtain an accurate reading of the magnetic field. As part of this thesis work, a new type of magnetic sensor is therefore demonstrated, based on this principle, observed in perpendicular junctions, usually used for MRAMs. To achieve this, the key concept of such sensors consists in the application of an alternating voltage allowing the periodic reversal of the storage layer between the two states, P and AP, combined with a system for detecting the reversal at each period. Hence, measuring the reversal threshold allows a measurement of the magnetic field at high-speed and at the nanoscale level. Unfortunately, such devices suffer from a major defect, called stochasticity. This phenomenon induces a random variation of the reversal threshold in the absence of variations in the magnetic field, resulting in a significant noise at the sensor output, which can then only be averaged to be reduced, either by multiplying the number of sensitive elements, or by multiplying the measurements on a single element.

This new generation of sensors aims to compete with existing technologies of integrated magnetic sensors, almost exclusively based on Hall effect, or magnetoresistive effect (AMR, TMR or GMR). These integrated sensors come with significant drawbacks. Hall effects sensors dimensions are usually limited to few μm by physical limits, as the currents lines are not deviated enough at small dimensions, resulting in the absence of measurable sensitivity. MR sensors also suffer from such dimension related issues, as lower dimensions MR sensors result in higher noise.

For these reasons, most existing sensors remain in the μm range and above, limiting the possible applications requiring true punctual measurements, such as photolithographic mask alignment or magnetic particles and beads detection. In addition, these sensors also suffer from bandwidth limitations, in the tens of kHz range, resulting in the absence of applications at high frequency. This includes for instance current measurements at high bandwidth, required to meet new industrial requirements, or rotation counters. Lower power consumption or CMOS compatibility are also among advantages of such technology. Hence, this STT-MTJ based integrated magnetic sensor aims to relieve drawbacks observed in standard technologies.

- **Chapter 1** starts by introducing all the necessary notions required to understand the topics addressed in this manuscript. In the first place, most important notions of magnetism will be introduced, describing all the physical aspects of magnetic field and physical phenomena observed in the scope of this work. In a second time, we will introduce important notions about magnetic memories and magnetic tunnel junctions, that are used in magnetic memories and magnetic sensors. Finally, a brief description about magnetic sensors and few of the most important integrated sensing technologies will be detailed. Through this chapter, the reader will have an overview of all the basic notions used in next chapters.

- **Chapter 2** introduces all the key principles and elements of the newly demonstrated magnetic sensor. The working principle of the sensor, the junctions used as well as the electronics developed to use these junctions as sensing elements are described, allowing for the understanding of such new measurement principle.

- **Chapter 3** continues the description of this new generation of magnetic sensor through slightly different principle, by presenting new junctions, developed for sensing applications, presenting low coercive fields, associated with new electronics, developed to remain compatible with these new MTJs, allowing for enhanced performance to be reached.

- **Chapter 4** finishes the discussion of the work achieved over this Ph. D., by comparing the performance achieved with existing technologies, as well as different approaches attempted for the enhancement of the performance of the sensor.

- **Conclusion** finally summarizes all the results obtained over this entire project as a global outlook, allowing the reader to have an overview of the future perspectives to be achieved for the improvement of the technology.

This thesis was conducted as a collaboration through three different institutions and was supervised by Jean-Baptiste KAMMERER (Ph. D. director, ICube laboratory) and Ricardo SOUSA (Ph. D. co-director, Spintec laboratory) as well as coadvised by Joris PASCAL (Ph. D. coadvisor, HLS).

School of Life Sciences (HLS) - FHNW, Muttenz, Switzerland

ICube laboratory - UMR 7357, University of Strasbourg/CNRS, France

Spintec laboratory - University of Grenoble Alpes CEA/CNRS, Grenoble, France

The project was co-funded through the SNI (Swiss Nanoscience Institute) NanoArgovia projects Nanocompass (A16.10) and NanoHighSens (A18.6). This work was partially supported by the National Research Agency (ANR) under France 2030 program, within the ADAGE project (ANR-22-EXSP-0006).

Chapter 1

Magnetism

1.1 Physics of magnetism

1.1.1 Introduction

Magnetism is a natural and well-known phenomenon, used for centuries by humans, in which some objects tend to be attracted or repelled by others. This phenomenon was already described by Greeks 500 years B.C. [18], [59]. However, it remained unexplained for a long time before the first scientific explanations and has only been mathematically and accurately described less than a century ago. Hence, if the phenomenon has been known and used for centuries, its origin was discovered only in the 18^{th} century and is today attributed to quantum physics and electronic properties. Magnetism is a very important phenomenon in physics and is present almost everywhere. Indeed, several experiments and theories demonstrated in the 19^{th} century that the magnetic field and the electric field are strongly related by the electromagnetic force, one of the four fundamental forces of the universe.

1.1.2 General concepts

In physics, a magnetic field is usually described as a vector field ruled by mathematical and physical equations to describe behaviours observable in nature like movements of charges, current-induced fields, behaviour of magnets or behaviour of specific materials. As any vectors, the magnetic field vectors have a direction (along a line) and a magnitude. Hence, it is important to differentiate three different vector fields, $\vec{B}$, $\vec{H}$ and $\vec{M}$, that will be used in this manuscript.

- The magnetic field flux density ($\vec{B}$), measured in Tesla (T) or Gauss (G) (1 G = 100 μT).
- The magnetic field strength ($\vec{H}$), measured in A/m or Oersted (Oe), with (only in vacuum) 1 T = 10 kOe (1 Oe = 100 μT).
- The magnetization ($\vec{M}$), measured in A/m or Oe, which represents how much a region of a material is magnetized (i.e., the magnetic dipole moment per unit volume), and does not exist outside the material.

These three vectors are linked by the equation $\vec{B} = \mu_0(\vec{H} + \vec{M})$, with μ_0 being the vacuum permeability. Outside materials or in the air, where $\vec{M} \approx \vec{0}$, it is usually acceptable to approximate $\vec{B} \approx \mu_0\vec{H}$ ($\vec{B} = \mu_0\vec{H}$ only in pure vacuum). One can also express $\vec{M} = \chi\vec{H}$, with χ being the magnetic susceptibility, dimensionless, representing how much the material will become magnetized in the presence of an external magnetic field.

1.2 Physical effects

1.2.1 General concepts

Electronics and spintronics, where the main actors involved are the electrons, are subject to quantum physics. These quantum effects start to be strong and non-negligible when reaching extremely small dimensions, typically at the nanoscale level, and are sometimes beneficial or problematic depending on the situation.

Electrons are fundamental elementary particles (i.e., not made by any known sub-particles) with intrinsic properties, meaning that these properties exist and are inseparable from the object such as the mass, the electric charge ($-e$) or the spin (also called spin angular momentum, in opposition to the orbital angular momentum). This last property, experimentally discovered between 1921 and 1922 by the famous Stern-Gerlach experiment [36], [81] and only explained with quantum physics, is the foundation of spintronics (spin-electronics).

The spin is represented by a number s, taking only integer values (e.g., 0, 1, 2) or half-integer values (e.g., $\frac{1}{2}$), and a secondary number m_s, ranging from $-s$ to $+s$. For an electron, $s = \frac{1}{2}$ and $m_s = \pm\frac{1}{2}$. Hence, electrons, which are points, often inaccurately considered as spheres, can be "pointing" either in one direction (called spin up, or $\uparrow$, $m_s = +\frac{1}{2}$) or in the opposite direction (called spin down, or $\downarrow$, $m_s = -\frac{1}{2}$) **following an arbitrary direction**. This direction will be defined by the chosen measurement coordinate system, and measurements of the spin of random electrons will usually result in 50 % $\uparrow$ and 50 % $\downarrow$. The spin, combined with the charge of the electron, creates the magnetic dipole moment (called the total magnetic dipole moment), which makes the electrons behave like small magnets.

For an electron with only two possible values of m_s, the equation describing the possible states is given by $|\nearrow\rangle = x\,|\uparrow\rangle + y\,|\downarrow\rangle$, where x and y are complex numbers, known as the Bloch sphere. When measuring the spin of such systems, the probability of finding either $\uparrow$ or $\downarrow$ (following the chosen direction) will depend on these numbers, and when measured, the system will be definitely fixed in one unique state, $\uparrow$ or $\downarrow$. This property allows the electron to be simultaneously in the two states, used, for instance, in quantum computing.

Usually, for an electron with a given spin angular and orbital momentum, another electron with the opposite spin angular and orbital momentum exists. Both cancel each other out, creating a net $\vec{M}$ of zero. However, in some materials or situations, this equilibrium state is not present, meaning that a majority of electrons will have the same magnetic dipole moment orientation along a given direction, creating a magnetization $\vec{M}$ or a spin polarized current.

For instance, the filling of the atomic orbitals following Klechkowski's rule can lead in some materials to partially filled shells, where one electron $\uparrow$ is not cancelled by an opposite spin $\downarrow$, as required by Pauli's exclusion principle. This creates a magnetic dipole moment for the atom (exceptions exist). These small magnetic dipole moments will be aligned with neighboured atoms in small areas (magnetic domains), and under some conditions, these domains will be aligned, as

in ferromagnetic (FM) materials, such as iron (Fig. 1.1) as a consequence of the partially filled 3d orbitals. However, while the exchange energy tends to align the magnetization of nearby domains within the material, creating a net local magnetization, these domains will also be subject to demagnetizing fields at the edges or at domain boundaries, with energy minimization dictating the equilibrium magnetization direction. Hence, there is a competition between these two effects. For instance, a FM material has a positive exchange, but the exchange energy can also be negative leading to an antiferromagnetic material. To observe a FM material, a fully saturated domain should exist, when the creation of a reversed region will not lower its total energy. Each magnetic domain is separated from the other domains by transition regions, called domain walls, with a width of a couple of nanometres to tens of nanometres.

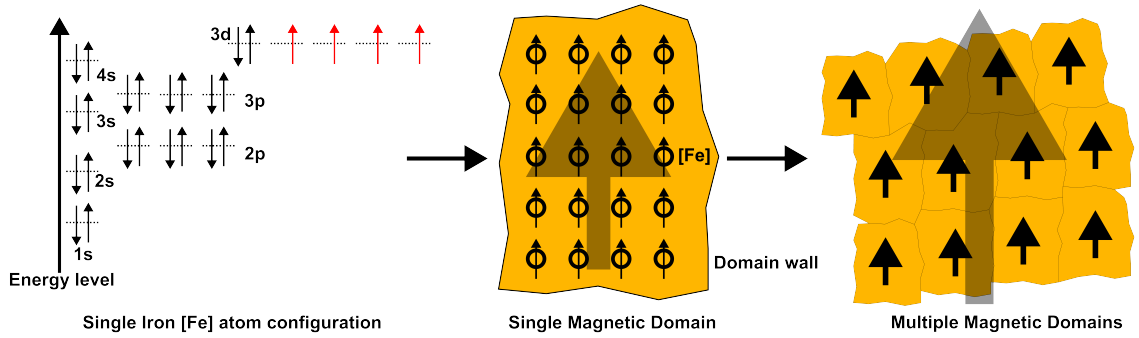

Figure 1.1: Iron [Fe] electron configuration, with 8 valence electrons ([Ar] 3d6 4s2). The magnetic dipole moment of multiple [Fe] atoms can point in the same direction within a defined volume, called magnetic domain, which presents a defined magnetization in one direction, and multiple domains can be aligned, resulting in the creation of a FM material with a general magnetization.

For ferromagnetic materials, if the sample is small enough (typically tens of nanometres), it can be considered as a single domain with a uniform magnetization (macrospin) which behave like a macroscopic spin, allowing the use of simplified physical models such as the Stoner-Wohlfarth model, introduced in 1948 by two scientists, Wohlfarth and Stoner [82]. In other cases, the ferromagnet needs to be considered as a multi-domain instead (micromagnetic), requiring the use of other equations and models (e.g., LLG equations), generalized by Brown during the 20^{th} century [48] and based on the works from Landau, Lifshitz and Gilbert, introduced earlier, at the beginning of the 20^{th} century.

In a FM material where the magnetization has some arbitrary direction, the magnetic dipole moment of a majority of electrons is aligned along this direction, spin ↑ by convention, while a minority of electrons, spin ↓ by convention, are aligned in the opposite direction. In such materials, **the density of states (DOS) of electrons ↑ and ↓ is different**, whereas in nonmagnetic materials, the DOS is identical for both electrons ↑ and ↓. In the case of iron (Fig. 1.2), the orbital 3d for electrons ↑ is below the Fermi level E_F and as a result is completely filled but only partially filled for electrons ↓, since the 3d band for electrons ↓ is slightly shifted above the Fermi level.

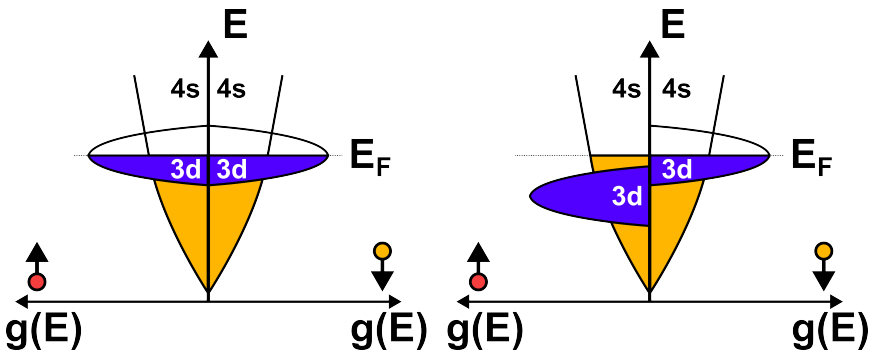

Figure 1.2: DOS of the 3d and 4s bands for both electrons ↑ and ↓ in a non-FM metal (left) and in a FM metal (right). g(E) is a function and represents the density of states.

In these ferromagnetic materials, physicist Mott proposed a model, experimentally verified in the middle of the 20^{th} century [60], where the conduction current through a ferromagnetic material can be divided into **two parallel sub-currents of electrons ↑ and ↓** (Fig. 1.3). Electrons with the same spin as the majority (i.e., with a magnetic dipole moment aligned with the magnetization) will have less difficulty flowing than electrons with the opposite spin. In these materials, the electrical resistance to the flow of electrons with the majority spin direction ($R_{\uparrow}$) will be lower than that of electrons with the opposite direction ($R_{\downarrow}$) (i.e., the mean time between two collisions will be shorter for these antiparallel electrons, hence higher resistance). Based on this, the total electrical resistance R of such FM materials can then be calculated using the formula of two parallel resistors, given by $R = \frac{R_{\uparrow}R_{\downarrow}}{R_{\uparrow}+R_{\downarrow}}$, with $R_{\uparrow} < R_{\downarrow}$.

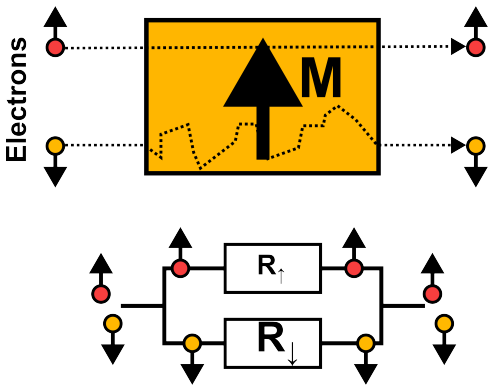

Figure 1.3: Two current model for electrons ↑ and ↓ in a FM material with a magnetization.

Furthermore, the magnetic dipole moment of electrons aligned with the magnetization of the material will be more energetically favourable than non-aligned ones, such that electrons entering the material will tend to align parallel (majority, ↑) or antiparallel (minority, ↓) along this direction, creating a **spin polarized current along the direction of the magnetization**.

1.2.2 Types of magnetism

Different types of magnetism exist, depending on the material and, among other things, the value of χ and the electronic configuration (e.g., paired $\uparrow\downarrow$ electrons or not in the orbitals). Magnetism is usually divided into five different types: paramagnetic, diamagnetic, ferromagnetic, antiferromagnetic and ferrimagnetic.

For very small χ values, two main types of materials can be distinguished, paramagnetic ($\chi > 0$) and diamagnetic ($\chi < 0$). Most of the known chemical elements are called paramagnetic, meaning that they are attracted by an external magnetic field and will form an induced internal magnetic field in the same direction. In these materials, the magnetic moment of all particles is randomly oriented in the absence of an external magnetic field (e.g., magnesium [Mg], aluminium [Al], etc.). Diamagnetic materials are repealed by an external magnetic field and will form an induced internal magnetic field in the opposite direction (e.g., copper [Cu], boron [B], gold [Au], etc.). In these materials, the magnetic moment of all particles is null in the absence of an external magnetic field.

Furthermore, magnetic materials can exhibit three distinct behaviours: ferromagnetic, antiferromagnetic, and ferrimagnetic. These materials will usually have a larger χ. These properties exist only within a given temperature range. Above a temperature threshold called the Curie temperature, T_C, ferromagnetic and ferrimagnetic materials become paramagnetic (for antiferromagnetic materials, this threshold is called the Néel temperature, T_N). Above these thresholds, the thermal energy becomes high enough such that the magnetic order is suppressed, creating paramagnetic behaviour.

- Some materials are called ferromagnetic, meaning that all the magnetic moments (strength and orientation of entities producing a magnetic field, such as electrons) are aligned inside the material. These materials will be permanent magnets (e.g., cobalt [Co], iron [Fe], etc.).
- Some materials are called ferrimagnetic, meaning that each magnetic moment is partially cancelled by its neighbour, pointing in the opposite direction. In these materials, spontaneous magnetization will also be present (e.g., magnetite [Fe_3O_4], etc.).
- Some materials are called antiferromagnetic, meaning that each magnetic moment is totally cancelled by its neighbour, pointing in the opposite direction. In these materials, no spontaneous magnetization will be present (e.g., manganese oxide [MnO], etc.).

1.2.3 Magnetic anisotropy

The magnetic anisotropy is the property of an object which will react differently depending on its position or its orientation inside an external magnetic field. Different types of magnetic anisotropy can be described, and one can distinguish at least three main types of anisotropy; the shape anisotropy, the magnetocrystalline anisotropy and the exchange anisotropy.

- Exchange anisotropy is a type of anisotropy observed at the interface of multilayer materials, resulting in an exchange coupling of different magnetic materials. This anisotropy is particularly interesting when used between a ferromagnetic and an antiferromagnetic layer for the creation of very stable magnetic structure that will be detailed in later sections.
- Shape anisotropy is observed for instance in non-symmetrical samples (such as ellipsoidal samples), where it is easier to magnetize the material along the longer axis of the sample rather than along the shorter axis due to the demagnetizing field.
- Magnetocrystalline anisotropy is induced by the spin-orbit coupling within the crystal structure, and result in preferred magnetization direction within the material. In such material, the magnetization in some direction requires more energy than in other direction.

In some materials, the magnetic anisotropy creates two preferential magnetization directions, called the easy axis and the hard axis. The hard axis is the direction within a material along which a large magnetic field needs to be applied to reach the saturation of the magnetization while the easy axis is the direction of magnetization minimizing the system energy.

In addition, in thin film (nm to μm), **perpendicular magnetic anisotropy (PMA)**, induced by one of the three types of anisotropy, can also be obtained, where the preferential magnetization of the sample will be perpendicular to the sample plane and not in the film plane. PMA plays a critical role in the creation of magnetic memories and magnetic sensors, which will be detailed in later sections.

1.2.4 Magnetic hysteresis

The magnetic hysteresis corresponds to a specific cycle that the magnetization $\vec{M}$ of some materials (often ferromagnetic) exhibits when exposed to an external magnetic field $\vec{H}$ (Fig. 1.4). The different origins of this phenomenon can be found in the evolution of magnetic domains and domain walls in response to the external magnetic field.

Although the evolution of the magnetization looks continuous, in reality, it is a discrete process. Each domain and domain wall behave on their own under the influence of the external field, and when looking from a close view at the evolution of $\vec{M}$, one can actually see discrete steps induced by the evolution of each domain. This effect, discovered in 1919 by the German scientist Barkhausen [31], and known as the Barkhausen effect, causes serious inconvenience, especially in the scope of magnetic sensors, by creating magnetic noise, which will be detailed in later sections.

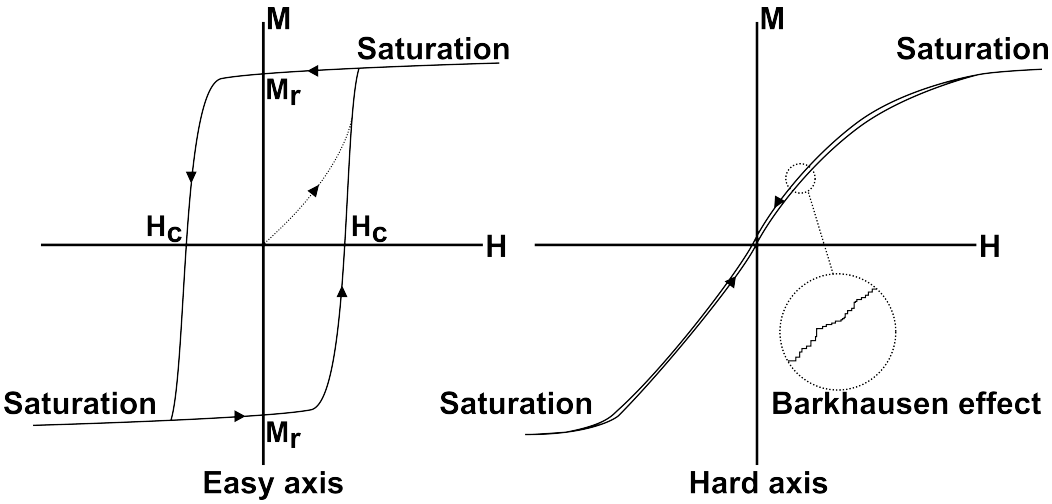

Figure 1.4: Magnetic hysteresis cycle along the easy and hard axis of a FM material.

Over the whole hysteresis cycle, two important points can be defined: the coercive field and the remanent or retentivity field. The coercive field (H_c) is the intensity of the magnetic field required to demagnetize (reduce $\vec{M}$ down to zero) the material after being driven to saturation. The remanent field (M_r) is the remaining magnetization of the object after being driven to saturation (H_s) and removing the applied magnetic field ($\vec{H} = \vec{0}$). Saturation occurs when (almost) all domains are aligned in the same direction, producing the strongest magnetization. In addition, one can also classify materials as soft, presenting low coercivity (e.g., nickel-iron alloys [NiFe]), or hard (e.g., neodymium-Fe/Co alloys [Nd] or Co-Pt multilayers, used in this thesis), presenting a large coercivity. Depending on the type of material, soft or hard, the overall shape of the hysteresis will be different. Finally, in some conditions or situations, one can also note that the hysteresis cycle can be shifted by a coupling field referred as an offset field H_0.

1.2.5 Quantum tunnelling

Among different quantum effects involved in the scope of magnetic memories that needs to be introduced, an important one is called the quantum tunnelling effect, in which an electron can tunnel through a potential barrier, which would not be possible using the rules of classical physics and can only be explained by quantum physics.

This property, discovered in 1927 by Hund [45] and confirmed later by Nordheim and Fowler [58], is becoming very important and problematic with the reduction of classical electronic device sizes down to the nanoscale, such as CMOS transistors, leading, for instance, to current leaks. However, this property can also be interesting in some devices, especially in some magnetic memories, tunnel diodes (Esaki diodes, discovered in 1957 by Esaki [33] and rewarded with a Nobel Prize in 1973) or specific tunnel field effect transistors (TFETs), developed in 1965 [42].

The counterintuitive explanation of the tunnelling effect is only possible with mathematical equations and can be briefly described by recalling that quantum physics relies on probabilities and wave functions. Hence, if an electron is shot with a defined energy towards a higher energy potential barrier, when calculating the probability of finding the electron on the other side of the potential barrier using quantum principles, a non-zero probability can be obtained, whereas using classical physics, this probability would strictly be zero. In this way, electrons can "pass through" the barrier with a specific probability depending on different factors (e.g., height of the potential barrier, physical width of the barrier), while classical physics states that electrons could only be reflected back in that situation. In addition, when an electron tunnels through a barrier, it is admitted that **its magnetic dipole moment orientation is conserved over a short distance of typically a few nanometres**. This property is very important and allows several other effects, described below, to take place.

1.2.6 Magnetoresistance

Magnetoresistance (MR) is another important type of effect present in some materials, where the electrical resistance of such material will vary depending on the surrounding magnetic field. Different magnetoresistance effects exist with their specificity. Some MR effects appear within the same material, such as AMR (anisotropic magnetoresistance), whereas GMR (giant magnetoresistance) or TMR (tunnel magnetoresistance) effects can only take place in very specific multilayer materials and are caused by quantum phenomena. All of these effects are very important in the creation of magnetic sensors and magnetic memories.

Anisotropic magnetoresistance

Anisotropic magnetoresistance, initially discovered in 1857 by Thomson [84], is a MR effect observed within specific FM materials, where the resistance of the device is affected by the angle between the direction of the electrical current passing through the device and the magnetization of the material. The origin of the AMR effect arises from different physical phenomena, depending on the material. Usually, in FM materials, the orientation of the electron's orbital is affected by the magnetic field (induced by the spin-orbit coupling). Hence, depending on the direction of the current in regard of the magnetization, the scattering of electrons is affected, resulting in resistance variations [75], [88], [57]. This includes, for instance, 4s-3d electron scattering, due to the band energy difference for electrons $\uparrow$ and $\downarrow$.

In such material, it can be shown that the resistivity ρ of the device (i.e., resistance $R = \frac{\rho L}{A}$, with A the cross section area and L the length of the device) depends on the angle θ between the current I and the magnetization $\vec{M}$, and can be given by equation 1.2.1 [69], with $\rho_\perp$ and $\rho_\parallel$ being the resistivity of the device for θ of respectively 90° and 0°. In most cases, the ratio between $\rho_\perp$ and $\rho_\parallel$ does not exceed a few percent (< 5 %) at room temperature (300 K) [75].

$$\rho(\theta) = \rho_\perp + (\rho_\parallel - \rho_\perp).\cos^2(\theta) \tag{1.2.1}$$

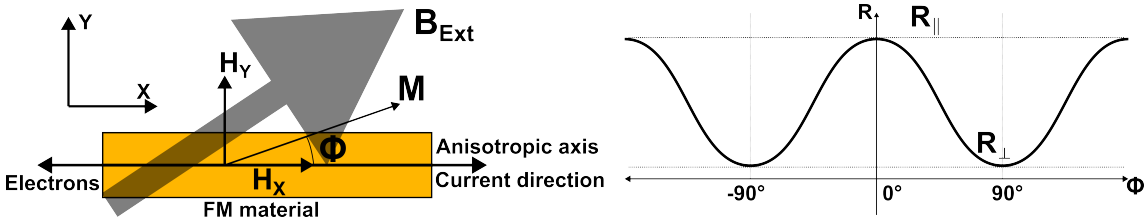

Figure 1.5: AMR effect principle in a FM material.

In addition, by applying an external magnetic field $\vec{B}_{Ext}$, non-aligned with the magnetization $\vec{M}$ of the material, the magnetization of this material will rotate by an angle ϕ, given by equation 1.2.2, with H_x and H_y being the field values along x and y directions of $\vec{B}_{Ext}$, and H_s being the saturation field of the material [69].

$$\phi = \arcsin\left(\frac{H_y}{\frac{H_x}{\cos(\phi)} + H_s}\right) \tag{1.2.2}$$

For small angle of ϕ, $\cos(\phi) \approx 1$ and the relation can be simplified to:

$$\phi = \arcsin\left(\frac{H_y}{H_x + H_s}\right) \tag{1.2.3}$$

However, this describes a non-linear relationship as well as a resistance dependency affected by both axes (H_x and H_y), which are not very suitable for sensors. Therefore, by placing the device in a situation where $H_x = 0$, one can create a situation much more suitable for a magnetic sensor, whose resistance will only be affected by the magnetic field along a unique direction, H_y, perpendicular to the anisotropic axis of the material. In this configuration, the AMR effect can then be used in the creation of magnetic sensors, which will be detailed in later sections.

Giant magnetoresistance and tunnel magnetoresistance

Discovered at the end of the 20^{th} century by Fert and Grünberg [21], [25] (both Nobel prize in 2007), the name of the GMR effect comes from the fact that, when discovered, the change of resistance induced by the magnetic field (i.e., MR) was higher than anything existing at that time, observed through the AMR effect, whereas the name of the TMR effect, discovered by Jullière during the same period, in 1975 [50], comes from the fact that it involves the tunnel effect. The origin of these two effects can only be explained by quantum physics and spin of electrons. Moreover, a specific multilayer structure is required to observe these magnetoresistance effects. The required structure where TMR and GMR can be observed is made of **two ferromagnetic layers (FM) separated by a non-magnetic layer (NM), FM/NM/FM**.

These ferromagnetic layers have their own orientation of magnetization, which can be changed by the external magnetic field following a hysteresis loop. Depending on the relative orientation of the two layers, the resistance of the device will vary, with the magnetization of the two layers having two stable limit states: aligned in the same direction or in opposing directions. When the orientation of the two layers is identical, called the parallel state (P), the resistance of the device is low, whereas when their orientation is opposed, called the antiparallel state (AP), the resistance of the device is high. The GMR and TMR ratios are defined by equation 1.2.4, usually expressed as percentage values.

$$\frac{(R_{AP} - R_P)}{R_P} \text{ or } \frac{(R_{\uparrow\downarrow} - R_{\uparrow\uparrow})}{R_{\uparrow\uparrow}} \tag{1.2.4}$$

It is important to note that in order to get a MR effect, the magnetization of one layer needs to remain fixed (called the pinned layer, PL) (i.e., not affected by the external magnetic field), while the other layer should be free to rotate (called the free layer, FL), depending on the magnetic field. Indeed, if the two ferromagnetic layers are free, then both layers would always change together at the same time and always remain with the same parallel orientation, leading to the absence of a TMR or GMR effect (assuming that the coercive fields of the two layers are identical). The main difference between the TMR (Fig. 1.7) and the GMR (Fig. 1.6) devices is in the non-ferromagnetic layer present between the PL and FL. In one case, the electrons will have to pass through either a tunnelling barrier (TMR) through the tunnel effect, or simply through a non-magnetic metal as is the case in GMR. However, in the two situations, **their magnetic orientation will remain the same** over the short thickness of the NM layer (typically $\approx$ nm).

To understand this behaviour, let us first use a classical GMR device (Fig. 1.6) as described above, with a NM layer between two FM layers and apply a current through the structure from the FL to the PL (i.e., electrons from the PL to the FL). The GMR effect can then be easily understood, using the two-current approximation $\uparrow$ and $\downarrow$, previously described, applied at each layer. At the output of the PL, the majority of the electrons $\uparrow$ will have the same spin orientation as the magnetization of this layer and will reach the FL. If the magnetization of this layer is parallel to the PL (P), the majority of electrons $\uparrow$ inside will be oriented along the same direction such that the electrons from the PL will be able to pass through without any major scattering, leading to low resistance (i.e., high current). However, if the orientation of the magnetization of the FL is opposite (AP), the majority of electrons coming from the PL will be in the opposite direction compared to the majority in the FL, resulting in a large scattering and only a minority of electrons at the output of the device (i.e., high resistance). Through this configuration, the achieved GMR ratio could only be around 20 % up to a maximum reported of around 100 % at room temperature (300 K) [41], [39], remaining significantly higher than AMR but much lower than what could be achieved through the TMR.

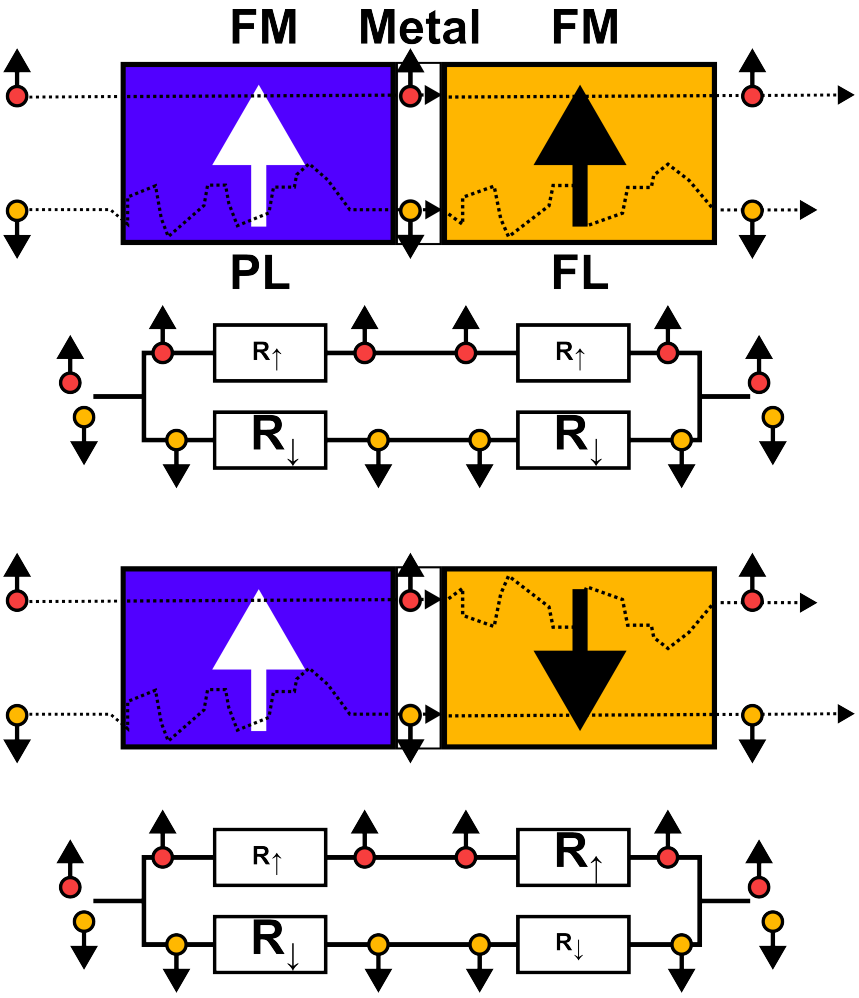

Figure 1.6: GMR effect principle for both P (top) and AP (bottom) configuration.

TMR effect is a little more challenging to explain, as it involves the less intuitive tunnel effect, and was first theorized by Jullière at low temperature (4.2 K, temperature of liquid helium). In the case of TMR, the probability of observing tunnelling electrons depends exponentially on the potential barrier, as well as on the DOS of both layers. To tunnel through the barrier, electrons with a given magnetic moment ↑, must find a free state ↑ in the other layer, and the same applies for electrons ↓. Hence, in the AP configuration, the electrons ↑ are opposite in both layers, and only a minority of electrons can tunnel through the barrier, leading to a high resistance. On the other hand, in the P configuration, electrons ↑ are in the same direction in both layers, and much more electrons can tunnel through the barrier, leading to a smaller resistance.

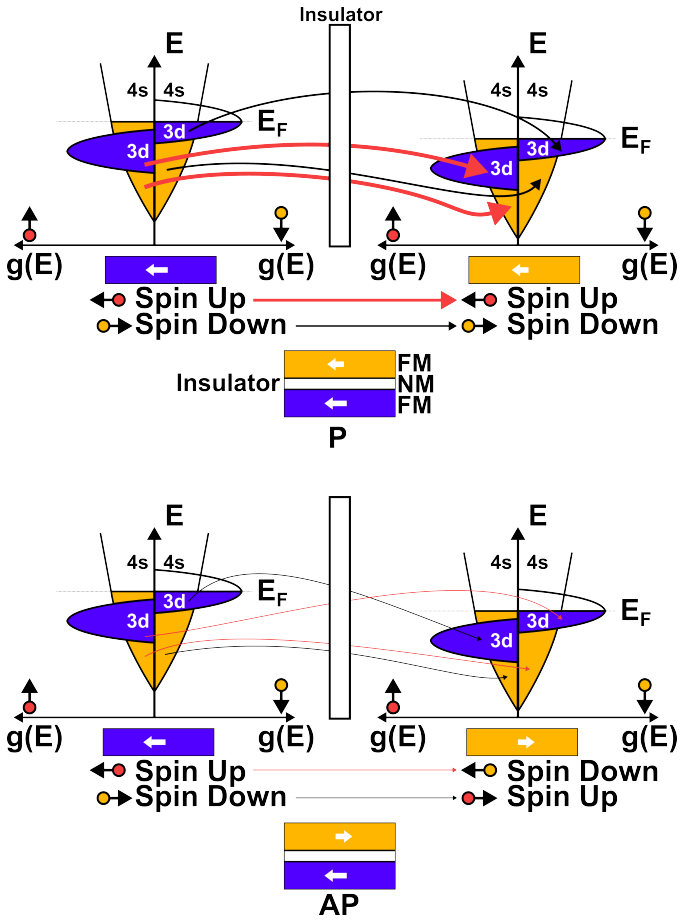

Figure 1.7: TMR effect principle for both P (top) and AP (bottom) configuration.

In the first experimental approaches, using a barrier made of alloys of aluminium oxide [Al_xO_y] with [Fe] FM layers, a TMR ratio of 10 to 20 % could be observed at room temperature [50]. Rapidly, improvements with Fe/Al_xO_y devices achieved a TMR of 50 to 100 %, much higher compared to existing GMR devices. However, modern TMR structures, made of [Fe] and magnesium oxide [MgO] and reaching 100 to 400 % [49], were later discovered and failed to be explained by Jullière's theory, based simply on the spin polarization from ferromagnetic electrodes and not taking into account additional spin filtering by the tunnel barrier. Further analysis at the beginning of the 21^{th} century introduced more complex theories, discovering that, in reality, the probability of tunnelling electrons is not identical for each band structure [94], [92], [27], which is known as the spin filtering effect. This new approach successfully explained why Fe/MgO/Fe devices were exceptionally good, as the spin filtering is almost perfect between the [MgO] and the [Fe] [94], [92] in comparison to [Al_xO_y] barrier. Today, the most optimized Fe/MgO-TMR devices can go up to 600 % at 300 K and over 1000 % at low temperature (5 K), demonstrated at Tohoku University in Japan in 2008 [46].

1.2.7 Spin-transfer torque

If the local magnetization of a FM layer can polarize an electrical current, a polarized current can also affect the local magnetization of a FM layer. Hence, if a magnetic field can affect the orientation of the magnetization of a FM layer, a strong enough polarized current can also achieve it, through what is known as the STT (spin-transfer torque) effect.

Discovered at the end of the 20^{th} century by Berger and Slonczewski [80], [24] and confirmed a few years later experimentally by Tsoi [87], [86], [85], this effect can be considered the reciprocal of MR effects and is a fundamental effect in spintronics. STT effect can be used to change the orientation of the magnetization of the FL in TMR or GMR devices, allowing an accurate and external, but electronic, control of the state of the device. Therefore, STT is of tremendous importance in the field of magnetic memories. Similarly to the magnetic hysteresis of a FM material, the switching of the FL between the AP and P states through the STT effect will also show a similar hysteresis effect.

To observe this effect (Fig. 1.8), a strong current (or voltage) is applied through a compatible device, either a GMR or TMR device, made of two FM material separated by a non-magnetic material. As seen in previous sections, at the exit of any ferromagnetic layer, electrons flow will be polarized along the direction of the magnetization. These electrons will then tunnel through the barrier (TMR) or simply pass through a metal (GMR), where it can be assumed that **they will keep their original magnetic orientation** as this NM layer is thin (≈ 1 nm). Depending on the desired configuration (P or AP), the polarity of the current required is reversed. In both cases (PAP or APP), if the applied current is not large enough to affect the magnetization, the FL will remain in the same orientation. However, it is important to note that, in the case of any current, even low, the torque on the magnetization of FL will still be present but not strong enough to reverse the orientation, the magnetization of the FL will be disturbed and tilted from its equilibrium direction, then go back to its initial state when the current is removed. In addition, **a torque is also exerted on the magnetization of the PL from electrons with the opposite orientation coming from the FL**. However, since the magnetization of the PL can not easily rotate due to its higher anisotropy as detailed in later sections, the effect of electrons from the FL on the PL can be ignored in this general overview of the STT effect.

- Regardless of the direction of $\vec{M}$ in the FL, when a current is applied from the FL to the PL, polarized electrons $\uparrow$ are sent from the PL to the FL, which, by applying a torque to the magnetization of the FL, will change the orientation of the magnetization of the FL to match the direction of the PL magnetization and set the device to the P state.
- When a current passes from the PL to the FL in the P state, polarized electrons $\uparrow$ are sent from the FL to the PL. Electrons with their magnetic moment aligned with the magnetization of the PL will have a higher tunnel probability. This initially represents a majority of electrons $\uparrow$ since both layers are parallel. However, a minority of electrons with opposite moment $\downarrow$ cannot tunnel through the barrier and will mainly be reflected back to the FL. These electrons will create a torque on the FL, changing its orientation

to be antiparallel. When the AP state is reached, electrons ↓ (minority) will be able to tunnel to the PL, while electrons ↑ (majority) from the FL can no longer tunnel, will be reflected back and apply a torque to the FL, maintaining the AP state.

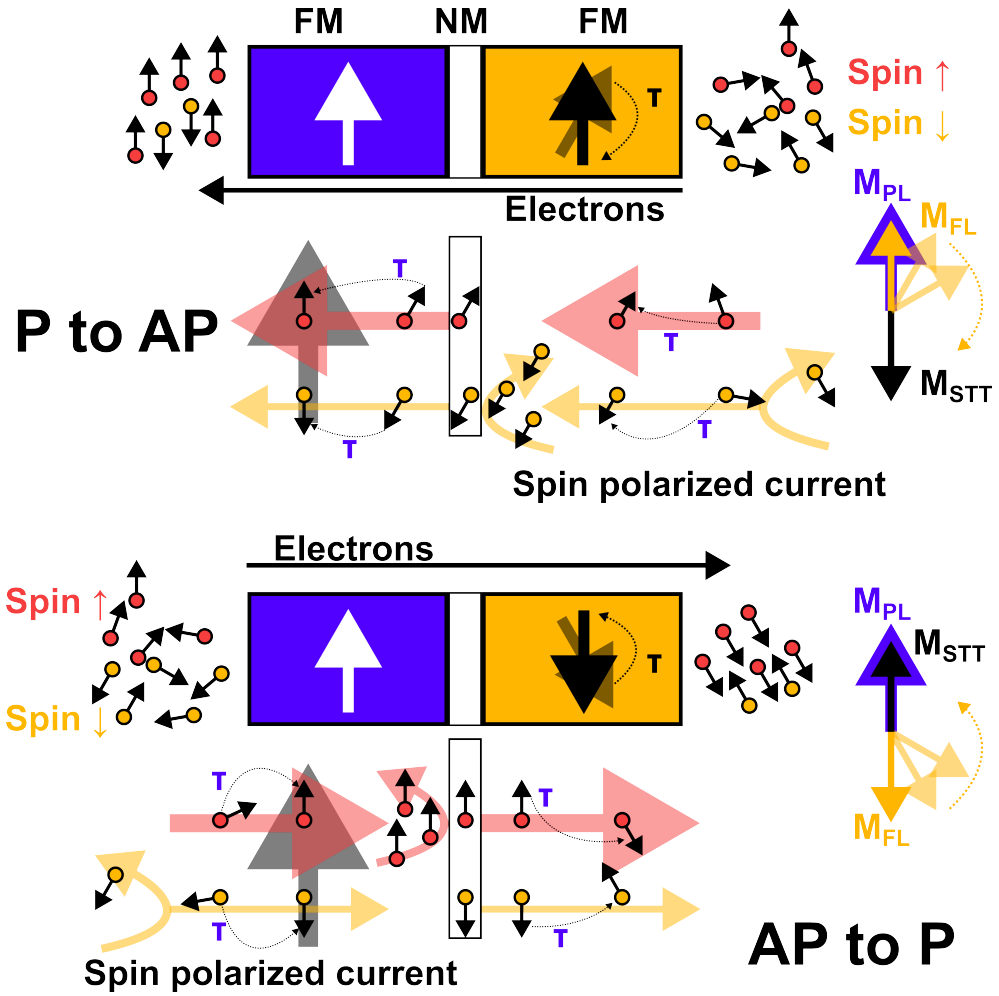

Figure 1.8: STT effect principle, either in a TMR or GMR device, for both P to AP (PAP) and AP to P (APP) switching. The majority of electrons with a magnetic moment opposite to the magnetization of the entry layer (PL for APP or FL for PAP) are reflected.

STT effect is a complex phenomenon to mathematically describe and is based on the conservation of the total angular momentum of the whole system. The equations describing these phenomena are usually called the **LLGS equations**, from the name of the four physicists, Landau-Lifshitz-Gilbert-Slonczewski, who successively worked on this question during the 20^{th} century [95], [55], [37], [80].

1.3 Magnetic random-access memory

1.3.1 Introduction

Magnetic random-access memory (MRAM) is an emerging type of memory, with the particularity of storing binary information ("1" or "0") using magnetic properties of electrons instead of electrical properties of electrons, as in standard memory technologies (e.g., Flash memories, dynamic RAMs, DRAMs, or static RAMs, SRAMs). MRAMs represents a growing market with, depending on the sources, an estimated weight of 2 to 30 billion dollars in the incoming ten years [44], [28]. This significantly contributes to the memory market, which already represents an impressive 200 billion dollars in 2023 [17], compared to the semiconductor industry (almost 500 billion dollars in 2018 [13]), especially due to the growth of the Internet of Things (IoT).

Although MRAMs are considered emerging technologies, storing information using magnetic elements is not very new, and some technologies, quite old, are very well established such as the well-known HDDs (Hard Drive Disks), first created in 1956 by IBM Corporation and still used to this day with an 11 billion dollars market in 2018 [4]. However, with recent advances in electronics, HDDs have progressively been replaced with SSDs (Solid State Drives), with a market of 20 to 40 billion dollars in the last few years [43], [14], first developed in 1980 by Toshiba Corporation [2], being up to hundreds of times faster, operating without mechanical parts, and with the particularity of being also based on the electrical charge properties of electrons.

Each type of memory presents their own advantages and drawbacks and is selected depending on the application's requirements (e.g., slow, μs to seconds, but large mass storage, GBs to PBs, used in data centres or servers, or very fast, sub-ns, but small, few kBs, L1 cache memory for the processor). Key characteristics of any memory include the access speed (write and read speeds from sub-nanoseconds to multiple seconds) or the cost, often normalized as the cost per bit. In addition, the volatility or retention, describes how long the integrity of the data can be maintained while the volatility corresponds to the loss of the information if the cell is not powered. The cell size describes the total area on the wafer for one bit, which is directly related to the achievable density. Finally, the endurance describes the capability of the memory cell to be written multiple times ranging from few thousands up to 10^{15} cycles or more.

Main drawbacks of existing memories (summarized in the table below for Flash memories, DRAM, SRAM and MRAM) often include volatility for SRAMs and DRAMs, and speed for Flash memories, being significantly slower than other technologies (sub-ns of access time for the fastest SRAMs compared to tens of μs and higher for Flash memories). These major drawbacks are creating a need for a new technology (i.e., a market gap to fill), one necessary condition to observe the development of a new technology. To overcome these issues and create a memory technology that combines most of the advantages of existing memory, MRAMs are considered strong candidates to outperform standard technologies in different applications.

	Speed	Cost	Volatility	Cell Size	Endurance
Flash					
DRAM					
SRAM					
MRAM					

Typically, MRAMs are based on arrays of multiple devices (i.e., memory cells) where the TMR effect is present, such that the memory cells can be either highly or weakly resistive, with the possibility of controlling externally (electrically) their states using the STT effect or other effects. With only two stable states possible, these devices are therefore very well suited for binary applications. Hence, when the resistance of the device is low (P), it can be seen as "0", while when it is high (AP), it can be seen as "1". To do so, each memory cell is connected within the whole array using transistors (word line and bit line), allowing individual addressing of each cell for the writing or reading of the binary information. Due to the lower MR ratio between the two resistive states observed through the GMR effect, making it more difficult to differentiate between "0" and "1" than TMR effect, as well as lower P and AP resistance values in these devices (i.e., higher idle consumption), MRAMs no longer relies on GMR devices. Instead, the GMR effect was first used by IBM Corporation in 1997, in hard disk drives as a sensing element, described in a further section, to read bits [1], while in 2004, Seagate Technology introduced TMR devices as reading sensing elements [1].

Different quantum effects are used in MRAMs, resulting in different types of MRAMs [64], [19], [83], [30]. Like every memory, magnetic memories can be read or written. While the reading part will usually always be done using the TMR effect, the writing part can be done using different effects such as the STT effect, the spin orbit torque (SOT), or the spin Hall effect (SHE). In addition, other types of MRAM can be found, such as thermally assisted (TAS-MRAMs) or field-assisted MRAMs. However, STT-MRAMs, based on the STT effect, currently represent the most common type of MRAM investigated and in production.

As seen previously, the resistance of TMR devices can be switched from one state (P or AP) to another (AP or P) either electrically by applying a strong enough current (STT), or magnetically by applying a strong magnetic field ($> H_c$ of the FL). However, when using STT-MRAMs in nominal conditions, the only expected switching cause is current-induced switching, often controlled in voltage for practical reasons, which is used to write information into the device. To write the memory cell, a strong voltage will be applied, increasing the strength of the STT effect enough to change the orientation of the free layer and set the MRAM cell in the desired state (P or AP). Since the memory is non-volatile, the writing voltage can then be removed without worrying about losing the information. Hence, writing voltages will very often come in the form of short pulses (typically shorter than 10 to 100 ns) with a trade-off between power consumption and speed, with shorter pulses requiring higher current or voltage. In addition, to avoid affecting the state of the memory during the reading operation through the STT effect, a significantly lower voltage must be applied during the reading operation. While this lower reading voltage is applied, the current is measured to read

the resistance of the memory cell (i.e., read the binary information stored). In any case, voltages and currents must remain below the breakdown values, critical limits above which the device is damaged or destroyed. Furthermore, switching of the memory cells with an external magnetic field can occur in extreme cases, when exceeding the physical limits of the memory cells ($> H_c$ of the FL) and will result in the transient corruption of stored data or even the permanent corruption of the memory cells if the reference layer is affected ($> H_c$ of the PL). In addition, another important parameter for MRAMs is the thermal stability (Fig. 1.9), Δ, defined by $\Delta = \frac{E_b}{k_b T^\circ}$, with T° the temperature and E_b being the barrier energy, representing the ratio between the energy required to reverse the state of the memory cell and the thermal energy. For industrial compliance, Δ must be around 60 to 100 (> 45) [68]. This ensures data retention, $\propto \exp(\Delta)$, as well as a barrier high enough not to suffer from unwanted bit error over a long period of time (induced, for instance, by thermal energy), while keeping the barrier low enough to be controlled through the STT without reaching the breakdown limits of the device or presenting high-power consumption. Such stability becomes challenging to maintain at low diameter (< 20 nm) [68], necessary dimensions to reach high density and compete with other technologies.

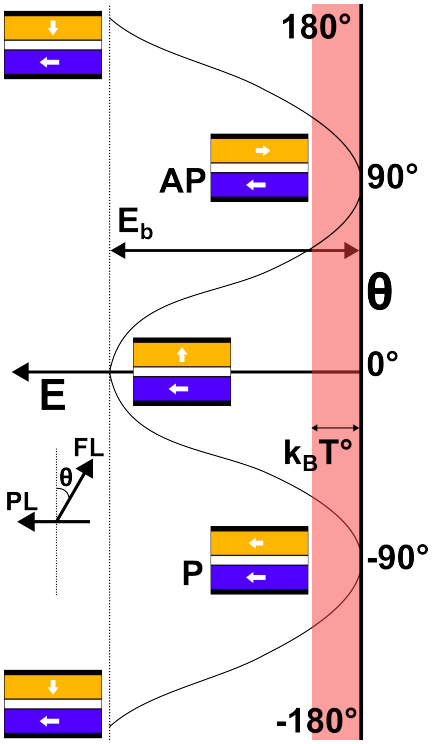

Figure 1.9: Energy configuration in MRAMs.

Therefore, despite the existence of various other MRAM types, STT-MRAMs are presently regarded as one of the leading contenders for the near future and also as one of the most advanced technologies, with numerous multinational corporations actively participating in this sector (e.g., Samsung Group, Western Digital Technologies, Intel Corporation, or IBM Corporation). For example, in 2019, Samsung Group indicated that they started mass production of ICs implementing MRAMs, with a reading and writing time of 20 to 50 ns in a 28 nm process [12] and in 2018, Intel Corporation announced at the ISSCC that the mass production of STT-MRAMs was ready in 22 nm process [90]. In 2020, IBM Corporation published an article demonstrating the first fabrication of CMOS STT-MRAMs chips with 14 nm technology [32] and more recently, in 2024, Japanese company Renesas Electronics demonstrated through an ISSCC paper the world's fastest STT-MRAMs products with 200 MHz capability [11], while in 2023, Samsung Group announced its ability to produce MRAM devices with unprecedented high energy efficiency [16].

If MRAMs are still the subject of many research and industrial projects in order to achieve best performance, several companies are already offering commercial devices. However, even if a limited number of commercial products are already available from different companies, the prices of MRAMs remain significantly higher compared to classical technologies, while the size and speeds also suffer from some technological limitations. To this day, MRAM technologies

still suffer from different important problems, resulting in more expensive (up to hundreds of times more than SRAMs/DRAMs and thousands of times more than Flash memories) or non-marketable products. These problems [77], classified as permanent faults such as barrier breakdown or variability, or transient faults, such as retention failure (i.e., data stability), write failure, read failure, or write asymmetry (i.e., different voltages are required to write a "0" or "1"), are actively being investigated by multiple actors.

1.3.2 Magnetic tunnel junction

To create memory cells that can be used as STT-MRAMs, the goal is to create a technological structure where the TMR effect can arise, therefore also allowing the use of the STT effect, to obtain a readable and writable memory cell. As explained in previous sections, the GMR and TMR effect will occur in multilayer structures, with two layers of conductive ferromagnetic materials separated by a thin layer of non-magnetic material (FM/NM/FM). If the non-magnetic layer is conductive, such as copper [Cu], the device will be called a spin valve (SV) and will rely on the GMR effect. If the non-magnetic layer is a tunnel barrier, such as magnesium oxide [MgO], the device will be called a magnetic tunnel junction (MTJ) and will allow the use of the TMR effect. Because of the lower MR ratio achieved through the GMR effect, SVs will preferentially be used in sensors, whereas MTJs will be used for MRAMs and magnetic sensors.

In many MTJs, the FL and PL are usually made of an alloy of iron-cobalt-boron (FeCoB), while the tunnel barrier is fabricated with a thin layer of oxidized magnesium [MgO], with each layer being less than one or two nanometres thick. These three layers represent the core structure of the MTJ where the binary information will be stored. The investigated materials, FeCoB-MgO materials are a frequent choice due to their high TMR ratio and fabrication compatibility since FeCoB / MgO-MTJs are known to withstand a high temperature [66], [47], required for the CMOS BEOL (CMOS back-end of line, fabrication step during which metal interconnections are made) where performance of MTJs should be maintained over a certain temperature (350 °C to 450 °C) and during a given period of time of several minutes. However, other core configurations (e.g., double barrier) or materials (e.g., oxidized aluminium [Al_xO_y] barrier) can also be used to enhance the performance of memory cells. In any case, these three layers, the fundamental structure of any MTJs, are usually completed by several other layers to form the full stack of the MTJ, which contains up to ten layers. These additional layers are used to enhance performance, allowing the manufacturing of MTJs, for instance, by acting as photolithographic masks or are used as top and bottom electrical conductors, which can be made of tantalum [Ta].

The manufacturing of MTJs usually relies on thin-film deposition of multiple layers on wafers to create the stack of the MTJs, followed by physical etching (through reactive ion etching, RIE, or ion beam etching, IBE) to obtain a device with a vertical cylindrical shape, complete by a final step of magnetization of the layers in strong magnetic fields. In some cases, the shape can also be a vertical ellipsoid or even a rectangle. The dimensions of the cylinder range from a few nanometres in diameter, as low as 3.8 nm, demonstrated at Tohoku University in 2018 [89] for the smallest MTJs ever fabricated up to 100's of μm, with a typical height of tens of nm.

The magnetization of the PL and FL can be in the plane of the junctions (in-plane MTJs, iMTJs) or perpendicular to the plane of the junctions (also called out-of-plane or perpendicular MTJs, pMTJs). While iMTJs are based on shape anisotropy, pMTJs are based on PMA. Due to the different properties observed in these two devices (Fig. 1.10), iMTJs will almost always be used in magnetic sensors while perpendicular MTJs will be used for MRAMs. Reasons for this include thermal stability and current consumption issues observed at low diameters, limiting the compatibility of iMTJs with high-density memories [53], [22]. In pMTJs, the path of the magnetization of the FL during reversals induced by the STT or thermal agitation is identical, whereas in iMTJs, these paths are orthogonal. This leads to larger switching currents in comparison to pMTJs. In addition, the thermal stability of the iMTJs is proportional to their volume, causing stability issues at low diameter. Such MTJs also require an asymmetric shape ratio (e.g., ellipsoidal shape) to obtain their shape anisotropy, which also increases technological challenges at low dimensions, as controlling an uneven aspect ratio is highly challenging at nanoscale dimensions [67].

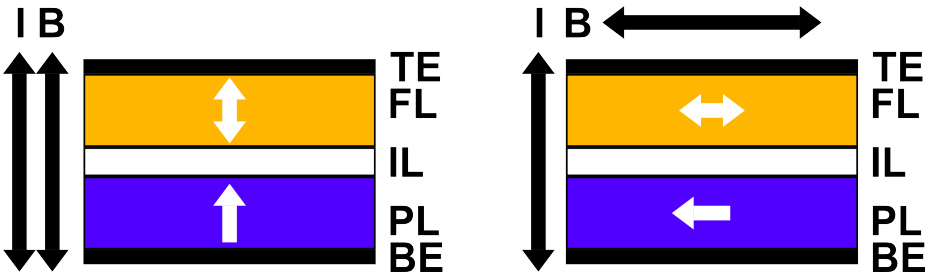

Figure 1.10: Perpendicular (left) and in-plane (right) MTJ (side view). The white arrows indicate the direction of the magnetization for the PL and FL. The black arrows indicate the direction of the current and the field used to set the FL in the desired state. TE: Top electrode, FL: Free layer, IL: Insulating layer, PL: Pinned layer, BE: Bottom electrode.

To create these devices and use the TMR or GMR effect, one layer (specifically, the magnetization of one layer) needs to remain fixed (PL) under normal condition, while the other should be free (FL) to rotate. To obtain such a PL/FL configuration, one possibility is to use two layers with different coercivity, with the PL presenting high coercivity and the FL presenting lower coercivity. Because of the coercivity difference, the magnetic field required to change the orientation of the PL will be bigger than the magnetic field required to change the FL, creating a steady reference layer under normal conditions. However, if the magnetic field exceeds H_c of the PL, the devices will be corrupted because their PL will be altered. Although this simple technique allows the creation of a PL (usually in pseudo-SV), the creation of a PL can also be done using an antiferromagnetic layer directly in contact with the PL (MTJs or SVs). Due to the large exchange bias between the two layers, caused by the exchange interaction, the PL will usually keep its orientation fixed under normal conditions, creating a steady reference.

In more complex devices, a specific multilayer structure will be used to artificially create an antiferromagnet, called a synthetic antiferromagnet (SAF), which will be in contact with the PL to pin its magnetization through the exchange interaction. SAFs (Fig. 1.11) are made by two or multiple ferromagnetic layers, such as cobalt [Co] or platinum [Pt], separated with a spacer (i.e., thin layer), such as ruthenium [Ru], with a very precise thickness to obtain an antiferromagnetic coupling through the RKKY interaction. This interaction (named after the physicist who worked on this topic, Ruderman-Kittel-Kasuya-Yosida during the 20^{th} century [76], [51], [93], [91]) is a very important phenomenon observed when two FM layers are separated with a very thin layer of non-magnetic but conductive material. It results in a magnetic coupling between the two FM layers, induced by the conduction electrons, which oscillate between a ferromagnetic and antiferromagnetic coupling depending on the thickness of the non-magnetic spacer. The SAF structure has the advantage of reducing the dipolar field generated by standard and single ferromagnetic or antiferromagnetic layers which can affect the FL and the overall performance of the memory cell (e.g., create switching voltages asymmetry) or even surrounding cells [78].

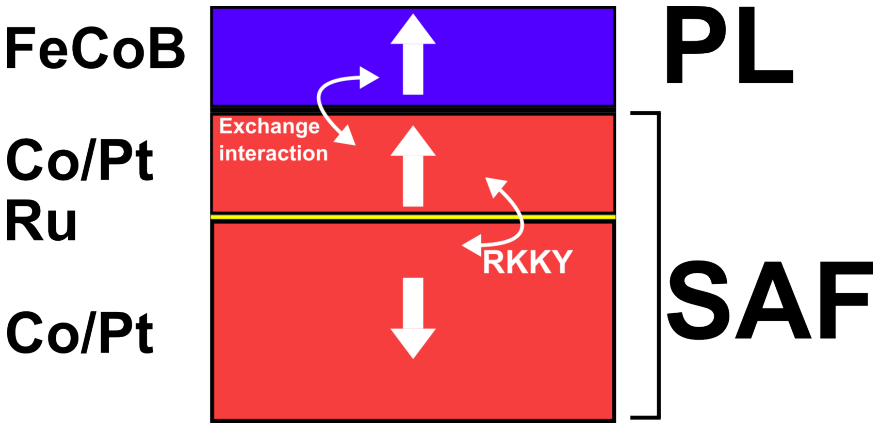

Figure 1.11: Typical SAF structure in a perpendicular MTJ (side view). In this example, the thickness of both Co/Pt layers is chosen to cancel the dipolar field exerted on the core of the MTJ by using a specific thickness ratio between the first and second Co/Pt layers. To further reduce this dipolar field, the Co/Pt layers are actually made by alternating thin individual layers of successive Co and Pt. For instance, the stack of a SAF with a 3-to-6 ratio could be described (thickness of each layer not indicated for this general example) by Co/Pt/Co/Pt/Co/Pt/Co/**Ru**/Co/Pt/Co/Pt/Co/Pt/Co/Pt/Co/Pt/Co/Pt/Co/Pt, or Co/$[Pt/Co]_3$/**Ru**/Co/$[Pt/Co]_6$/Pt.

1.4 Magnetic sensors

To efficiently study magnetic fields, magnetometers, also known as magnetic sensors, are almost always required. By definition, magnetic sensors convert the magnetic field information through a variety of physical principles, into another form of information, almost always electrical, which can then be digitized and used for further analysis. Magnetic sensors are now heavily used in almost all areas of science, from biology to physics or industrial applications, and are available in many different types, through a very wide range of applications [52]. According to various sources [10], [6], the market for magnetic sensors could reach up to 2 to 7 billion dollars on the horizon of 2030.

The table below represents a few but well-known examples of magnetic-based applications with their typical magnitude of magnetic field involved, ranging from 50 billion times smaller up to 200 000 times bigger than the Earth magnetic field (25 μT to 65 μT). Despite being unrepresented in this table, many applications are found in the dynamic range of tens of nT to few mT in several domains. This can be explained by the fact that such dynamic range is covered by many available technologies and not limited to a unique one, such as the fT, limited mainly to SQUID sensors (superconducting quantum interference device) and more recently with OPMs (optically pumped magnetometers), or the T, mainly limited to Hall effect sensors.

Application	**Objective**	**Magnitude**
Extremely weak measurements		**1 fT**
MEG (Magnetoencephalography)	Brain activity measurements	1 pT
MCG (Magnetocardiography)	Heart activity measurements	100 pT
Earth magnetic field		**50 μT (0.5 Oe)**
TMS (Transcranial Magnetic Stimulation)	Medical treatment	500 mT
MRI B_0 (Magnetic Resonance Imaging)	Medical imagery	3 T
Superconducting Electromagnets	Particle collider (LHC)	8 T
NMR (Nuclear Magnetic Resonance)	Chemical measurements	10 T

Hence, while tens of technologies are available nowadays, some types of magnetic sensors are much more popular than others. Among the most popular technologies (Fig. 1.12), one can find **Hall effect sensors, magnetoresistive (MR) sensors** and **fluxgate sensors**, which will be introduced in the next sections. Different reasons can explain the popularity of both Hall effect and MR sensors, including their availability as small and low-cost monolithic integrated circuits (ICs), with room-temperature operating range and complementary performance over a large dynamic range, from sub-nT up to several T.

Comparison between sensors performance is typically made through different parameters of the sensors (sensing element dimensions, dynamic range, power consumption, cost, etc.), among which the resolution, being critical and representing the smallest changes of magnetic field that can be detected. Hence, performance achieved with these three popular technologies can be put into perspective using as reference the highest resolution ever achieved (fT) with SQUID sensors,

which, despite using a sensitive element being possibly a nanoscale device, are still considered large due to their very low working temperature, as low as a few K, requiring heavy and large surrounding cooling infrastructures, involving liquid nitrogen [N] or helium [He].

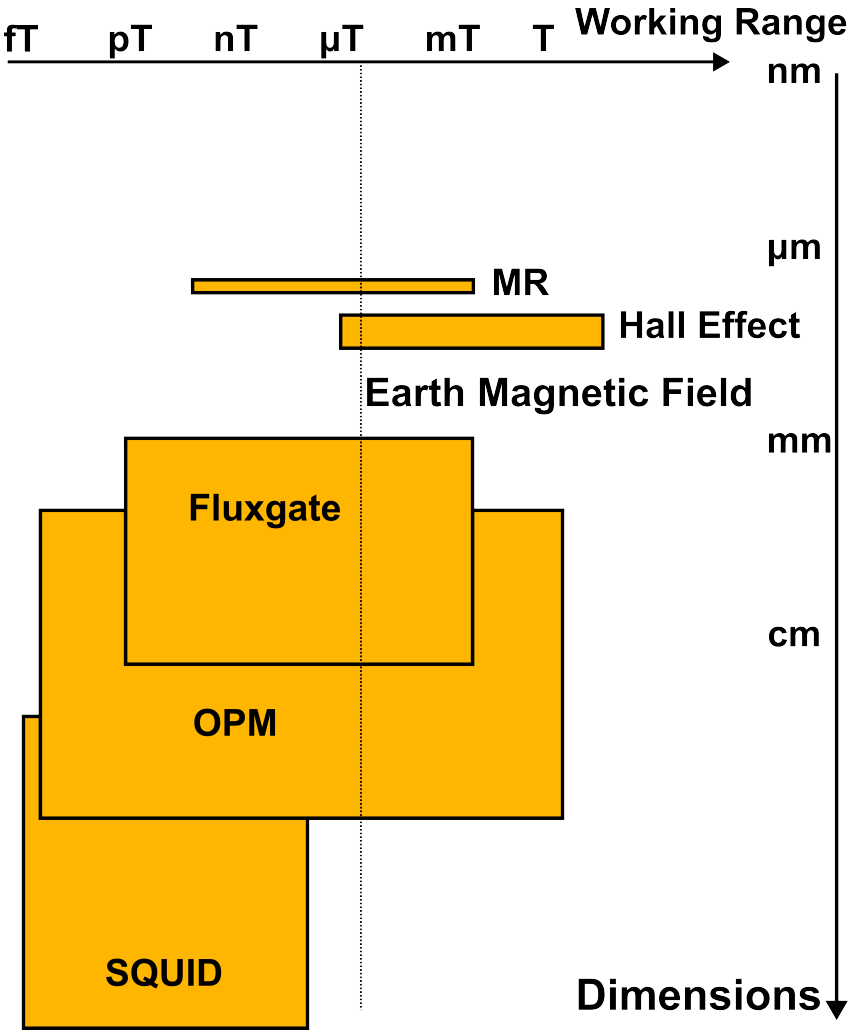

Figure 1.12: Common types of magnetic sensors with their typical dimensions and working range.

1.4.1 Hall effect sensors

Discovered in 1879 by the American scientist Edwin Herbert Hall [38], the principle of Hall effect sensors is based on the Lorentz force $\vec{F_L}$, which affects the movement of electrons travelling at a speed $\vec{v}$ in the presence of an external magnetic field $\vec{B}$. The force applied to the electrons is given by $\vec{F_L} = -q\vec{v} \times \vec{B}$.

In the most basic form of integrated Hall effect sensors, a rectangular shaped area made of an N-doped semiconductor is used, on a P-substrate silicon [Si] wafer, with a length L, a width W (L>W criteria must be met for the Hall effect to be used) and with four contact points P_1 to P_4. Such a device, which is very easy to fabricate, is often called the Hall plate or Hall element. A constant polarizing current is then applied through the device (Fig. 1.13) along the length L of the device, from P_2 to point P_1 (electrons travelling from point P_1 to point P_2). In this configuration, and as a result of the Lorentz force in the presence of an external magnetic field $\vec{B}$ perpendicular to the plane of the wafer, current lines will be deviated within the material. Electrons will be affected by $\vec{F_L}$ and will deviate toward the point P_4 of the device, while holes (pseudoparticles with positive charge $+q$) will be repealed towards the opposite direction (point P_3) of the device. This charge gradient generates an electric field along the width W of the device, called the Hall field $\vec{E_H}$, between points P_3 to P_4. Hence, the voltage difference between points P_4 to P_3, called Hall voltage V_H, and defined by $V_H = -\int_{P_3}^{P_4} E_H dW$, can then be measured or sampled and will be proportional to the external magnetic field.

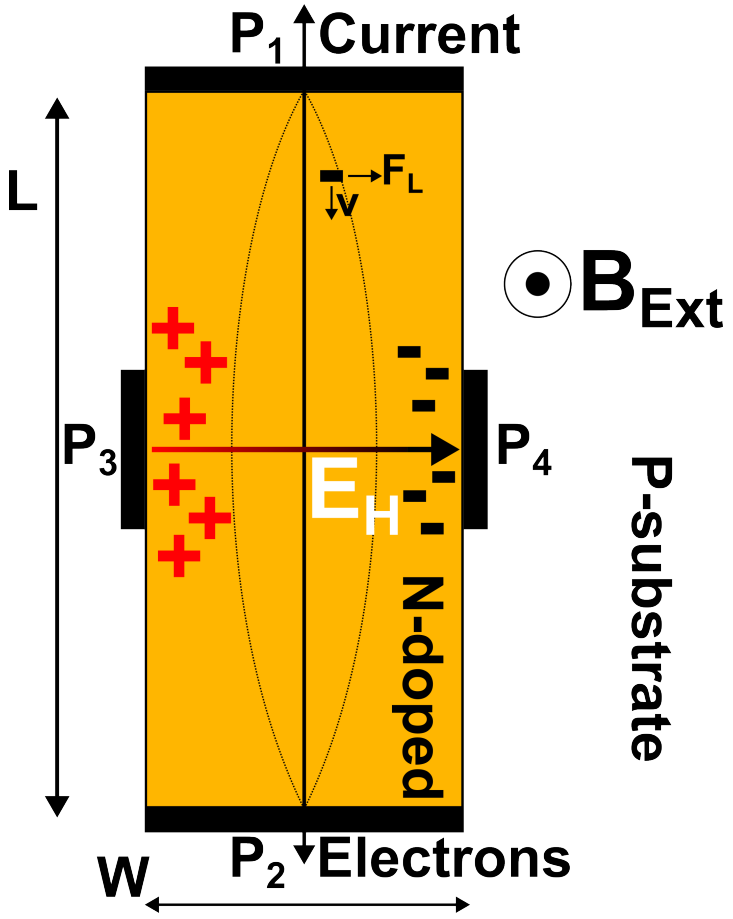

Figure 1.13: Integrated Hall effect plate (top view).

Typically, the lateral size (W and L) of the Hall plate is in the micrometre range, from 10 to 100's of μm, even if some devices can go in the sub-μm range [26], for a few μm of thickness. One of the limitations to the miniaturization of the Hall plate result from the effects observed at lower dimensions, where current lines are not deviated enough to observe a significant Hall voltage and parasitic effects becoming non-negligible, leading to performance degradation.

Hall effect sensors allow measurements with a very large dynamic range of up to several T (such as the MV2 sensor, from the Swiss company Metrolab Technology SA, offering a range of up to 3 T to 30 T [7]), present a very good nonlinearity error, typically 0.1 % of the entire dynamic range of the sensor and offer bandwidth of up to several hundreds of kHz. Since the Hall plate can be made in the same materials as standard CMOS circuits such as silicon, these sensors are intrinsically CMOS compatible, making them easy and inexpensive to manufacture and integrate with larger CMOS circuits (e.g., analog or digital signal conditioning). In addition, it is also possible to modify the Hall plate in a specific configuration (known as a vertical Hall device) to allow measurements of the magnetic field along the plane of the wafer, which allows built-in 3-axis measurements of $\vec{B}$ within the same CMOS chip.

However, the resolution of Hall effect sensors is usually limited to a few μT. Furthermore, Hall effect sensors tend to present strong offset (μT), strong $1/F$ noise from 100 Hz up to a few kHz (above which thermal noise dominates) and temperature dependence (e.g., offset and sensitivity drift) [63], [72]. Since the sensitivity of these sensors also depends on the polarization current, high-sensitivity Hall effect sensors typically consume more current than MR sensors, and very high sensitivity cannot be obtained by increasing the current infinitely ($\lessapprox$ mA) due to technological limitations (e.g., breakdown voltage), making them less suitable for very low power applications as well as for very precise measurements compared to MR or Fluxgate sensors. Hall effect sensors are also sensitive to mechanical constraints (e.g., vibrations or IC packaging) due to the piezoresistive effect observed in silicon [69], [63]. To address these different drawbacks and minimize these effects, different geometries of the Hall plate, other than rectangular, can be used. Furthermore, other materials, often more expensive than silicon (such as gallium arsenide [GaAs]), can also be used, offering better performance, and other more advanced signal conditioning techniques, such as the spinning current approach [29], [70], [9], [61], [69], [62], [35], can also be implemented to minimize the impact of offset and to reduce the $1/F$ noise.

In most commercially available integrated Hall effect sensors, 3-axis sensing is nowadays available with complete embedded circuits of the analog and digital signal processing, with noise levels as low as 100 to 500 nT/$\sqrt{Hz}$ over bandwidths of few kHz and higher. In addition, in these integrated sensors, advanced signal processing circuits and thermal compensation circuits, such as the spinning current, are almost always included, to remove thermal drift, $1/F$ noise and offset from the output signal. These chips are nowadays available as small packages with a size of a few mm^2 and a cost of a few dollars from several companies (e.g., Texas Instruments Incorporated, Asahi Kasei Microdevices Corporation, Melexis or Allegro MicroSystems), allowing them to be easily mounted on printed circuit boards (PCBs) and embedded in more complex systems.

1.4.2 Magnetoresistive sensors

While Hall effect sensors represent a very specific class of magnetometers, MR sensors actually regroup many different technologies, all related by their main characteristic; a resistance change in the sensing element will be measured and proportional to the external magnetic field. Such a category of sensors includes AMR, TMR, or GMR sensors.

AMR sensors

In AMR sensors, a FM material is used, and a current is applied along the anisotropic axis of the device to observe the AMR effect. Hence, the resistance of this material will vary depending on the angle between the direction of the current and the magnetization of the material. However, modern AMR sensors use a variety of techniques to enhance the performance of the basic sensing principle described previously, which suffer from some drawbacks.

By fabricating a structure made of a thin layer of FM material (such as alloys of 80 % nickel [Ni] and 20 % iron [Fe], called permalloy, exhibiting up to 5 % of AMR ratio) covered with thin bands of a more conductive material (such as aluminium [Al] or copper [Cu]) oriented 45° with respect to the easy axis, one can obtain a very important structure called barberpole structure, due to its resemblance to a barber's pole (Fig. 1.14), introduced by the Dutch company Philips in 1975 [54]. This allows cancellation of the impact H_x on the sensor output response (hence no cross-sensitivity H_x-H_y) without the need to use a permanent magnet or electromagnet, allowing the sensitive element to operate in the most linear way possible, as described previously. This structure, which is easy to fabricate in integrated technologies, can then be used to create a Wheatstone bridge to further reduce the offset of the sensor.

Modern AMR sensors are very often based on the Wheatstone bridge of barberpole structures and offer good performance with a dynamic range of a few mT and a resolution of tens of nT/$\sqrt{Hz}$ over bandwidth of hundreds of Hz to several MHz. The non-linearity error of such sensors is typically worse than that of Hall effect sensors, with most commercial products offering non-linearity error inferior to 2 to 5 % of the whole dynamic range. These sensors are nowadays also available as small monolithic IC (mm^2) at a low cost with 3-axis sensing, thermal compensation, and various linearization methods as well as all the analog and digital electronics required. The lateral size of the sensing element of most AMR sensors is typically in the μm range, from 10 to 100 micrometres. In addition, these sensors are the easiest to fabricate in comparison to other MR sensors, making them the first choice for simple integrated systems requiring magnetic sensing.

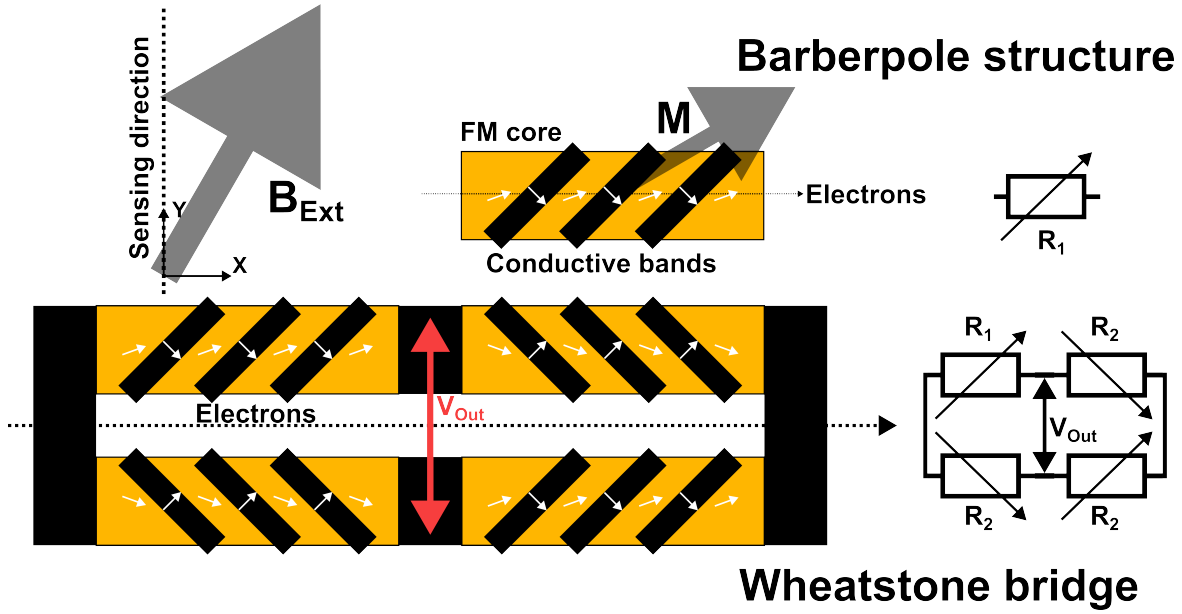

Figure 1.14: AMR Barberpole structure (top view), arranged in a Wheatstone bridge. The white arrows indicate how the current lines are deviated within the structure.

Since AMR sensors are based on FM materials (which can be affected by external magnetic fields), and because $\vec{M}$ should be precisely in the same direction to the current when no field is applied, AMR sensors are usually fabricated with built-in coils, called set-reset coils, used to generate strong magnetic field and restore the magnetization of the FM material along its original direction, which can be affected when the sensor is exposed to a strong magnetic field. Such coils use dedicated circuits capable of generating a very strong pulse of up to several A for a very short duration, as low as tens of ns, that can generate a strong magnetic field pulse capable of restoring $\vec{M}$ of the FM material.

For instance, in the integrated AMR sensor MMC5603NJ (12 nT$\sqrt{Hz}$ over $\pm$ 3 mT), manufactured by the Chinese company Memsic Semiconductor, available in the smallest package among all magnetic sensors with a 400 μm lateral size, this pulse typically last for 375 ns [8] for approximately 130 mA while on the HMC1001 (187 pT$\sqrt{Hz}$ over $\pm$ 200 μT), manufactured by the American company Honeywell International, the pulse can reach 3 A for 2 μs [5]. Hence, while this allows the sensor to be exposed to a strong magnetic field without being permanently damaged as well as reduces the offset through periodic reversals, it adds complexity to the layout of the chip due to the coils, driving circuits, and large storing capacitors required, and increases the power consumption and surface area of such sensor.

TMR and GMR sensors

TMR and GMR sensors are another type of MR sensors, which are extremely popular. These sensors are based on the previously described TMR and GMR principle observed, respectively, in MTJs and SVs and are based on the effect of the external magnetic field $\vec{B}_{Ext}$, capable of tilting the magnetization of the FL while the PL remains stable, thanks to various approaches described previously, resulting in linear resistance variations between R_{AP} and R_P which can be measured. However, to obtain a working sensor, the field must be applied perpendicularly (hard axis) to the anisotropic axis (easy axis) of the FL, because of the hysteresis cycle of any FM material. Otherwise, the FL will remain stable until H_c has been reached, after which sudden resistance changes (PAP or APP) will occur, resulting in the impossibility to observe a linear change. To do so, several approaches can be implemented, among them the use of crossed anisotropy axis or shape anisotropy as well as the use of external magnetic field biasing [79].

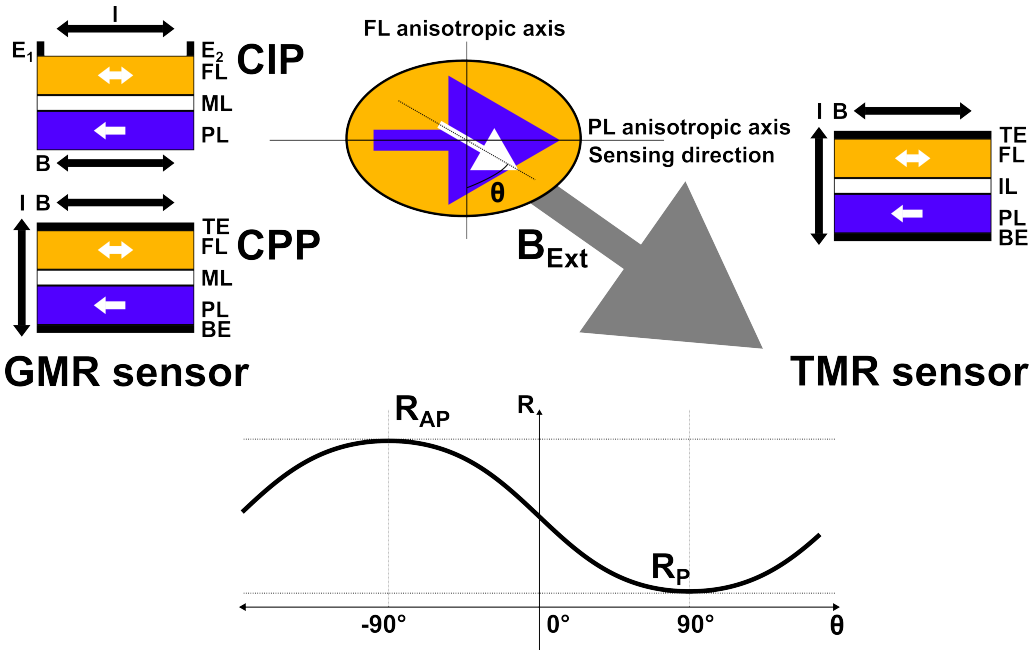

Figure 1.15: GMR and TMR sensor principle (lateral and top view of the SV/MTJ are shown).

In the case of GMR sensors, the current can also be applied sideway of the SV, between two electrodes E_1 and E_2, and not vertically (Fig. 1.15). This configuration, called CIP (current in-plane), in opposition to CPP (current perpendicular plane), offers different performance but is nowadays being replaced by the more recent CPP, usually offering higher GMR ratio and simpler designing equations [23], [41]. However, for a TMR sensor, since the current must tunnel through the barrier of the MTJ, only one configuration of current direction, through the top and bottom electrodes, described previously can be used.

TMR and GMR sensors are widely used, especially in biological applications, because of their very high resolution, often better than AMR sensors and even better than some Fluxgate sensors. Both sensors frequently exhibit resolution down to the sub-nT level (such as the TMR sensor from the Chinese company MultiDimension Technology, the TMR9082 with a noise of 250 pT/$\sqrt{Hz}$ over $\pm$ 400 μ T [15]), with a similar dynamic range compared to AMR sensors (up to few mT) and bandwidth of several kHz and higher. The typical size of these sensing elements (MTJs or SVs) remains in the micrometre domain (typically 1 to 100 μm). One of the most critical reasons for determining such minimal dimensions is related to the noise of such sensors, which is inversely proportional to their dimensions, with lower dimensions leading to higher noise [56], [34], [40]. TMR sensors also offer very low power consumption compared to GMR and AMR sensors, in the μA range. Hence, with very low power consumption and small dimensions, TMR sensors are frequently based on arrays of MTJs, in the form of several MTJs connected in parallel, allowing the sensor noise to be lowered by a factor of $\sqrt{N}$, with N being the number of MTJs. This method allows measurements at room temperature (300 K) with impressive resolution down to the pT level and below [65].

Similarly to AMR sensors, one can also use MTJs or SVs in a Wheatstone bridge to reduce the offset of the sensor. However, such configuration requires the fabrication of devices with opposed response, which is difficult to accurately achieve, as this would require the use of two reference layers that need to be magnetized in opposite directions. To achieve this, several approaches can be used, with one of the most straightforward ways being to fabricate two types of devices with opposed structure, despite other more complex methods also being possible. In addition to such difficulty, TMR and GMR sensors also remain dependent on the temperature (due to the temperature dependence of TMR and GMR effect) and are usually requiring thermal compensation, as well as presenting stronger offset than Fluxgate sensors. TMR devices (i.e., MTJs) are also extremely sensitive to ESDs (electrostatic discharges), which can easily break the thin insulating layer and destroy the sensor. Finally, for physical reasons, GMR and TMR sensors are almost always based on in-plane configuration of MTJs and SVs, resulting in sensing capabilities along the plane of the wafer. Perpendicular GMR or TMR sensors would require the use of pMTJs or pSVs, based on PMA, resulting in poor performance from a sensor point of view as it becomes very difficult to maintain the equilibrium position between the two states. Furthermore, due to manufacturing capability, the fabrication of 90°-rotated MTJs or SVs is impossible (which would allow measurements along the vertical axis of the wafer), making the production of three-dimensional integrated TMR or GMR sensing highly challenging (one of the reasons is the impossibility to fabricate thin film other than along the plane of the wafer). Hence, almost all existing TMR or GMR sensors are sensitive only to the axis parallel to the plane of the wafer. Measurements along the vertical axis require the use of other technologies capable of vertical sensing (e.g., Hall effect, AMR, Fluxgate), or use in-plane TMR/GMR sensing elements mechanically rotated. To this day, a unique TMR sensor that allows 3-axis sensing is commercially available, manufactured by the Japanese company Asahi Kasei Microdevice Corporation, the AK09940A available in small 1.6 mm x 1.6 mm package and with an average noise of 5 nT/$\sqrt{Hz}$ over $\pm$ 1.2 mT.

1.4.3 Fluxgate sensors

Discovered in the mid-50's [20], fluxgate sensors rely on a soft ferromagnetic core, made of a soft FM material, such as permalloy, surrounded by at least two different coils (Fig. 1.16). On one side of the FM core, an excitation coil is driven with an alternating (ac) current, typically in the range of a few kHz to tens of kHz, resulting in the generation of an ac magnetic field $\vec{B}_1$, at its centre. This ac magnetic field will be strong enough so that it will periodically saturate the magnetization $\vec{M}$ of the soft FM core, positively or negatively.

If an ac current passing through a coil, made of N loops, can generate a magnetic field, an ac magnetic field passing through the same coil will also generate an induced output voltage due to Faraday's law, expressed as $\varepsilon = -N\frac{d\phi}{dt}$, where ε is the induced electromotive force, expressed in V, and ϕ is the magnetic flux passing through the coil ($\phi = \iint_S \vec{B} d\vec{S}$ with $\vec{S}$ being the surface of the coil).

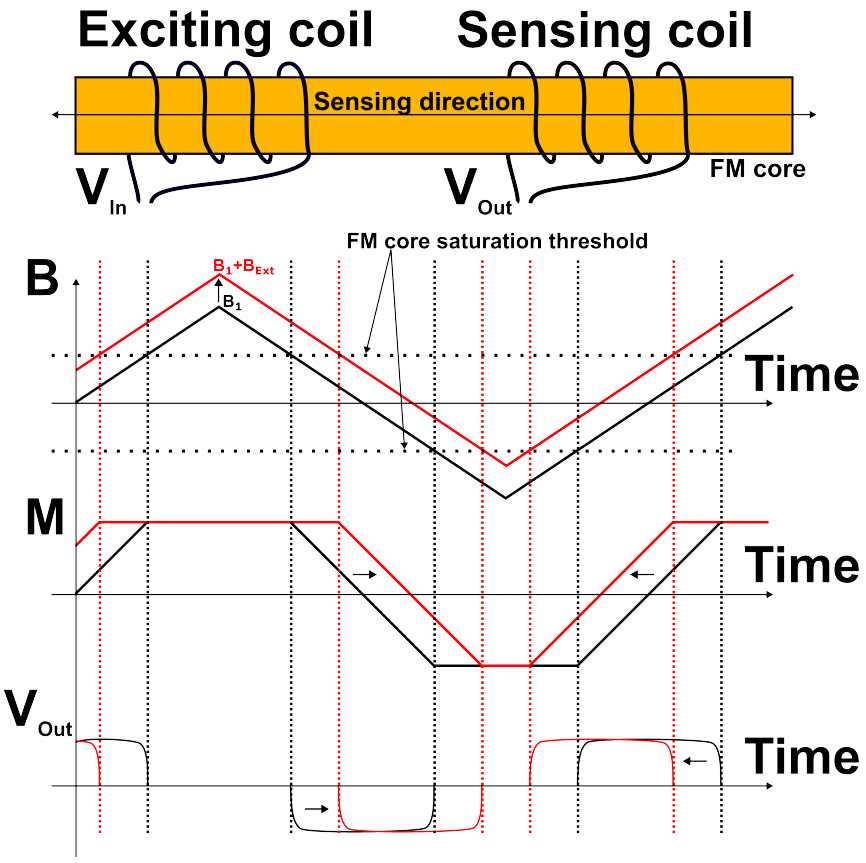

Figure 1.16: Fluxgate sensor principle.

Therefore, on the other side of the FM core, the second coil, called the sensing coil, will be excited by the alternating magnetization of the FM core and will generate an output voltage proportional to it. According to the hysteresis cycle of the material, the FM core will generate a magnetic field at the centre of the sensing coil which can be approximated by $\vec{B}_2 \approx \mu_0 \vec{M}$. In addition, considering that $\vec{B}_{Ext}$ is a very low frequency (over one period of the excitation signal, V_{In}) or even a constant field (dc), it can be assumed that its contribution to the output of the sensing coil, through Faraday's law is null, $d\phi_{\vec{B}_{Ext}}/dt \approx 0$.

Since the ac current driving the excitation coil is saturating the FM core at a known and fixed frequency and amplitude, any dc or low-frequency external magnetic field $\vec{B}_{Ext}$ will add up to the generated exciting field $\vec{B}_1$, resulting in the saturation of the FM core at a different time (earlier or later). As a result, the sensing coil will generate an output voltage that will vary over time according to the variations of the external magnetic field. Using the output voltage of the sensing coil through different signal processing patterns and circuits [74], [73], [71] magnetic field values can then be extracted.

Fluxgate sensors offer very high sensitivity with low noise (sub-nT/$\sqrt{Hz}$, as low as in the pT resolution) [74], [73], [71] over a dynamic range of a few mT and a few kHz to tens of kHz of bandwidth making this technology one of the best choices for high-resolution magnetic field measurements among the Hall effect and MR technologies described. Furthermore, 3-axis sensing can be easily achieved by using three different coils mounted in the three directions. These sensors are also less sensitive to temperature variations and have a smaller offset than other MR and Hall effect sensors, typically in the nT range. Finally, different geometries of coils or FM core material can also be used to improve the performance of the sensor.

However, the noise of fluxgate sensors is mainly induced by the Barkhausen effect, described previously, being a type of noise observed in ferromagnetic materials. Barkhausen noise is due to the discrete changes in the different magnetic domains within the material, causing a non-continuous evolution of the magnetization in the hysteresis loop (Fig. 1.4). For this reason, such noise can be minimized by using a larger FM core, to minimize the impact of each individual magnetic domain. Hence, in addition to the complexity of manufacturing coils in ICs, especially in three dimensions, the minimization of the noise of the Fluxgate sensor implies the use of a larger FM core, usually in the cm range, which is also in contradiction with microelectronics principles, targeting the miniaturization of components. For these two main reasons, fluxgate sensors are a poor choice in terms of integrability and dimensions, which can be directly observed in the market of integrated magnetic sensors. Over the entire market[1], one unique commercial and single axis integrated fluxgate sensor is currently available, the DRV425, fabricated in a compact 4 mm x 4 mm package with a noise of 1-2 nT/$\sqrt{Hz}$ over ± 2 mT [3], manufactured by the American company Texas Instruments Incorporated, with more than a thousand references available for Hall effect and MR sensors.

[1]Data extracted in May 2024 on Digikey.com.

Bibliography

[1] 1990: Magnetoresistive read-head HDD introduced | The Storage Engine | Computer History Museum. URL: https://www.computerhistory.org/storageengine/magnetoresistive-read-head-hdd-introduced/.

[2] 1991: Solid State Drive module demonstrated | The Storage Engine | Computer History Museum. URL: https://www.computerhistory.org/storageengine/solid-state-drive-module-demonstrated/.

[3] DRV425 data sheet, product information and support | TI.com. URL: https://www.ti.com/product/DRV425?utm_source=google&utm_medium=cpc&utm_campaign=asc-null-null-GPN_EN-cpc-pf-google-eu&utm_content=DRV425&ds_k=DRV425&DCM=yes&gad_source=1&gclid=EAIaIQobChMI7IH_7MG3hgMV5aloCR1W3glbEAAYASAAEgKIv_D_BwE&gclsrc=aw.ds.

[4] Global hard disk drive (HDD) shipments 1976-2022. URL: https://www.statista.com/statistics/398951/global-shipment-figures-for-hard-disk-drives/.

[5] Low Field High Precision Linear 1 and 2-Axis Analog Magnetic Sensors. URL: https://aerospace.honeywell.com/us/en/products-and-services/product/hardware-and-systems/sensors/low-field-high-precision-linear-1-and-2-axis-analog-magnetic-sen.

[6] Magnetic Sensor Market Size & Growth Forecast to 2023-2030. URL: https://www.kbvresearch.com/magnetic-sensor-market/.

[7] MagVector™ MV2 Magnetometer. URL: https://www.metrolab.com/products/magvector-mv2-magnetometer/.

[8] MMC5603NJ-AMR Magnetometer-MEMSIC Semiconductor Co., Ltd. URL: https://www.memsic.com/magnetometer-2.

[9] Monolithic Magnetic Hall Sensor ICs Using Dynamic Quadrature Offset Cancellation. URL: https://www.allegromicro.com/en/insights-and-innovations/technical-documents/hall-effect-sensor-ic-publications/monolithic-magnetic-hall-sensor-ics-using-dynamic-quadrature-offset-cancellation.

[10] On-board Magnetic Sensors Market. URL: https://www.futuremarketinsights.com/reports/on-board-magnetic-sensors-market.

[11] Renesas Develops Embedded MRAM Macro that Achieves over 200MHz Fast Random-Read Access and a 10.4 MB/s Fast Write Throughput for High Performance MCUs | Renesas. URL: https://www.renesas.com/us/en/about/press-room/renesas-develops-embedded-mram-macro-achieves-over-200mhz-fast-random-read-access-and-104-mbs-fast.

[12] Samsung to expand MRAM applications - THE ELEC, Korea Electronics Industry Media. URL: https://www.thelec.net/news/articleView.html?idxno=2314.

[13] Semiconductor market size 2024. URL: https://www.statista.com/statistics/266973/global-semiconductor-sales-since-1988/.

[14] Solid State Drives Market by Form Factor, Interface, Technology | COVID-19 Impact Analysis | MarketsandMarkets™. URL: https://www.marketsandmarkets.com/Market-Reports/solid-state-drives-market-75076578.html.

[15] TMR9082 - Low Noise Series - Sensors - MDT - MultiDimension Technology | Magnetic Sensor Manufacturer(TMR · GMR · AMR). URL: http://www.dowaytech.com/en/2427.html.

[16] Developing the "Industry's Most Energy-Efficient" Next-Generation MRAM, Selected as IEDM Highlight Paper, August 2023. URL: https://semiconductor.samsung.com/news-events/tech-blog/developing-the-industrys-most-energy-efficient-next-generation-mram-selected-as-iedm-highlight-paper.

[17] Yole Group - Follow the latest trend news in the Semiconductor Industry, July 2023. URL: https://www.yolegroup.com/articles/.

[18] Magnetism in the Greco-Roman World, March 2024. URL: https://ethw.org/Magnetism_in_the_Greco-Roman_World.

[19] Dmytro Apalkov, Bernard Dieny, and J. M. Slaughter. Magnetoresistive Random Access Memory. *Proceedings of the IEEE*, 104(10):1796–1830, October 2016. Conference Name: Proceedings of the IEEE. doi:10.1109/JPROC.2016.2590142.

[20] Aviation Week. *Aviation Week 1943-10-18*. October 1943. URL: http://archive.org/details/Aviation_Week_1943-10-18.

[21] M. N. Baibich, J. M. Broto, A. Fert, F. Nguyen Van Dau, F. Petroff, P. Etienne, G. Creuzet, A. Friederich, and J. Chazelas. Giant Magnetoresistance of (001)Fe/(001)Cr Magnetic Superlattices. *Physical Review Letters*, 61(21):2472–2475, November 1988. doi:10.1103/PhysRevLett.61.2472.

[22] Prashanth Barla, Vinod Kumar Joshi, and Somashekara Bhat. Spintronic devices: a promising alternative to CMOS devices. *Journal of Computational Electronics*, 20(2):805–837, April 2021. doi:10.1007/s10825-020-01648-6.

[23] J Bass and W. P Pratt. Current-perpendicular (CPP) magnetoresistance in magnetic metallic multilayers. *Journal of Magnetism and Magnetic Materials*, 200(1):274–289, October 1999. doi:10.1016/S0304-8853(99)00316-9.

[24] L. Berger. Emission of spin waves by a magnetic multilayer traversed by a current. *Physical Review B*, 54(13):9353–9358, October 1996. doi:10.1103/PhysRevB.54.9353.

[25] G. Binasch, P. Grünberg, F. Saurenbach, and W. Zinn. Enhanced magnetoresistance in layered magnetic structures with antiferromagnetic interlayer exchange. *Physical Review B*, 39(7):4828–4830, March 1989. doi:10.1103/PhysRevB.39.4828.

[26] G. Boero, M. Demierre, P. . A. Besse, and R. S. Popovic. Micro-Hall devices: performance, technologies and applications. *Sensors and Actuators A: Physical*, 106(1):314–320, September 2003. doi:10.1016/S0924-4247(03)00192-4.

[27] J. Callaway and C. S. Wang. Energy bands in ferromagnetic iron. *Physical Review B*, 16(5):2095–2105, September 1977. Publisher: American Physical Society. doi:10.1103/PhysRevB.16.2095.

[28] Jeongdong Choe. Memory Technology 2021: Trends & Challenges. In *2021 International Conference on Simulation of Semiconductor Processes and Devices (SISPAD)*, pages 111–115, September 2021. ISSN: 1946-1577. doi:10.1109/SISPAD54002.2021.9592547.

[29] Michel Demierre, Sergio Pesenti, Javad Frounchi, Pierre-André Besse, and Radivoje S. Popović. Reference magnetic actuator for self-calibration of a very small Hall sensor array. *Sensors and Actuators A: Physical*, 97-98:39–46, April 2002. doi:10.1016/S0924-4247(01)00857-3.

[30] Bernard Dieny and I. Lucian Prejbeanu. Magnetic Random-Access Memory. In *Introduction to Magnetic Random-Access Memory*, pages 101–164. John Wiley & Sons, Ltd, 2017. Section: 5 _eprint: https://onlinelibrary.wiley.com/doi/pdf/10.1002/9781119079415.ch5. doi:10.1002/9781119079415.ch5.

[31] Gianfranco Durin and Stefano Zapperi. The Barkhausen effect, April 2004. arXiv:cond-mat/0404512. URL: http://arxiv.org/abs/cond-mat/0404512.

[32] D. Edelstein, M. Rizzolo, D. Sil, A. Dutta, J. DeBrosse, M. Wordeman, A. Arceo, I. C. Chu, J. Demarest, E. R. J. Edwards, E. R. Evarts, J. Fullam, A. Gasasira, G. Hu, M. Iwatake, R. Johnson, V. Katragadda, T. Levin, J. Li, Y. Liu, C. Long, T. Maffitt, S. McDermott, S. Mehta, V. Mehta, D. Metzler, J. Morillo, Y. Nakamura, S. Nguyen, P. Nieves, V. Pai, R. Patlolla, R. Pujari, R. Southwick, T. Standaert, O. van der Straten, H. Wu, C.-C. Yang, D. Houssameddine, J. M. Slaughter, and D. C. Worledge. A 14 nm Embedded STT-MRAM CMOS Technology. In *2020 IEEE International Electron Devices Meeting (IEDM)*, pages 11.5.1–11.5.4, December 2020. ISSN: 2156-017X. doi:10.1109/IEDM13553.2020.9371922.

[33] Leo Esaki. New Phenomenon in Narrow Germanium p - n Junctions. *Physical Review*, 109(2):603–604, January 1958. doi:10.1103/PhysRev.109.603.

[34] C. Fermon and M. Pannetier-Lecoeur. Noise in GMR and TMR Sensors. In Candid Reig, Susana Cardoso, and Subhas Chandra Mukhopadhyay, editors, *Giant Magnetoresistance (GMR) Sensors: From Basis to State-of-the-Art Applications*, pages 47–70. Springer, Berlin, Heidelberg, 2013. doi:10.1007/978-3-642-37172-1_3.

[35] V. Frick, L. Hebrard, P. Poure, and F. Braun. CMOS Microsystem Front-End for MicroTesla Resolution Magnetic Field Measurement. *Analog Integr. Circuits Signal Process.*, 36(1-2):165–174, July 2003. doi:10.1023/A:1024426420583.

[36] Walther Gerlach and Otto Stern. Der experimentelle Nachweis der Richtungsquantelung im Magnetfeld. *Zeitschrift fur Physik*, 9(1):349–352, December 1922. doi:10.1007/BF01326983.

[37] T.L. Gilbert. A phenomenological theory of damping in ferromagnetic materials. *IEEE Transactions on Magnetics*, 40(6):3443–3449, November 2004. Conference Name: IEEE Transactions on Magnetics. doi:10.1109/TMAG.2004.836740.

[38] E. H. Hall. On a New Action of the Magnet on Electric Currents. *American Journal of Mathematics*, 2(3):287–292, 1879. Publisher: Johns Hopkins University Press. doi:10.2307/2369245.

[39] Michael Harder, Yongsheng Gui, and Can-Ming Hu. Electrical detection of magnetization dynamics via spin rectification effects. *Physics Reports*, 661:1–59, November 2016. doi:10.1016/j.physrep.2016.10.002.

[40] K. Hayakawa, S. Kanai, T. Funatsu, J. Igarashi, B. Jinnai, W. A. Borders, H. Ohno, and S. Fukami. Nanosecond Random Telegraph Noise in In-Plane Magnetic Tunnel Junctions. *Physical Review Letters*, 126(11):117202, March 2021. doi:10.1103/PhysRevLett.126.117202.

[41] Atsufumi Hirohata, Keisuke Yamada, Yoshinobu Nakatani, Ioan-Lucian Prejbeanu, Bernard Diény, Philipp Pirro, and Burkard Hillebrands. Review on spintronics: Principles and device applications. *Journal of Magnetism and Magnetic Materials*, 509:166711, September 2020. doi:10.1016/j.jmmm.2020.166711.

[42] S.R. Hofstein and G. Warfield. The insulated gate tunnel junction triode. *IEEE Transactions on Electron Devices*, 12(2):66–76, February 1965. Conference Name: IEEE Transactions on Electron Devices. doi:10.1109/T-ED.1965.15455.

[43] Market Research Future https://www.marketresearchfuture.com. Solid State Drive (SSD) Market Trends, Share and Forecast 2032. URL: https://www.marketresearchfuture.com/reports/solid-states-drives-market-1028.

[44] Technavio https://www.technavio.com. MRAM Market Size, Share & Trends [2023 Report]. URL: https://www.technavio.com/report/mram-market-industry-analysis.

[45] F. Hund. Zur Deutung der Molekelspektren. I. *Zeitschrift fur Physik*, 40(10):742–764, October 1927. doi:10.1007/BF01400234.

[46] S. Ikeda, J. Hayakawa, Y. Ashizawa, Y. M. Lee, K. Miura, H. Hasegawa, M. Tsunoda, F. Matsukura, and H. Ohno. Tunnel magnetoresistance of 604% at 300K by suppression of Ta diffusion in CoFeB\/MgO\/CoFeB pseudo-spin-valves annealed at high temperature. *Applied Physics Letters*, 93(8):082508, August 2008. doi:10.1063/1.2976435.

[47] S. Ikeda, K. Miura, H. Yamamoto, K. Mizunuma, H. D. Gan, M. Endo, S. Kanai, J. Hayakawa, F. Matsukura, and H. Ohno. A perpendicular-anisotropy CoFeB–MgO magnetic tunnel junction. *Nature Materials*, 9(9):721–724, September 2010. Publisher: Nature Publishing Group. doi:10.1038/nmat2804.

[48] Y. P. Ivanov and O. Chubykalo-Fesenko. 14 - Micromagnetic simulations of cylindrical magnetic nanowires. In Manuel Vázquez, editor, *Magnetic Nano- and Microwires*, Woodhead Publishing Series in Electronic and Optical Materials, pages 423–448. Woodhead Publishing, January 2015. doi:10.1016/B978-0-08-100164-6.00014-X.

[49] Vinod Kumar Joshi, Prashanth Barla, Somashekara Bhat, and Brajesh Kumar Kaushik. From MTJ Device to Hybrid CMOS/MTJ Circuits: A Review. *IEEE Access*, 8:194105–194146, 2020. doi:10.1109/ACCESS.2020.3033023.

[50] M. Julliere. Tunneling between ferromagnetic films. *Physics Letters A*, 54(3):225–226, September 1975. doi:10.1016/0375-9601(75)90174-7.

[51] Tadao Kasuya. A Theory of Metallic Ferro- and Antiferromagnetism on Zener's Model. *Progress of Theoretical Physics*, 16(1):45–57, July 1956. doi:10.1143/PTP.16.45.

[52] Mohammed Asadullah Khan, Jian Sun, Bodong Li, Alexander Przybysz, and Jürgen Kosel. Magnetic sensors-A review and recent technologies. *Engineering Research Express*, 3(2):022005, June 2021. Publisher: IOP Publishing. doi:10.1088/2631-8695/ac0838.

[53] Jongyeon Kim, Hui Zhao, Yanfeng Jiang, Angeline Klemm, Jian-Ping Wang, and Chris H. Kim. Scaling analysis of in-plane and perpendicular anisotropy magnetic tunnel junctions using a physics-based model. In *72nd Device Research Conference*, pages 155–156, June 2014. ISSN: 1548-3770. doi:10.1109/DRC.2014.6872344.

[54] K. Kuijk, W. van Gestel, and F. Gorter. The barber pole, a linear magnetoresistive head. *IEEE Transactions on Magnetics*, 11(5):1215–1217, September 1975. Conference Name: IEEE Transactions on Magnetics. doi:10.1109/TMAG.1975.1058886.

[55] L. Landau and E. Lifshitz. On the theory of the dispersion of magnetic permeability in ferromagnetic bodies. In L. P. Pitaevski, editor, *Perspectives in Theoretical Physics*, pages 51–65. Pergamon, Amsterdam, January 1992. doi:10.1016/B978-0-08-036364-6.50008-9.

[56] Z. Q. Lei, G. J. Li, William F. Egelhoff, P. T. Lai, and Philip W. T. Pong. Review of Noise Sources in Magnetic Tunnel Junction Sensors. *IEEE Transactions on Magnetics*, 47(3):602–612, March 2011. Conference Name: IEEE Transactions on Magnetics. doi:10.1109/TMAG.2010.2100814.

[57] T. McGuire and R. Potter. Anisotropic magnetoresistance in ferromagnetic 3d alloys. *IEEE Transactions on Magnetics*, 11(4):1018–1038, July 1975. Conference Name: IEEE Transactions on Magnetics. doi:10.1109/TMAG.1975.1058782.

[58] Eugen Merzbacher. The Early History of Quantum Tunneling. *Physics Today*, 55(8):44–49, August 2002. doi:10.1063/1.1510281.

[59] Abdeljalil Metioui. Brief Historical Review about Magnetism: From the Ancient Greeks up the Beginning of the XXth Century. *Journal of Biomedical Research & Environmental Sciences*, 3(9):1101–1107, October 2022. doi:10.37871/jbres1561.

[60] N. F. Mott. Metal-Insulator Transition. *Reviews of Modern Physics*, 40(4):677–683, October 1968. doi:10.1103/RevModPhys.40.677.

[61] P. J. A. Munter. A low-offset spinning-current hall plate. *Sensors and Actuators A: Physical*, 22(1):743–746, June 1990. doi:10.1016/0924-4247(89)80069-X.

[62] P. J. A. Munter and D. C. van Duyn. Spatial symmetry of transduction effects in Hall plates. *Sensors and Actuators A: Physical*, 31(1):206–209, March 1992. doi:10.1016/0924-4247(92)80105-C.

[63] C. Müller-Schwanneke, F. Jost, K. Marx, S. Lindenkreuz, and K. von Klitzing. Offset reduction in silicon Hall sensors. *Sensors and Actuators A: Physical*, 81(1):18–22, April 2000. doi:10.1016/S0924-4247(99)00163-6.

[64] Hideo Ohno, Tetsuo Endoh, Takahiro Hanyu, Naoki Kasai, and Shoji Ikeda. Magnetic tunnel junction for nonvolatile CMOS logic. In *2010 International Electron Devices Meeting*, pages 9.4.1–9.4.4, December 2010. ISSN: 2156-017X. doi:10.1109/IEDM.2010.5703329.

[65] Mikihiko Oogane, Kosuke Fujiwara, Akitake Kanno, Takafumi Nakano, Hiroshi Wagatsuma, Tadashi Arimoto, Shigemi Mizukami, Seiji Kumagai, Hitoshi Matsuzaki, Nobukazu Nakasato, and Yasuo Ando. Sub-pT magnetic field detection by tunnel magnetoresistive sensors. *Applied Physics Express*, 14(12):123002, November 2021. Publisher: IOP Publishing. doi:10.35848/1882-0786/ac3809.

[66] Stuart S. P. Parkin, Christian Kaiser, Alex Panchula, Philip M. Rice, Brian Hughes, Mahesh Samant, and See-Hun Yang. Giant tunnelling magnetoresistance at room temperature with MgO (100) tunnel barriers. *Nature Materials*, 3(12):862–867, December 2004. Publisher: Nature Publishing Group. doi:10.1038/nmat1256.

[67] S.z. Peng, Y. Zhang, M.x. Wang, Y.g. Zhang, and Weisheng Zhao. Magnetic Tunnel Junctions for Spintronics: Principles and Applications. In *Wiley Encyclopedia of Electrical and Electronics Engineering*, pages 1–16. John Wiley & Sons, Ltd, 2014. _eprint: https://onlinelibrary.wiley.com/doi/pdf/10.1002/047134608X.W8231. doi:10.1002/047134608X.W8231.

[68] N. Perrissin, S. Lequeux, N. Strelkov, A. Chavent, L. Vila, L. D. Buda-Prejbeanu, S. Auffret, R. C. Sousa, I. L. Prejbeanu, and B. Dieny. A highly thermally stable sub-20 nm magnetic random-access memory based on perpendicular shape anisotropy. *Nanoscale*, 10(25):12187–12195, July 2018. Publisher: The Royal Society of Chemistry. doi:10.1039/C8NR01365A.

[69] R. S. Popovic, J. A. Flanagan, and P. A. Besse. The future of magnetic sensors. *Sensors and Actuators A: Physical*, 56(1):39–55, August 1996. doi:10.1016/0924-4247(96)01285-X.

[70] R. S Popovic, Z Randjelovic, and D Manic. Integrated Hall-effect magnetic sensors. *Sensors and Actuators A: Physical*, 91(1):46–50, June 2001. doi:10.1016/S0924-4247(01)00478-2.

[71] F. Primdahl. The fluxgate magnetometer. *Journal of Physics E: Scientific Instruments*, 12(4):241, April 1979. doi:10.1088/0022-3735/12/4/001.

[72] P. Ripka. Noise and stability of magnetic sensors. *Journal of Magnetism and Magnetic Materials*, 157-158:424–427, May 1996. doi:10.1016/0304-8853(95)01177-3.

[73] Pavel Ripka. Review of fluxgate sensors. *Sensors and Actuators A: Physical*, 33(3):129–141, June 1992. doi:10.1016/0924-4247(92)80159-Z.

[74] Pavel Ripka. Advances in fluxgate sensors. *Sensors and Actuators A: Physical*, 106(1):8–14, September 2003. doi:10.1016/S0924-4247(03)00094-3.

[75] Philipp Ritzinger and Karel Výborný. Anisotropic magnetoresistance: materials, models and applications. *Royal Society Open Science*, 10(10):230564, October 2023. Publisher: Royal Society. doi:10.1098/rsos.230564.

[76] M. A. Ruderman and C. Kittel. Indirect Exchange Coupling of Nuclear Magnetic Moments by Conduction Electrons. *Physical Review*, 96(1):99–102, October 1954. doi:10.1103/PhysRev.96.99.

[77] Soheil Salehi, Deliang Fan, and Ronald F. Demara. Survey of STT-MRAM Cell Design Strategies: Taxonomy and Sense Amplifier Tradeoffs for Resiliency. *ACM Journal on Emerging Technologies in Computing Systems*, 13(3):1–16, July 2017. doi:10.1145/2997650.

[78] Takanobu Shinoda, Junta Igarashi, Butsurin Jinnai, Shunsuke Fukami, and Hideo Ohno. Pitch Scaling Prospect of Ultra-Small Magnetic Tunnel Junctions for High-Density STT-MRAM: Effects of Magnetostatic Interference From Neighboring Bits. *IEEE Electron Device Letters*, 45(2):184–187, February 2024. Conference Name: IEEE Electron Device Letters. doi:10.1109/LED.2023.3345743.

[79] Ana V. Silva, Diana C. Leitao, João Valadeiro, José Amaral, Paulo P. Freitas, and Susana Cardoso. Linearization strategies for high sensitivity magnetoresistive sensors. *The European Physical Journal Applied Physics*, 72(1):10601, October 2015. doi:10.1051/epjap/2015150214.

[80] J. C. Slonczewski. Current-driven excitation of magnetic multilayers. *Journal of Magnetism and Magnetic Materials*, 159(1):L1–L7, June 1996. doi:10.1016/0304-8853(96)00062-5.

[81] Otto Stern. Ein Weg zur experimentellen Prüfung der Richtungsquantelung im Magnetfeld. *Zeitschrift fur Physik*, 7(1):249–253, December 1921. doi:10.1007/BF01332793.

[82] Edmund Clifton Stoner and E. P. Wohlfarth. A mechanism of magnetic hysteresis in heterogeneous alloys. *Philosophical Transactions of the Royal Society of London. Series A, Mathematical and Physical Sciences*, 240(826):599–642, January 1997. Publisher: Royal Society. doi:10.1098/rsta.1948.0007.

[83] S. Tehrani, J.M. Slaughter, M. Deherrera, B.N. Engel, N.D. Rizzo, J. Salter, M. Durlam, R.W. Dave, J. Janesky, B. Butcher, K. Smith, and G. Grynkewich. Magnetoresistive random access memory using magnetic tunnel junctions. *Proceedings of the IEEE*, 91(5):703–714, May 2003. Conference Name: Proceedings of the IEEE. doi:10.1109/JPROC.2003.811804.

[84] William Thomson. XIX. On the electro-dynamic qualities of metals:—Effects of magnetization on the electric conductivity of nickel and of iron. *Proceedings of the Royal Society of London*, 8:546–550, January 1997. Publisher: Royal Society. doi:10.1098/rspl.1856.0144.

[85] M. Tsoi, R. E. Fontana, and S. S. P. Parkin. Magnetic domain wall motion triggered by an electric current. *Applied Physics Letters*, 83(13):2617–2619, September 2003. doi:10.1063/1.1578165.

[86] M. Tsoi, A. G. M. Jansen, J. Bass, W.-C. Chiang, M. Seck, V. Tsoi, and P. Wyder. Excitation of a Magnetic Multilayer by an Electric Current. *Physical Review Letters*, 80(19):4281–4284, May 1998. doi:10.1103/PhysRevLett.80.4281.

[87] M. Tsoi, A. G. M. Jansen, J. Bass, W.-C. Chiang, V. Tsoi, and P. Wyder. Generation and detection of phase-coherent current-driven magnons in magnetic multilayers. *Nature*, 406(6791):46–48, July 2000. Publisher: Nature Publishing Group. doi:10.1038/35017512.

[88] S. Tumanski. *Thin Film Magnetoresistive Sensors*. CRC Press, Boca Raton, June 2001. doi:10.1201/9781420033243.

[89] K. Watanabe, B. Jinnai, S. Fukami, H. Sato, and H. Ohno. Shape anisotropy revisited in single-digit nanometer magnetic tunnel junctions. *Nature Communications*, 9(1):663, February 2018. Publisher: Nature Publishing Group. doi:10.1038/s41467-018-03003-7.

[90] Liqiong Wei, Juan G. Alzate, Umut Arslan, Justin Brockman, Nilanjan Das, Kevin Fischer, Tahir Ghani, Oleg Golonzka, Patrick Hentges, Rawshan Jahan, Pulkit Jain, Blake Lin, Mesut Meterelliyoz, Jim OrDonnell, Conor Puls, Pedro Quintero, Tanaya Sahu, Meenakshi Sekhar, Ajay Vangapaty, Chris Wiegand, and Fatih Hamzaoglu. 13.3 A 7Mb STT-MRAM in 22FFL FinFET Technology with 4ns Read Sensing Time at 0.9V Using Write-Verify-Write Scheme and Offset-Cancellation Sensing Technique. In *2019 IEEE International Solid-State Circuits Conference - (ISSCC)*, pages 214–216, San Francisco, CA, USA, February 2019. IEEE. doi:10.1109/ISSCC.2019.8662444.

[91] Y. Yafet. Ruderman-Kittel-Kasuya-Yosida range function of a one-dimensional free-electron gas. *Physical Review B*, 36(7):3948–3949, September 1987. doi:10.1103/PhysRevB.36.3948.

[92] Kay Yakushiji, Kenji Noma, Takeshi Saruya, Hitoshi Kubota, Akio Fukushima, Taro Nagahama, Shinji Yuasa, and Koji Ando. High Magnetoresistance Ratio and Low Resistance–Area Product in Magnetic Tunnel Junctions with Perpendicularly Magnetized Electrodes. *Applied Physics Express*, 3(5):053003, May 2010. Publisher: IOP Publishing. doi:10.1143/APEX.3.053003.

[93] Kei Yosida. Magnetic Properties of Cu-Mn Alloys. *Physical Review*, 106(5):893–898, June 1957. doi:10.1103/PhysRev.106.893.

[94] S. Yuasa and D. D. Djayaprawira. Giant tunnel magnetoresistance in magnetic tunnel junctions with a crystalline MgO(0 0 1) barrier. *Journal of Physics D: Applied Physics*, 40(21):R337, October 2007. doi:10.1088/0022-3727/40/21/R01.

[95] S. Zhang, P. M. Levy, and A. Fert. Mechanisms of Spin-Polarized Current-Driven Magnetization Switching. *Physical Review Letters*, 88(23):236601, May 2002. Publisher: American Physical Society. doi:10.1103/PhysRevLett.88.236601.

Chapter 1 has presented all the necessary notions required to understand the topics addressed in this manuscript. In the first place, most important notions of magnetism are introduced, describing all the physical aspects of magnetic field and physical phenomena observed in the scope of this work. In a second time, we introduced important notions about magnetic memories and magnetic tunnel junctions, that are nowadays used in magnetic memories and magnetic sensors. Finally, a brief description about magnetic sensors and few of the most important integrated sensing technologies are detailed. Through this chapter, the reader has an overview of all the basic notions used in Chapter 2 and 3, where the sensor principles are detailed and described.

Subsequently, **Chapter 2** introduces all the key principles and elements of the newly demonstrated magnetic sensor. The working principle of the sensor, the junctions used as well as the electronics developed to use these junctions as sensing elements are described, allowing for the understanding of such new measurement principle.

Chapter 2

High-Coercivity STT-MTJ Magnetic Sensor

2.1 Introduction

Although TMR sensors are based on a relatively straightforward way to operate MTJs as sensing units, as described in Chapter 1, the goal of this Ph. D. thesis is to demonstrate the use of perpendicular and nanoscale STT-MTJs, originally designed for MRAMs applications, in an unconventional way, to operate them as magnetic sensing units. Such type of magnetic sensor offers several advantages, which will be described in Chapter 4, compared to existing integrated technologies (Hall effect, AMR/GMR/TMR or Fluxgate sensors), as described in the previous chapter and in the introduction.

These integrated sensors come with significant drawbacks. Hall effect sensors dimensions are usually limited to few μm by physical limits, as the currents lines are not deviated enough at small dimensions, resulting in the absence of measurable sensitivity. MR sensors also suffer from such dimension related issues, as lower dimensions MR sensors result in higher noise. For these reasons, most existing sensors remain in the μm range and above, limiting the possible applications requiring true punctual measurements, such as photolithographic mask alignment or magnetic particles and beads detection. In addition, these sensors also suffer from bandwidth limitations in the tens of kHz range, resulting in the absence of applications at high frequency. This includes, for instance, current measurements at high bandwidth, required to meet new industrial requirements, or rotation counters. Lower power consumption or CMOS compatibility are also among the advantages of such technology. Hence, such STT-MTJ integrated magnetic sensor aims to alleviate drawbacks observed in standard technologies.

Chapter 2 aims to present the basics and key elements of the newly demonstrated magnetic sensor based on STT-MTJs. This chapter is divided into five main sections that will serve as a basis for the rest of the manuscript.

- The first part of Chapter 2 presents the general working principle of this new type of sensor, that will be used over the rest of the manuscript
- The second part of the chapter introduces the STT-MTJs used, with their performance, stack fabricated and behaviour as magnetic sensing elements
- The third section of Chapter 2 presents the different test setups and experimental assessment of the MTJs, that have been used for the entire work, allowing the characterization of the junctions, and electronics
- The fourth part presents new electronic circuits developed to operate these MTJs as sensing elements, offering better rms noise at the expense of a lower bandwidth
- The last section of this chapter presents alternative ways of using parts of these circuits, allowing for single-period measurements and higher bandwidth to be achieved, while increasing the rms noise

2.2 STT-MTJ magnetic sensor principle

The working principle of this new type of magnetic sensor is based on the fact that **both the magnetic field and the electrical current can be used to reverse the state of the FL** (free layer) and set the MTJ in the P or AP state [3], [6]. A sufficiently strong external magnetic field ($> H_c$ of the FL) or a strong enough current (through the STT effect) can both affect the state of the device. However, these two effects can occur at the same time, such that the magnetic field will reduce the energy barrier for FL magnetization reversal to significantly alter the current required to switch the magnetization direction. As a result, such switching currents (or voltages, V_{PAP} or V_{APP}) will be lower or higher than in the zero-field configuration. In this entire work, for technical simplicity, the MTJs are operated with voltage signals and not current signals, even if the important parameter for switching is the current density. This is because most electronic circuits are usually easier to design when working with voltage compared to current circuits. Hence, the key principle of this new type of magnetic sensor, based on STT-MTJs, consists of **the periodical reversal of a perpendicular MTJ between the P and AP states through the STT effect, combined with the continuous sensing of the switching thresholds**. These switching thresholds are affected by the external magnetic field, and the measurement of these AP to P (APP) and P to AP (PAP) thresholds allows the measurement of the magnetic field (Fig. 2.1).

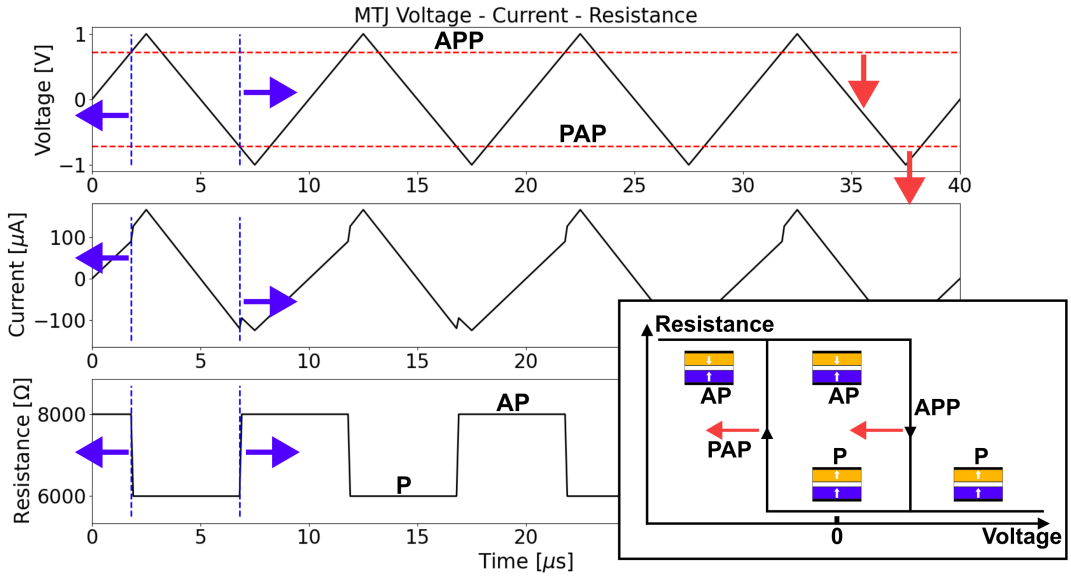

Figure 2.1: STT-MTJ magnetic sensor principle (simulation). The voltage applied to the MTJ of ± 1 V, the current through the MTJ and the resistance of the MTJ are shown, for a MTJ with a TMR ratio of 33 % (R_{AP} and R_P of respectively 8 kΩ and 6 kΩ). When the voltage reaches the critical thresholds, the resistance changes (APP or PAP). The arrows indicate how the signals or thresholds (dashed red line) are changing when an external magnetic field is applied.

2.3 High-coercivity STT-MTJs

In order to demonstrate the working principle of the sensor, high-coercivity MTJs were tested, originally developed for MRAM applications, and manufactured at the Plateforme Technologique Amont (PTA), cleanroom facility located at the CEA of Grenoble, France.

These MTJs are vertical cylinders (Fig. 2.2), based on PMA (i.e., pMTJs) and use a Co/Pt-based SAF to pin the magnetization of the PL (pinned layer) along the perpendicular plane of the wafer. Through this configuration, the presented sensor is sensitive to the perpendicular axis of the wafer, as opposed to TMR sensors, based on in-plane MTJs, and sensitive to fields parallel to the plane of the wafer. These devices are manufactured on 100 mm wafers on SiO_2 substrates and are based on the standard $FeCo_8B_{20}/MgO/FeCo_8B_{20}$ configuration.

After depositions of the thin layers on the wafer, the wafers were then annealed at 350 °C for 10 minutes and the MTJs were etched by physical processing as vertical nanopillars. The MgO barrier is made by the natural oxidation of the Mg layer during a given period of time (a few seconds to a few minutes) and pressure (a few mbar); in that case, 240 seconds at 0.03 mbar. The diameters of the fabricated MTJs range from 20 nm to 100 (nominal) for a vertical height of tens of nm. To access the MTJs, two pads are connected to the top and bottom electrode of each MTJ, as seen in Fig. 2.2, and the electronics is connected to the MTJ through a testing probe. At the end of the fabrication process, a strong magnetic field is applied to set the magnetizations of the layers in the correct orientation. In addition, the wafer was fabricated with two wedges (i.e., thickness gradient), allowing for a fast and efficient screening of the effect of the thickness of two layers on the performance of the memory cells, in this case, one wedge on the Mg layer and one on the FeCoB of the FL.

The stack of MTJs presenting high coercivity, used in this chapter, is described below, from top layers to bottom layers (thicknesses in nanometres), with the free layer connected to the top electrode and the pinned layer to the bottom electrode.

- Top electrode: Ru(8)/Pt(2)/Ta(1)/W(2)/
- MTJ core: $FeCo_8B_{20}$(1)/Mg(0.5)/Nat. Ox. (240 sec.)/Mg(1.1)/$FeCo_8B_{20}$(1.14)/Ta(0.3)/
- SAF: Co(0.5)/$[Pt(0.25)/Co(0.5)]_3$/Ru(0.9)/Co(0.5)/$[Pt(0.25)/Co(0.5)]_6$/Pt(5)/
- Bottom electrode: Ta(1)/W(3)/Ru(15)/Ta(3)

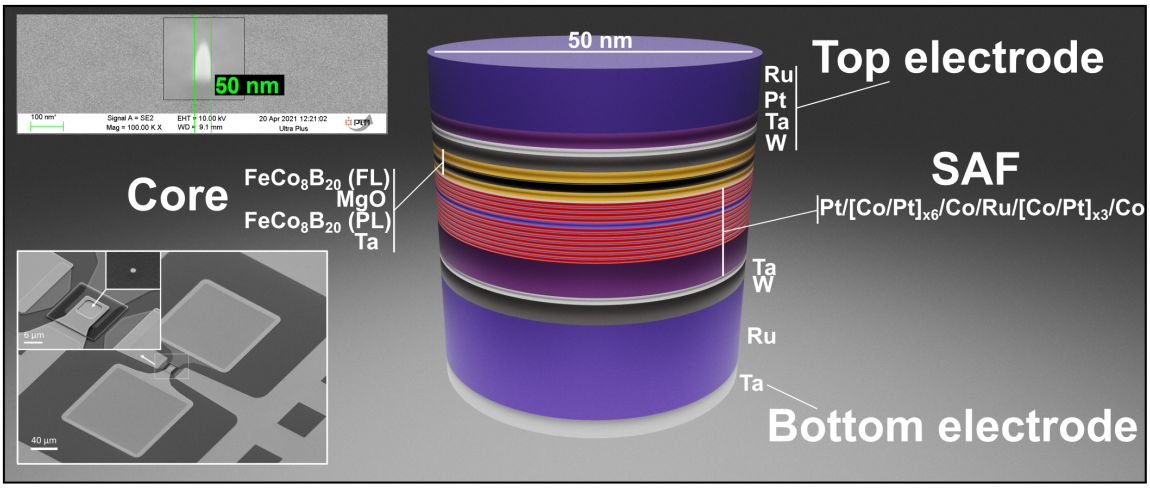

Figure 2.2: Scale model of a typical 50 nm STT-MTJ used. The thickness of the layers relative to the diameter are respected. On the top left image is the SEM image of a real 50 nm STT-MTJ and on the bottom left is the SEM view of a device on the wafer, showing the two pads (each pad with a typical size of $\approx$ 200 μm x 200 μm) used to access the top and bottom electrodes, with the MTJ located at the centre.

The average antiparallel resistance (R_{AP}) and parallel resistance (R_P) are, respectively, 14 kΩ and 7 kΩ. These values are mainly affected by the diameter of the devices, with lower resistance for larger MTJs. The typical coercive field H_c of these MTJs is 400 Oe, with an offset field H_0 of 140 Oe. Since these devices were originally developed for MRAMs, they exhibit an average thermal stability factor Δ of 41 and a strong TMR of 91 %. The resistance area product (RA) usually ranges from 12 to 40 $\Omega.\mu m^2$. The typical APP and PAP absolute voltages are around between 0.5 to 1 V for a typical breakdown voltage of 1.2 V and above. In addition, these observed variations are mainly the result of the wedges and not due to fabrication variability. Industrial fabrication processes, with much more controlled steps, and, in addition, the absence of wedges is much more likely to demonstrate much higher homogeneity over the entire wafer [4], reducing the variations of these parameters.

The phase diagrams of these MTJs (Fig. 2.3), showing the voltage, resistance, and magnetic field relationships, show the clear evolution in the APP and PAP switching voltages. The slopes of the two transition lines APP and PAP represent the intrinsic sensitivity of the MTJ, expressed in mV/mT. The typical intrinsic sensitivity achieved ranges between 2 and 10 mV/mT and is very similar between APP and PAP.

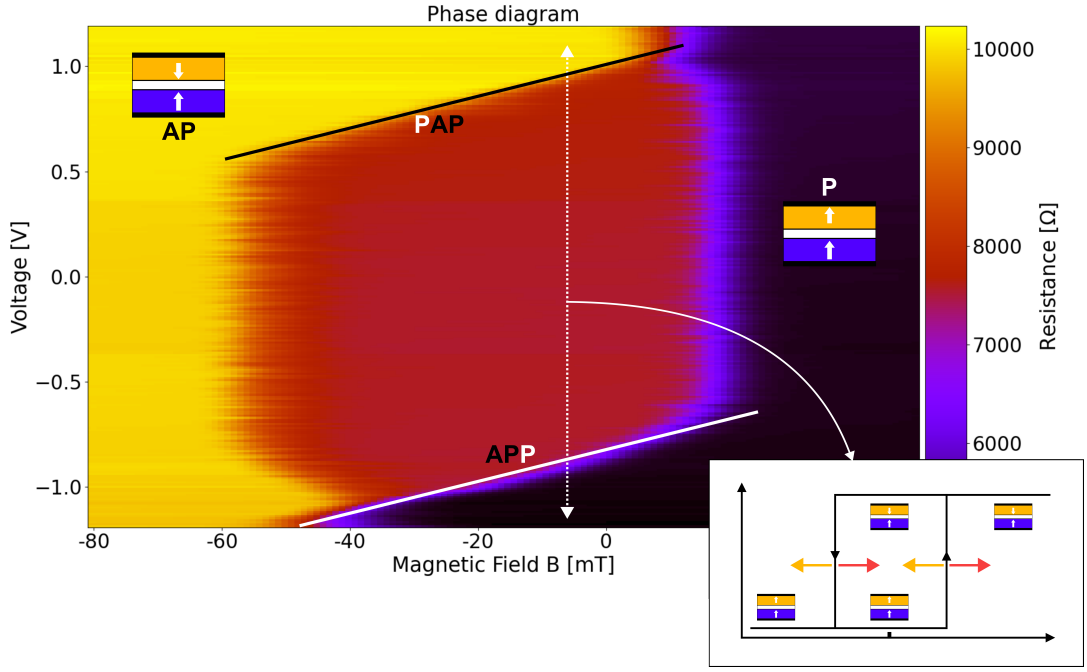

Figure 2.3: Typical 50 nm high-coercivity STT-MTJ phase diagram (experimental results). The evolution of the APP and PAP switching voltages is shown with the white and black lines. The corresponding hysteresis cycle is shown for reference, with the arrows indicating how the cycle is shifting for variations of magnetic field.

The reversal of the magnetization of the FL is actually a **stochastic process**. This implies that for any voltage or magnetic field applied to the MTJ, a probability exists (called the switching probability, SP) for the reversal of the FL (Fig. 2.4). This probability is highest when the applied voltage and / or magnetic field is significantly above the critical threshold ($SP = 1$) and lowest ($SP = 0$) when no field or current is applied. When the applied voltage or magnetic field is equal to the critical threshold, there is a 50 % chance for the reversal. The typical mathematical function that allows us to describe the probability of reversal in a first approximation is a Gaussian distribution, even if more complex but precise models can be used [5], involving the exponential and complementary error function (erfc).

Hence, in the case of magnetic memories, the goal is to apply a voltage, high enough to ensure that the correct state is set during writing operations ($SP = 1$), and low enough to guarantee that the FL is not altered during reading operations ($SP = 0$). For better power consumption, these voltages should also be as low as possible while ensuring a large thermal stability, creating a trade-off to adjust. To ensure the proper behaviour of the devices, the writing and reading voltages are chosen by using appropriate voltages based on the characterization of the device and should be uniform on all of the memory cells. In the case of magnetic memory, while this situation is not ideal, it can be safely handled with the appropriate voltages.

On the other hand, in the case of magnetic sensors, based on STT-MTJs and switching thresholds sensing, this creates a major issue, leading to the creation of a large noise, since the tracked switching voltages APP and PAP are subject to random variations, even in the absence of field variations. This represents the biggest source of noise in this type of sensor.

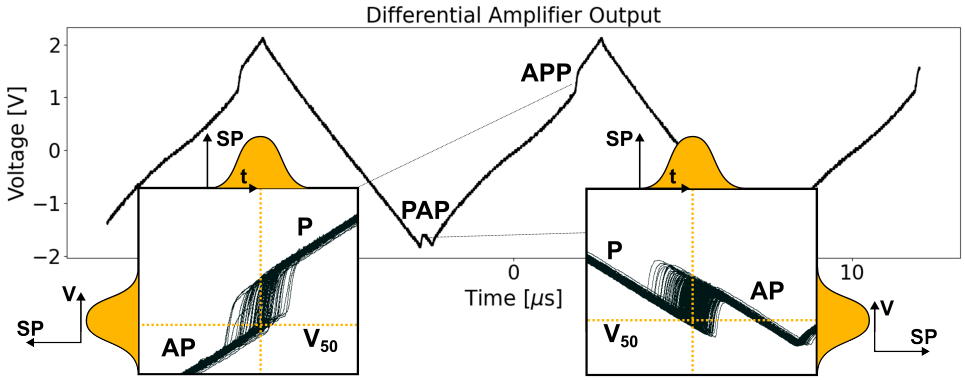

Figure 2.4: Switching probability in STT-MTJs (experimental results). Cumulative measurements, performed over a few seconds (1 to 3 s) of the current through the MTJ (measured through a shunt resistor with a differential amplifier measuring the voltage across the resistor), show multiple reversals at different thresholds, demonstrating the clear stochasticity in the STT-MTJs.

2.4 Experimental setup

To assess the performance of the junctions and the electronics, two test setups have been used at two different locations (one located at Spintec laboratory, Grenoble, France, and the other at the FHNW, Muttenz, Switzerland), allowing for a complementary performance evaluation of the MTJs throughout this work.

In both cases, each setup implements RF probes, made with custom dimensions and non-magnetic materials, allowing signals up to 40 GHz to be applied to the MTJs, through the two pads of each device, as seen in the previous section, each tip of the probe being separated by 220 μm. Since memory cells (i.e., MTJs) are usually controlled with very short pulses of 1 to 100 ns, such a very high bandwidth allows sharp edges to be applied to the MTJ. On each wafer, MTJs are regrouped in area (dies) shown in Fig. 2.5 with nominal diameters of 20, 50, 80, 100 and 150 nm (150 nm being untested in the scope of this work due to their large dimension deviating from the expected macrospin behaviour underpinning their use as sensors).

During the typical measurement sequence, the wafer is moved until the MTJ to be tested is placed right below the probe, and the two pads are aligned with the two tips of the probe. At this point, either the wafer (Setup A) or the probe (Setup B) is moved, respectively, up or down, allowing for the contact to take place and connects the two pads to the electronics. The measurements are then performed, and the operation can then be repeated for another MTJ. This implies that the two terminals within the electronic circuit, connecting to the two electrodes of the MTJ, are open during the movement of the wafer. Hence, in the case of current-operated circuit, this could create some issues, as the current source will try to inject a current into an open-circuit, and as a result will create a strong voltage difference, which will break the MTJ as soon as the probe contacts the MTJ. In addition, turning on and off the input waveform generator during the movement is also not practical since some overshoot can happen when turning on the waveform generator, when the MTJ is already contacting the probe, also resulting in the breakdown of the MTJ. This makes the test for MTJs unpractical through current approaches and is one of the reasons for the choice of the voltage-operated circuits.

2.4.1 Experimental setup A

The first setup is based on a wafer prober, allowing fully automated measurements to be performed on entire wafers (Fig. 2.5). The wafer to be tested is moved under the test probe, followed by the measurement sequence as described. To generate magnetic fields, electromagnets combined with iron-based flux concentrator allow for a strong vertical magnetic field to be generated, allowing for the entire dynamic range of any MTJ to be tested, up to a maximum of $\pm$ 200 mT ($\pm$ 2000 Oe).

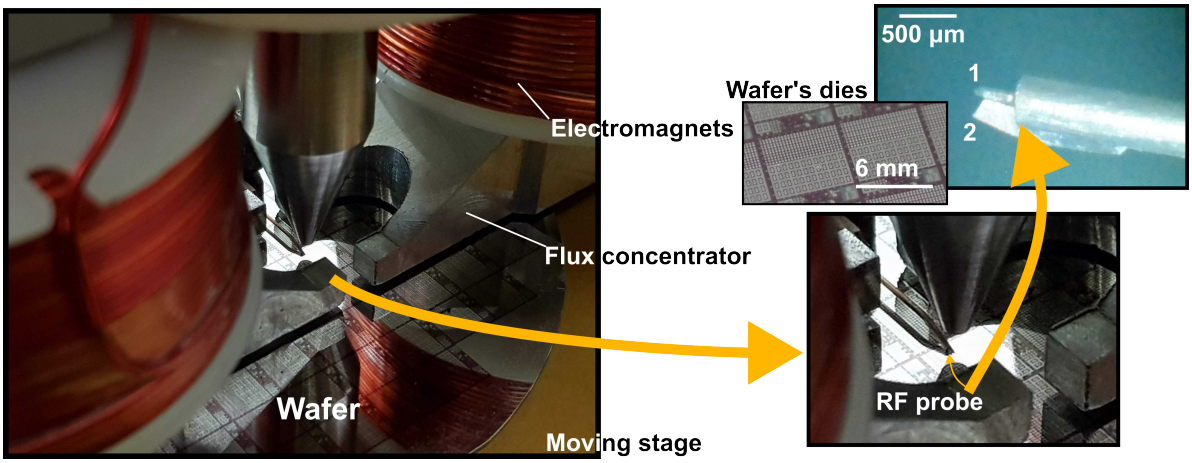

Figure 2.5: Test setup A used for the characterization of MTJs. The probe, identical in both setups, is shown for reference with the two-contact point 1 and 2 connecting to the top and bottom electrodes of the MTJ as well as the dies fabricated on the wafer.

2.4.2 Experimental setup B

A second test setup was developed (Fig. 2.6), allowing for more precise characterization at lower field and higher frequency. This setup, manually controlled, is based on a Helmholtz coil allowing for the generation of a field up to ± 8 mT along the vertical direction. Since the setup does not involve any flux concentrator, no hysteresis is observed in the field generated with this, as opposed to the first setup. To compensate for the lower field capabilities, a strong permanent neodymium magnet can be added right under the wafer support, and moved up and down, to generate a dc field, allowing for any offset to be approximately cancelled.

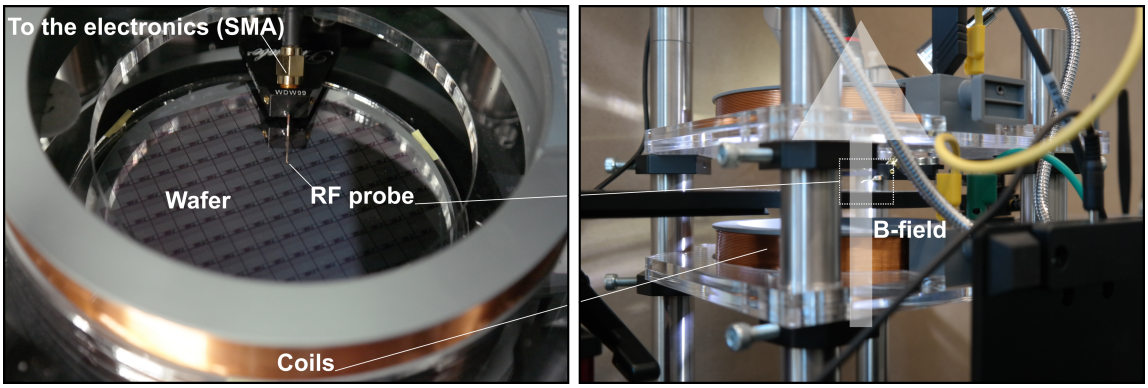

Figure 2.6: Test setup B used for the characterization of MTJs. The left and right views show the Helmholtz coil placed around the wafer and generating a homogeneous field in its centre, the position where the probe and the MTJ to be tested are located.

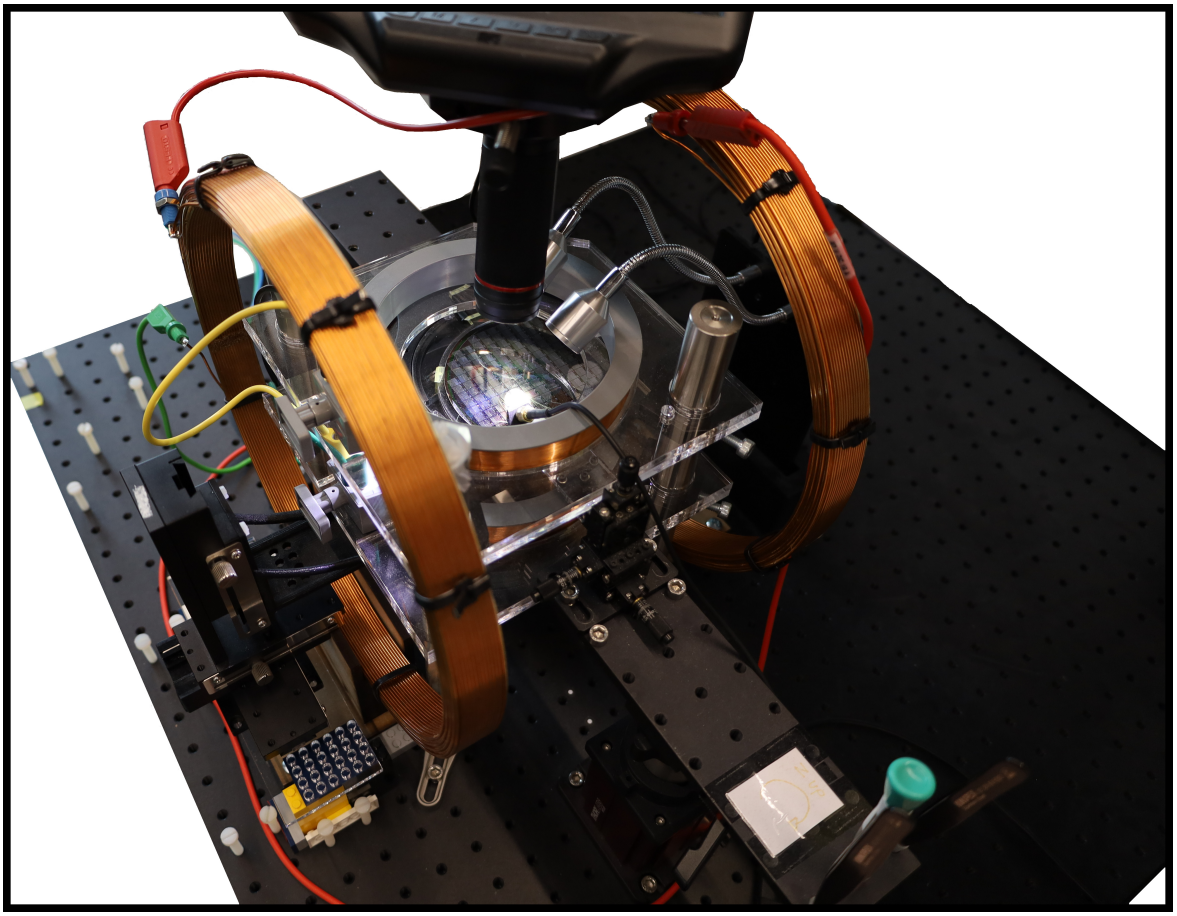

Figure 2.7: Complete view of the fully custom developed test setup B used for the characterization of MTJs. A second Helmholtz coil can be observed, allowing the generation of in-plane field, used in Chapter 4.

2.4.3 Electronic circuits

Finally, all the circuits detailed in the next sections and chapters of this manuscript are fabricated on dedicated custom 4-layer printed circuit boards (PCB) (Fig. 2.8), implementing the circuits depicted in each of the sections. All PCBs are connected to the MTJs through the RF probe via an SMA connector and cable, as short as possible to minimize the parasitic capacitance (typically 50 to 100 pF/m). All of the triangular signals were externally generated using standard waveform generators or digital direct synthesizers (DDS) and injected to the PCB through a second SMA connector. All passive components were chosen to be as standard surface mounted packages (SMD) and all the active components were chosen from commercially available references, with standard performance, compatible with performance achieved in simple monolithic integrated circuits (bandwidth, power consumption, etc.). This allows a proper

demonstration of what could be achieved in future integrated versions. In addition, to avoid using negative power supplies (e.g., as the power supply for the negative rail of the OpAmps), the choice has been made to work with a single 5 V external supply (as in typical ICs, powered through one single pin), with a common internal reference at 2.5 V in respect to the ground (i.e., the external 5 V corresponds to the internal 2.5 V and the external ground corresponds to internal -2.5 V, in respect to this internal reference at 2.5 V). Hence, all the circuits presented in this work are working at ± 2.5 V.

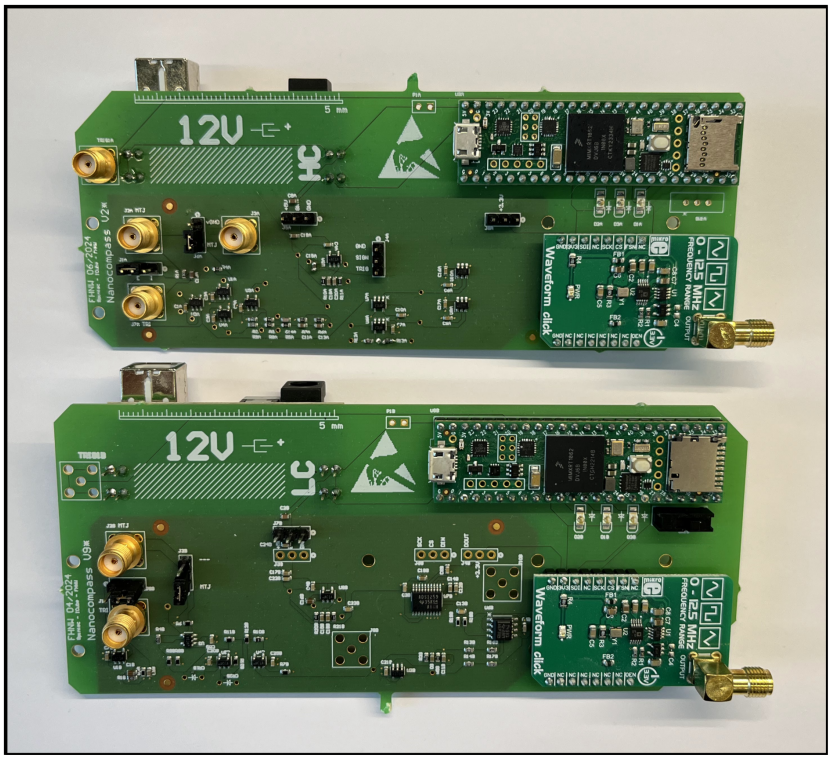

Figure 2.8: Typical view of the high coercivity (HC) and low coercivity (LC) PCB boards designed and used over this entire project. This includes the connections to the MTJ and from the waveform generator through the SMA connectors, the analog and digital electronics, with the main microcontroller in charge of transmitting the data to the computer.

2.5 High-resolution circuit

2.5.1 Circuit description

The technical principle of the sensor is based on the application of a triangular voltage V_{In} at a given frequency F $(= 1/T)$ of up to hundreds of kHz to the MTJ (typically 100 to 200 kHz), with a peak amplitude A covering the switching voltages of the MTJ (typically peak-to-peak amplitude $\pm$ 1 V), while the current through the MTJ is measured. This is done using a shunt resistor R_s (typically 100 to 1000 Ω) in series with the MTJ, and a differential amplifier connected to both terminals of the shunt, which amplify the voltage across the shunt with a gain G (typically 2 to 10), proportional to the current through the MTJ (< 0.5 mA). This allows the monitoring of the resistance of the MTJ. The voltage across the R_s is given by:

$$V_{R_s}(t) = R_s \frac{V_{In}(t)}{R_s + R_{MTJ}(V_{In}(t), \vec{B})} \approx R_s \frac{V_{In}(t)}{R_{MTJ}(V_{In}(t), \vec{B})} \tag{2.5.1}$$

When the voltage across the device reaches the switching voltage (either PAP or APP), the resistance of the MTJ switches brutally. As a result, the current also exhibits a sudden change, which corresponds to the moment when the current applied input voltage should be saved, as it represents the targeted APP or PAP threshold, proportional to $\vec{B}$. To detect the event, the signal obtained at the output of the differential amplifier V_{Rs} is then applied through a high-pass filter (HPF) with a cutoff frequency significantly higher than the frequency of the triangular voltage, in that case, 725 kHz, arbitrarily chosen to remove the first 4^{th} odd harmonics of a 100 kHz signal (100, 300, 500 and 700 kHz).

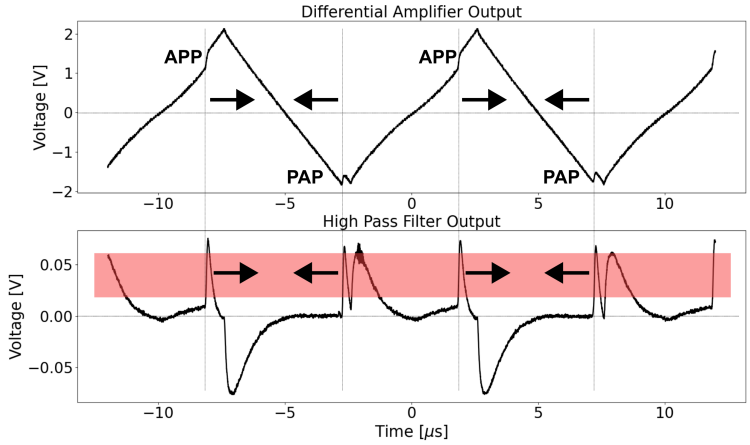

Figure 2.9: Output of the differential amplifier, showing the clear APP and PAP reversals and output of the HPF, exhibiting the pulses during the reversal events (experimental results). The window within which the detection threshold can be set is shown for reference.

Such a cutoff allows for the suppression of the fundamental as well as the first largest signal harmonics while keeping the strong discontinuities from the switching events, occurring at a much higher frequency, as the reversal of the resistance typically takes tens of ns. At the output of the HPF, V_{HPF}, peaks with amplitudes of tens to hundreds of mV (depending on the TMR of the MTJ, 20 to 300 mV) are seen and can be differentiated from background noise (Fig. 2.9). For these reasons and due to the GBW of the amplifiers, G should be kept relatively low, allowing the bandwidth of the amplifier to remain high enough ($>$ 1 to 2 MHz minimum) to allow strong discontinuities to pass and allowing commercial amplifiers with low GBW to be used. Since the circuit should remain compatible with monolithic integration, very high GBW amplifiers become also difficult and expensive to design. To compensate for such a lower gain, a higher R_s is used (430 Ω in this example), still lower than R_{MTJ}. While many circuits allow the implementation of HPF, the choice has been made to use a second-order passive capacitor-resistor (CR) configuration. This allows the working principle to be demonstrated while keeping the design very simple and compact, as opposed to active implementation. Reversal events can then be detected using a comparator with a defined fixed threshold V_{TH}, above the background noise, which outputs short digital level pulses (Trig) of 5 V at the moment of reversals (PAP or APP). The typical amplitude of these pulses to be detected is 10 to 100 mV with a duration of tens of ns. **The durations between these pulses are directly related to the external magnetic field.**

To use these pulses and output a signal proportional to $\vec{B}$, the pulses are combined through a clocked set-reset flip-flop (cSR flip-flop) made of 4 NAND gates (Fig. 2.10), with the input polarity of the triangular signal (Sign) and an inverted polarity signal (nSign). To obtain the polarity of the input triangular signal, a second comparator is used, comparing the input signal with respect to the ground, outputting a "1" for positive input and a "0" for negative input, while a simple inverter is used to invert Sign and obtain nSign. As a result, rigorously, the final circuit achieved represents a D flip-flop. This cSR flip-flop structure is based on the rising edge of the CLK signal and also has the advantage of natively outputting differential signals, V_{FF} and nV_{FF}, due to the complementary output of the architecture.

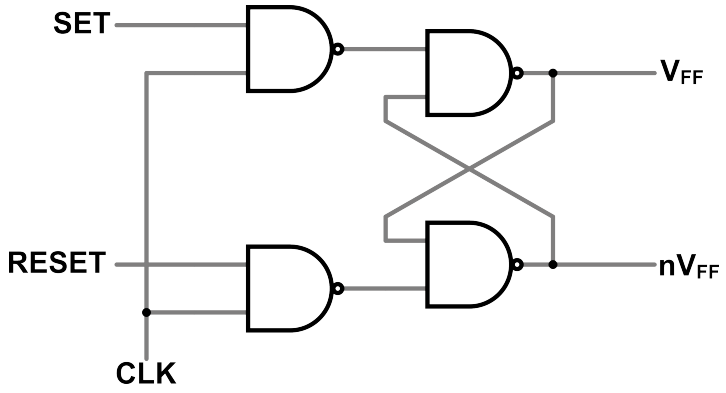

Figure 2.10: cSR flip-flop architecture, made of 4 CMOS NAND gates. Each NAND gate can be made of 2 NMOS and 2 PMOS, making this structure highly compact (total of 16 transistors).

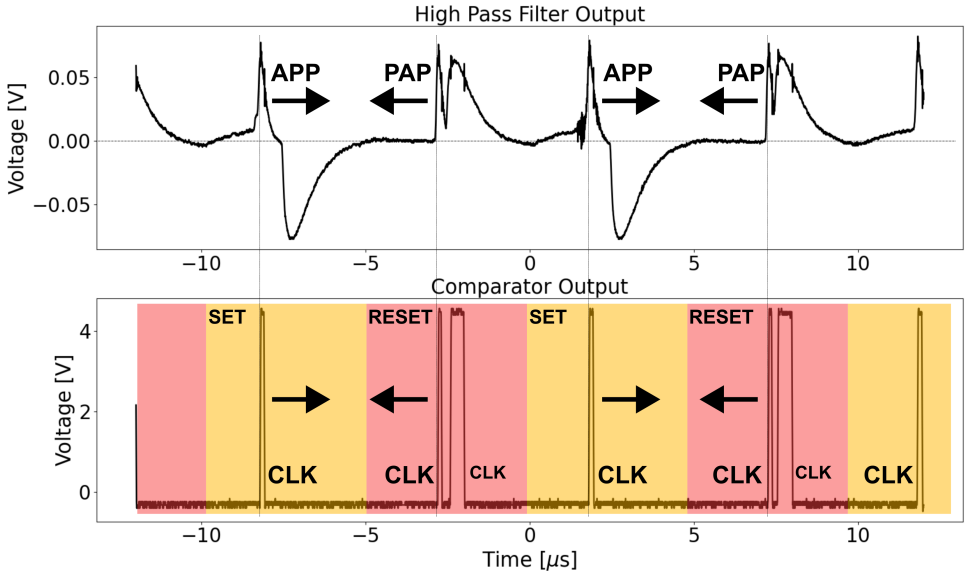

Figure 2.11: Output of the first comparator, showing the digital pulses used as the CLK input of the cSR flip-flop for each reversal (experimental results). The yellow and red colour indicate the sign on the input voltage, with yellow being positive (i.e., SET) and the red being the negative part (i.e., RESET), obtained from the second comparator. In addition, the triangular signal induces a second CLK pulse during the negative part. However, at this time, the flip-flop is already in the RESET state, due to the first CLK pulse, induced by the reversal, and, as a result, does not cause any issue.

The clock input (CLK) of the cSR flip-flop is connected to the output of the first comparator Trig, while the SET and RESET signals are using the second comparator and connected to the polarity signals of the input triangular signal. Hence, the polarity of the input signal Sign is connected to the SET, while the inverted polarity nSign of the input signal is connected to the RESET of the cSR flip-flop, resulting in the following truth table for the cSR flip-flop. Since a rising edge of the CLK signal indicates a switching event, either APP or PAP, the polarity of the input signal, Sign and nSign, allows for the differentiation between APP and PAP.

CLK (Trig)	**SET (Sign)**	**RESET (nSign)**	**Out (V_{FF})**	**nOut (nV_{FF})**
↗ (APP or PAP)	1 (APP)	0 (APP)	1	0
↗ (APP or PAP)	0 (PAP)	1 (PAP)	0	1
Others	Hold	Hold	Hold	Hold

This method allows the creation of a pulsed width modulated signal (PWM), with differential outputs (Fig. 2.12). In addition, since the reversal events can only take place at a significant high voltage ($> \pm$ 0.5 V), it becomes physically impossible to observe glitches. Such glitches can

only occur if the SET input changes at the same time as the CLK edge, which, by construction, is impossible in this circuit, as the SET and RESET signals change only when the input voltage crosses 0 V, where no reversal (i.e., no CLK pulse) is possible under nominal conditions.

Since the duty cycle is controlled by the time between the APP and PAP pulses, **the duty cycle of the PWM signals is directly proportional to** $\vec{B}$. Hence, a simple low-pass filter (LPF), made of two RC stages is used with a cutoff frequency of 100 to 2000 Hz, in this case 160 Hz, can be used to retrieve a dc level proportional to the magnetic field. The output of the LPF is then injected into analog buffers and directly to an analog-to-digital converter (ADC). For the same reasons as for the HPF, the LPF is implemented as a passive RC structure. Since the cutoff frequency of the LPF is designed to be between 100 and 2 kHz, this allows the averaging of few hundreds (100 to 1000) of reversals to minimize the impact of the stochasticity and lower the rms noise at the output of the sensor.

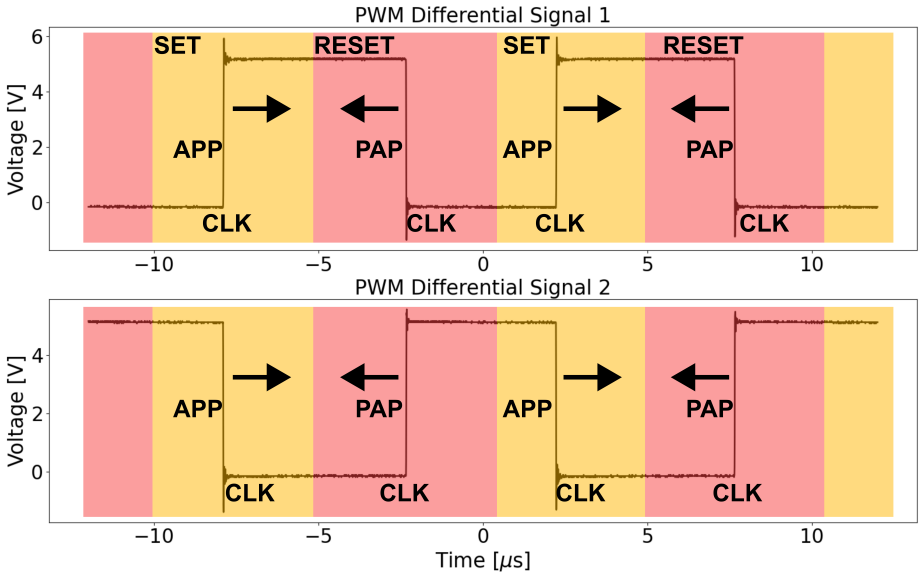

Figure 2.12: Output of the cSR flip-flop (i.e., PWM signals) which will be filtered by the LPFs (experimental results). The differential signals can be seen, which can be obtained using both the output and the complementary output of the flip-flop.

The complete circuit, which allows the use of STT-MTJs as sensing units, is shown in Fig. 2.13. This circuit includes, in the order of implementation, the measurements of the current of the MTJ, injected to the HPF followed by the comparators, directly to the cSR flip-flop and the LPFs, and sampled by the ADC. If necessary, unipolar output is also possible, using only V_{FF}, which can be filtered and sampled using any unipolar ADC.

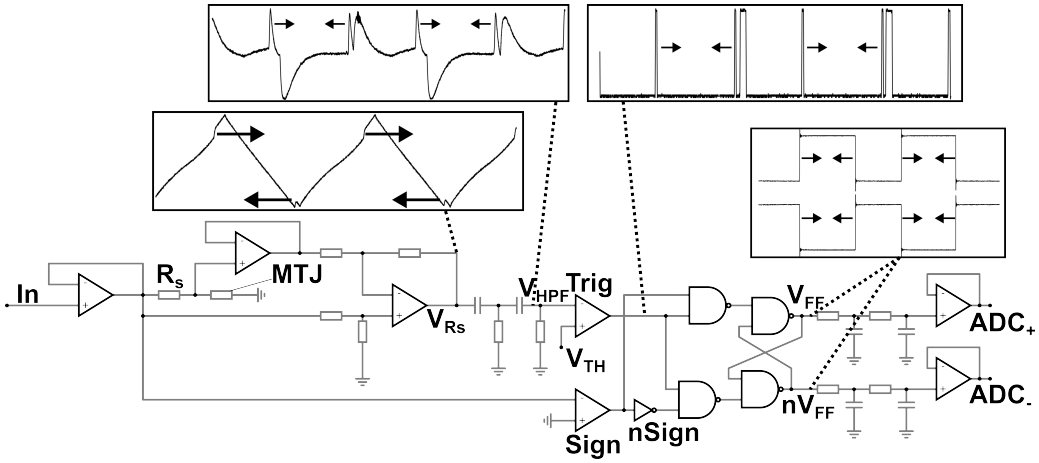

Figure 2.13: PWM complete conditioning electronics circuit.

The average value of any PWM signals, V_{PWM} based on on-off signals (i.e., square signals) is given by equation 2.5.3, with D the duty cycle, between "0" and "1", V_{OH} and V_{OL} the high and low voltage of the square signal, and, if $V_{OL} = 0$ V, the relation can be further simplified. The duty cycle is calculated with equation 2.5.2, with $T_{on+off} = T$, the period of the square signal.

$$D = \frac{T_{on}}{T_{on+off}} \tag{2.5.2}$$

From this, it can be seen that if the voltages for the APP and PAP transitions are symmetric, $T_{on} = T/2$, the output voltage is simply $V_{OH}/2$. If the voltages are not perfectly identical, this creates an offset at the output of the sensor.

$$V_{PWM} = D.V_{OH} + (1 - D)V_{OL} = D.V_{OH} = V_{OH}\frac{T_{on}}{T_{on+off}} = V_{OH}\frac{T_{on}}{T} \tag{2.5.3}$$

The variations of V_{PWM} with respect to the variation of the external magnetic field $\vec{B}$ represent the output sensitivity of the sensor (i.e., the derivative of V_{PWM} to $\vec{B}$). Hence, using the PWM principle, the output sensitivity of the sensor can be given by equation 2.5.4. Since T_{on} represents the time between the APP and PAP transitions, (i.e., $T_{APP\rightarrow PAP}$), $\frac{dT_{APP\rightarrow PAP}}{dB}$ represent the time sensitivity, given by 2.6.1.

$$\frac{dV_{PWM}}{dB} = \frac{V_{OH}}{T}[\frac{dT_{APP\rightarrow PAP}}{dB}] \tag{2.5.4}$$

Using the values described for equation 2.6.1 with $V_{OH} = 5$ V, this gives an expected sensitivity of approximately 2.5 to 12.5 mV/mT, which can further be multiplied by two if differential signals are used, giving a sensitivity of 5 to 25 mV/mT.

2.5.2 Achieved performance

Using this principle and the circuit described in this section, the experimental measurements of the MTJs showed a successful working principle. Through an input signal of ± 1.2 V at 100 kHz with unipolar output, the sensitivity of MTJs could be extracted. To evaluate this parameter, a discrete sweep of $\vec{B}$ was performed. For each point, magnetic field was set at a constant dc level using either one of the two setups described, and the voltage at the output of the LPF was sampled by the ADC. For each magnetic field step, 8192 data points were sampled, and the median was calculated to obtain the output value of the sensor for each particular step. The sensor output characteristic was measured and is shown in Fig. 2.14. Sensitivity of 5 to 15 mV/mT was achieved, with non-linearity error of ± 1 to 2 % FS (full scale) and as low as 0.5 % FS, over a dynamic range of up to 60 mT (i.e., ± 30 mT centred around the offset).

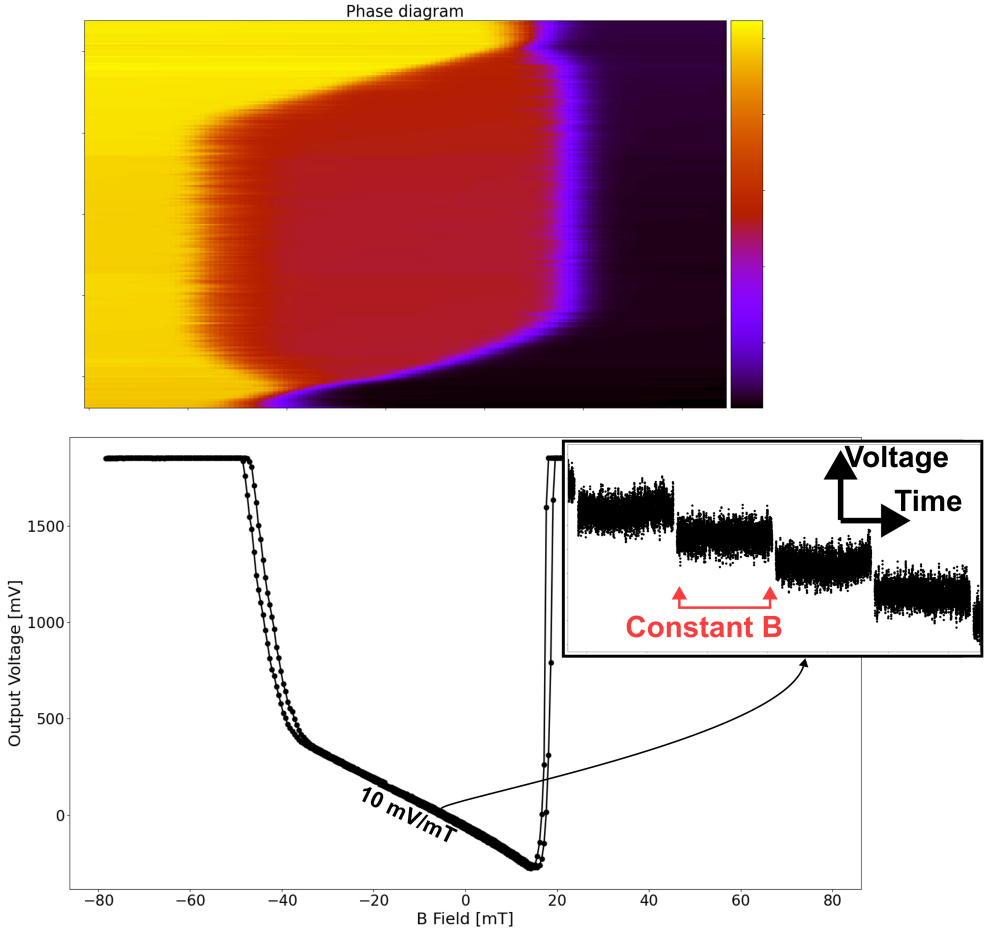

Figure 2.14: Output characteristics achieved of the proposed PWM circuit for a 100 nm MTJ (experimental results). A typical phase diagram of a high-coercivity STT-MTJ is shown for reference

Noise measurements were also performed, with the corresponding spectrum, shown in Fig. 2.15. Similarly to the output characteristics, noise measurements were performed during constant dc field steps over the same sample size. The noise power spectral density (NPSD) achieved was typically 0.1 mV/$\sqrt{Hz}$, corresponding to 10 μT/$\sqrt{Hz}$, with best performance obtained around the offset field. The reported rms noise was typically 1 to 3 mV, which corresponds to 100 to 300 μT of rms magnetic noise. Contrary to most magnetic sensors, no 1/F noise was reported with a flat spectrum until the cutoff frequency of the LPF, in this example, 160 Hz.

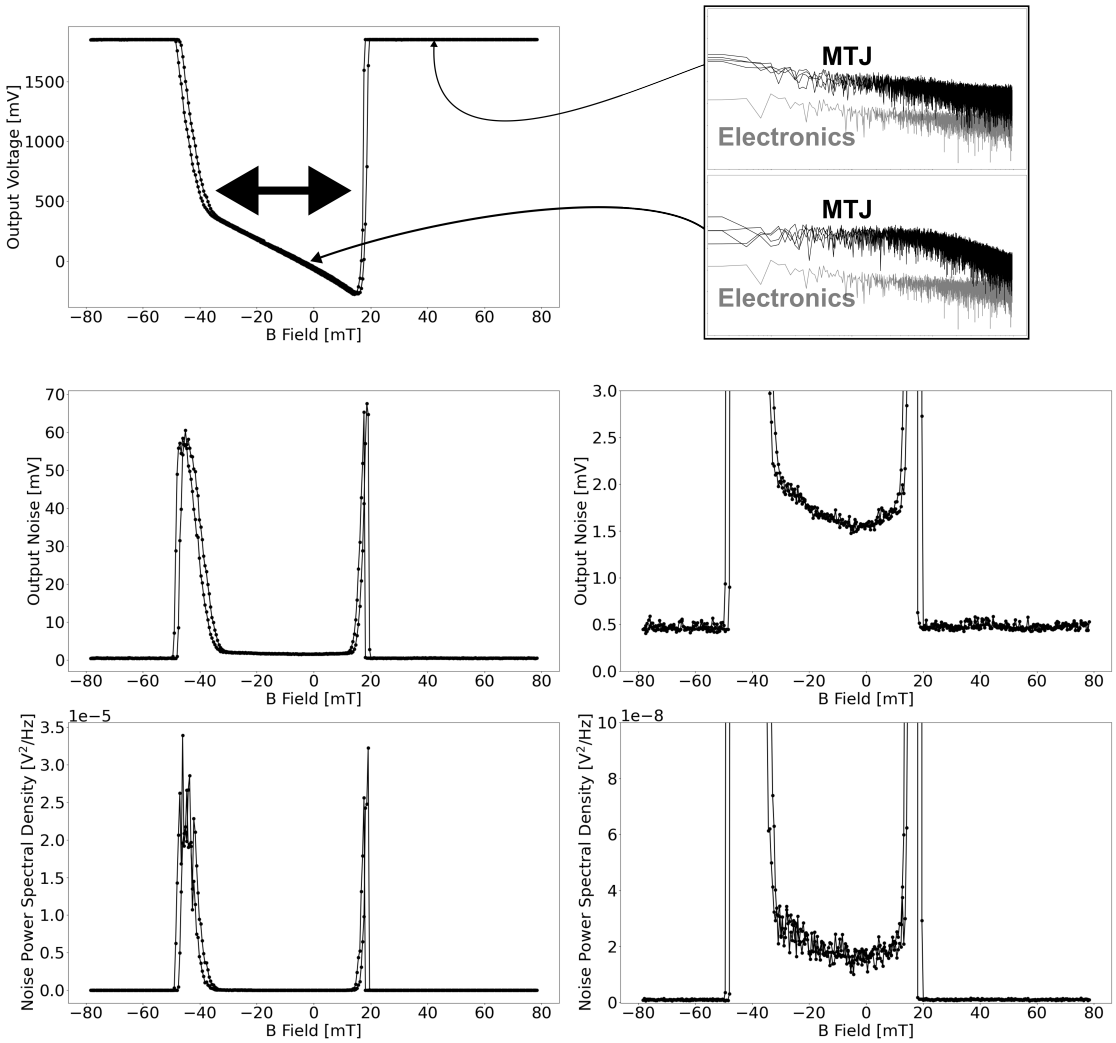

Figure 2.15: Noise performance (rms and NPSD) achieved through the proposed PWM circuit for a 100 nm MTJ (experimental results). The corresponding frequency spectrum are shown at two values of applied external field, in the working and outside the working area of the sensor, showing the impact of the reversals on the noise. A close up look at both the rms noise and NPSD is also shown.

Finally, measurements of ac, sine wave magnetic field signals at 5 Hz over ± 8 mT showed appropriate outputs, as shown in Fig. 2.16, demonstrating the dynamic metrological capabilities of the sensor. Due to the non-linearity error and noise, a small peak can be seen at the second harmonics of 10 Hz, with an amplitude depending on the MTJ.

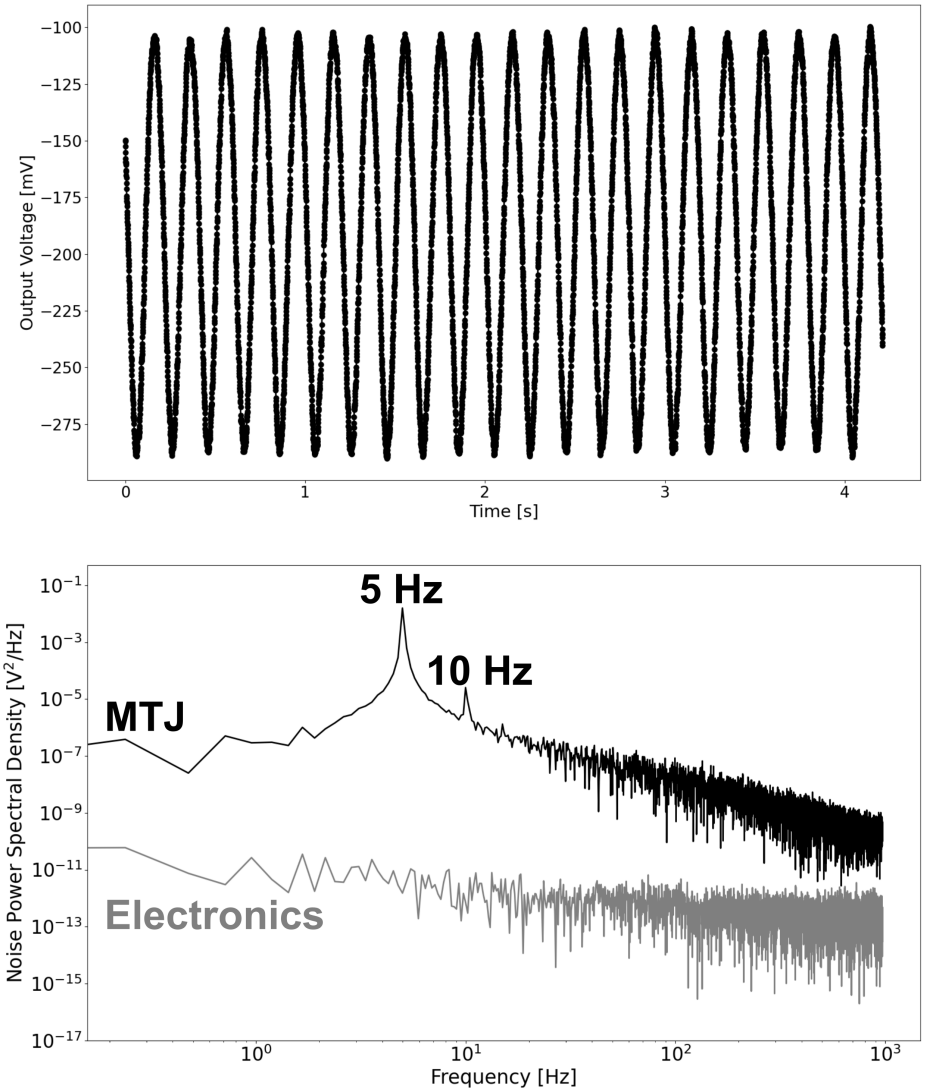

Figure 2.16: Measurements achieved of the proposed PWM circuit in the case of ac sine wave magnetic field signal at 5 Hz ± 8 mT for a 100 nm MTJ (experimental results). Both time domain and frequency domains are shown.

2.6 High-frequency circuit

2.6.1 Circuit description

While the method presented above, based on filtered PWM signals, allows for built-in analog averaging of the output voltage signals, lowering the rms noise, it requires significant silicon surface on the wafer due to the necessity of an ADC, requiring a large layout, depending on the architecture and resolution targeted, as well as large capacitors, required to perform the filtering of the PWM signals into dc levels. This represents a significant downside for the integration into monolithic chips with the smallest footprint possible, as the sensing element is already at a very small scale. In addition, the PWM-method exhibits reduced bandwidth, as the LPF is necessary of a significantly lower cutoff frequency than the input triangular signal. To compensate for this, another approach has been demonstrated, allowing for a much simpler and compact layout as well as increased bandwidth, at the expense of an increased rms noise and more intense signal processing requirements.

To do so, the circuit described above was reused (Fig. 2.18), up to the two comparators, allowing the polarity of the input signal Sign and reversal pulses Trig to be obtained. These two signals are directly injected into an external microcontroller (MCU) with a simple internal digital binary counter, used as a time-to-digital converter (TDC) (Fig. 2.17).

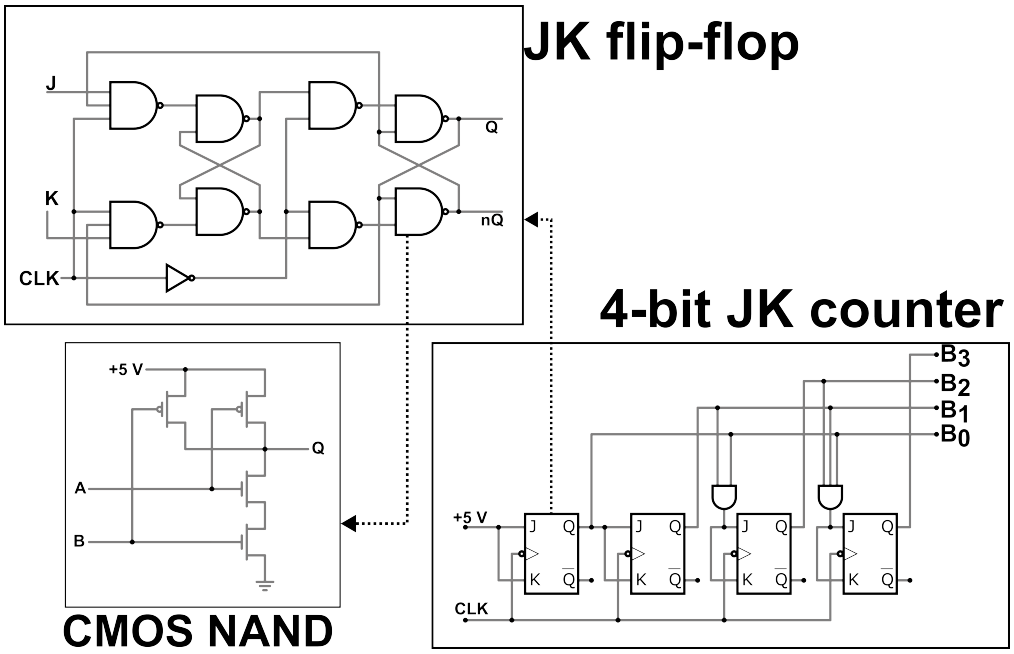

Figure 2.17: Example of the basic TDC implementation as a synchronous counter, in that case a 4-bit JK counter. This 4-bit counter typically uses less than 150 transistors. The design can then be extended for larger counting capabilities than 2^4. In addition, other counter architectures can also be used.

For the demonstration, either the internal counter of an STM32F411 microcontroller (STMicroelectronics, Switzerland), based on an ARM core M4 running at 96 MHz, or the internal counter of an IMXRT1062DVJ6 (NXP Semiconductors, Netherlands), based on an ARM core M7 running at 600 MHz were used. Such TDC architecture, based on a basic digital counter, is a fully digital circuit, and can be made of small but fast digital transistors, as opposed to analog transistors, often much larger than digital transistors, designed with larger width (W) and length (L) to obtain their targeted characteristics and lower the noise, therefore reducing the silicon surface in the case of monolithic integration. Due to the necessity of high-precision measurements, synchronous counters are preferred despite being more complex to design. However, if precision is not an issue, or at relatively low speed, asynchronous counter can also safely be used, such as in the case of high-bandwidth, low-precision measurements (e.g., if used, for instance, as a rotating sensor).

The counters are set into a continuous up-mode counting, one tick per clock cycle, at a frequency of 96 MHz or 600 MHz, depending on the hardware used. Similarly to the previous method, the signal Sign allows the differentiation between APP and PAP, while the signal Trig allows the detection of any reversal event. However, two software approaches can be implemented to handle pulses.

- The rising edge of the Trig pulses can be used to trigger an interrupt within the MCU. Inside the ISR (interrupt service routine), the software is programmed to save the value of the counter as well as the polarity of the input signal Sign, as a Boolean variable, at this exact moment, in the internal memory. Offline signal processing can then be performed to calculate the time between each APP and PAP event, simply by subtracting the value of the counter saved for two successive APP/PAP events, allowing for a measurement of $\vec{B}$ on each period of the input signal
- The rising edge of the Trig pulses as well as the rising edge of the Sign signal trigger two different interrupt within the MCU. The interrupt of the Sign signal resets the counter, allowing the counter to start from 0 for each new period of the input signal. Then, the rising edge of the Trig pulse triggers another interrupt in the MCU. For each of these interrupts, the software save the counter value in one of two buffers, depending on the current value of the Sign signal (one buffer for the APP and one for the PAP is necessary). This allows a separate measurement of $\vec{B}$ on each period of the input signal for both APP and PAP events.

These two approaches can both be translated into a simple state machine and offer different advantages. The first approach allows for simpler design, as only one interrupt is used, and removes the need for the control of the counter, since the counter is running continuously. On the other hand, the second approach offers the possibility to use only one of the two reversals, at the expense of higher complexity from both software (two interrupts) and hardware (control and reset of the counter) point of view. However, while the second approach allows to do measurements of single period events, it also allows to recreate the first method and is therefore highly convenient for performance analysis.

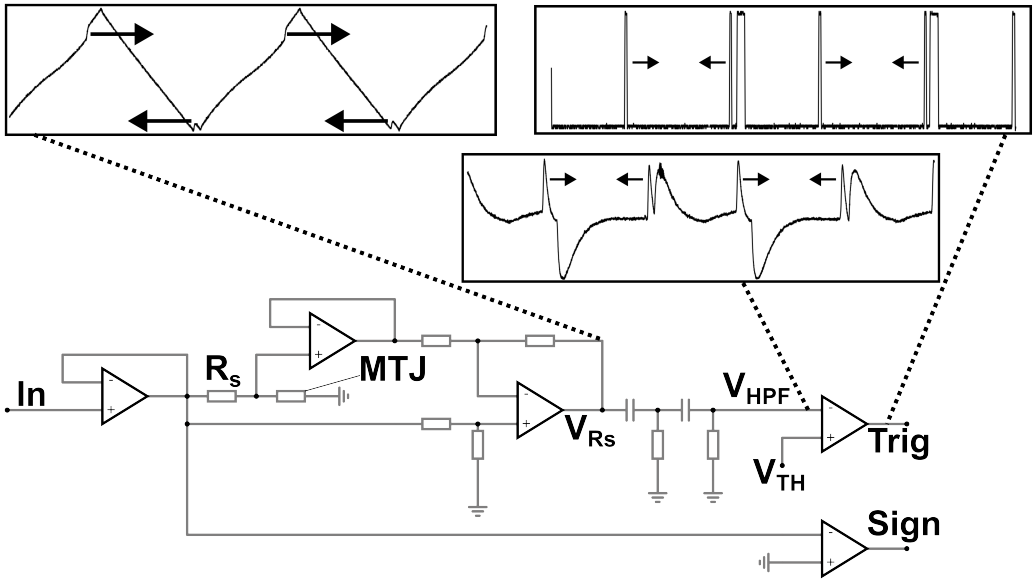

Figure 2.18: TDC complete conditioning electronics circuit.

The output sensitivity of such circuit, through the first method, is given by equations 2.6.1 and 2.6.2, with S_{APP} and S_{PAP} respectively being the intrinsic APP and PAP sensitivity of the MTJ (i.e., the slope on the phase diagram).

$$\frac{dT_{APP\rightarrow PAP}}{dB} = \frac{-T}{4A}[\frac{S_{APP}(R_s + R_{AP})}{R_{AP}} + \frac{S_{PAP}(R_s + R_P)}{R_P}] \tag{2.6.1}$$

$$\frac{dT_{PAP\rightarrow APP}}{dB} = \frac{T}{4A}[\frac{S_{PAP}(R_s + R_P)}{R_P} + \frac{S_{APP}(R_s + R_{AP})}{R_{AP}}] \tag{2.6.2}$$

Through the second method, the output sensitivity is given by 2.6.3 and 2.6.4.

$$\frac{dT_{APP}}{dB} = \frac{-T}{4A}[\frac{S_{APP}(R_s + R_{AP})}{R_{AP}}] \tag{2.6.3}$$

$$\frac{dT_{PAP}}{dB} = \frac{T}{4A}[\frac{S_{PAP}(R_s + R_P)}{R_P}] \tag{2.6.4}$$

Using a triangular input signal at 100 kHz of ± 1 V ($A = 1$ V, $F = 100$ kHz, $T = 10$ μs) with these junctions, and assuming the shunt resistance is significantly lower than the MTJ to simplify the equations 2.6.1 to 2.6.4 to be independent of R_{MTJ}, this gives an expected sensitivity for the first method of approximately 5 to 25 ns/mT. For a 30 kHz signal, this gives an expected sensitivity of 16 to 82 ns/mT. In the case of the second method, this gives approximately 2.5 to 12.5 ns/mT (100 kHz) or 8 to 41 ns/mT (30 kHz).

2.6.2 Achieved performance

Following theoretical analysis of the circuit, experimental measurements were performed on the MTJs, allowing the validation of the proposed measurement approach. Using an input signal of ± 1.2 V at 30 kHz with the 600 MHz timer, the results described below could be obtained. Assessment of sensor output characteristic was performed and is shown in Fig. 2.19. Sensitivity of 40 to 70 ns/mT was achieved, with non-linearity error of ± 10 % FS over a dynamic range similar to the PWM method, for both APP and PAP events. However, the use of both the APP and PAP events, as previously described as the first method (PAP-APP), allows a better linearity to be reached, with ± 1 to 2 % FS, with a sensitivity of 100 ns/mT, as expected, approximately twice the sensitivity of a single event, and similar to the theoretical values expected, calculated in the previous section.

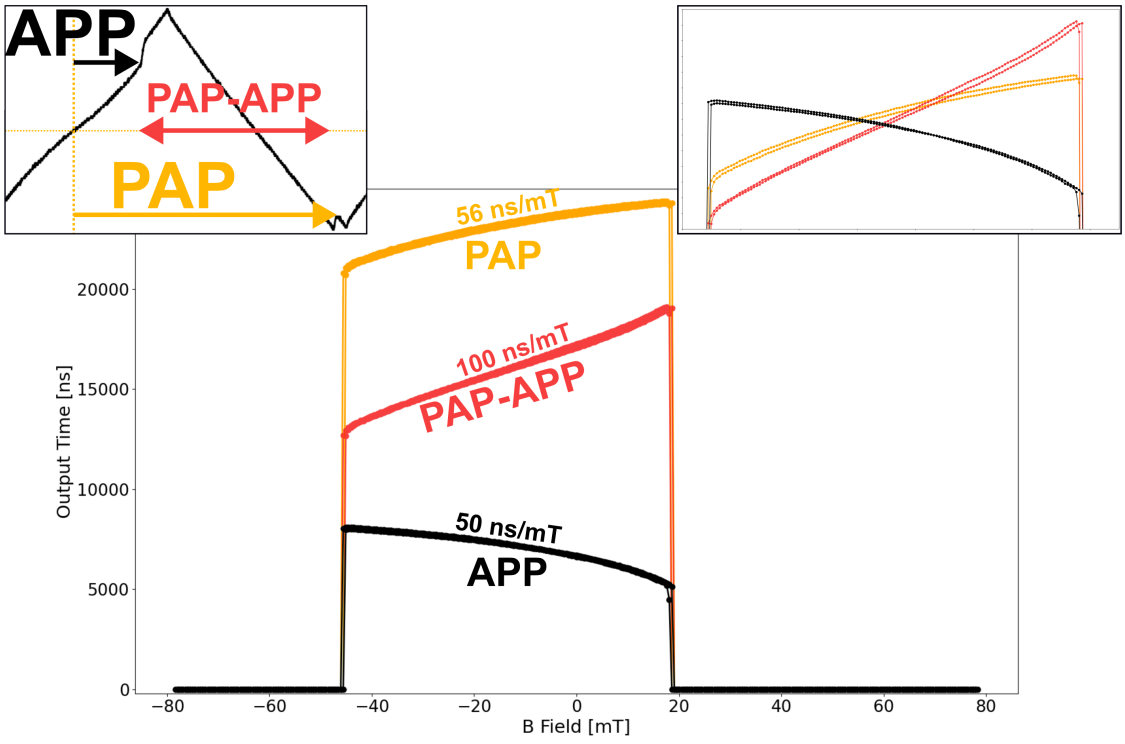

Figure 2.19: Output characteristics achieved (APP, PAP and PAP-APP) of the proposed TDC circuit of a 100 nm MTJ (experimental results). The close-up look shows the superposition of the three types of events (APP, PAP and PAP-APP), with their respective offset artificially removed for better clarity.

Noise measurements were also performed, with the corresponding spectrum shown in Fig. 2.20. NPSD achieved was typically 1.4 ns/$\sqrt{Hz}$, corresponding to 10 to 30 μT/$\sqrt{Hz}$, with best performance obtained around the offset field for both APP and PAP. Similarly, no 1/F noise was reported with a flat spectrum up to the Nyquist frequency. The typical rms noise was approximately 100 to 300 ns, corresponding to 1 to 5 mT over a bandwidth of 15 kHz up to 100 kHz. In addition, noise differences could also be observed between APP and PAP events. Hence, one can observe that the APP or PAP events are favourable depending on the field, while the use of both events results in the worst noise possible, as always dominated by the largest noise (either from the APP or PAP events).

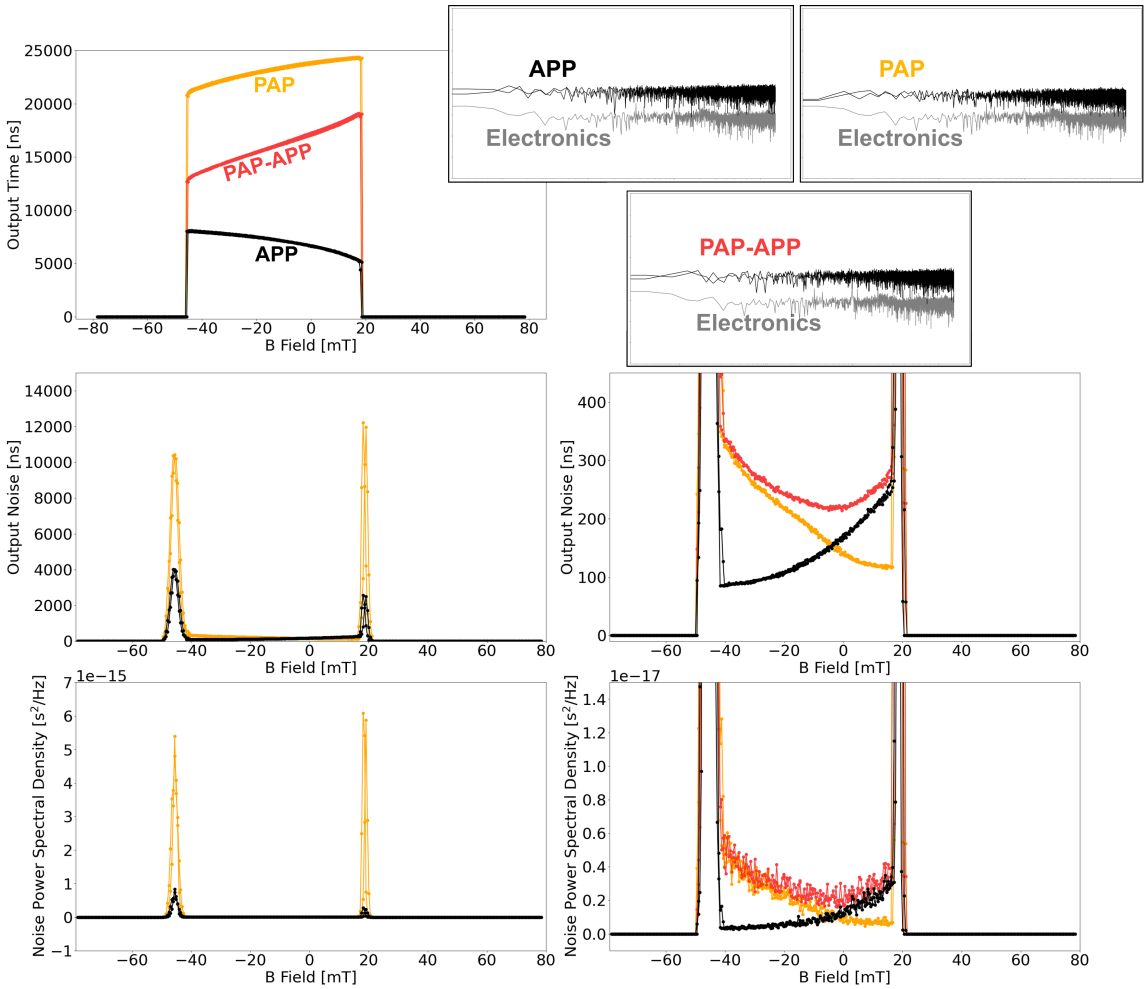

Figure 2.20: Noise performance (rms and NPSD) achieved (APP, PAP and PAP-APP) through the proposed TDC circuit of a 100 nm MTJ (experimental results). The corresponding frequency spectrum are shown at the offset field for APP, PAP and PAP-APP events, showing the similarities in the frequency spectrum. A close-up looks at both the rms noise and NPSD is also shown.

Finally, measurements of ac signals at 20 Hz over ± 8 mT showed proper oscillating outputs, as shown in Fig. 2.21, demonstrating the dynamic measurement capabilities of the sensor through the proposed TDC approach. Due to the limited number of periods measured, limited by the internal memory of the MCU and the maximum number of points, as well as the stronger rms noise, the frequency peak is less sharp than in the PWM method.

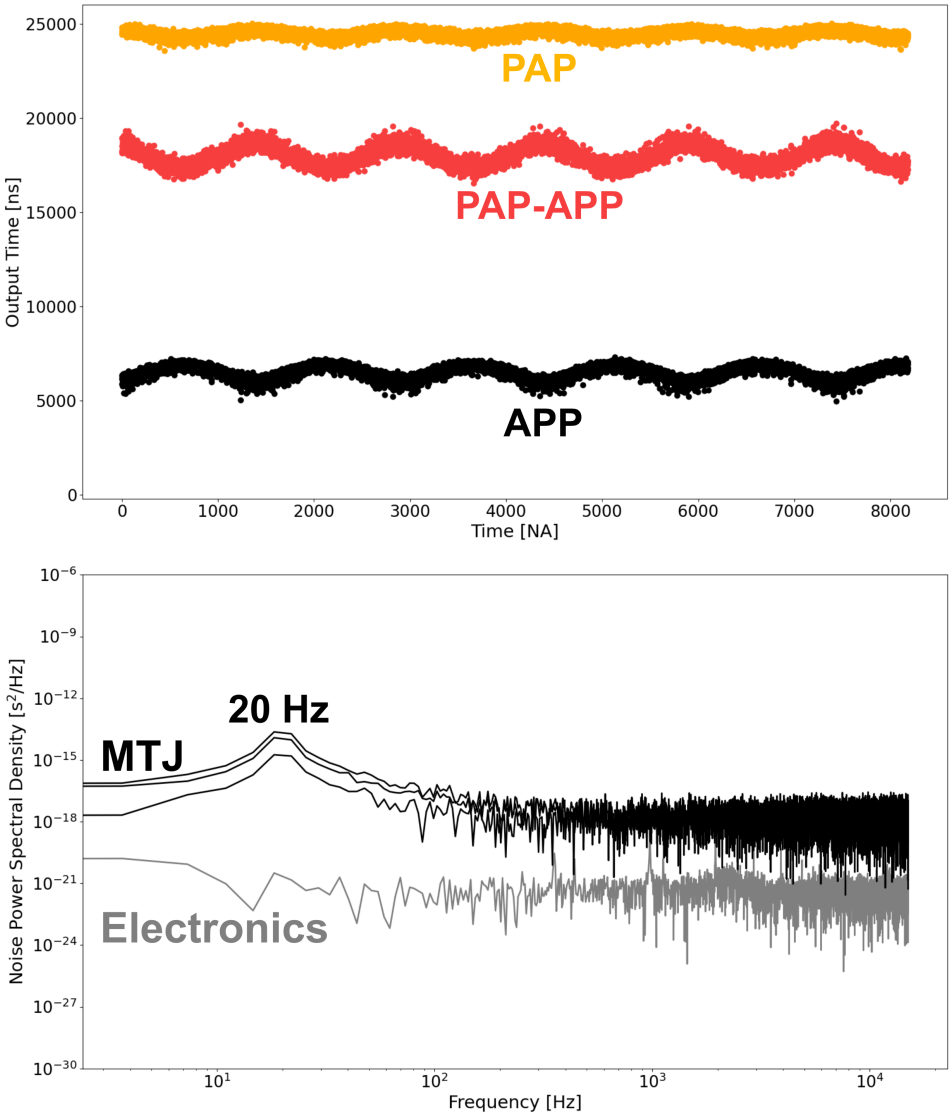

Figure 2.21: Measurements achieved (APP, PAP and PAP-APP) of the proposed TDC circuit in the case of ac sine wave magnetic field signal at 20 Hz ± 8 mT of a 100 nm MTJ (experimental results). Both time domain and frequency domains are shown for APP, PAP and PAP-APP events.

2.7 Conclusion

Chapter 2 presents the use of nanometric perpendicular spin transfer torque magnetic tunnel junctions as nanoscale magnetic sensing units through two different and specific reading architectures, based on standard CMOS microelectronics components and simple reading methods. Through a unique way of using STT-MTJs, relatively similar to the working principle of the fluxgate, a successful proof-of-concept has been achieved.

Such sensing elements, representing the smallest sensing element reported to this day, with nominal diameter of 20 to 100 nm, and with several advantages, as described in Chapter 4, are intrinsically suitable for monolithic integration, thanks to the use of pMTJs, originally developed for MRAMs.

Two different approaches are demonstrated. The first one, based on filtered PWM signals, offers better rms noise and a more standard layout with a classical digital output, based on an ADC, at the expense of a larger silicon surface and lower bandwidth. This method, outputting a voltage proportional to $\vec{B}$ has a stronger potential for future integration into monolithic circuits and mass production due to its possibility of easy implementation into larger systems such as existing Hall effect or MR sensors.

On the other hand, the second approach, based on TDCs and outputting a time signal proportional to $\vec{B}$, offers a larger bandwidth, with single-switching event capability, at the expense of an increased rms noise and offline processing requirements, since the high-bandwidth measurements require significant and fast processing power. In these examples, 16 to 64 bits counters were used because of their existing implementations within the hardware used. This represents large counting possibilities (65535 up to 18^{18} ticks). However, at 100 kHz of input triangular signal frequency and 96 MHz counter, any switching events occur in less than 1024 ticks (i.e., 2^{11}) and an 11-bit counter is enough. With a 600 MHz counter, less than 8192 ticks are used, and 13 bits is already enough. This limits the size of the counter to be designed for an integrated circuit. To further enhance the time resolution of the circuit, limited by the TDC counting frequency, different or mixed approaches can be used for the design of the TDC, implementing other architectures, offering better time resolution but shorter counting time [1], [2]. This includes for instance the combined use of high-precision but short conversion-time circuits, with basic counters, one circuit being used for sub-ns resolution over one to tens of ns, while the other is used with ns resolution over longer time. These circuits are well documented and are often implemented for the calculation of time-of-flight or physics applications. Such TDC-based methods represent a more promising method for specific applications, for instance industrial or physics applications, where the bandwidth should be maximized or if the sensing element and electronics can be separated, allowing for more complex but dedicated existing electronics to be used or better signal processing to be done.

However, to enhance the noise performance of such STT-MTJ magnetic sensor, mainly limited by the sensing element itself, Chapter 3 demonstrates the use of newly developed lower coercivity MTJs, used in a similar way and exhibiting promising performance.

Bibliography

[1] Stephan Henzler. Time-to-Digital Converter Basics. In Stephan Henzler, editor, *Time-to-Digital Converters*, pages 5–18. Springer Netherlands, Dordrecht, 2010. doi:10.1007/978-90-481-8628-0_2.

[2] Józef Kalisz. Review of methods for time interval measurements with picosecond resolution. *Metrologia*, 41(1):17, December 2003. doi:10.1088/0026-1394/41/1/004.

[3] Ricardo Sousa and Ioan-Lucian Prejbeanu. Procédé de mesure d'un champ magnétique extérieur par au moins un point mémoire magnétique, March 2022. URL: https://patents.google.com/patent/WO2022043292A1/en?oq=WO2022043292A1.

[4] S. Tehrani, J.M. Slaughter, M. Deherrera, B.N. Engel, N.D. Rizzo, J. Salter, M. Durlam, R.W. Dave, J. Janesky, B. Butcher, K. Smith, and G. Grynkewich. Magnetoresistive random access memory using magnetic tunnel junctions. *Proceedings of the IEEE*, 91(5):703–714, May 2003. Conference Name: Proceedings of the IEEE. doi:10.1109/JPROC.2003.811804.

[5] L. Tillie, E. Nowak, R. C. Sousa, M.-C. Cyrille, B. Delaet, T. Magis, A. Persico, J. Langer, B. Ocker, I-L Prejbeanu, and L. Perniola. Data retention extraction methodology for perpendicular STT-MRAM. In *2016 IEEE International Electron Devices Meeting (IEDM)*, pages 27.3.1–27.3.4, December 2016. ISSN: 2156-017X. doi:10.1109/IEDM.2016.7838492.

[6] A. A. Timopheev, R. Sousa, M. Chshiev, L. D. Buda-Prejbeanu, and B. Dieny. Respective influence of in-plane and out-of-plane spin-transfer torques in magnetization switching of perpendicular magnetic tunnel junctions. *Physical Review B*, 92(10):104430, September 2015. Publisher: American Physical Society. doi:10.1103/PhysRevB.92.104430.

Chapter 2 has presented the use of nanometric perpendicular spin transfer torque magnetic tunnel junctions (STT-MTJs) as nanoscale sensing units through two different and specific reading architectures, based on standard CMOS microelectronics components and simple reading methods. Through a unique way of using STT-MTJs, relatively similar to the working principle of the fluxgate, a successful proof-of-concept has been achieved and experimentally validated.

However, to enhance the noise performance of STT-MTJ magnetic sensor, mainly limited by the sensing element itself, **Chapter 3** demonstrates the use of newly developed low coercivity MTJs, used in a similar way and exhibiting promising performance.

Chapter 3

Low-Coercivity STT-MTJ Magnetic Sensor

3.1 Introduction

To enhance the performance of the presented sensor, mainly in terms of noise, low coercivity MTJs were fabricated and evaluated and will be introduced in this chapter. The principle of the sensor based on these low coercivity MTJs remains exactly the same as described in Chapter 2, in that a triangular voltage signal is applied, allowing for APP and PAP events to occur. The thresholds at which these reversals occur are also directly related to the external magnetic field, and the measurement of such a threshold allows for measurements of $\vec{B}$. However, new electronics have to be developed to overcome some issues and comply with some of the specificity of low-coercivity MTJs. These MTJs were also evaluated using the same setups and methods as described in the previous chapter. Hence, this chapter is divided into three main parts.

- The first part of Chapter 3 presents the newly developed low coercivity STT-MTJs with their specificity in comparison to high coercivity STT-MTJs and behaviour observed as magnetic sensing units
- The second part presents the new electronic circuits developed to operate these MTJs as sensing elements, offering better rms noise at the expense of a lower bandwidth
- The last part of the chapter presents modifications performed on these circuits, allowing for single-period measurements and higher bandwidth to be achieved

3.2 Low-coercivity STT-MTJs

STT-MTJs were manufactured under the same conditions as described in Chapter 2, with the same equipment or techniques. The only difference being the stack developed, which differs from the high-coercivity MTJs, allowing higher sensitivities to be reached. In contrast to the other MTJs, these devices are only targeting sensing applications and are not usable as magnetic memories. Since these devices require a voltage to be applied to maintain one of the two states (Fig. 3.1), this creates a situation in which these MTJs are unable to properly behave as non-volatile memory cells and very inconvenient in volatile memory, as the power consumption will be much higher in one of the two states.

Similarly, the wafers fabricated and used in this chapter were also fabricated with wedges, allowing for a fast and efficient screening of the effect of the thickness of two layers on the output of the sensor, in all cases, one wedge on the FeCoB of the FL and one wedge on a Ru layer in the top electrode.

To assess the best stack, two wafers were tested, both of which implemented low coercivity MTJs with a similar stack. The main differences between the two stacks are in the thickness of a few specific layers. The stacks of the MTJs tested in this chapter are described below, from top layers to bottom layers (thicknesses in nanometres).

Wafer 1

- Top electrode: Ru(8)/Ta(3)/W(2)/Ru(NA[1])/
- MTJ core: $FeCo_8B_{20}$(0.85)/Mg(0.5)/Nat. Ox. (15 sec.)/Mg(0.75)/$FeCo_8B_{20}$(1)/W(0.2)/
- SAF: Co(0.4)/$[Pt(0.3)/Co(0.5)]_2$/Ru(0.9)/Co(0.5)/$[Pt(0.3)/Co(0.5)]_6$/Pt(8)/
- Bottom electrode: $FeCo_8B_{20}$(0.8)/Ta(14)

In wafer 1, the average antiparallel resistance (R_{AP}) and parallel resistance (R_P) are, respectively, 2200 Ω and 1500 Ω. The typical coercive field H_c of these MTJs is 130 Oe (13 mT), with an offset field H_0 of 140 Oe (14 mT). These devices exhibit an average TMR of 42 %. The typical APP and PAP absolute voltages are around between 0 and 350 mV for a typical breakdown voltage of 450 mV. Similarly, the variations observed within the wafers are mainly the result of the wedges and not the result of fabrication variability.

Wafer 2

- Top electrode: Ru(8)/Ta(3)/W(2)/Ru(NA[2])/
- MTJ core: $FeCo_8B_{20}$(1)/Mg(0.5)/Nat. Ox. (15 sec.)/Mg(0.75)/$FeCo_8B_{20}$(1)/W(0.2)/
- SAF: Co(0.5)/$[Pt(0.3)/Co(0.5)]_2$/Ru(0.9)/Co(0.5)/$[Pt(0.3)/Co(0.5)]_6$/Pt(8)/
- Bottom electrode: $FeCo_8B_{20}$(0.8)/Ta(14)

In wafer 2, the average antiparallel resistance (R_{AP}) and parallel resistance (R_P) are, respectively, 2900 Ω and 2100 Ω. The typical coercive field H_c of these MTJs is 30 Oe (3 mT), with an offset field H_0 of 220 Oe (22 mT). These devices exhibit an average TMR of 35 %. The typical APP and PAP absolute voltages and breakdown voltages are similar to those of the first wafer, and the variations are also a result of the wedges.

Similarly to the behaviour of high coercivity MTJs, stochasticity is observed in these devices, creating a large noise. The measurements of the phase diagrams of the MTJs show the clear evolution of the transition region P/AP and AP/P with respect to the magnetic field (Fig. 3.1 and 3.2). Hence, the goal is to track this threshold, proportional to $\vec{B}$, through different approaches, described in the next sections. However, while different high coercivity MTJs showed similar shape in their phase diagrams, mainly being different in their parameter values, low coercivity MTJs demonstrated stronger variability in their phase diagram shape, possibility induced by fabrication variability and/or stronger effect of some layer thickness. Intrinsic sensitivity, measured from the phase diagrams as the slope of the APP/PAP transition region, could reach up to 40 or 50 mV/mT in some MTJs.

[1] Not Available
[2] Not Available

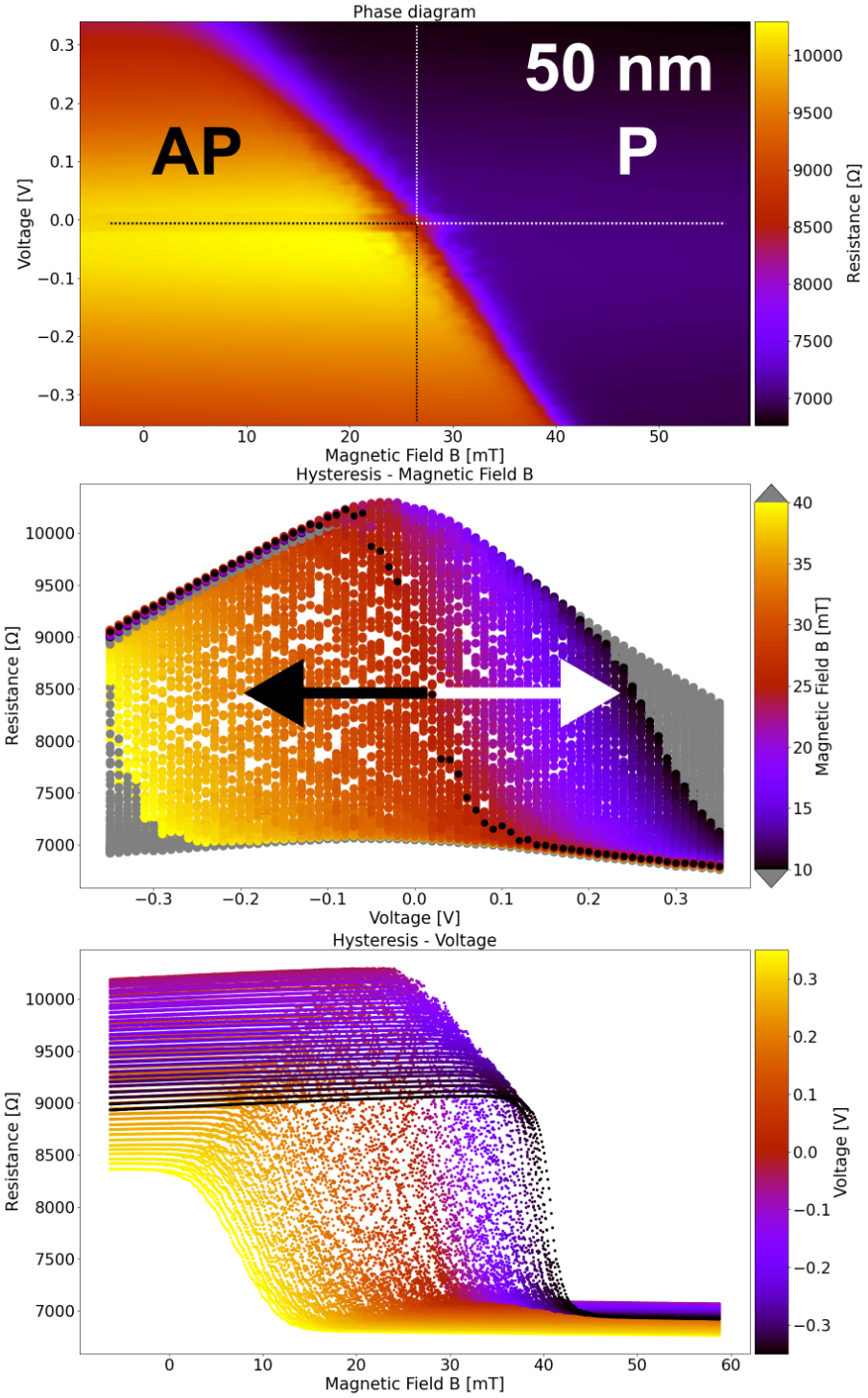

Figure 3.1: Typical 50 nm low coercivity STT-MTJs phase diagram. The typical voltage and magnetic hysteresis cycles are shown, demonstrating the clear shift in the magnetic or voltage cycles (experimental results).

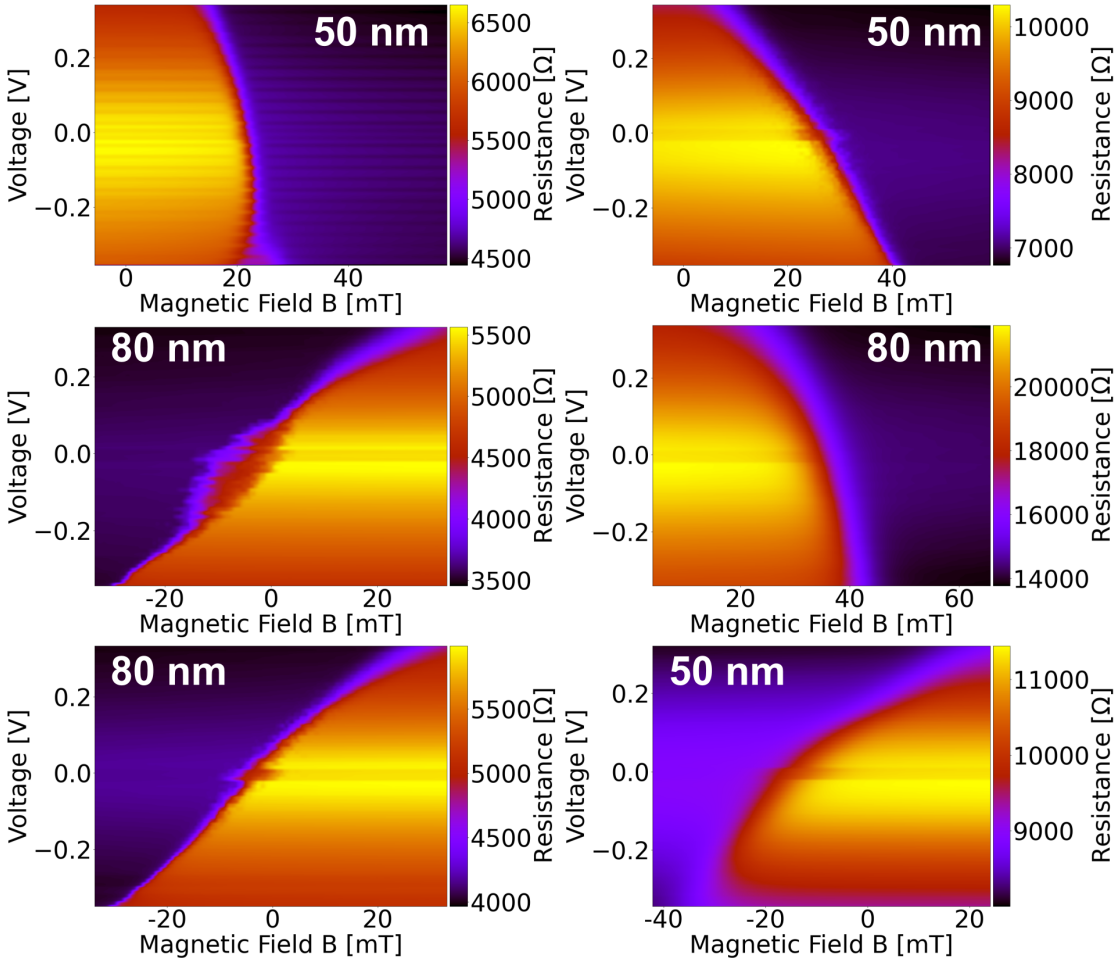

Figure 3.2: Phase diagrams obtained for six different low coercivity MTJs, demonstrating the possible variations in the shape and values of the phase diagrams of these devices (50 nm to 100 nm) (experimental results). The artefacts around 0 V are induced by the impossibility to measure currents below specific low voltages (close to 0 V), requiring the use of post-processing interpolation, which results in these artefacts.

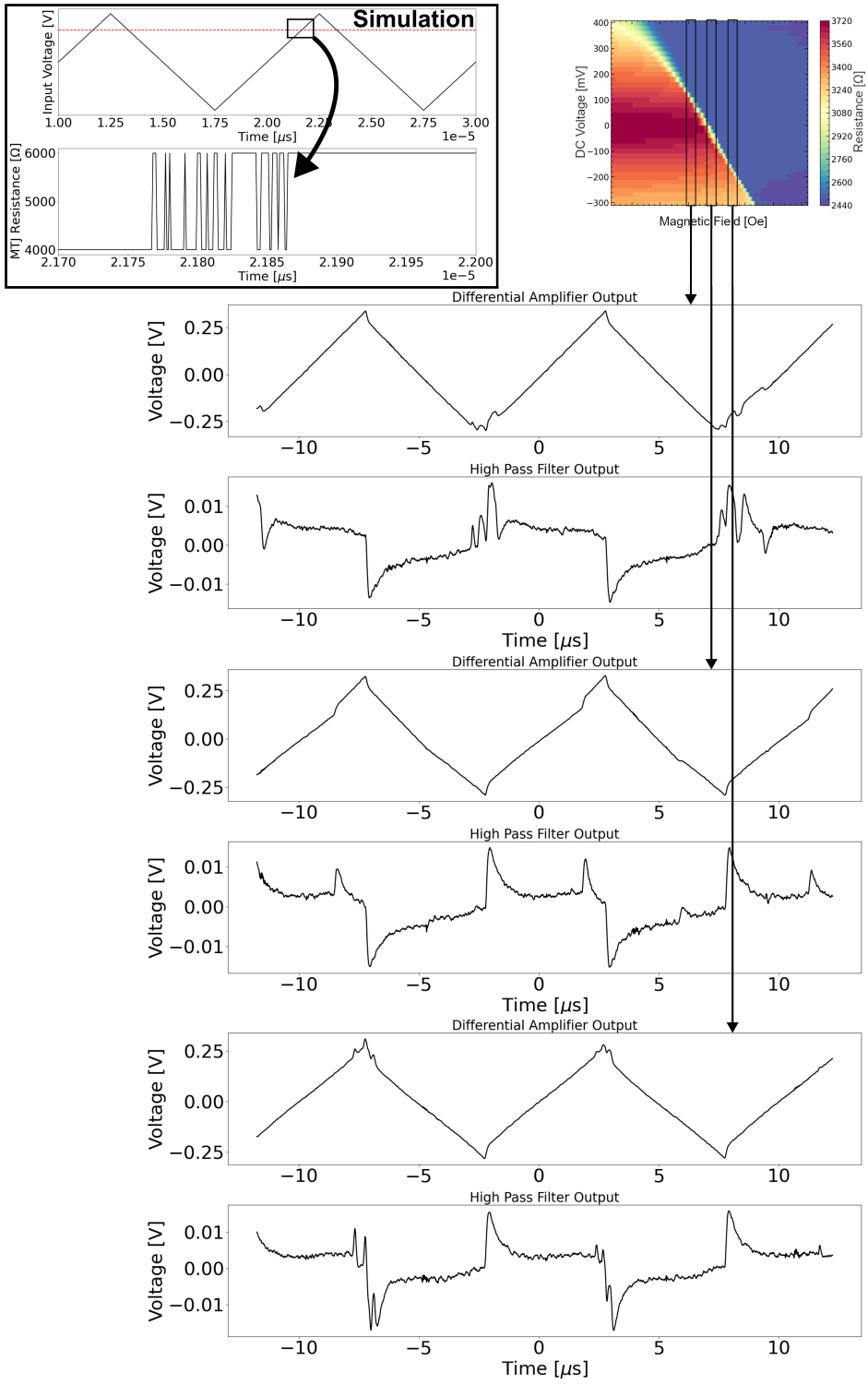

Figure 3.3: Current measurements of a 50 nm low coercivity MTJ with its associated HPF output, as described in Chapter 2 for high coercivity MTJs, at three different magnetic field values, showing the incompatibility of low coercivity MTJs with such measurement method, as pulses at the output of the HPF are very close to the background noise, making the detection challenging (experimental results). A simulation of possible oscillations between the P and AP states at the approach of the switching threshold in low coercivity MTJs is also shown, that could possibility lead to larger noise, in addition of the stochasticity, and could explain the visible oscillations in the current measurements.

3.3 High-resolution circuit

Despite a significant TMR of up to 40 to 60 %, these low coercivity MTJs exhibit a much softer reversal compared to high coercivity MTJs, as seen in the phase diagrams, making detection of reversals through HPFs impossible. To operate these devices as sensing units, other approaches have been developed, based on operational amplifiers and standard microelectronic components, which will be detailed in this section.

To operate the MTJs within their maximal dynamic range while keeping them intact, a triangular input signal with a peak amplitude A of 300 mV (i.e., $\pm$ 300 mV) was used, at a frequency F of 100 kHz. This creates periodic reversals between the AP and P states, allowing the presented principle of the switching threshold and $\vec{B}$ field dependency to take place.

3.3.1 Integrator-based approach

Circuit description

In the first approach tested, the MTJ was implemented as a variable resistor within a typical integrator circuit, depicted in Fig. 3.4. The MTJ was connected between the input signal, coming from the waveform generator, and the virtual ground of the OpAmp, ensuring, for proper behaviour, that the voltage applied between the two electrodes of the MTJ is always referenced to a constant potential, the ground.

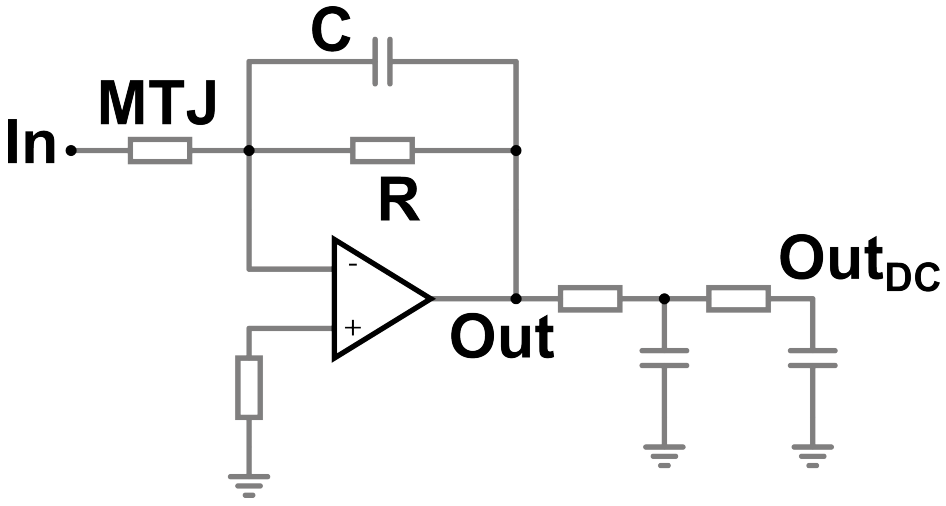

Figure 3.4: Integrator-based conditioning electronics circuit. A resistor can be added on the non-inverting input to compensate for the input bias current of the inverting input, with a value comparable to the impedance seen on the inverting input.

Hence, the circuit works by integrating the input signal with a gain G which is defined by the resistance of the MTJ, R and C. The resistor R and capacitor C used were chosen to be 82 kΩ and 1 nF. In this configuration, the integration of any triangular waveform results in a quadratic signal at the output of the amplifier. Since the resistance is constantly alternating between the P and AP states, this creates a variable gain over one period of the input signal. As the MTJ stays in one state longer or shorter than in the other state, this creates an asymmetry in the gain, resulting in an output signal proportional to the magnetic field. In this condition, **the dc offset of the quadratic signal is affected by the external magnetic field**. Therefore, a simple passive second-order RC LPF with a cutoff frequency of few hundreds of Hz (100 to 500 Hz, in that case 160 Hz) is then used to retrieve the dc offset of the signal and output a signal directly proportional to $\vec{B}$, which is sampled by the ADC.

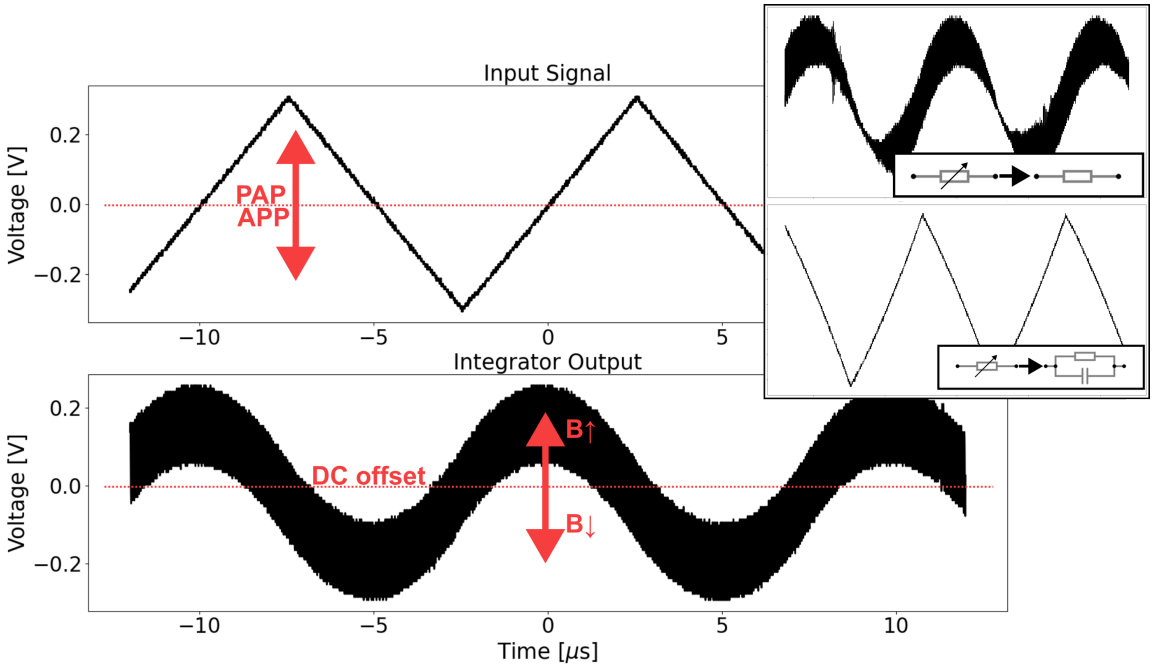

Figure 3.5: Integrator-based working principle. The input signal, applied to the MTJ is shown, with the corresponding output, filtered by the LPF. The impact of using a simple resistor instead of the MTJ, or a resistor with parallel capacitor is shown on the top right (experimental results).

While the output signal exhibits the proper behaviour, a parasitic oscillation can be seen, at a frequency of approximately 35 MHz with an amplitude peak-to-peak of 200 mV. To assess the source of the oscillation, the MTJ was replaced by a simple resistor of 5 kΩ. As a result (Fig. 3.5), the oscillation was still present, indicating an issue within the circuit that could be solved by more complex solutions. The addition of a small capacitor of 2 nF in parallel of the resistance allows for a filtering of the signal. However, since the output LPF removes all of this noise, such issue has not been investigated more in detail for this first proof of concept and the parallel capacitor has not been implemented during MTJ measurements.

The equation describing the output V_{Out} of the circuit is given by equation 3.3.1, and the derivative of this gives the output sensitivity, which is highly challenging to express analytically.

$$V_{Out}(V_{In}(t),\vec{B}) = \frac{1}{e^{\int \frac{1}{RC}dt}}\left(\int e^{\int \frac{1}{RC}dt}\frac{-V_{In}(t)dt}{R_{MTJ}(V_{In}(t),\vec{B}).C} + Cst\right) \tag{3.3.1}$$

In the case of input sine signals, the output of the circuit can then be expressed as equation 3.3.2, as long as the input signal is given by $V_{In} = V_0 + A\sin(2\pi Ft)$, with V_0 being the offset of the circuit. Through this equation, the constant Cst needs to be recalculated at each switching event T_0 (APP or PAP), using the output voltage at the moment of the switches, using equation 3.3.3. Since one can express every signal as a sum of sine and cosine signals through the Fourier series, this allows the modelling of the output signal for every input signal. Using this property, one can achieve the calculation of the expected output characteristic, given in Fig. 3.6, which matches the output given by the LTspice analytical simulator.

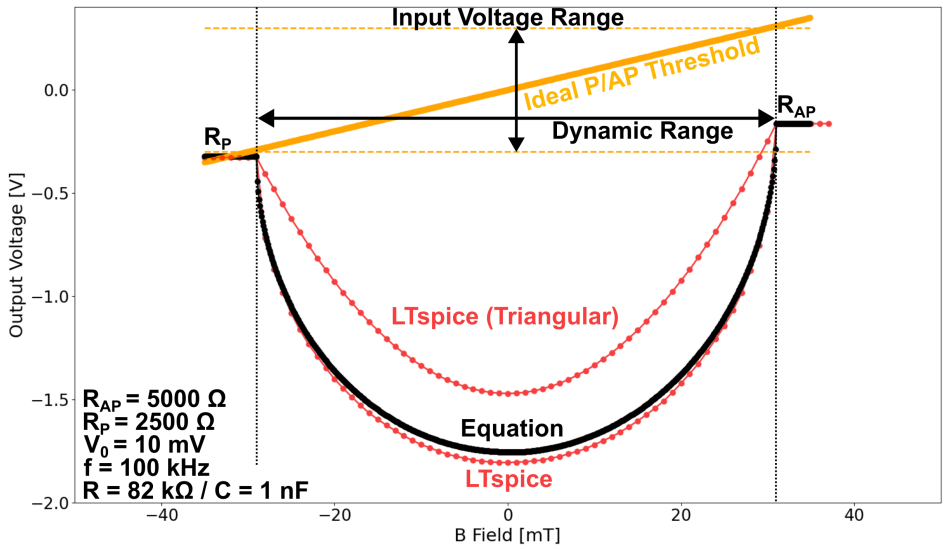

Figure 3.6: Integrator-based theoretical output, calculated using the proposed equation or LTspice. The parameters of the MTJ, input signal and resistance value are shown for reference, and the switching P/AP threshold used is also visible.

$$V_{Out}(V_{In}(t),\vec{B}) = e^{\frac{-t}{RC}}Cst - \frac{R\left(C^2R^2(2\pi F)^2V_0 - RCA(2\pi F)\cos(2\pi Ft) + V_0 + A\sin(2\pi Ft)\right)}{R_{MTJ}(C^2R^2(2\pi F)^2+1)} \tag{3.3.2}$$

$$Cst(t=T_0) = \frac{V_{Out}(T_0)}{e^{\frac{-t}{RC}}} + \frac{Re^{\frac{t}{RC}}\left(C^2R^2(2\pi F)^2V_0 - RCA(2\pi F)\cos(2\pi Ft) + V_0 + A\sin(2\pi Ft)\right)}{R_{MTJ}(C^2R^2(2\pi F)^2+1)} \tag{3.3.3}$$

Achieved performance

Using such principle, the experimental measurements of the MTJs showed a successful working principle. The sensitivity of MTJs could be extracted as well as noise measurements, through the same experimental protocol described for high coercivity MTJs. Hence, a discrete sweep of $\vec{B}$ was performed. For each point, magnetic field was set at a constant dc level using either one of the two setups described, and the voltage at the output of the LPF was sampled by the same ADC. For each magnetic field step, 8192 data points were sampled, and the median was calculated to obtain the output value of the sensor for each particular step. The output characteristic of the sensor was obtained and shown in Fig. 3.7. Sensitivities of 5 to 15 mV/mT were achieved.

The complete magnetic field range where output voltage variations can be observed ranges up to 40 mT (i.e., ± 20 mT around the offset field), depending on the MTJ, always through the typical "U" shape. Due to the output characteristics shape, the assessment of the non-linearity is more complicated to define. However, ± 1 to 3 % FS can be achieved over up to 10 mT in the most linear region, and more complicated linearization techniques (e.g., lookup table, offset cancellation with feedback coils) could be used for better performance over the entire dynamic range.

Noise measurements were also performed, with the corresponding spectrum shown in Fig. 3.8. NPSD achieved was typically 0.1 to 0.3 mV/$\sqrt{Hz}$, corresponding to 10 to 40 μT/$\sqrt{Hz}$, with best performance obtained from both sides of the offset field, as low as 2 to 5 μT/$\sqrt{Hz}$ depending on the MTJ. The typical rms noise achieved was 1 to 10 mV, corresponding to up to 500 μT over a bandwidth of hundreds of Hz, defined by the cutoff frequency of the LPF, typically ranging from 100 to 500 Hz, in this example 160 Hz.

Finally, measurements of ac signals at 5 Hz over ± 8 mT showed proper oscillating output, as shown in Fig. 3.9, demonstrating the dynamic metrological capabilities of the sensor. However, because of the non-linearity, more harmonics can be seen than in previous high coercivity methods. This issue can be minimized by precisely offsetting the field to be in the most linear range of the sensor, as well as by using linearization circuits and methods.

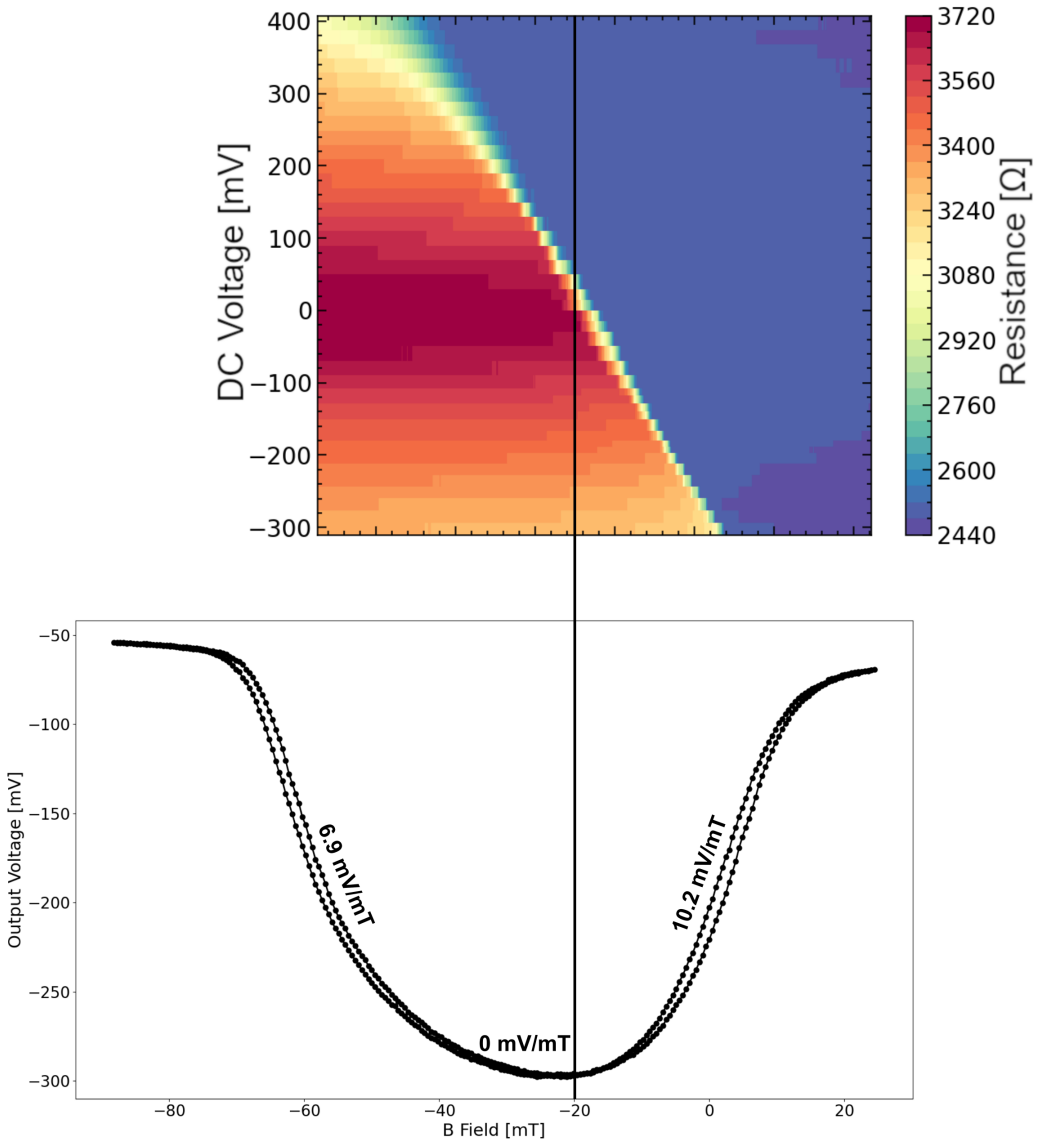

Figure 3.7: Output characteristics achieved of the proposed integrator-based circuit for a 80 nm MTJ (experimental results). The corresponding phase diagram is shown for reference.

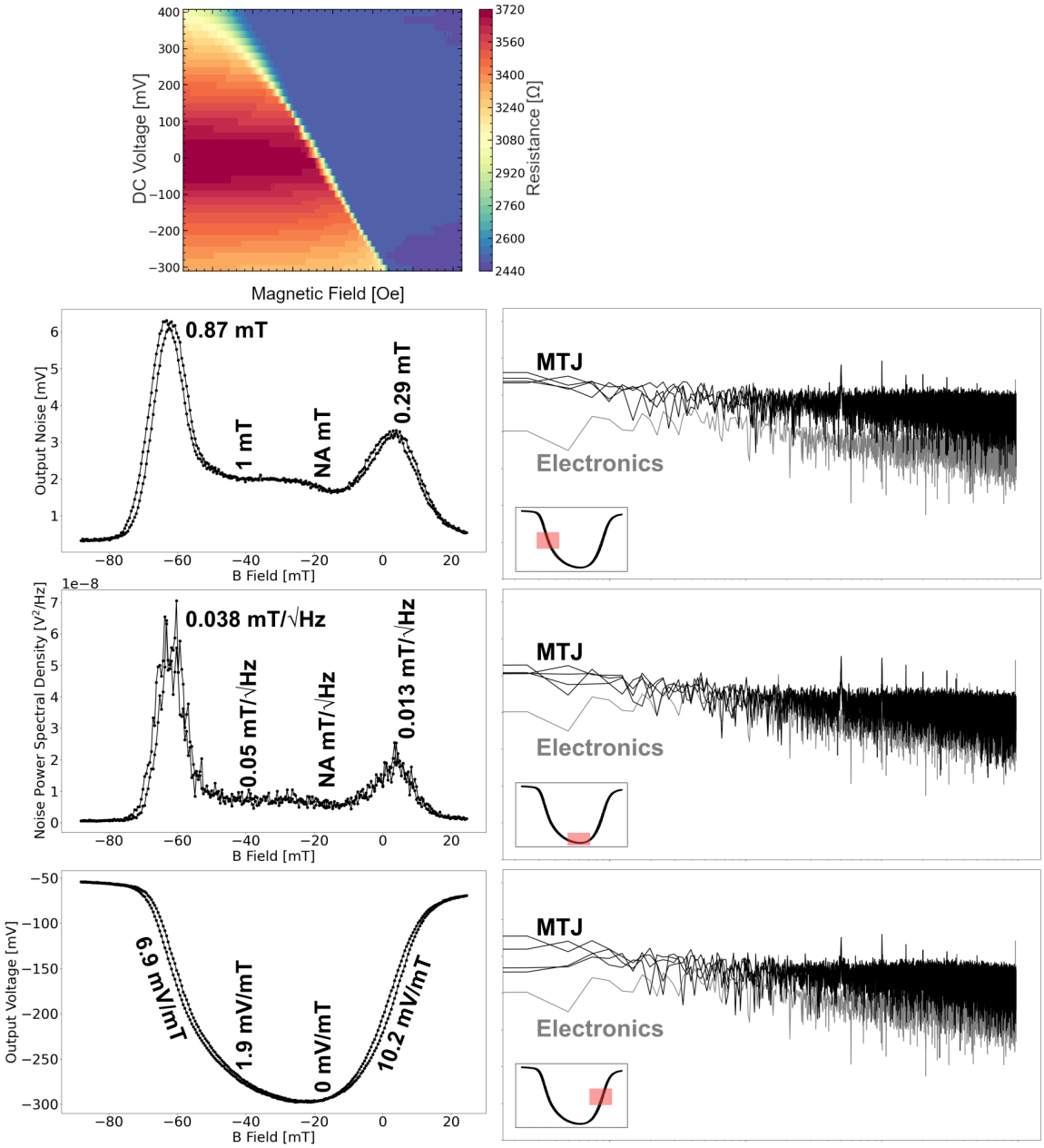

Figure 3.8: Noise performance (rms and NPSD) achieved through the proposed integrator-based circuit for a 80 nm MTJ (experimental results). The corresponding phase diagram is shown for reference. A close up look at both the rms noise and NPSD is also shown.

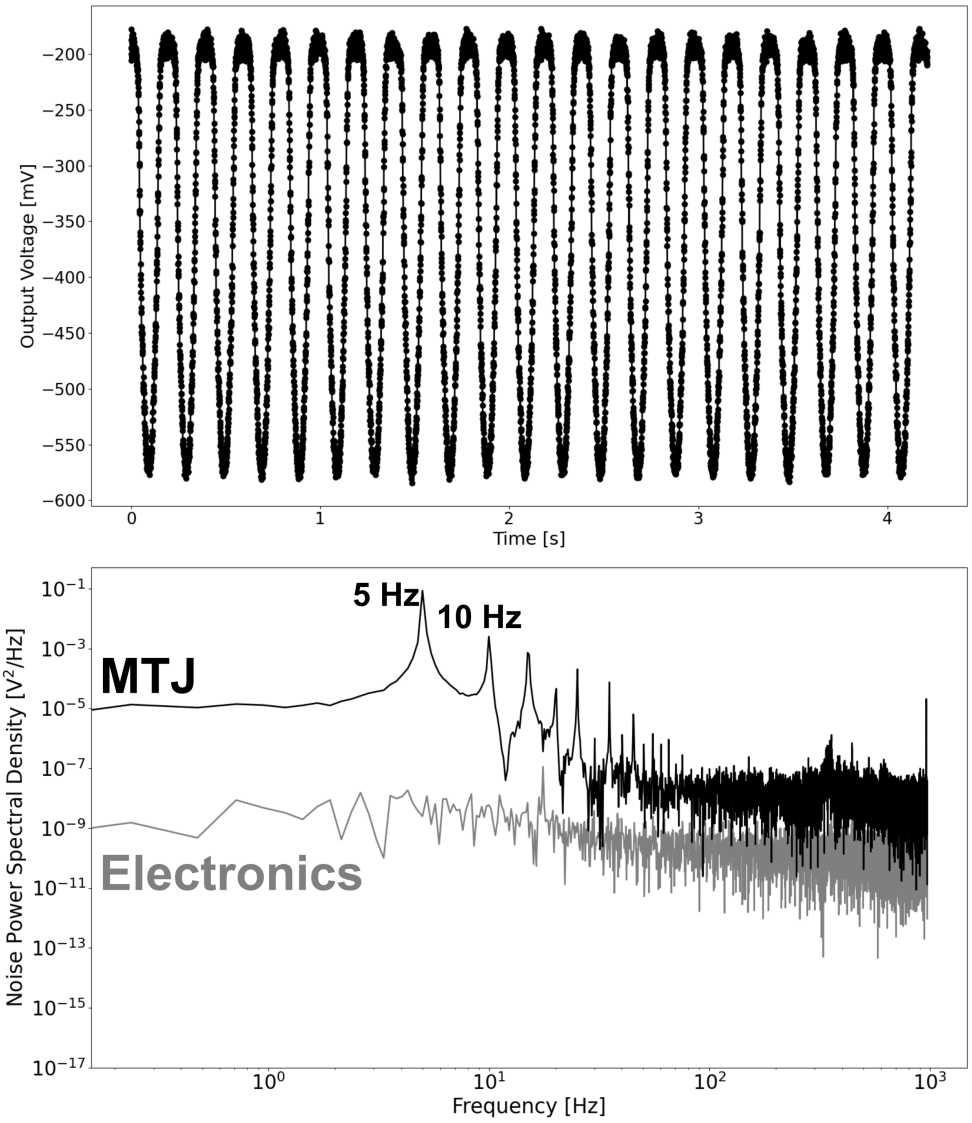

Figure 3.9: Measurements achieved of the proposed integrator-based circuit in the case of ac sine wave magnetic field signals for a 100 nm MTJ (experimental results). Both time domain and frequency domains are shown.

3.3.2 Rectifier-based approach

Circuit description

As seen in the output characteristics, the presented initial method demonstrates the working principle with, however, two main issues. The first is a symmetry in the output voltages, making it impossible to differentiate positive or negative magnetic fields centred around the offset. The second observed issue is a dead zone, located around the offset field, where a null sensitivity is observed. Hence, a second approach described in this section aims to overcome these metrological problems.

To overcome these drawbacks, the circuit described above can be slightly modified (Fig. 3.10). In this second approach, the MTJ is placed as the input resistor of an inverting amplifier. In the same condition as in the first method, the gain G of the circuit changes over one period, as the MTJ alternates between the P and AP states, and as a result, the output signal corresponds to the input signal amplified with a variable gain proportional to the external magnetic field.

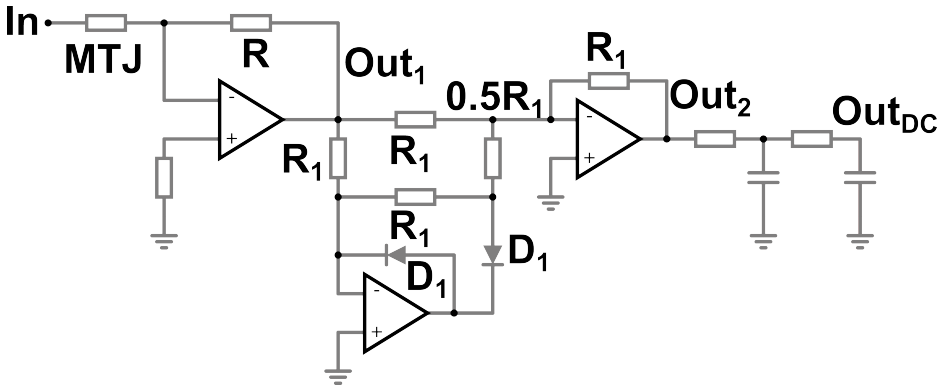

Figure 3.10: Rectifier-based conditioning electronics circuit.

However, this does not solve the symmetry problems, as the filtering of this output signal still demonstrates such a symmetry issue. To address the issues directly, this signal needs to be injected into a precision OpAmp-based rectifying circuit, whose input signal V_i is fully rectified at the output V_o ($V_o =\mid V_i \mid$). The output of the rectifying circuit can then be filtered through a second order, RC LPF, with a similar cutoff frequency than in the first method, resulting in a signal proportional to $\vec{B}$ that can be sampled by the ADC. Through such an approach, **it is the average value of V_o that is proportional to $\vec{B}$** and not the dc offset as in the integrator-based approach (Fig. 3.11).

Similarly to the previous approach, a parasitic oscillation can also be observed (Fig. 3.11). To assess the origin, the MTJ was also replaced by a simple resistor of 5 kΩ, resulting in the suppression of the oscillations, indicating that the parasitic capacitance of the MTJ and / or the parasitic capacitance of the cable was the source. The addition of a small capacitor of 100 pF

in parallel of the resistance resulted in a similar output, confirming the hypothesis. Although the use of integrated circuit including the MTJ would remove the parasitic capacitance of the SMA cable, the intrinsic capacitance of the MTJ is likely to continue producing such type of oscillation, and more advanced solutions or layout would need to be designed for the suppression of such oscillation. However, at low frequency, the noise induced can be filtered by the output LPF and the issue can be ignored in such first approach.

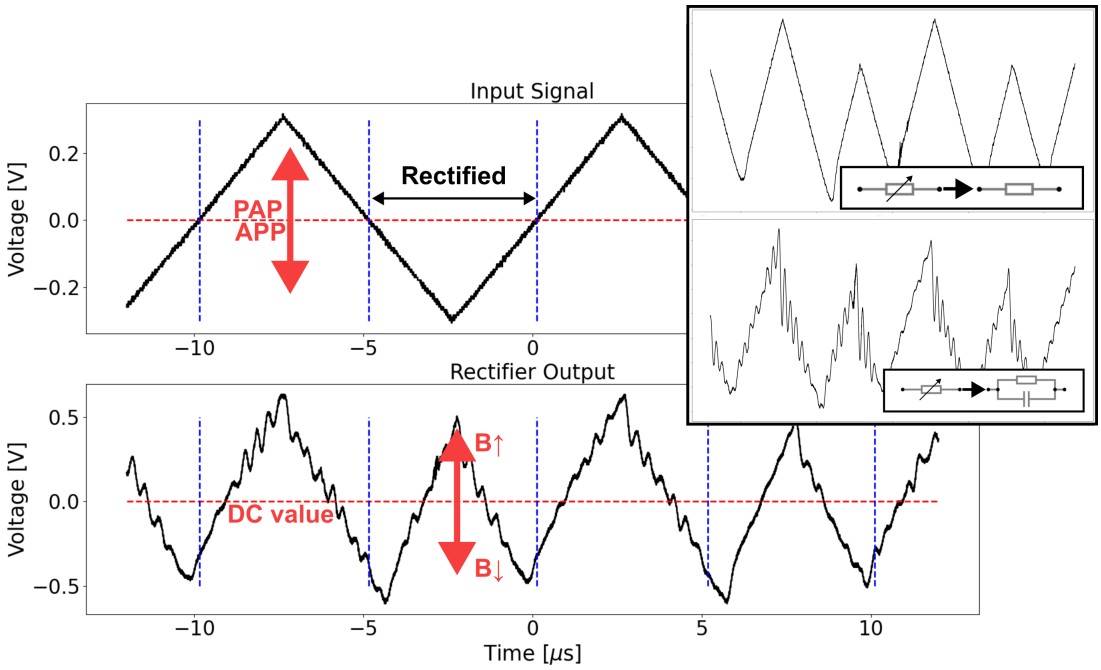

Figure 3.11: Rectifier-based working principle. The input signal, applied to the MTJ is shown, with the corresponding rectified output (ac coupled), filtered by the LPF. The impact of using a simple resistor instead of the MTJ, or a resistor with parallel capacitor is shown on the top right (experimental results).

The gain of the proposed circuit is given directly by 3.3.4, with R chosen to be 8.2 kΩ in that case. This value of R allows different MTJs to be tested without saturating the amplifier. Similarly to the previous approach, the simulation of the predicted output can be achieved using LTspice or through the proposed equation, shown in Fig. 3.12. In addition, regardless of the diodes implemented in the rectifying circuit, the theoretical equation, ignoring their effects (given by the Shockley diode equation), exhibits the same precision to LTspice simulation thanks to the architecture. Finally, it can be seen that the use of non-null coercivity in the MTJ does not appear to have any impact on the dead zone around the offset field.

$$V_{Out}(V_{In}(t), \vec{B}) = \left| -V_{In}(t) \frac{R}{R_{MTJ}(V_{In}(t), \vec{B})} \right| \tag{3.3.4}$$

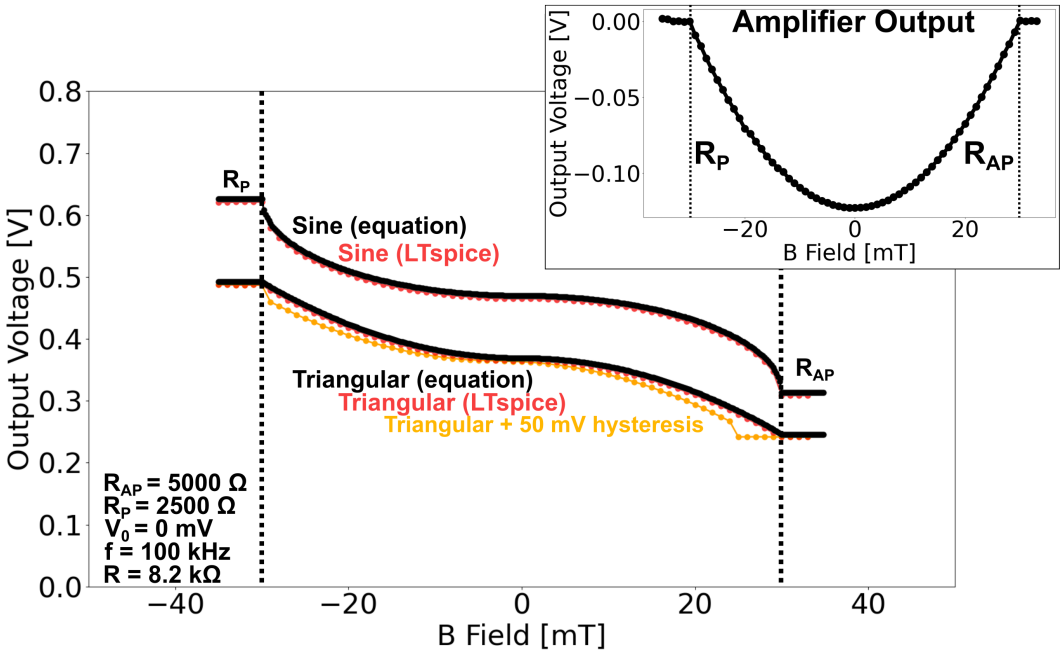

Figure 3.12: Rectifier-based theoretical output, calculated using the proposed equation or LTspice. The parameters of the MTJ, input signal and resistance value are shown for reference, and the switching P/AP threshold limits are also visible. The effect from the use of input sine or triangular signals is visible.

Achieved performance

Using such principle, the experimental measurements of the MTJs showed a successful working principle. The sensitivity of MTJs could be extracted as well as noise measurements. The output characteristic of the sensor was performed and shown in Fig. 3.13. Sensitivity of 1 to 5 mV/mT was achieved, with non-linearity error of ± 1 to 3 % FS over a dynamic range of up to 30 mT, even if the entire magnetic field dynamic range can reach up to 50 mT.

Noise measurements were also performed, with the corresponding spectrum shown in Fig. 3.14. NPSD achieved was typically 0.04 to 0.1 mV/$\sqrt{Hz}$, corresponding to 10 to 40 μT/$\sqrt{Hz}$, with best performance obtained around the offset field, as low as 2 to 5 μT/$\sqrt{Hz}$ depending on the MTJ. The typical rms noise achieved was 0.5 mV, corresponding to 200 to 300 μT over a bandwidth of hundreds of Hz, similarly to the previous method, defined by the cutoff frequency of the LPF, in this case 160 Hz.

Finally, measurements of ac signals at 5 Hz over ± 8 mT showed proper oscillating output, as shown in Fig. 3.15, demonstrating the dynamic metrological capabilities of the sensor. Similarly, the harmonics are induced by the non-linearity, which can be minimized depending on the MTJ and field offset chosen during the measurement sequence.

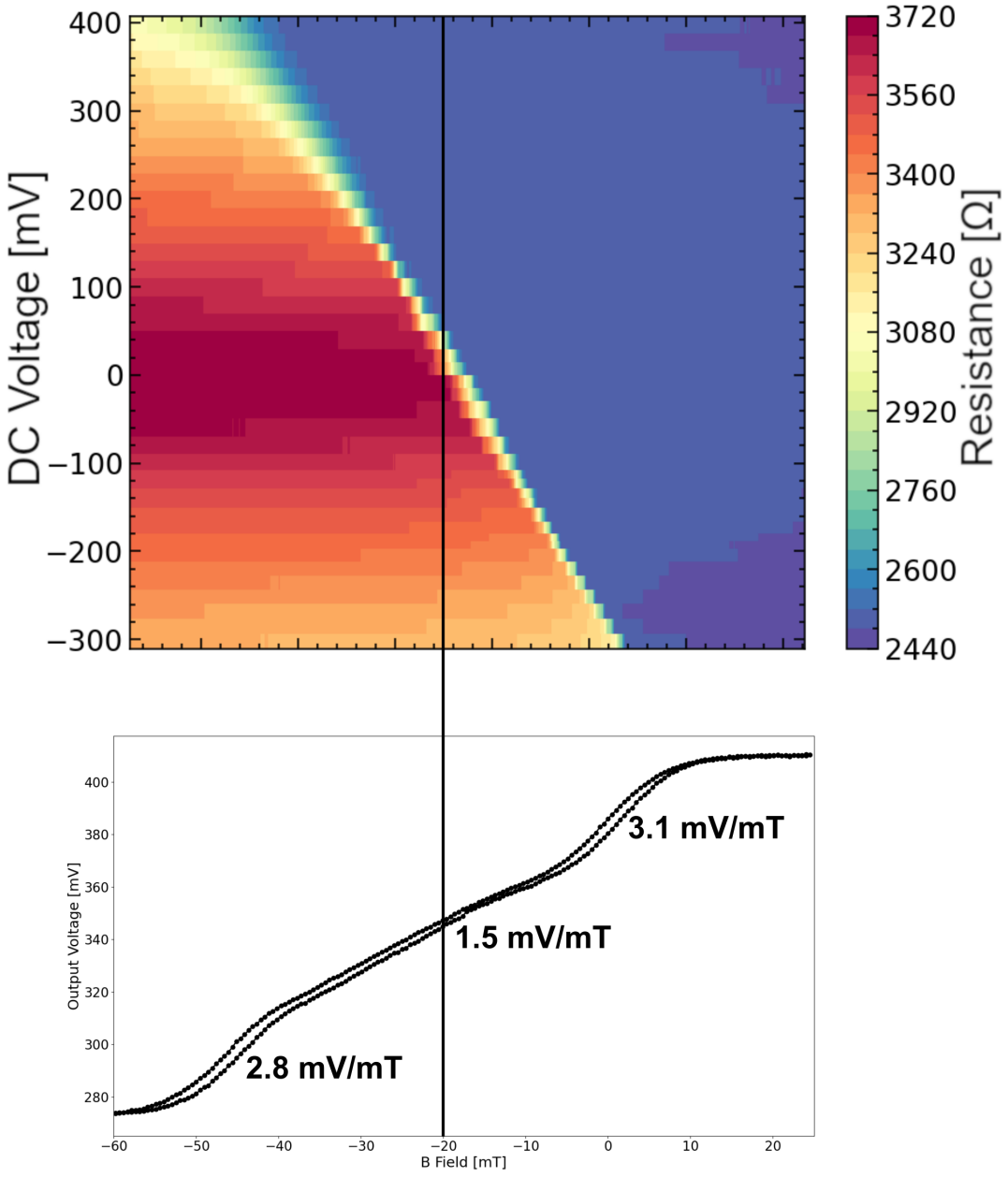

Figure 3.13: Output characteristics achieved of the proposed rectifier-based circuit for a 80 nm MTJ. The corresponding phase diagram is shown for reference (experimental results).

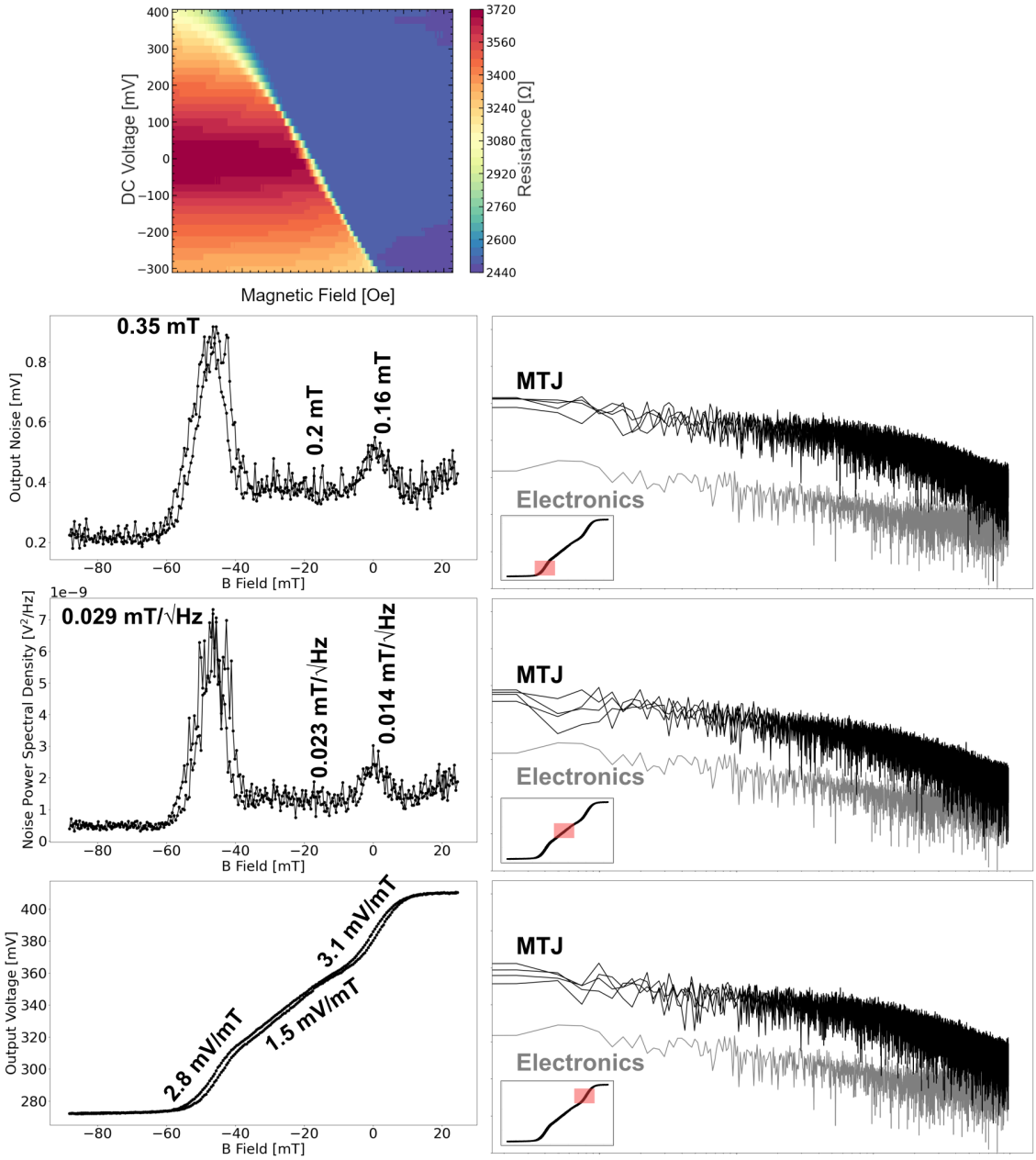

Figure 3.14: Noise performance (rms and NPSD) achieved through the proposed rectifier-based circuit for a 80 nm MTJ (experimental results). The corresponding phase diagram is shown for reference. A close-up looks at both the rms noise and the NPSD is also shown.

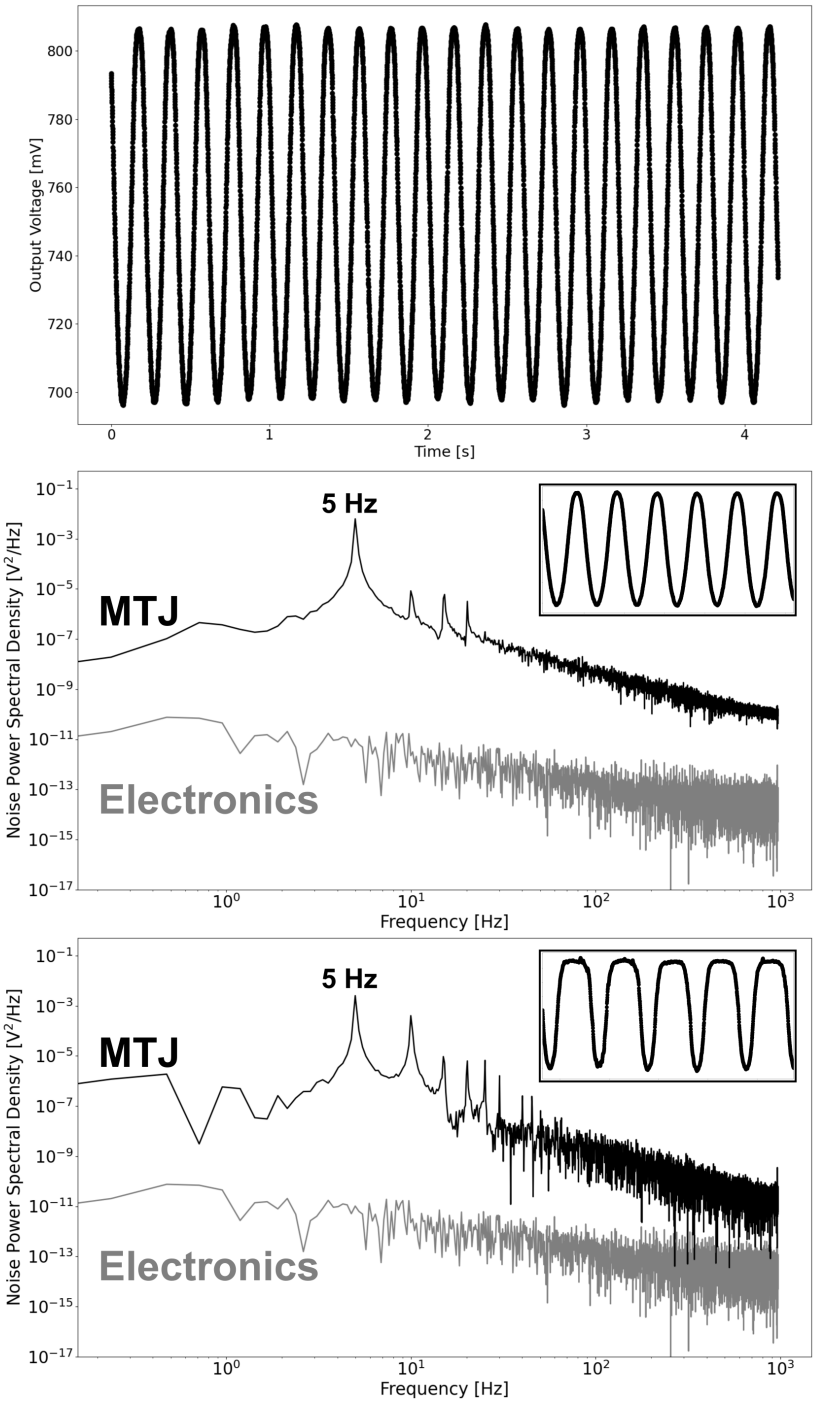

Figure 3.15: Measurements achieved of the proposed rectifier-based circuit in the case of ac sine wave magnetic field signals for two 100 nm MTJs. The difference between the two signals, measured on the two different MTJs shows the importance of the field offset on the output signal to obtain the best linearity (experimental results). Both time domain and frequency domains are shown.

3.3.3 Rectifier vs integrator circuits

To assess the differences between the two electronics presented in the previous two sections, measurements with the two versions of the electronics were performed on the same MTJs, allowing a comparison between the two approaches, shown in Fig. 3.16.

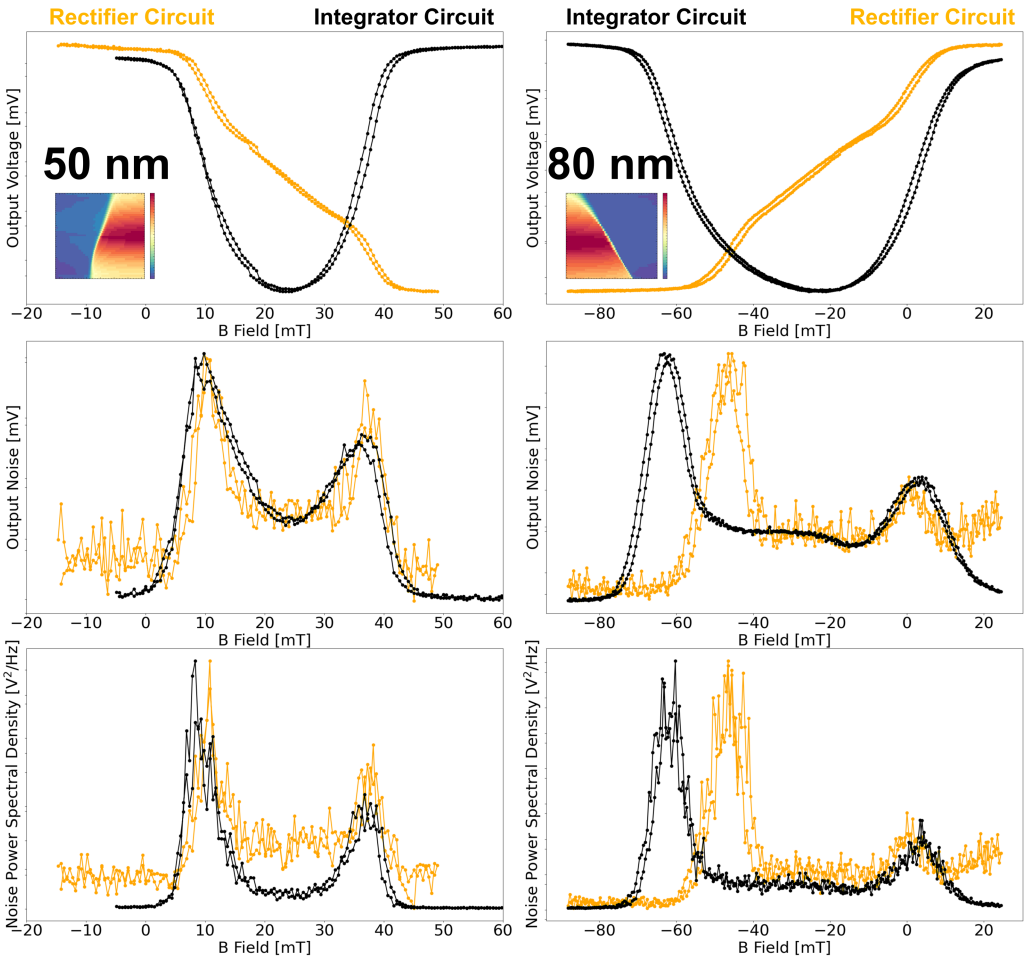

Figure 3.16: Output characteristics difference between the two low coercivity approaches demonstrated for the same STT-MTJs (50 and 80 nm). The respective offset voltages were artificially removed for better clarity (experimental results).

Hence, one can observe the advantages offered by the second version of the electronics (based on the rectifier), allowing for easier output characteristics to work with, as such approach exhibits an unsymmetrical output (monotonic). In both MTJs tested and in both versions of the electronics, one can see that the highest sensitivity (i.e., highest slope) is also reached when the noise is the strongest (i.e., largest stochasticity). However, this can also result in the best working area, with the most favourable magnetic SNR (depending on the MTJ). NPSD and rms (magnetic) noise remains similar in both circuits, with no clear distinction between the two. Since both circuits are relatively similar in terms of complexity, despite the rectifier requiring the use of two Schottky diodes and two additional amplifiers, such an approach, offering monotonic output, appears to be the best so far, to use low coercivity MTJs as sensing elements. In the possible case of extreme dimensions requirements, the first approach (based on the integrator), offering the simplest and most compact layout, remains the best in such situation.

Finally, in the case of high-frequency measurements, the first approach also offers the simplest circuits, as the dc offset is proportional to $\vec{B}$, therefore a simple peak detector can be used, synchronized with the input signal allowing for a single period to be sampled. In the case of high-frequency measurements with the second approach, allowing for monotonic output to be achieved, more complex methods are required, as described in the following section.

In addition, as can be observed, the zero-sensitivity region is absent from the experimental measurements compared to the simulated results for the rectifier approach. This is a consequence of the low-coercivity MTJs not being true bistable systems, with two well-defined resistance states. Experimentally, the transition between the two limit states has intermediate values that were not taken into account in the simulation. These values can be observed in the hysteresis cycles measured at different bias voltages for different applied external fields (Fig. 3.2). This significantly affects the output characteristics around the offset field.

3.4 High-frequency circuit

3.4.1 Circuit description

Similarly to high coercivity MTJs, single period measurement can be achieved by simply modifying the circuits compatible with proposed low coercivity MTJ compatible circuits, allowing high-frequency measurements to be performed. However, the detection of single events, as in the previously demonstrated TDC method, is not possible with these MTJs, and a dedicated method has to be developed. While all the other approaches, based on ADCs so far, are based on low frequency, high resolution ADCs, or based on TDC for high frequency measurements, such high frequency measurement method for low coercivity MTJs relies on high-speed ADCs which can be achieved through SAR ADCs (successive approximation register), frequently achieving sampling rate of several MHz with resolution of 12 to 16 bits.

The most straightforward way to modify these circuits would be simply to increase the cutoff frequency of the LPF to be slightly below the input signal frequency, with extreme attenuation. However, this requires very high-order LPF (e.g., Butterworth LPF), which requires many passive or even active components. In addition, infinite attenuation is unlikely from a practical point of view, resulting in real-life situations in aliasing the output signal. To avoid this, the circuit presented in this section aims to obtain an output voltage which allows synchronous sampling, synchronized with the input signal, removing any aliasing possibility and simplifying the overall circuit. Hence, based on the second circuit described above, simple modifications allow a single-period reversal to be sampled and offer high-bandwidth capability. To achieve this, the second low coercivity approach demonstrated in this chapter, based on the rectifying circuit, was reused. However, the output voltage obtained at the output of the rectifying circuit needs to be injected directly into a second stage, based on a standard OpAmp integrating circuit, which integrates the resulting signal over the duration of one period of the input signal. To precisely control this, a simple reset switch, placed in parallel of the integrating capacitor, is then used (instead of the resistor as in the first integrator-based method), allowing for the value of the final output stage to be reset at each new period.

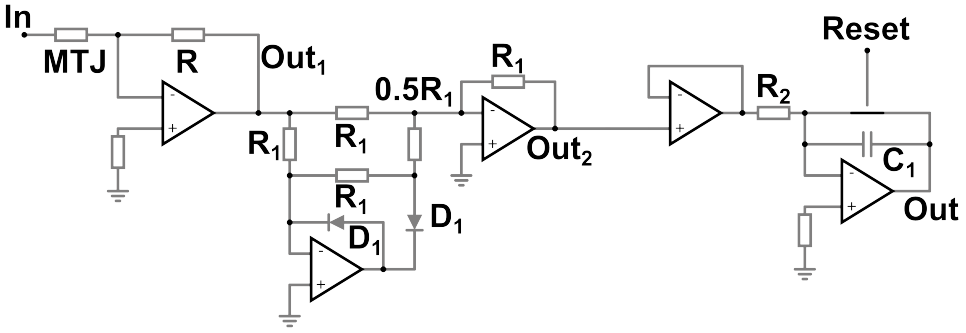

Figure 3.17: High frequency conditioning electronics circuit.

For each completion of a period of the input signal, the ADC is configured to sample the value at the output of the integrating circuit, followed by a reset of the circuit, allowing for a new period to be integrated. This corresponds to one cycle, which is then repeated for every new period, allowing high-frequency measurement to be performed. This reset switch is controlled by an external MCU, which is also in charge of triggering and reading the ADC. Finally, to detect the periods, a simple comparator was used, comparing the input signal with the ground, allowing a new rising edge for each new period to be produced, triggering the MCU to perform the reading of the ADC and the reset of the circuit, following the custom sequence. The complete circuit is depicted in Fig. 3.17 with the control signals, shown in Fig. 3.18. The chosen values are R of 8.2 kΩ, and R_2 and C_1 chosen to have a high cutoff frequency, in this case 79 kHz. However, as seen in these figures, such an architecture only allows the signal to be sampled at a frequency of half the input frequency, as every other period is used for the reset and conversion. To allow complete sampling at maximum bandwidth, one can simply invert the Sign signal to obtain nSign, and inject it into a second integrator stage, running in parallel of the first stage, allowing for the sampling of all periods.

The output signals obtained for the proposed circuit are shown in Figs. 3.19 and 3.20. In addition, the output voltage of the final integration stage at the end of every integration cycle can be given by 3.4.1.

$$V_{Out}(V_{In}(t), \vec{B}) = \frac{-R_2}{C_1} \int_0^T \left| -V_{In}(t) \frac{R}{R_{MTJ}(V_{In}(t), \vec{B})} \right| dt \tag{3.4.1}$$

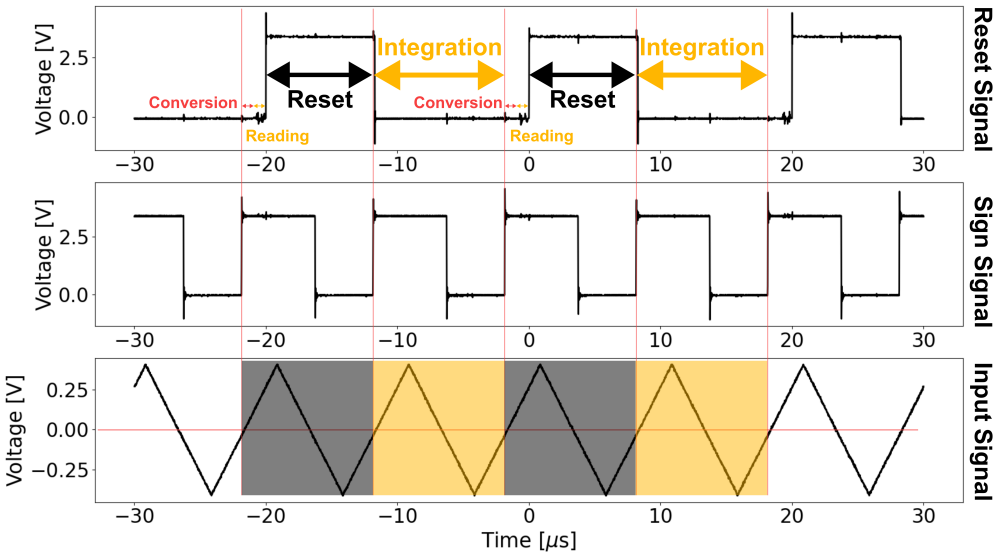

Figure 3.18: Control signals of the proposed high frequency circuit (experimental results).

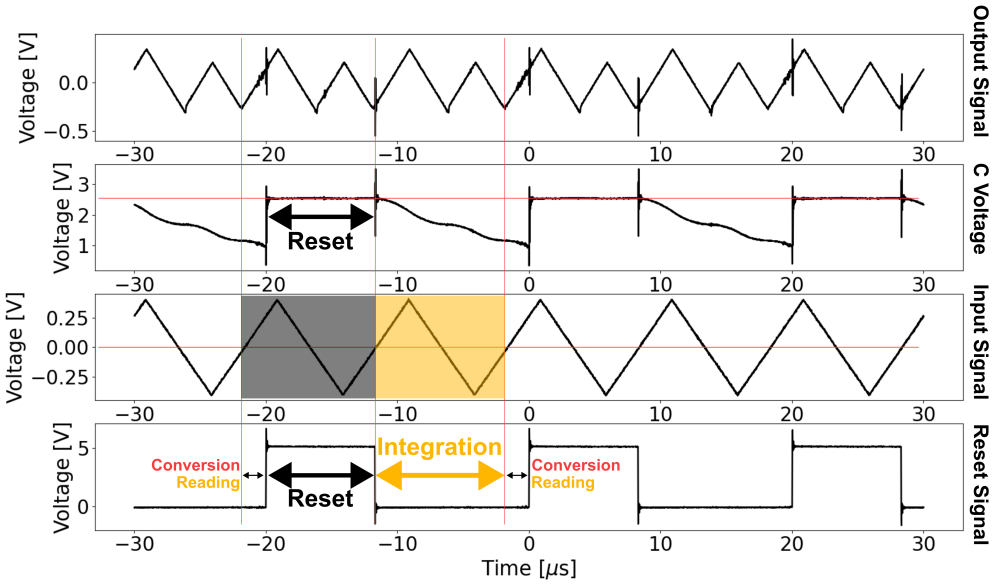

Figure 3.19: Output signals of the proposed high frequency circuit (experimental results). The rectified output signal, capacitor voltage, input and reset signals are shown.

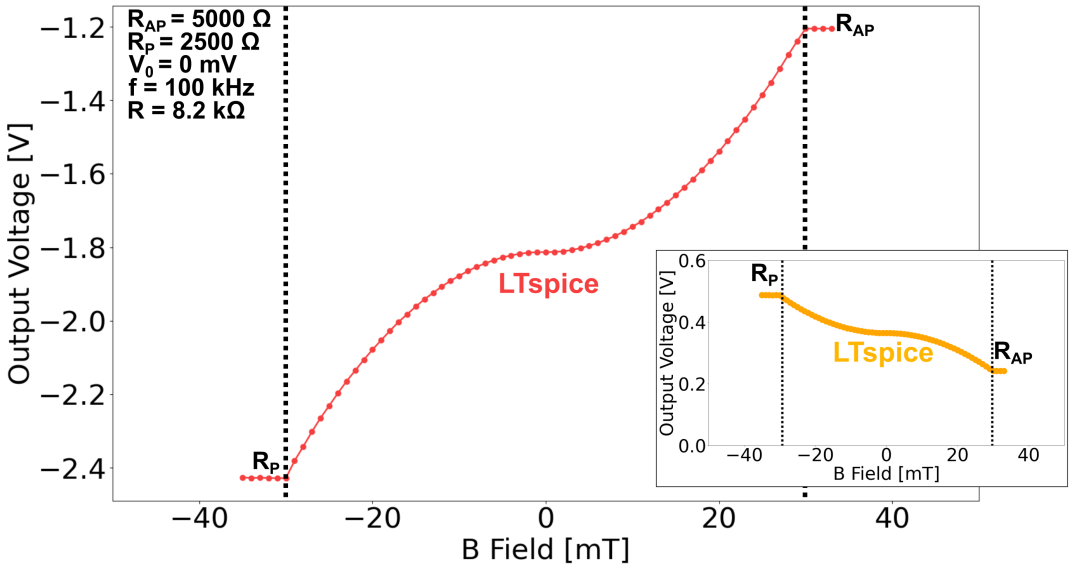

Figure 3.20: Rectifier-based high-frequency theoretical circuit output, simulated using LTspice. The output using the standard rectifier approach is also shown for reference.

3.4.2 Achieved performance

Finally, assessment of the performance of the demonstrated high-frequency circuit was performed and shown in Fig. 3.21, validating the working principle, with proper oscillating outputs, and demonstrating the dynamic metrological capabilities of the sensor.

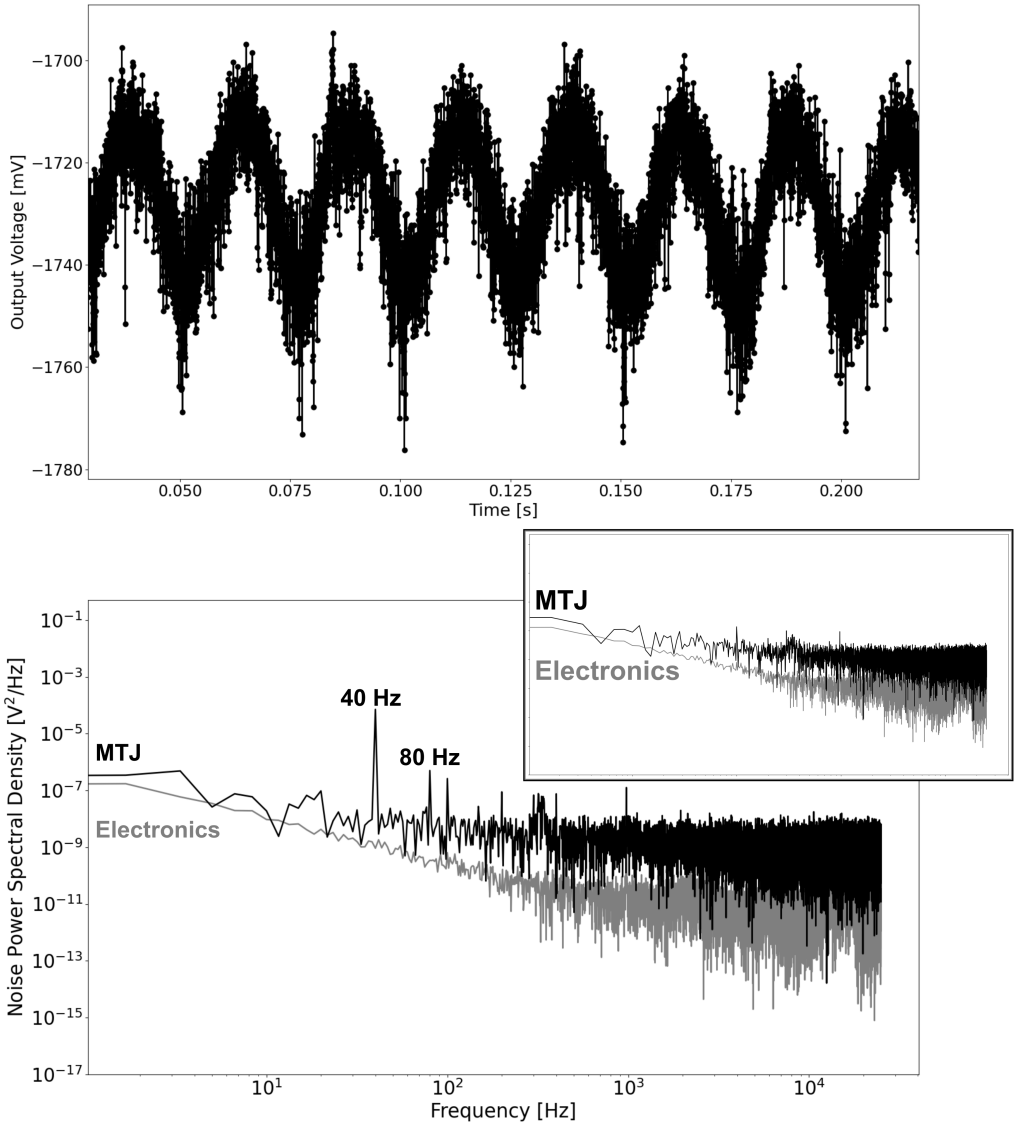

Figure 3.21: NPSD achieved of the proposed high frequency circuit and measurement of an ac sine wave magnetic field of ± 5 mT at 40 Hz of a 100 nm MTJ (experimental results). Both time domain and frequency domains are shown. The close-up look shows the NPSD in the absence of field.

3.5 Conclusion

Chapter 3 presents the use of dedicated low coercivity STT-MTJs as sensing units in a similar way to the high coercivity MTJs presented in Chapter 2. Such modifications of the stack of the MTJs allow for improved sensitivity and better noise performance while keeping most of the advantages of the high coercivity STT-MTJs approaches, including a higher dynamic range or lower power consumption than most existing MR and/or Hall effect technologies. Although the circuits designed for high coercivity MTJs based on HPFs are unusable through such new approaches, because of softer APP/PAP reversals, other simple operational amplifier-based solutions have been successfully proposed and demonstrated through experimental measurements.

Three different circuits have been proposed and validated experimentally. The first based on a simple integrator allows for easy implementation of the proposed STT-MTJ measurement principle. This allows for very compact measurement systems through a unique operational amplifier. The second one, based on an OpAmp-based precision rectifier, allows for the suppression of the symmetrical output issue by adding a few additional components and two diodes. In addition, in both cases, because these MTJs exhibit switching voltages close and crossing 0 V, this creates a reduced sensitivity or even a dead zone, and a complicated situation to solve, as electronics working at very low voltages become highly challenging to design. Hence, if electronics solutions and circuits could eventually be implemented to minimize this effect, the most effective solution would be to shift the entire response of the MTJs in a single polarity, either positive or negative, allowing the switching voltages to remain far from 0 V, at the expense of higher power consumption. However, in-depth studies have not yet been performed on the physical feasibility of such solutions, but in any case, would require significant effort from the design and fabrication of the devices.

Finally, another approach, based on a modified version of these circuits, allows for single-period measurements without adding significant complexity, and maximizes the bandwidth at the expense of a larger rms noise, allowing even larger bandwidth than high coercivity MTJs to be reached, of up to several hundreds of kHz (100 to 1000 kHz), covering more specific applications requiring high-speed measurements.

Further improvements of the stack are also still required to reach null offset fields and increase the sensitivity even further. Dedicated analysis of the stochasticity will allow for a better understanding of the origin and solutions of such phenomena, allowing for lower noise to be achieved through stack optimization and better control of the MTJs.

Bibliography

Chapter 3 has presented the use of dedicated low coercivity STT-MTJs as sensing units in a similar way compared to the high coercivity MTJs presented in Chapter 2. Such modifications of the stack of the MTJs allow for improved sensitivity and better noise performance while keeping most of the advantages of the high coercivity STT-MTJs approaches, including a higher dynamic range or lower power consumption than most existing MR or Hall technologies. Although the circuits designed for high coercivity MTJs based on HPFs are unusable through such new approaches, due to softer APP/PAP reversals, other simple operational amplifier-based solutions have been successfully proposed and demonstrated through experimental measurements.

Finally, **Chapter 4** acts as an overview of final parts of this work, including optimization attempts, sensing elements variability assessment and performance comparison with existing technologies.

Chapter 4

STT-MTJ Magnetic Sensor Performance

4.1 Introduction

While Chapters 2 and 3 have presented the working principles of STT-MTJ magnetic sensors, based on either high coercivity or low coercivity MTJs, Chapter 4 aims to allow for a better understanding of both approaches (high coercivity and low coercivity) in comparison to existing technologies with their strengths and weaknesses, and present various attempts of performance enhancements. This chapter is divided into three different parts.

- The first part of Chapter 4 presents the different attempts performed in order to lower the noise and increase the sensitivity of the sensor, by adjusting the input signal parameters or external parameters (input voltage offset, input voltage amplitude, input voltage frequency or temperature)
- The second part introduces the different performance achieved over different MTJs, illustrating the diversity and similarity of evaluated MTJs. While Chapter 2 and 3 have demonstrated the working principles through different approaches, mainly by focusing on the electronics, this section aims to introduce various types of MTJs, and performance obtained to give an overview of the possible variations in terms of sensing elements
- Finally, the last part of the chapter positions and compares this work within existing experimental and commercial products and outlines the advantages of such sensing technology

4.2 STT-MTJ magnetic sensor optimization

To enhance the performance of the sensor without modifying the electronics or the MTJs, input signal parameters have been evaluated to assess their impact on the performance of the device. This includes the dc offset, ac amplitude and input frequency of the triangular signal. In addition, impact of the temperature, only above room temperature (RT), has been evaluated and will also be presented over this section. To assess the temperature dependency, Setup A was used, which implements the possibility of heating the entire wafer support and control its temperature. The heating of the support is performed with a resistive element, and the wafer is heated through conduction with the holder, while the cooling of the entire system (wafer and support) is passively performed through convection with ambient air.

4.2.1 Input offset impact

Assessment of the effect of the offset of the input triangular signal on the performance of the sensor have been attempted, by performing the measurements of the output characteristics of different MTJs at different magnetic fields and different offset values, ranging from -100 mV

to +100 mV. Results obtained are shown in Fig. 4.1 for different low coercivity MTJs. Measurements were performed in a similar way as described in the previous chapter for low coercivity MTJs, but with a reduced input amplitude to avoid breaking down the junction as the input offset increases, with a typical peak-to-peak amplitude of ± 100 mV. The evaluation of the output characteristics of the sensor was made through the use of the rectifier approach.

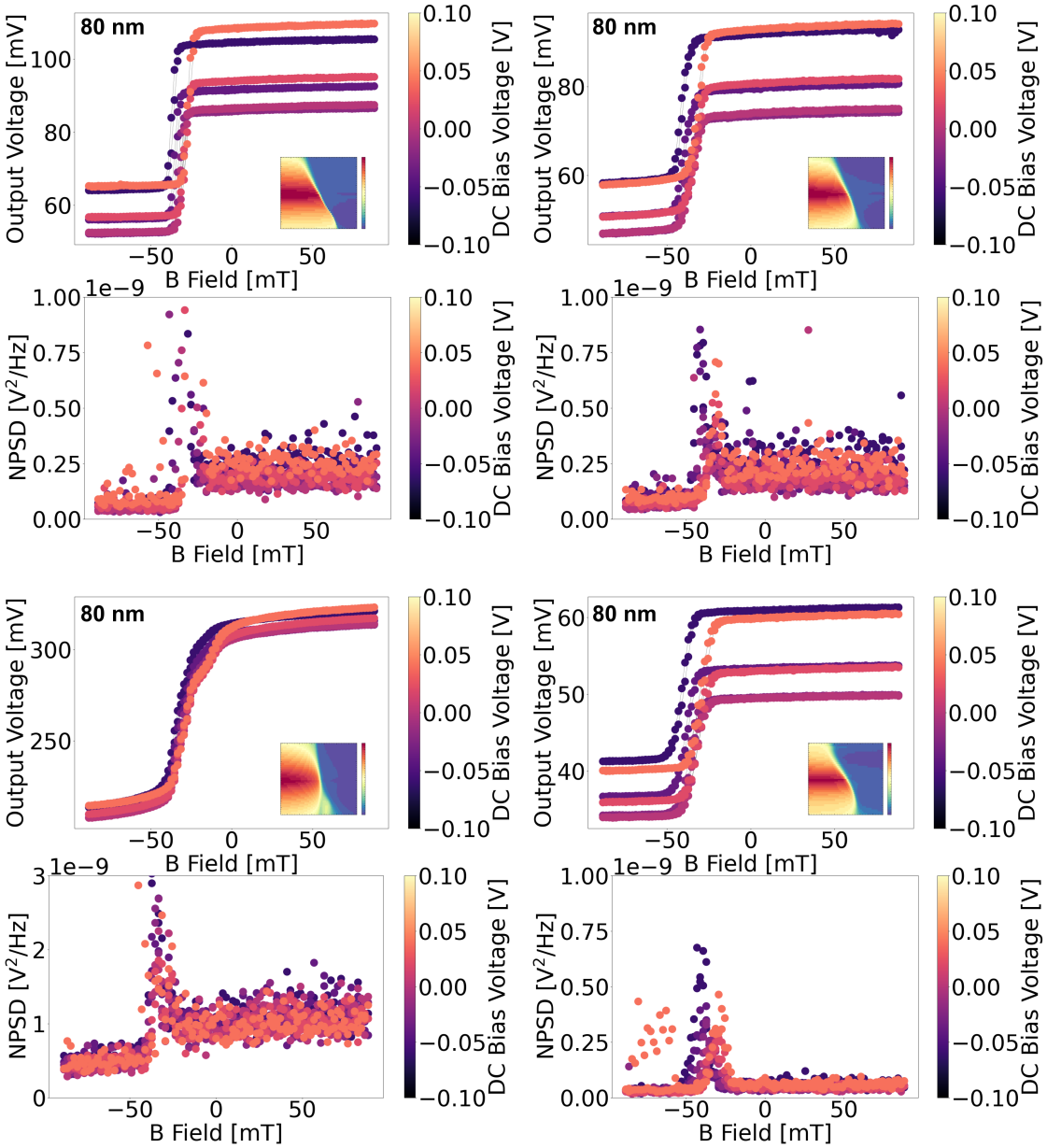

Figure 4.1: Influence of the input signal offset in STT-MTJ magnetic sensors (experimental results). Output characteristics and NPSD are shown for four different low coercivity MTJs.

As seen on the figure, for each MTJ evaluated, the output characteristic at each input offset values exhibit the same monotonic shape, with the same increase of the NPSD around H_0, corresponding to the working area of the sensor (i.e., maximum sensitivity and stochasticity). For each input offset value assessed, one can see that the output characteristic of the sensor presents a modification in its output offset but no visible changes in the sensitivity (identical slope), or changes in the noise (identical NPSD). Hence, based on these measurements, one can conclude that such parameter does not influence the performance of the sensor (both the noise, not lowered, or output characteristic, no modification of the sensitivity), and should therefore remain at 0 V, for circuit simplicity, as generating any dc offset requires the use of an additional voltage source in the circuit.

In addition, despite remaining not quantified so far, it is also interesting to note that, by using a pure dc voltage as a bias, these low coercivity MTJs can also be used as conventional linear sensors, through their RH loop whose offset can be adjusted with their bias through the STT effect, allowing the use of such sensing element in various dynamic range, as depicted in Fig. 3.1, without the need of external compensation circuits as in standard MR sensors.

4.2.2 Input frequency impact

Assessment of the effect of the frequency of the input triangular signal on sensor performance has also been attempted, by performing measurements of the output characteristic of different MTJs at different magnetic fields and different frequencies, ranging from 100 kHz up to 1 MHz. The results obtained are shown in Fig. 4.2 for low coercivity MTJs. Measurements were performed in a way similar to that described in the previous chapters for low coercivity MTJs. The evaluation of the output characteristics of the sensor was made through the use of the rectifier approach.

As seen on the figure for each MTJ evaluated, the output characteristic at each input frequency exhibits the same monotonic shape, with the same increase of the NPSD around H_0, corresponding to the working area of the sensor. For each input frequency assessed, one can see that the output of the sensor presents no visible changes in the sensitivity (identical slope), or changes in the noise (identical NPSD). Despite minor changes in the NPSD that can be observed, these modifications are not significant enough to be investigated. In addition, minor changes, depending on the MTJ evaluated, can be seen in the shape of the output characteristic which are also not significant enough to give any advantages. Hence, based on these measurements, one can conclude that such parameter does not significantly influence the performance of the sensor (both the noise, not lowered, or output characteristic, no modification of the sensitivity). Reversals up to 1 MHz could be observed, allowing possible high-frequency measurements with the proper dedicated electronics as described previously.

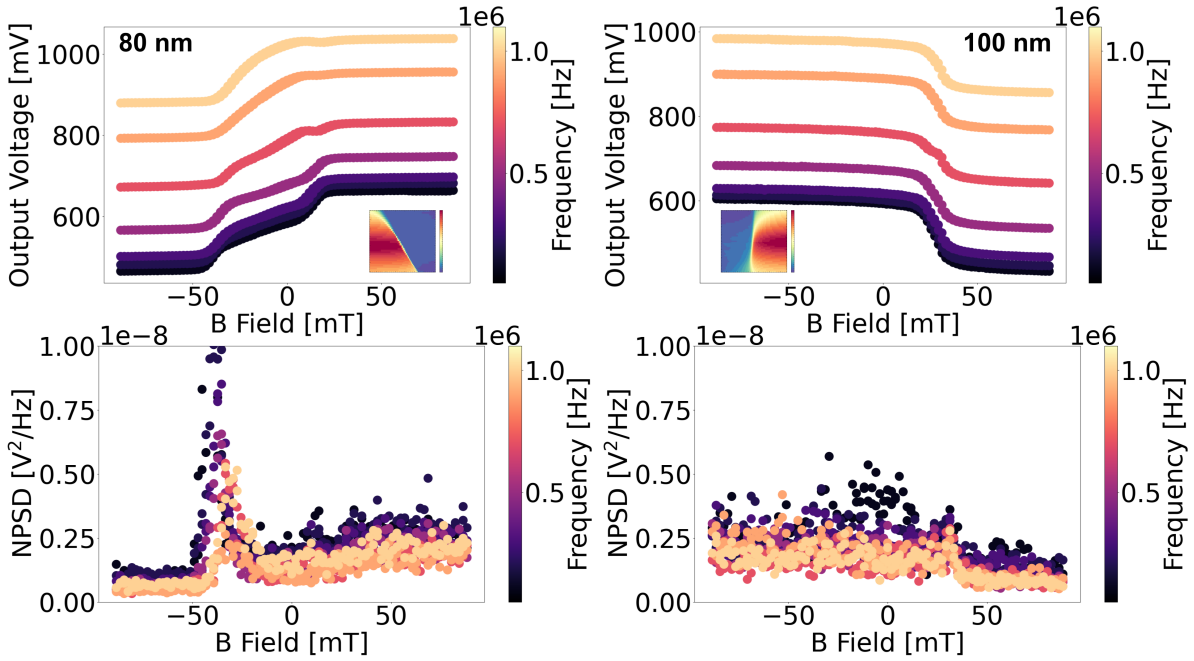

Figure 4.2: Influence of the input signal frequency in STT-MTJ magnetic sensors (experimental results). Output characteristics and NPSD are shown for two different low coercivity MTJs.

However, as the input frequency increases, the total number of events averaged by the LPF increases, leading to a decrease in the overall rms output noise, with a $\sqrt{F}$ relationship. The switching probability (time probability ΔT and voltage probability ΔV) remains unaffected by the input frequency, as a ΔV independent from F should result in constant values, and a ΔT independent from F should result in a 1/F relationship, as observed in Fig. 4.3. In these measurements, the time switching probability ΔT represents the switching probability when observing this probability from a time point-of-view. Since the switching of the MTJ is induced by the voltage, linearly sweep, such time switching probability is expected to follow a 1/F relationship.

On the other hand, the switching voltages also rise with the increase of the frequency, hence, as the input frequency increases, the dynamic is progressively reduced. For these reasons (trade-off between the rms noise and the dynamic range), input frequencies in the order of typically 100 kHz to 1000 kHz appear to be the best frequency ranges for low coercivity MTJs. For high coercivity MTJs, since the writing voltages are higher, lower frequencies are required, leading to a maximum frequency of typically 200 to 300 kHz.

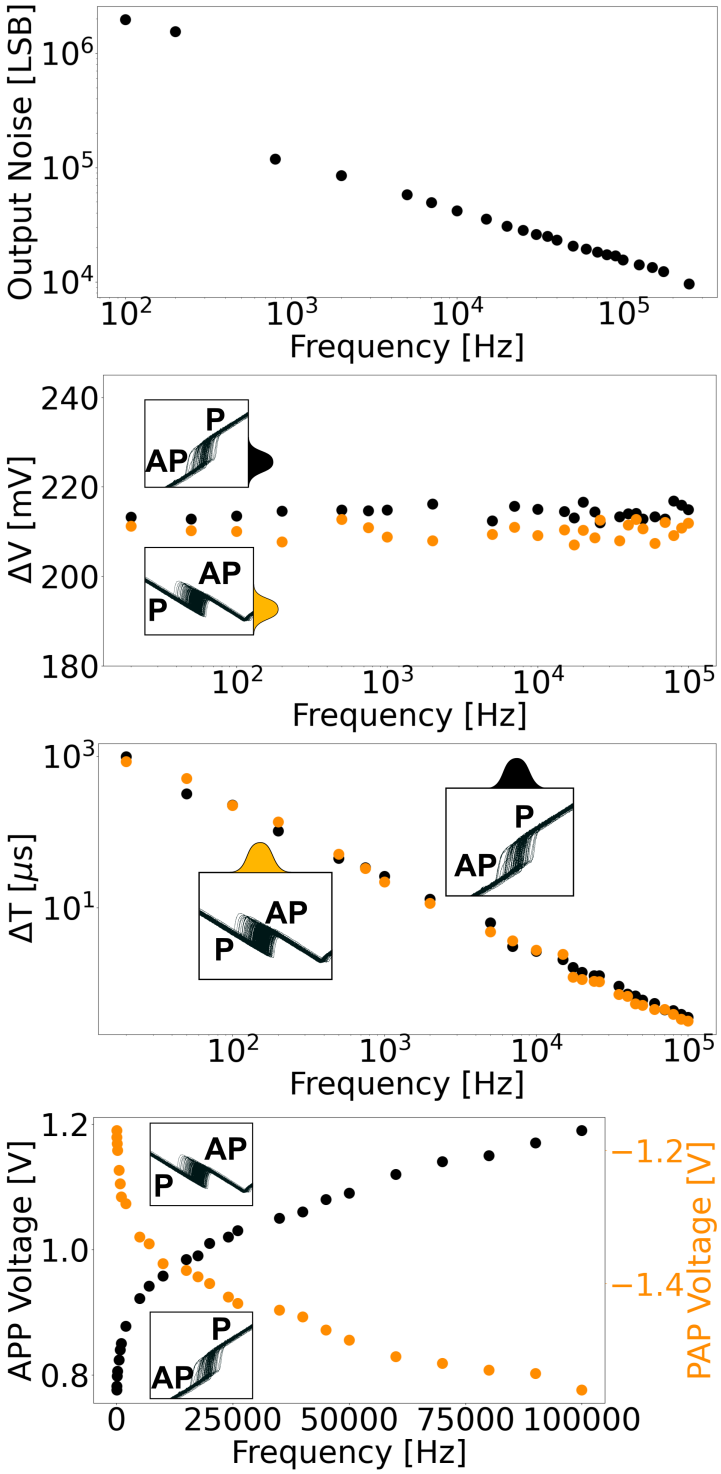

Figure 4.3: Influence of the input signal frequency in STT-MTJ magnetic sensors in the case of high coercivity MTJs (PWM method) on the voltages and noise performance (experimental results). The evolution of the APP and PAP switching voltages, rms noise, ΔV and ΔT with the input frequency is shown.

4.2.3 Input amplitude impact

Assessment of the effect of the amplitude of the input triangular signal on the performance of the sensor has also been attempted, by performing measurements of the output characteristics of different MTJs at different magnetic fields and different amplitudes, ranging from a peak value of 50 to 400 mV (low coercivity MTJs) and 700 to 1300 mV (high coercivity MTJs). The results obtained are shown in Fig. 4.4 for both types of MTJs. Measurements were performed in a way similar to that described in the previous chapters for low coercivity and high coercivity MTJs. The evaluation of the sensor output characteristics was performed through the use of the rectifier approach for low coercivity MTJs and the TDC approach for high coercivity MTJs.

As seen in the figure for each MTJ evaluated, the output characteristic at each input amplitude exhibits the same monotonic shape, with the same increase in the NPSD around H_0, corresponding to the working area of the sensor. For each increased input amplitude assessed, one can see that the output of the sensor presents an increasing dynamic range, with an increase in the NPSD as the MTJ starts to enter larger and larger switching regions. However, no visible changes in the sensitivity (identical slope) or changes in the noise (identical NPSD) can be observed. Hence, based on these measurements, one can conclude that such parameter does not influence the performance of the sensor (both the noise, not lowered, or output characteristic, no modification of the sensitivity) and should therefore remain as high as possible (without breaking down the MTJ), allowing for the largest possible dynamic range to be achieved. For low coercivity MTJs, this corresponds to a peak amplitude of approximately 350 to 400 mV. In the case of high coercivity MTJs, as the writing voltages are higher, this corresponds to a peak amplitude of approximately 1 to 1.2 V.

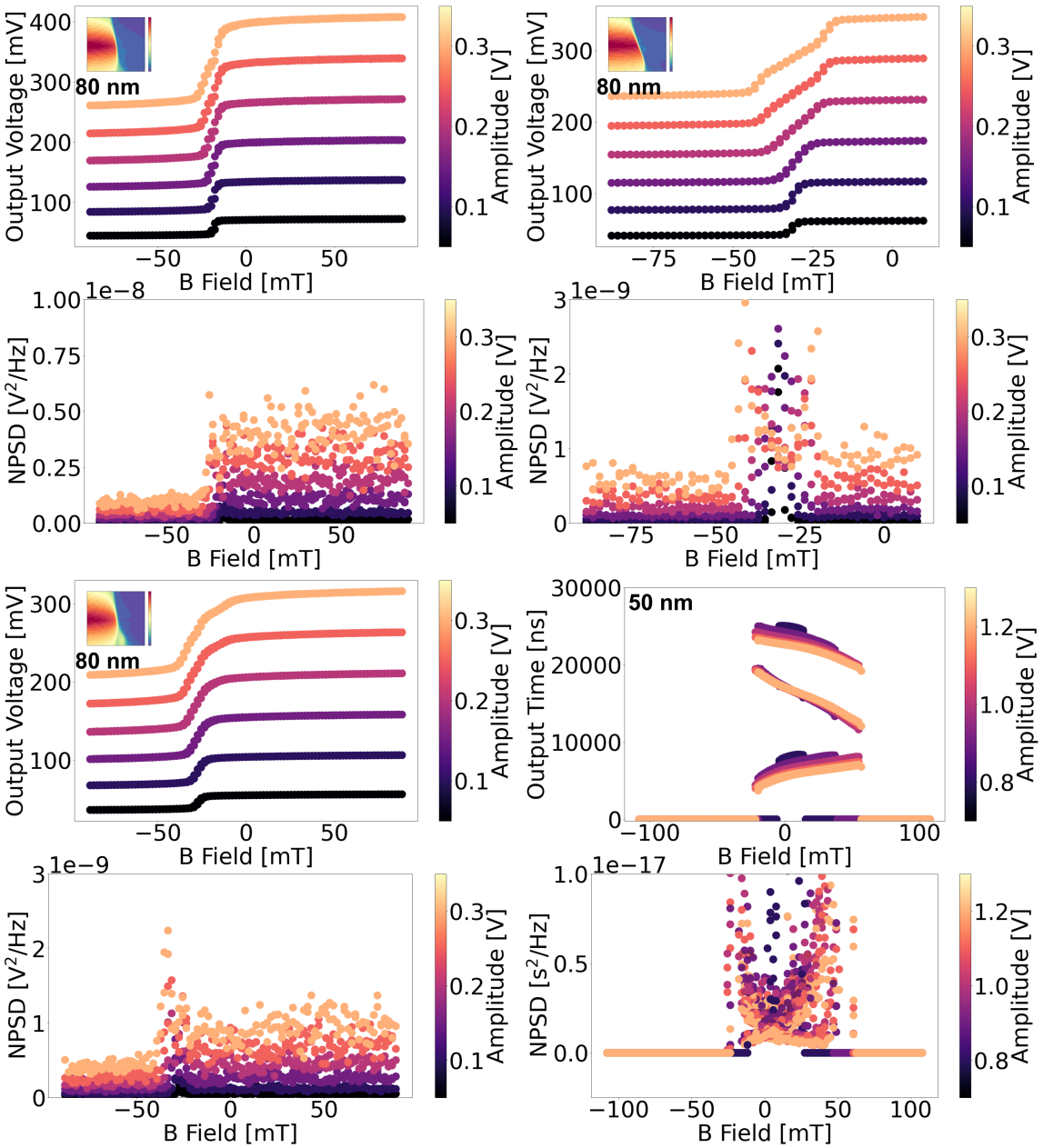

Figure 4.4: Influence of the input signal amplitude in STT-MTJ magnetic sensors (experimental results). Output characteristics and NPSD are shown for three different low coercivity MTJs and one high coercivity MTJ.

4.2.4 Temperature impact

Finally, assessment of the effect of the temperature on the performance of the sensor have been attempted, by performing the measurements of the output characteristics at different magnetic fields and different temperatures, ranging from room temperature up to 80 °C (typical upper value for standard industrial-grade commercial ICs, lower limit being -40 °C). Results obtained are shown in Fig. 4.5 for both high coercivity and low coercivity MTJs. Measurements were performed in a way similar to that described in the previous chapters for low coercivity and high coercivity MTJs. The evaluation of the output characteristics of the sensor was made through the use of the rectifier approach for low coercivity MTJs and through the TDC approach for high coercivity MTJs.

As seen on the figure for each MTJ evaluated, the output characteristic at each temperature exhibits the same monotonic shape, with the same increase of the NPSD around H_0, corresponding to the working area of the sensor. For each temperature assessed, one can see that the output of the sensor presents no visible changes in the sensitivity (identical slope), or changes in the noise (identical NPSD). Despite minor changes in the NPSD that can be observed, these modifications are not practically significant. In addition, minor changes, depending on the MTJ evaluated can be seen in the shape of the output characteristic which are also not significant enough to give any advantages or induce any issues. Hence, based on these measurements, one can conclude that such parameter does not significantly influence the performance of the sensor (both the noise, not lowered, or output characteristic, no modification of the sensitivity). This allows the presented STT-MTJ magnetic sensor to operate up to 80 °C, as required for typical commercial devices, without significant degradation of the performance. Assessment of temperature below room temperature remains however necessary to fully validate the industrial-grade temperature range, and in-depth comparisons with existing commercial technologies in terms of temperature dependency are required to quantify such impact on the characteristic shape changes.

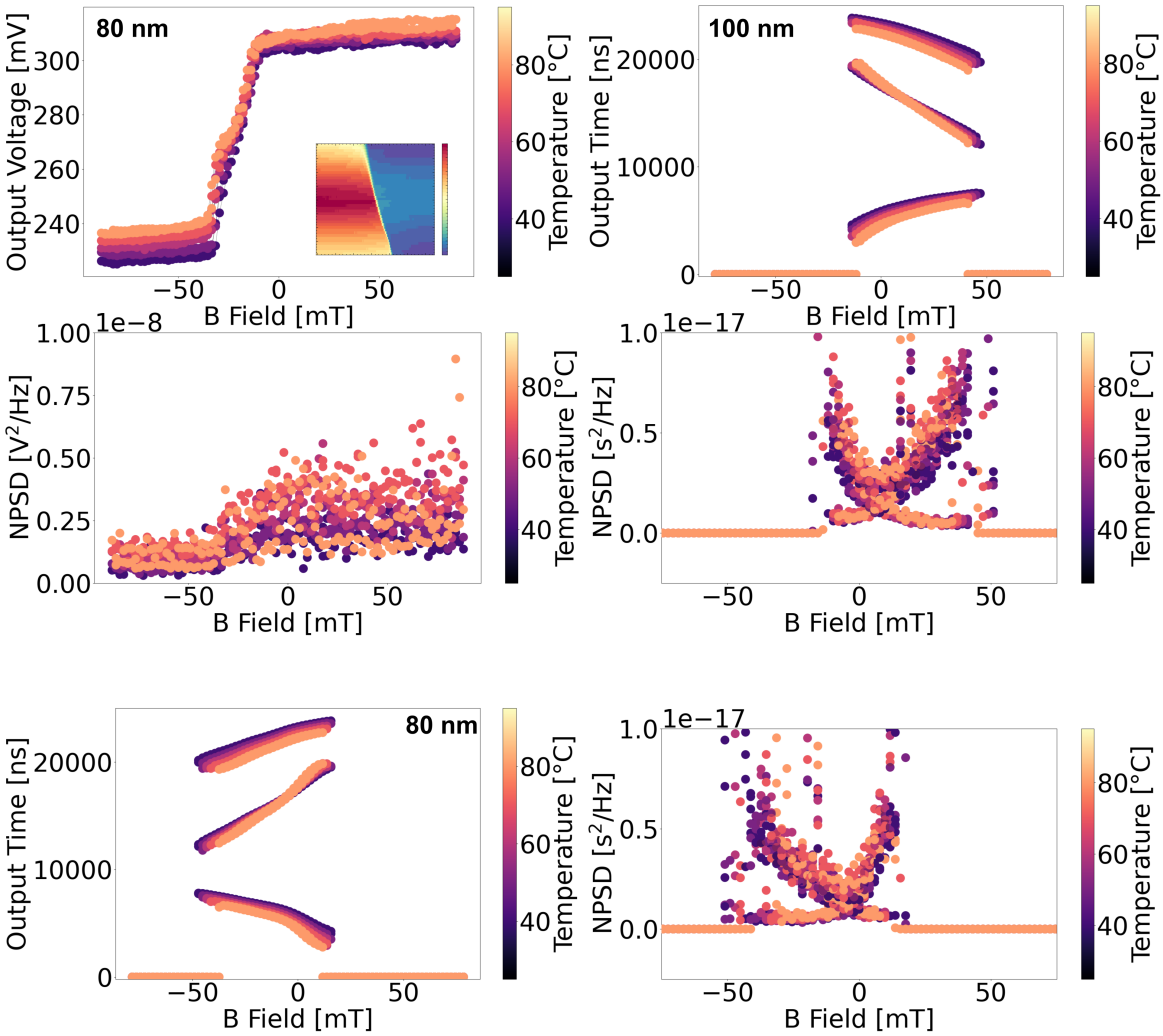

Figure 4.5: Influence of the temperature in STT-MTJ magnetic sensors (experimental results). Output characteristics and NPSD are shown for two different high coercivity MTJs and one low coercivity MTJ.

4.3 STT-MTJ magnetic sensor performance

4.3.1 In-plane field influence

Magnetic sensors are usually characterized by an important parameter representing the immunity of the device to fields orthogonal to their sensing axis, sometimes referred to as the cross-sensitivity or transverse sensitivity. In the case of perpendicular STT-MTJs, as the MTJs are sensitive to the out-of-plane field, this implies evaluating the effect of the in-plane field (i.e., parallel to the plane of the wafer) on the sensor performance.

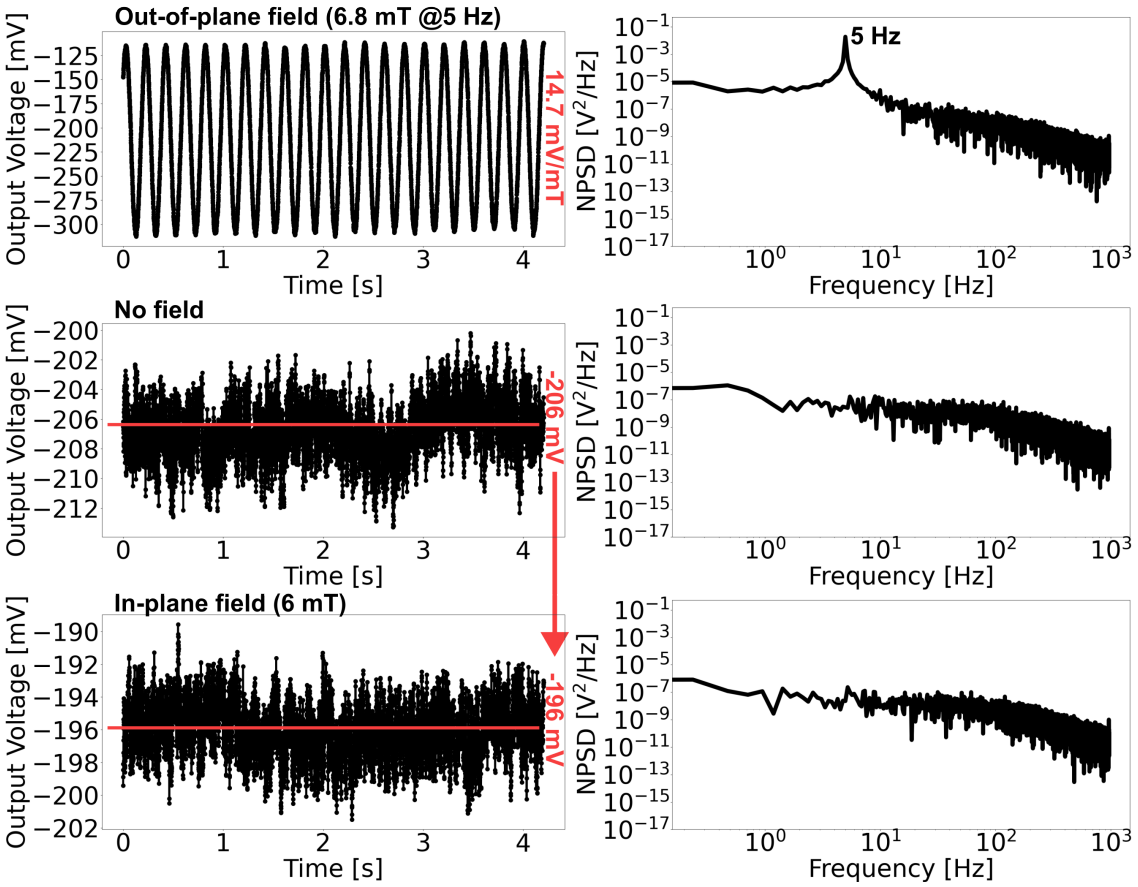

Figure 4.6: Influence of the in-plane and out-of-plane field in high coercivity STT-MTJs (PWM approach) magnetic sensors (experimental results). Measurements of a sine wave at 6.8 mT ± 5 Hz along the perpendicular direction, measurement of the output value of the sensor in the absence of field, and in the presence of an dc in-plane field are shown for a 80 nm MTJ.

To assess this, Setup B (Fig. 2.7) was modified by adding coils allowing an in-plane field to be generated through a horizontal Helmholtz coil, capable of generating approximately ± 5 to 10 mT dc fields at 10 A and calibrated using Hall effect sensors to ensure the presence of no to minimal perpendicular fields. High coercivity MTJs were then evaluated through the PWM method for the impact of the in-plane field on their output voltages under three conditions: perpendicular ac field for reference, no field, and in-plane dc field.

This effect has been analysed in various studies such as [21] and [20], predicting that the influence of the in-plane field is not expected to be zero. Hence, according to [20], where simulations of the phase diagrams of pMTJs have been made under different field angle conditions, the impact of the in-plane field is going to be depended on the ratio between the perpendicular anisotropy of the device and the applied in-plane field, leading to a tilt of the magnetization from its perpendicular easy axis and resulting in modifications in the phase diagram (e.g., sensitivity). Accordingly, experimental measurements (Fig. 4.6) did confirm a non-zero influence, with measured values of ± 10 %.

With these measured values, one could also compare such performance with existing technologies. Hall effect sensors are typically exhibiting values in the range of less than 1 %, while MR sensors can be in the range of 2 to 5 %, such as in the MMC5603NJ (Memsic Semiconductor, China), and as low as ± 0.5 % FS for the AMR2302 (MultiDimension Technology, China) or HMC1041Z (Honeywell International, USA). Hence, such sensing technology based on STT-MTJs exhibits a larger transverse sensitivity than some of the existing technologies, that needs to be further investigated.

4.3.2 Sensing elements variations

Over this entire project, various MTJs have been tested, providing various output characteristics. Hence, this section aims to present the different types of measurement obtained, allowing the reader to have an idea of the variability of possible sensing element responses (Fig. 4.7). As it can be observed, in the case of high coercivity MTJs, two main types of curves were obtained, either fully linear over the entire dynamic range or presenting a drop in their sensitivity at some point that can be linked to the phase diagrams (induced by the effect of strong fields on the PL which results in this drop in the sensitivity). On the other hand, low coercivity MTJs exhibit slightly different output characteristic shapes, especially in the lower sensitivity/dead zone, around their offset field, with some MTJs exhibiting a distinctive dead-zone, and others presenting a purely linear curve. In all cases, these variations are the results of fabrication variability and wedged layers thickness (over the same wafer), as well as differences in the stacks between different wafers, in the case of low coercivity MTJs with wafer 1 and 2.

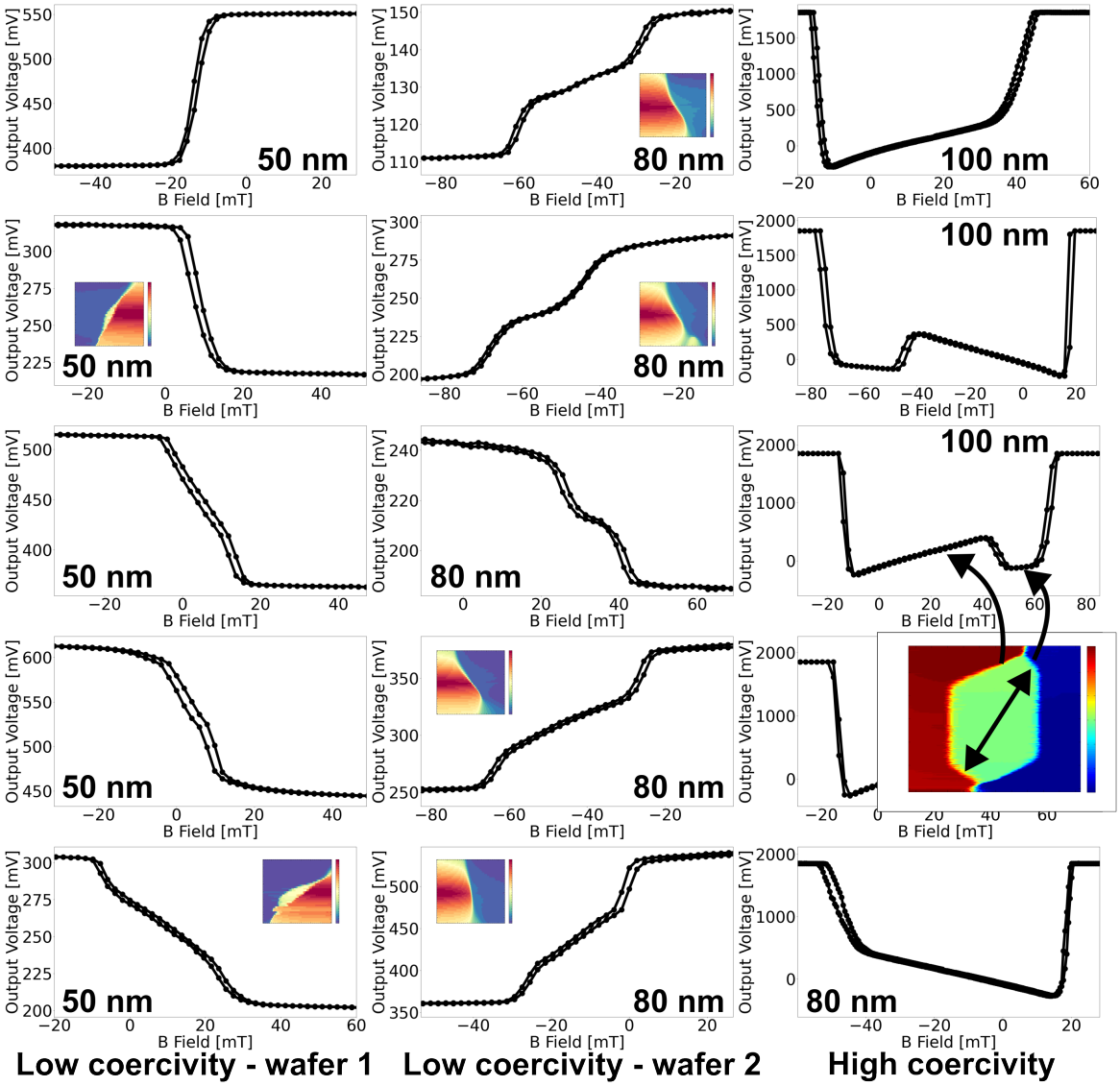

Figure 4.7: Output characteristics obtained for various low coercivity (rectifier approach) and high coercivity (PWM approach) STT-MTJs (experimental results).

4.3.3 Layer thickness impact

In addition, to further evaluate variability and the impact of the thickness of Mg layer and FeCoB FL on the sensor performance (sensitivity and rms noise), measurements of 39 MTJs within the area where thickness of these layers is considered optimal (Mg: 0.53 to 0.72 nm, FeCoB FL: 1.05 to 1.24 nm) have been performed and shown in Fig. 4.8. Due to the increase of critical voltages for thicker MgO barrier, MTJs with Mg thickness above 0.72 nm were unable

to show reliable switching without breaking down and were excluded from the measurements. Hence, one can also observe the variations within a small area on the wafer for high coercivity MTJs, showing good homogeneity in terms of noise or sensitivity among various measured high coercivity junctions.

Within the area, the measured average sensitivity is 23.5 mV/mT and the average rms noise is 0.227 mV. The analysis of experimental data indicates that both the sensitivity and rms noise remain homogeneously distributed within the area, with weak to non-existing correlation to the thickness of Mg and FeCoB layers. Measured minimum (min) and maximum (max) variations of sensitivity range from 15.9 to 32.5 mV/mT and 0.178 to 0.343 mT for the rms noise. This corresponds to variation around the average (nominal) values (min, max) of less than ± 35 %. Standard deviation σ of the sensitivity is 4.30 mV/mT (± 18 %) and rms noise is 0.047 mT (± 20 %). The size of MTJs does not show a significant impact on the measured parameters. Because these variations are also present on different MTJs at almost identical thicknesses (i.e., very close on the wafer, separated by 200 μm such as J_A and J_B as example in Fig. 4.8), it can be concluded that these variations are not directly or not only related to the nominal thickness of these layers but rather due to standard fabrication variability. One can also conclude that MTJs presenting higher sensitivity tend to also exhibit lower rms magnetic noise. This is the result of higher-sensitivity MTJs exhibiting constant voltage rms noise and therefore lower rms magnetic noise.

These observed variations are similar or only one to five times larger than typical variations of parameters of commercially available magnetic sensors, such as the sensitivity of the Hall effect sensor MV2 (Metrolab Technology SA, Switzerland), within ± 4.5 % of the nominal value (min, max) or ± 7 % for the LIS2MDL (STMicroelectronics, Switzerland), based on proprietary technology. AMR (anisotropic MR) sensors such as the MMC5603NJ (Memsic Semiconductor, China) exhibit sensitivity within ± 5 % of the nominal value (min, max). These technologies are highly or natively compatible with CMOS technology, and as a result, present the lowest variability in sensor parameters. These variations are used as reference values and targeted for the presented STT-MTJ sensor. For TMR sensors, variations due to fabrication processes dispersion can be higher because of the very thin films involved and the need for high control over the interface FeCoB and MgO. The CT100 TMR sensor (Allegro MicroSystems, USA) shows a sensitivity reported to have variations of ± 15 % around the nominal value (min, max), or for the TMR2901 (MultiDimension Technology, China) with a sensitivity within +8 to -20 % of the nominal value (min, max), as well as for the TMR2922 (MultiDimension Technology, China) with a sensitivity within ± 44 % of the nominal value (min, max). It is important to note that the fabrication processes involved in this work are experimental such that potential optimization of the fabrication processes involved for the industrialization of STT-MTJ sensors, as well as wafers fabricated without wedges (i.e., uniform layer thicknesses) are more likely to reduce these variations.

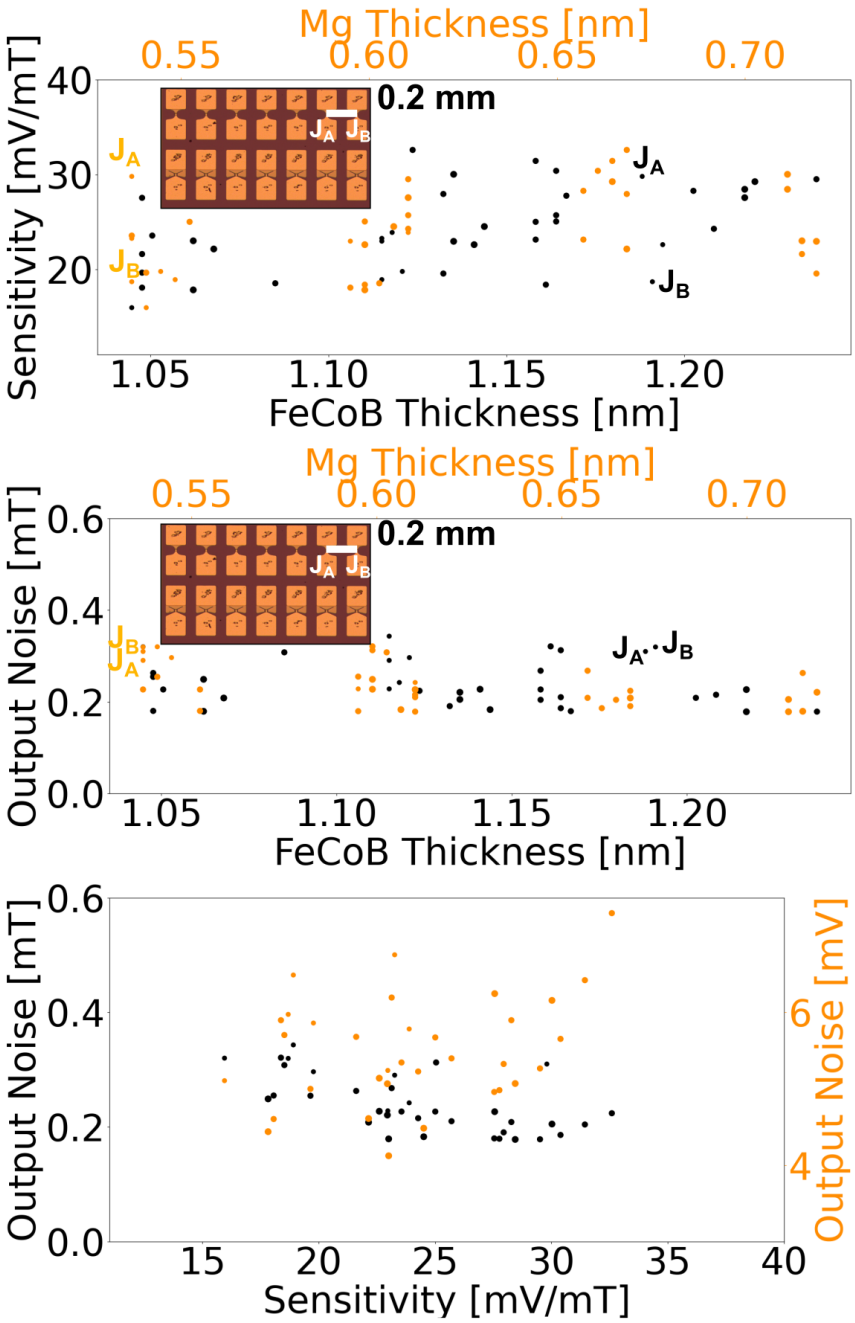

Figure 4.8: Output characteristics between various high coercivity MTJs (PWM method) (experimental results). Correlation between the sensitivity of MTJs with FeCoB free layer and Mg layer thickness are shown. The size of the dots represents different diameters of MTJs. The inset shows an optical microscope (OM) image of tested devices on the wafer, with J_A and J_B indicated as an example of MTJs considered to have identical Mg thickness and almost identical FeCoB FL thickness. Correlation between the rms noise of MTJs with FeCoB free layer and Mg layer thickness and correlation between the sensitivity with the magnetic and voltage rms noise of MTJs are also shown.

4.4 STT-MTJ magnetic sensors and existing technologies

While many technologies of magnetic sensors exist, only few of them are available as integrated circuits, as depicted in the first chapter, and represents the typical competitive technologies targeted by the presented new measurement principle. This includes almost exclusively Hall effect, TMR and AMR sensors, with the exception of a few GMR, MEMS or proprietary technologies. Hence, to assess how the sensing elements presented in this work perform compared to existing sensors, this section aims to review existing devices and compare their performance with results achieved throughout this work. However, among commercial products, sensing elements are often industrial secrets and only few references with available dimensions can be analysed. In addition, few experimental works exist targeting the development of nanoscale magnetic sensors, with less than 10 research approaches found. This is due to several factors, including technological challenges, applications limitations, cost or physics limitations (e.g., noise vs dimensions relationship in some MR technologies).

Among other nanoscale, non-integrated magnetic sensors, one can also cite NV-centre (nitrogen-vacancy) sensors, which can be as small as tens of nm with a NPSD as low as few $\mu T/\sqrt{Hz}$, despite requiring much more complex electronics as well as optical components for the polarization of the sensing element [3], [7]. SQUID sensors can also be based on nanoscale sensing elements (Josephson junction) but also require much more complex electronics, making the overall size of the sensor much bigger than the targets of this work. Finally, one can also cite inductive sensors, such as search coils which can operate in the mHz up to the MHz frequency range, with a resolution as low as few $pT/\sqrt{Hz}$, with simple electronics, large dynamic range and at room temperature. However, since these sensors are based on coils, they suffer from the same drawbacks as fluxgate sensors, including technological challenges making their integration challenging or relatively large [19]. Hence, these sensors typically also present much larger dimensions than the targets of this work and are not included in the following parts of the section.

The different relevant sensors and works found are compared with the proposed STT-MTJ magnetic sensors in Fig. 4.9. As it can be observed, the dimensions of the MTJs used in this work are among the smallest sensitive elements ever reported, with noise performance comparable with nanoscale TMR experimental devices. In addition, since the presented sensing principle is similar to the fluxgate technique, one can also compare the performance achieved with existing fluxgate sensors, as shown in Fig. 4.10, where NPSD, current and sensing volume are compared, in addition to a comparison factor known as the figure of merit (FoM) and calculated as $(N.I.V^{1/3})^{-1}$, with N the NPSD, V the volume of the sensing element and I the polarization current. This demonstrates that the presented technology based on STT-MTJs is showing good performance in comparison to existing technologies when the size is taken into account, following the same linear trend, which, in the case of standard fluxgate, is most likely related to the Barkhausen noise, representing the noise limits.

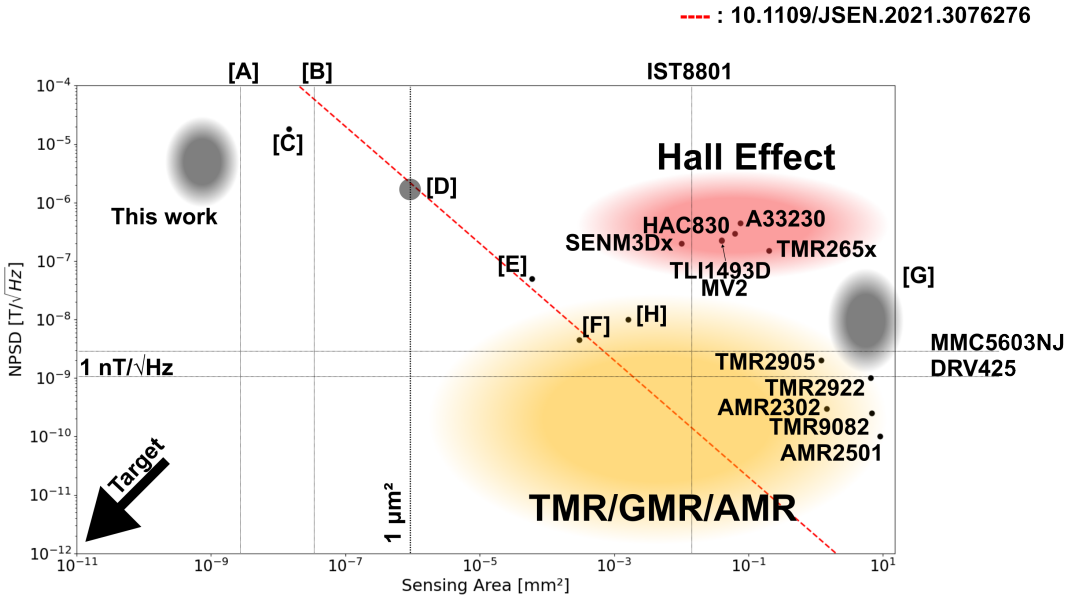

Figure 4.9: Comparison of existing magnetic devices with the presented STT-MTJ sensors (A: [22], B: [1], C: [14], D: [16], E: [2], F: [8], G: [6], H: [5]). The red line [17] represents the noise of a TMR sensor as a function of the sensing area of the MTJ.

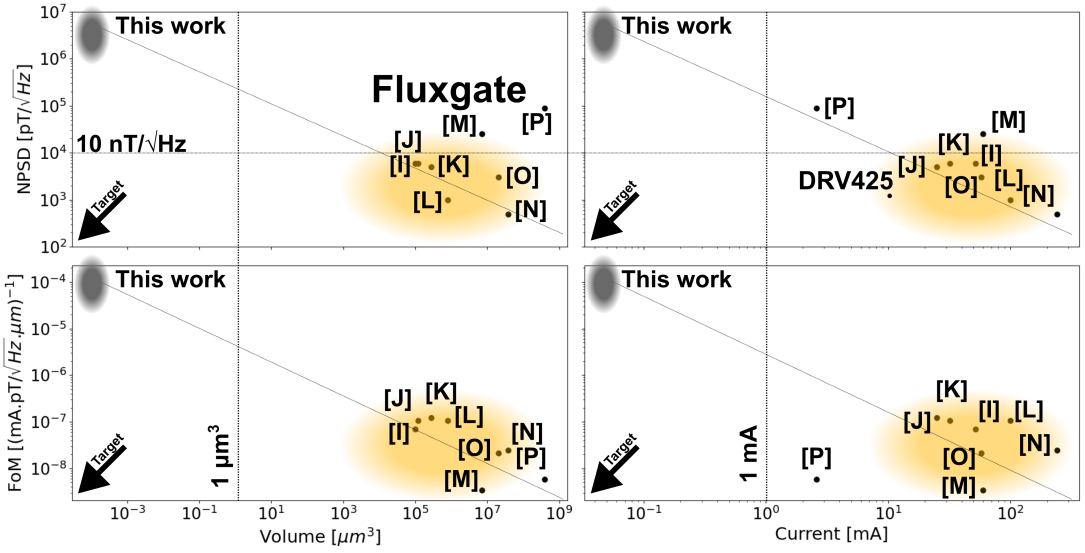

Figure 4.10: Comparison of existing fluxgate devices with the presented STT-MTJ sensors (I: [18], J: [12], K: [9], L: [11], M: [15], N: [13], O: [10], P: [4]). Noise (NPSD), sensing volume, current and comparison factor, figure of merit (FoM), are detailed.

However, the dimensions of the sensors and the noise power spectral density (NPSD) are not the only parameters that are important in magnetic sensors. Hence, among other parameters, one can also look at the following ones. This also includes CMOS compatibility, as MTJs for MRAM cells are or will become natively compatible with mass production processes with the development of the technology.

- **Dynamic range:** Hall effect sensors offer dynamic range as high as several Tesla. However, to offer the best SNR performance, the dynamic range can also be reduced, allowing for higher sensitivity and SNR to be achieved. Hence, low noise Hall effect sensors often present dynamic of up to ± 10 to 100 mT with NPSD of 200 to 500 nT/$\sqrt{Hz}$. On the other hand, MR sensors are typically much more restrained in their dynamic, with typically few mT for higher SNR. In comparison, the presented STT-MTJ sensor offer dynamic which can be as high as 100 mT, despite presenting a stronger noise, representing an interesting advantage for strong field applications.

- **Linearity:** Hall effect sensors are among the most linear sensors available, with frequent non-linearity error as low as ± 0.1 % FS. However, MR sensors are much less linear, and existing sensors are typically presenting linearity error of less than ± 2 % FS. In the case of the presented sensing methods through the high coercivity approach, non-linearity error achieved is already similar to such value (± 1 to 2 % FS), and, depending on the region chosen for the low coercivity approaches, in the same order of magnitude, making the presented sensing principle also competitive in this domain.

- **Power consumption:** integrated Hall effect and MR sensors typically consumes few mA of current at a voltage of 1.8 to 5 V (typically 1.8, 2.5, 3.3 or 5 V), powering either the entire analog and digital circuits (e.g., ADC or digital communication with a MCU) or only the sensing element (in the case of analog output devices). However, such current consumption values can be much higher, for instance in the case of higher polarization or spinning current architecture in Hall effect sensors (10 to 25 mA), or in the case of set-reset operation in AMR sensors (up to few A for short duration). In addition, since these sensors are based on variations in resistance of a physical device, higher resistances also come with stronger thermal noise ($\propto 4k_BT^{\circ}R$) and are therefore often avoided, leading to stronger current consumption.

  The presented STT-MTJ magnetic sensor is currently based on discrete components, hence, the power consumption is difficult to fairly compare. However, the entire PCBs used over this work typically consumes 10 to 20 mA, with up to 90 to 95 % being used by the ADC only. The MTJ (sensitive element) itself typically consume less than 200 to 100 μA at a voltage of 0.3 to 1 V (resulting in a power dissipation as low as 10 μW), depending on the type (high coercivity or low coercivity) and diameter of the MTJ, making the presented method very low power in comparison to existing technologies.

- **Sensing axis:** Hall effect sensors are nowadays available with three sensing axis (X, Y or Z) possibilities. However, AMR, GMR and TMR sensors are very frequently available as only sensitive to the plane of the wafer (X or Y), due to technical challenges and difficulties described above for Z-axis sensing, especially for TMR and GMR. Among more than 1200 references of magnetic sensors available on Digikey[1], only 244 are 3-axis magnetic sensors, and 204 are based on Hall effect. From the remaining, very few are GMR sensors, and only one or two are made from TMR elements, while the rest is mainly being based on AMR elements, in addition of few MEMS or custom technologies. Hence, most of these MR technologies remain only available as X- or Y-sensing capabilities. On the other hand, the presented STT-MTJ sensor is sensitive to the perpendicular plane of the wafer (Z), making it complementary to existing MR technologies.

- **Maximum field:** while Hall effect sensors can be virtually exposed to unlimited magnetic field without any damage, AMR sensors require a set-reset functionality to be exposed to stronger fields, and the absence of such architecture greatly reduces the maximum possible field exposure without affecting the performance of the device. TMR and GMR sensors are often based on a PL (through a different mechanism as explained previously), and the maximum field exposure can be significantly high depending on the H_c of the PL or the design of the SAF. Hence, the presented STT-MTJ falls into this last category, allowing it to withstand strong field exposure without any issue, of up to hundreds of mT ($>$ 200 to 500 mT) in the case of high coercivity MTJs.

- **Bandwidth:** Finally, such presented measurement principle based on the reversals of resistive states allows for high-frequency measurements to be performed, since MTJs for MRAMs cells are intrinsically low capacitance (nF to pF) and high-speed compatible with nanoseconds reversals. Hence, using such proprieties associated with the proper electronics, bandwidth up to hundreds of kHz (100 to 1000 kHz) have been achieved. Existing technologies usually exhibit some limitations, such as induced by the RC constant of the sensing elements. In the case of Hall effect sensors, the use of the spinning current approach, used to enhance the performance of the sensor as described in Chapter 1, is also among limitations in the maximum frequency achievable due to technical difficulties of the electronics (cost, size etc.). This makes the presented technologies also very interesting for high-speed measurements at low noise, often poorly addressed by standard existing technologies, as the use of multiple (for synchronous averaging), high-speed nanoscale sensing elements allows both of the issues to be addressed at the same time.

[1]Data extracted in August 2024 on Digikey.com.

Bibliography

[1] C. Albon, A. Weddemann, A. Auge, K. Rott, and A. Hütten. Tunneling magnetoresistance sensors for high resolutive particle detection. *Applied Physics Letters*, 95(2):023101, July 2009. doi:10.1063/1.3179241.

[2] José Amaral, João Gaspar, Vitor Pinto, Tiago Costa, Nuno Sousa, Susana Cardoso, and Paulo Freitas. Measuring brain activity with magnetoresistive sensors integrated in micromachined probe needles. *Applied Physics A*, 111(2):407–412, May 2013. doi:10.1007/s00339-013-7621-7.

[3] John F Barry, Jennifer M Schloss, Erik Bauch, Matthew J Turner, Connor A Hart, Linh M Pham, and Ronald L Walsworth. Sensitivity optimization for NV-diamond magnetometry. *Rev. Mod. Phys.*, 92(1), March 2020.

[4] Won-Youl Choi, Jun-Sik Hwang, and Sang-On Choi. The microfluxgate magnetic sensor having closed magnetic path. *IEEE Sensors Journal*, 4(6):768–771, December 2004. doi:10.1109/JSEN.2004.836851.

[5] Chloé Chopin, Jacob Torrejon, Aurélie Solignac, Claude Fermon, Patrick Jendritza, Pascal Fries, and Myriam Pannetier-Lecoeur. Magnetoresistive Sensor in Two-Dimension on a 25 um Thick Silicon Substrate for In Vivo Neuronal Measurements. *ACS Sensors*, 5(11):3493–3500, November 2020. Publisher: American Chemical Society. doi:10.1021/acssensors.0c01578.

[6] J. E. Davies, J. D. Watts, J. Novotny, D. Huang, and P. G. Eames. Magnetoresistive sensor detectivity: A comparative analysis. *Applied Physics Letters*, 118(6):062401, February 2021. doi:10.1063/5.0038187.

[7] Marcus W Doherty, Neil B Manson, Paul Delaney, Fedor Jelezko, Jörg Wrachtrup, and Lloyd C L Hollenberg. The nitrogen-vacancy colour centre in diamond. *Phys. Rep.*, 528(1):1–45, July 2013.

[8] L. Huang, Z. H. Yuan, B. S. Tao, C. H. Wan, P. Guo, Q. T. Zhang, L. Yin, J. F. Feng, T. Nakano, H. Naganuma, H. F. Liu, Y. Yan, and X. F. Han. Noise suppression and sensitivity manipulation of magnetic tunnel junction sensors with soft magnetic Co70.5Fe4.5Si15B10 layer. *Journal of Applied Physics*, 122(11):113903, September 2017. doi:10.1063/1.4990478.

[9] T. Jager, M. Audoin, M. Beranger, R. Cuchet, E. Delevoye, B. Guihlamat, and R. Hida. Microfluxgate Sensors for High Frequency and Low Power Applications. In *TRANSDUCERS 2007 - 2007 International Solid-State Sensors, Actuators and Microsystems Conference*, pages 2585–2588, June 2007. ISSN: 2164-1641. doi:10.1109/SENSOR.2007.4300700.

[10] Jen-Tzong Jeng, Chih-Cheng Lu, Hsiang-Wei Ku, Bo-Rei Huang, Meng-Huan Chia, and Xuan Thang Trinh. Three-Axis Micofluxgate With a Fluxguide. *IEEE Transactions on Magnetics*, 55(7):1–4, July 2019. doi:10.1109/TMAG.2019.2903107.

[11] H. Joisten, B. Guilhamat, M. Audoin, J.-M. Leger, R. Cuchet, G. Barrois, J.-B. Albertini, P. Gaud, P. Renaux, D. Bloch, and B. Viala. Microfluxgate performance improvement in microtechnology. *IEEE Transactions on Magnetics*, 41(11):4356–4358, November 2005. doi:10.1109/TMAG.2005.854794.

[12] S. Kawahito, C. Maier, M. Schneiher, M. Zimmermann, and H. Baltes. A 2D CMOS microfluxgate sensor system for digital detection of weak magnetic fields. *IEEE Journal of Solid-State Circuits*, 34(12):1843–1851, December 1999. doi:10.1109/4.808909.

[13] Chong Lei, Yan Liu, Xue-Cheng Sun, Tao Wang, Zhen Yang, and Yong Zhou. Improved Performance of Integrated Solenoid Fluxgate Sensor Chip Using a Bilayer Co-Based Ribbon Core. *IEEE Sensors Journal*, 15(9):5010–5014, September 2015. doi:10.1109/JSEN.2015.2432457.

[14] Diana C. Leitao, Elvira Paz, Ana V. Silva, Anastasiia Moskaltsova, Simon Knudde, Francis L. Deepak, Ricardo Ferreira, Susana Cardoso, and Paulo P. Freitas. Nanoscale Magnetic Tunnel Junction Sensing Devices With Soft Pinned Sensing Layer and Low Aspect Ratio. *IEEE Transactions on Magnetics*, 50(11):1–8, November 2014. doi:10.1109/TMAG.2014.2320606.

[15] Chih-Cheng Lu, You-Cheng Lin, Yao-Zhi Tian, and Jen-Tzong Jeng. Hybrid Microfluxgate and Current Transformer Sensor. *IEEE Transactions on Magnetics*, 58(8):1–5, August 2022. doi:10.1109/TMAG.2022.3157052.

[16] E Monteblanco, A Solignac, C Chopin, J Moulin, P Belliot, N Belin, P Campiglio, C Fermon, M Pannetier-Lecoeur, and Université Paris-Saclay. Constant TMR magnetic field sensor detectivity with bias voltage. 2021.

[17] Elmer Monteblanco, Aurelie Solignac, Chloe Chopin, Julien Moulin, Pierre Belliot, Noemie Belin, Paolo Campiglio, Claude Fermon, and Myriam Pannetier-Lecoeur. Normalization and correction factors for magnetic tunnel junction sensor performances comparison. *IEEE Sensors Journal*, 21(14):15993–15998, July 2021. doi:10.1109/jsen.2021.3076276.

[18] M. Schneider, S. Kawahito, Y. Tadokoro, and H. Baltes. High sensitivity CMOS microfluxgate sensor. In *International Electron Devices Meeting. IEDM Technical Digest*, pages 907–910, December 1997. ISSN: 0163-1918. doi:10.1109/IEDM.1997.650528.

[19] Saransh Sharma, Hayward Melton, Liliana Edmonds, Olivia Addington, Mikhail Shapiro, and Azita Emami. A monolithic 3D magnetic sensor in 65nm CMOS with ¡10μT_{rms} noise and 14.8μW power. In *2023 IEEE Custom Integrated Circuits Conference (CICC)*, pages 1–2. IEEE, April 2023.

[20] N. Strelkov, A. Timopheev, R. C. Sousa, M. Chshiev, L. D. Buda-Prejbeanu, and B. Dieny. Stability phase diagram of a perpendicular magnetic tunnel junction in noncollinear geometry. *Physical Review B*, 95(18):184409, May 2017. Publisher: American Physical Society. doi:10.1103/PhysRevB.95.184409.

[21] A. A. Timopheev, R. Sousa, M. Chshiev, L. D. Buda-Prejbeanu, and B. Dieny. Respective influence of in-plane and out-of-plane spin-transfer torques in magnetization switching of perpendicular magnetic tunnel junctions. *Physical Review B*, 92(10):104430, September 2015. Publisher: American Physical Society. doi:10.1103/PhysRevB.92.104430.

[22] Z. M. Zeng, P. Khalili Amiri, J. A. Katine, J. Langer, K. L. Wang, and H. W. Jiang. Nanoscale magnetic tunnel junction sensors with perpendicular anisotropy sensing layer. *Applied Physics Letters*, 101(6):062412, August 2012. doi:10.1063/1.4744914.

Chapter 5

General conclusion

5.1 Conclusion

This thesis, entitled "**Development of integrated magnetometers based on spin transfer torque magnetic tunnel junctions**", has successfully demonstrated the use of nanoscale perpendicular STT-MTJs, originally used for MRAMs, as magnetic sensing elements through innovative ways. With diameters ranging from 20 nm to 100 nm, these devices represent the smallest magnetic sensing elements ever reported to this date. In addition, using simple electronic circuits, based on standard microelectronics components, performance and working principle have been demonstrated. However, the stochasticity, observed in the reversals in STT-MTJs and inducing a large noise, remains one of the biggest drawbacks of such technology, requiring further work to reduce its impact.

After the introduction of all the necessary notions involved in this thesis, about main physics principles, magnetic sensors and magnetic memories, presented in **Chapter 1**, **Chapter 2** has presented the general working principle of the presented magnetic sensor, through a physical dependency between the switching voltages APP and PAP, and the external magnetic field $\vec{B}$ along the perpendicular direction of the wafer. The key principle of the sensor relies on the application of a triangular (i.e., linear) voltage sweep at a frequency of tens to hundreds of kHz (100 to 200 kHz) and with a peak amplitude of 1 V, allowing for a complete sweep of the entire APP and PAP switching voltage possibilities to be covered without breaking down the MTJ. When the voltage reaches the critical switching threshold (either APP or PAP), the resistance of the MTJ changes rapidly in a few nanoseconds. Through Ohm's law, this induces a current discontinuity at the moment of the reversal. Since the voltage sweep is linear, the time between two consecutive reversals is directly proportional to the external magnetic field. Hence, the use of dedicated circuits, described in this chapter and based on the detection of these discontinuities with high-pass filters, allows the use of this dependency and reversals events to be extracted. This allows the conversion of these events into measurable signals (either voltage or time signals) which are subsequently proportional to $\vec{B}$ and which can be digitized. Finally, adaptation in the conversion mechanism described in the first part of Chapter 2 allows single-reversal events to be sampled, allowing high-frequency measurements to be performed, up to 100 to 200 kHz with a flat spectrum. Through these mechanisms, NPSDs of 10 to 20 $\mu\mathrm{T}/\sqrt{Hz}$ have been achieved.

In an attempt to improve the performance achieved with high coercivity MTJs, **Chapter 3** presents the use of dedicated STT-MTJs, presenting coercive fields as low as 1 mT, designed for sensing applications, allowing higher sensitivity to be reached, which only differ from high coercivity MTJs by their stacks. However, this comes with softer reversals between the P and AP states, making the initial proposed approaches with high-pass filters, described with high coercivity MTJs, unusable. Therefore, new electronics are demonstrated, based on simple OpAmp circuits, allowing the presented STT-based principle to be implemented with these low coercivity MTJs, with switching voltages up to $\pm$ 350 mV at hundreds of kHz up to the MHz. Through these new approaches, successful measurements have been performed, demonstrating the working principle and allowing for NPSDs as low as 2 to 3 $\mu\mathrm{T}/\sqrt{Hz}$ to be reached over a large dynamics range of tens of mT. In addition, the use of a few additional components and

dedicated control sequences enables measurements of single periods, making the measurements at high frequency possible, with a bandwidth up to the MHz range.

Finally, **Chapter 4** compares the performance of the proposed sensor with existing commercial and experimental devices, at different levels. Existing sensors (based on the Hall effect or MR effect) are often fabricated in the range of the μm level, either to allow for the physical phenomena to take place (e.g., Hall plates) or to lower the noise (e.g., MR sensors). Hence, in comparison to existing technologies, commercially available or reported experimental work, one can observe the extreme dimensions achieved over this work, with sensing element among the smallest ever reported. In addition, despite exhibiting noise higher than standard technologies, this sensor offers state-of-the-art performance in terms of noise when normalized with the dimensions. Other metrological parameters remain also significantly similar or better than standard technologies values (e.g., linearity, power consumption, bandwidth, or dynamic range), making the proposed sensor also competitive in these domains. In addition, the assessment of the impact of the parameters of the input signal (e.g., offset, amplitude or frequency) as well as temperature dependency, allows for better understanding of the best possible configuration in future works and validate the capability of the sensor to perform in real life situation (e.g., different temperatures) or mass production compatibility through variability evaluation over part of the wafers.

5.2 The future of STT-MTJ magnetic sensors

This thesis has successfully demonstrated multiple aspects of this proof of concept of a new generation of integrated magnetic sensors based on perpendicular STT-MTJs. However, to further enhance the proposed STT-MTJ magnetic sensor, two aspects need to be further investigated: the electronics, mainly described in this work, and the MTJs.

Based on the existing and evaluated wafers in this work, presented in Chapters 2 and 3, the use of the fabricated wedges (FeCoB and Mg), through scanning of all wafers with the evaluation and comparison of sensing performance on each MTJ, will allow the best thicknesses of wedged layers to be obtained, by finding the best regions in the wafer presenting the highest SNR ratio. This will allow for the starting point of possible optimisations (either low coercivity or high coercivity MTJs) of the stacks, by playing with different thicknesses. In addition, completely new stacks, with the introduction of different layers, different layers orders, different materials, or other MTJ architectures (e.g., double MgO barrier, different SAFs, etc.), while trying to remain close to MRAM-dedicated MTJs, will possibility allow for higher sensitivity to be reached, and potentially achieve lower stochasticity as well as reduced offset, two of the main concerns of low coercivity and/or high coercivity MTJs. Furthermore, the analysis of impact of the diameters of the MTJs (20, 50, 80 or 100 nm in this work) will eventually allow us to conclude on the single-domain hypothesis on the stochasticity, with initial thoughts being lower dimensions presenting lower noise. Finally, the implementation of "perpendicular" flux concentrator or the evaluation of parallel MTJs (either as an individual sensing units or as a single, bigger unit) will also help

in the analysis of what could be achieved in terms of best SNR possible through such STT-based approach and assess the possible applications requiring low noise performance or sensing array (e.g., magnetic field cameras).

The future integration of the electronics as monolithic IC, possibility embedding the MTJ, with more carefully optimized layout, components choice, and through better simulations will also help to lower the overall noise (despite being less relevant due to the much higher noise induced by the MTJ especially for high coercivity MTJs) and the possibility to solve the oscillation problems depicted in Chapter 3 with low coercivity MTJs, by fine-tuning the electronics. Possible new architectures could also potentially help in the reduction of the main problem shown with low coercivity MTJs (dead zone/lower sensitivity region around the offset). In addition, the evaluation of more complex electronics can potentially help improve sensor performance. This includes, for instance, the use of non-linear electronics (e.g., analog divider) or custom lock-in amplifiers to lock onto the switching frequency, minimizing the rms noise of the sensor, as well as compensation circuits with coils for offset cancellation or better linearity. With the integration of the electronics and MTJ within a single chip, first assessment of real-life applications will also become possible.

With such proper investigations and optimizations, this innovative integrated sensing technology based on STT-MTJs will offer new possibilities in magnetic measurements, either implemented as a single sensor or as a high-density array, opening the way to different applications, ranging from the medical field to industrial or physics applications at low power consumption. This includes true punctual measurements at the nanoscale level, required in specific applications such as photolithographic mask alignment or magnetic particles and beads detection in biology or industrial domains, as well as high bandwidth applications, including current measurements, required to meet new industrial requirements.

Version résumée

Introduction

Les jonctions tunnel magnétiques (MTJs) représentent une avancée majeure dans le domaine de la spintronique, un domaine scientifique en pleine expansion ces dernières années, utilisant les électrons comme acteurs principaux, et qui se base sur la combinaison de la propriété électronique de l'électron avec sa propriété magnétique, par l'intermédiaire du spin, une propriété quantique aux multiples applications. Parmi les avancées technologiques majeures dans ce domaine, les jonctions tunnel magnétiques représentent l'une des plus prometteuses, utilisées dans de nombreux domaines scientifiques, avec un fort potentiel industriel.

Les jonctions magnétiques à effet tunnel (MTJs) sont constituées d'une couche nanométrique d'un matériau non magnétique et non conducteur, souvent de l'oxyde de magnésium (MgO), placée entre deux couches de matériaux ferromagnétiques conducteurs, typiquement à base d'un alliage de fer, de cobalt et de bore (FeCoB). Ces dispositifs sont fabriqués sous la forme de piliers cylindriques verticaux, de diamètres de l'ordre de 10 à 100 nm pour une hauteur similaire et sont fabriqués à l'aide de procédés de microélectroniques et nanoélectroniques en salle blanche. L'aimantation d'une des deux couches ferromagnétiques est fixe (également appelée couche de référence) dans une direction unique tandis que l'autre couche ferromagnétique a une aimantation libre d'être inversée. Lorsque ce vecteur d'aimantation est dans le plan de la jonction, appelées jonctions dans le plan, le dispositif est principalement utilisé comme capteur magnétique. En revanche, lorsque ce vecteur est perpendiculaire au plan de la jonction, le dispositif, appelé jonction tunnel magnétique perpendiculaire (pMTJ), est utilisé presque exclusivement dans les mémoires magnétiques (MRAMs), notamment grâce à plusieurs avantages physiques observés (dimensions, fabrication, stabilité, etc.) par rapport aux jonctions dans le plan. Dans les deux cas, on obtient un dispositif dont le vecteur de magnétisation libre présente deux états stables, un état dit parallèle (P), lorsqu'il est dans la même direction que la couche de référence, et un état dit antiparallèle (AP), lorsqu'il a une direction opposée à la couche de référence. La résistance de la jonction dans les deux états est différente, induite par l'effet de magnétorésistance tunnel (TMR), dont la variation peut facilement atteindre 100 à 200 %. Grâce à cette configuration bistable, ces dispositifs sont donc parfaitement adaptés au stockage d'informations binaires et sont utilisés comme mémoires magnétiques.

Les mémoires magnétiques, basées sur des jonctions perpendiculaires, font partie des applications les plus prometteuses de ces dispositifs, avec un fort potentiel pour concurrencer les technologies existantes dans des tâches spécifiques. Ces mémoires magnétiques basées sur les MTJs offrent des performances de consommation énergétique très intéressantes, avec des courants d'écriture et de lecture très faibles. De plus, elles offrent une capacité de stockage non volatile, des vitesses de lecture et d'écriture élevées, avec des dimensions nanométriques, et donc une possibilité de densité de stockage élevée. Enfin, ces dispositifs restent compatibles avec les procédés de fabrication CMOS, permettant une production à grande échelle, intégrée dans des circuits plus complexes. Ainsi, ces mémoires sont déjà produites à grande échelle dans les grandes fonderies (par exemple, TSMC, Samsung ou GF) bien qu'elles présentent encore

différents inconvénients. Par exemple, les mémoires magnétiques restent nettement plus chères que leurs concurrentes avec des technologies standard (Flash, SRAM ou DRAM), et restent difficiles à produire de manière reproductible.

Ainsi, contrôler ces jonctions en tant que cellules mémoires revient à contrôler l'état P et AP. Pour cela, deux méthodes sont possibles. La couche libre étant constituée d'un matériau ferromagnétique, l'application d'un champ magnétique externe suffisamment fort dans une direction précise permet de renverser son aimantation. Cette méthode est cependant peu pratique dans le cas de mémoires. En revanche, grâce à un autre phénomène physique, extrêmement important dans le domaine de la spintronique et appelé couple de transfert de spin (STT), l'application d'un courant (ou d'une tension) suffisamment fort à travers le dispositif permet de placer la jonction dans l'état P ou AP selon la polarité utilisée. Pour y parvenir, une tension spécifique doit être appliquée (positive ou négative) pour dépasser le seuil de retournement, typiquement autour de tensions (absolues) de 0.5 à 1 V. Cependant, la tension de commutation et le champ magnétique peuvent s'influencer mutuellement. Ainsi, le champ magnétique externe peut modifier le champ effectif et l'énergie nécessaire pour inverser le vecteur de magnétisation de la couche libre de telle sorte que la tension de seuil soit affectée. **Il en résulte un seuil de retournement proportionnel au champ magnétique externe**. Ce phénomène correspond au principe fondamental d'une nouvelle génération de capteurs magnétiques, étudiés au cours de ce travail de doctorat.

Cette thèse, intitulée "**Développement de magnétomètres intégrés à base de jonctions tunnel magnétiques à couple de transfert de spin**" a pour objectif de démontrer la preuve de concept d'une nouvelle génération de capteurs magnétiques intégrés, en utilisant ces dispositifs nanométriques, appelés jonctions tunnel magnétiques, de manière inhabituelle, grâce à l'effet de couple de transfert de spin, utilisés à l'origine pour les mémoires magnétiques, pour obtenir une mesure précise du champ magnétique. Dans le cadre de ce travail de thèse, un nouveau type de capteur magnétique est donc démontré, basé sur ce principe, observé dans les jonctions perpendiculaires, habituellement utilisées pour les MRAMs. Pour y parvenir, le concept clé de tels capteurs consiste en l'application d'une tension alternative permettant le retournement périodique de la couche de stockage entre les deux états, P et AP, combiné à un système de détection du retournement à chaque période. Ainsi, la mesure du seuil de retournement permet une mesure du champ magnétique à haute fréquence et à l'échelle nanométrique. Malheureusement, de tels dispositifs souffrent d'un défaut majeur, appelé stochasticité. Ce phénomène induit une variation aléatoire du seuil de retournement en l'absence de variations du champ magnétique, d'où un bruit important en sortie du capteur, qui ne peut alors être que moyenné pour être réduit, soit en multipliant le nombre d'éléments sensibles, soit en multipliant les mesures sur un seul élément.

Cette nouvelle génération de capteurs vise à concurrencer les technologies existantes de capteurs magnétiques intégrés, presque exclusivement basées sur l'effet Hall, ou l'effet magnétorésistif (AMR, TMR ou GMR). Ces capteurs intégrés présentent des inconvénients importants. Les dimensions des capteurs à effet Hall sont généralement limitées à quelques μm par des limites physiques, car les lignes de courant ne sont pas suffisamment déviées pour des

faibles dimensions, ce qui entraîne l'absence de sensibilité détectable. Les capteurs MR souffrent également de problèmes liés aux dimensions, car les capteurs MR de faibles dimensions entraînent généralement un bruit plus élevé. Pour ces raisons, la plupart des capteurs existants restent dans la gamme du μm et au-dessus, limitant les applications possibles nécessitant de véritables mesures ponctuelles, telles que l'alignement de masques photolithographiques ou la détection de particules magnétiques de petites tailles. De plus, ces capteurs souffrent également de limitations de bande passante, de l'ordre de quelques dizaines de kHz, ce qui entraîne l'absence d'applications à haute fréquence. Cela inclut par exemple les mesures de courant à bande passante élevée, nécessaires pour répondre aux nouvelles exigences industrielles, ou les compteurs de rotation. Une consommation d'énergie plus faible ou la compatibilité CMOS font également partie des avantages de cette nouvelle technologie. Ainsi, ce capteur magnétique intégré basé sur des STT-MTJs vise à pallier les inconvénients observés dans les technologies standards.

Ce manuscrit de thèse est organisé selon le plan suivant :

- **Le chapitre 1** commence par introduire toutes les notions nécessaires à la compréhension des sujets abordés dans ce manuscrit. En premier lieu, les notions les plus importantes du magnétisme seront introduites, décrivant tous les aspects physiques du champ magnétique et les phénomènes physiques observés dans le cadre de ces travaux. Dans un deuxième temps, nous introduirons des notions importantes sur les mémoires magnétiques et les jonctions tunnel magnétiques. Enfin, une brève description des capteurs magnétiques et de quelques-unes des technologies de mesure intégrées les plus importantes sera détaillée. Grâce à ce chapitre, le lecteur aura un aperçu de toutes les notions de base utilisées dans les chapitres suivants.

- **Le chapitre 2** présente tous les principes et éléments clés du capteur magnétique nouvellement démontré. Le principe de fonctionnement du capteur, les jonctions utilisées ainsi que l'électronique développée pour utiliser ces jonctions comme éléments sensibles sont décrits, permettant la compréhension de ce nouveau principe de mesure.

- **Le chapitre 3** continue la description de cette nouvelle génération de capteur magnétique à base de STT-MTJs au travers d'un principe légèrement différent, en présentant de nouvelles jonctions, développées pour des applications métrologiques, présentant des champs coercitifs faibles, associées à une nouvelle électronique, développée pour rester compatible avec ces nouvelles MTJs, permettant d'atteindre des performances améliorées.

- **Le chapitre 4** termine la discussion du travail réalisé au cours de ce doctorat, en comparant les performances obtenues avec les technologies existantes, ainsi que différentes approches tentées pour l'amélioration des performances du capteur.

- **La conclusion** résume enfin l'ensemble des résultats obtenus sur l'ensemble de ce projet sous forme d'une perspective globale, permettant au lecteur d'avoir un aperçu des perspectives futures à atteindre pour l'amélioration de la technologie.

Jonctions à haute coercivité

Bien que les capteurs TMR soient basés sur une manière relativement simple de faire fonctionner les MTJs comme éléments sensibles, l'objectif de cette thèse de doctorat est de démontrer l'utilisation de STT-MTJs perpendiculaires et nanométriques, conçus à l'origine pour des applications MRAMs, de manière non conventionnelle, pour les faire fonctionner comme éléments sensibles magnétiques.

Le principe de fonctionnement de ce nouveau type de capteur magnétique est basé sur le fait qu'à la fois le champ magnétique et le courant électrique peuvent être utilisés pour inverser l'état de la couche libre et placer la MTJ dans l'état P ou AP. Un champ magnétique externe suffisamment fort (supérieur au champ coercitif de la couche libre) ou un courant suffisamment fort (par l'effet STT) peuvent tous deux affecter l'état du dispositif. Cependant, ces deux effets peuvent se produire en même temps, de sorte que le champ magnétique réduit la barrière énergétique pour le retournement de la magnétisation de la couche libre pour modifier de manière significative le courant requis pour changer la direction de magnétisation. En conséquence, ces courants de commutation (ou tensions, V_{PAP} ou V_{APP}) seront plus ou moins élevés que dans la configuration à champ nul. Dans l'ensemble de ces travaux, pour des raisons de simplicité technique, les MTJs fonctionnent avec des signaux en tension et non des signaux en courant, même si le paramètre important pour la commutation est la densité de courant. En effet, la plupart des circuits électroniques sont généralement plus faciles à concevoir lorsqu'ils fonctionnent en tension plutôt qu'en courant. Par conséquent, le principe clé de ce nouveau type de capteur magnétique, basé sur les STT-MTJs, consiste en un retournement périodique d'une MTJ perpendiculaire entre les états P et AP via l'effet STT, combiné à la détection continue des seuils de commutation. Ces seuils de commutation sont affectés par le champ magnétique externe, et la mesure des seuils APP et PAP permet la mesure du champ magnétique.

Afin de démontrer le principe de fonctionnement du capteur, des MTJs à haute coercivité ont donc été testés, développés à l'origine pour des applications MRAMs, et fabriqués à la Plateforme Technologique Amont (PTA), une salle blanche située au CEA de Grenoble, en France. Ces MTJs se présentent sous la forme de cylindres verticaux, basés sur de l'anisotropie magnétique perpendiculaire (c'est-à-dire des pMTJs) et utilisent un SAF à base de Co/Pt pour fixer la magnétisation de la couche de référence le long du plan perpendiculaire au wafer. Grâce à cette configuration, le capteur présenté est sensible à l'axe perpendiculaire de la plaque, contrairement aux capteurs TMR, basés sur des MTJs dans le plan, et sensibles aux champs parallèles au plan de la plaque. Ces dispositifs sont fabriqués sur des wafers de 100 mm sur des substrats SiO_2 et sont basés sur la configuration standard $FeCo_8B_{20}/MgO/FeCo_8B_{20}$. Après le dépôt des couches minces sur le wafer, les wafers sont recuits à 350 °C pendant 10 minutes et les MTJs sont ensuite gravés par traitement physique sous forme de nanopiliers verticaux. La barrière de MgO est réalisée par l'oxydation naturelle de la couche de Mg pendant une période de temps donnée (quelques secondes à quelques minutes) et une pression donnée (quelques mbar) ; dans ce cas, 240 secondes à 0.03 mbar. Les diamètres des MTJs fabriqués varient de 20 à 100 nm

(nominal) pour une hauteur verticale de plusieurs dizaines de nm (20 à 100 nm). Pour accéder aux MTJs, deux pads sont connectés aux électrodes supérieure et inférieure de chaque MTJ, et l'électronique est connectée aux MTJs via une sonde de test. À la fin du processus de fabrication, un fort champ magnétique est appliqué pour fixer les aimantations des couches dans la bonne orientation. De plus, le wafer évalué a été fabriqué avec deux wedge (c'est-à-dire un gradient d'épaisseur), permettant une évaluation rapide et efficace de l'effet de l'épaisseur de deux couches sur les performances des cellules mémoire.

Dans ces MTJs, le retournement de l'aimantation de la couche libre est en fait un processus stochastique. Cela implique que pour toute tension ou champ magnétique appliqué à la MTJ, il existe une probabilité (appelée probabilité de commutation, SP) pour le retournement de la couche libre. Cette probabilité est la plus élevée lorsque la tension et/ou le champ magnétique appliqués sont significativement supérieurs au seuil critique ($SP = 1$) et la plus faible ($SP = 0$) lorsqu'aucun champ ou courant n'est appliqué. Lorsque la tension ou le champ magnétique appliqué est égal au seuil critique, il existe 50 % de probabilité pour observer un retournement. La fonction mathématique typique qui nous permet de décrire la probabilité de retournement en première approximation est une distribution gaussienne, même si des modèles plus complexes mais plus précis peuvent être utilisés.

Le principe technique du capteur repose donc sur l'application d'une tension triangulaire à une fréquence donnée pouvant atteindre des centaines de kHz sur la MTJ (typiquement 100 à 200 kHz), avec une amplitude de crête couvrant les tensions de commutation de la MTJ (amplitude crête à crête typiquement $\pm$ 1 V), pendant que le courant à travers la MTJ est mesuré. Cela se fait à l'aide d'une résistance de shunt (typiquement 100 à 1000 Ω) en série avec la MTJ, et d'un amplificateur différentiel connecté aux deux bornes du shunt, qui amplifie la tension aux bornes du shunt avec un gain G (typiquement 2 à 10), proportionnel au courant à travers la MTJ (< 0.5 mA). Cela permet ainsi de mesurer la résistance de la MTJ. Lorsque la tension aux bornes de la jonction atteint la tension de commutation (PAP ou APP), la résistance de la MTJ bascule brutalement. En conséquence, le courant présente également un changement soudain, qui correspond au moment où la tension d'entrée appliquée au courant doit être enregistrée, car elle représente le seuil APP ou PAP ciblé, proportionnel à $\vec{B}$. Pour détecter l'événement, le signal obtenu à la sortie de l'amplificateur différentiel est ensuite appliqué à travers un filtre passe-haut avec une fréquence de coupure significativement supérieure à la fréquence de la tension triangulaire, dans ce cas, 725 kHz, choisie arbitrairement pour supprimer les 4 premières harmoniques impairs d'un signal de 100 kHz (100, 300, 500 et 700 kHz). Une telle fréquence de coupure permet de supprimer les harmoniques fondamentales ainsi que les premières plus grandes harmonique du signal tout en conservant les fortes discontinuités des événements de commutation, se produisant à une fréquence beaucoup plus élevée, car le retournement de la résistance prend généralement quelques dizaines de ns. À la sortie du filtre passe-haut, des pics de tension d'amplitudes de plusieurs dizaines à plusieurs centaines de mV (20 à 300 mV selon le TMR de la MTJ) sont observés et peuvent être différenciés du bruit de fond. Pour ces raisons fréquentielles et en raison du GBW des amplificateurs, G doit être maintenu relativement bas, permettant à la bande passante de l'amplificateur de rester suffisamment élevée (> 1 à 2 MHz minimum) pour

laisser passer les fortes discontinuités et permettant d'utiliser des amplificateurs commerciaux à faible GBW. Étant donné que le circuit doit rester compatible avec une intégration monolithique, les amplificateurs à très haut GBW deviennent également difficiles et coûteux à concevoir et doivent donc être évités dans cette preuve de concept. Pour compenser un gain aussi faible, une valeur de shunt plus élevé est utilisée, toujours inférieur à R_{MTJ}. De plus, alors que de nombreux circuits permettent la mise en œuvre du filtre passe-haut, le choix a été fait d'utiliser une configuration condensateur-résistance passive (CR) du second ordre. Cette approche permet de démontrer le principe de fonctionnement tout en gardant la conception très simple et compacte, par opposition à une implémentation active du filtre. Les événements de retournements peuvent alors être détectés à l'aide d'un comparateur avec un seuil fixe défini, au-dessus du bruit de fond, qui délivre de courtes impulsions de niveau logique de 5 V au moment des retournement (PAP ou APP). L'amplitude typique de ces impulsions à détecter est de 10 à 100 mV avec une durée de plusieurs dizaines de ns. **Les durées entre ces impulsions sont directement liées au champ magnétique externe.**

Pour utiliser ces impulsions et produire un signal proportionnel à $\vec{B}$, les impulsions sont combinées via une bascule set-reset avec horloge (bascule cSR) constituée de 4 portes NAND, avec la polarité d'entrée du signal triangulaire et un signal de polarité inversée. Pour obtenir la polarité du signal triangulaire d'entrée, un deuxième comparateur est utilisé, comparant le signal d'entrée par rapport à la masse, produisant un "1" pour l'entrée positive et un "0" pour l'entrée négative, tandis qu'un simple inverseur est utilisé pour inverser le signal de polarité. Cette structure de bascule cSR est basée sur le front montant des impulsions et présente également l'avantage de délivrer nativement des signaux différentiels, en raison de la sortie complémentaire de l'architecture. L'entrée d'horloge de la bascule cSR est connectée à la sortie du premier comparateur générant les impulsions, tandis que les signaux SET et RESET utilisent le deuxième comparateur et sont connectés aux signaux de polarité du signal triangulaire d'entrée. Ainsi, la polarité du signal d'entrée est connectée au SET, tandis que la polarité inversée du signal d'entrée est connectée au RESET de la bascule cSR. Étant donné qu'un front montant du signal d'horloge indique un événement de commutation, soit APP, soit PAP, la polarité du signal d'entrée permet de différencier APP et PAP. Cette méthode permet ainsi de générer un signal modulé en largeur d'impulsion (PWM), avec une sortie différentielle. Comme le cycle de service est contrôlé par le temps entre les impulsions APP et PAP, le cycle de service des signaux PWM est donc directement proportionnel à $\vec{B}$. Par conséquent, un simple filtre passe-bas, composé de deux étages RC est utilisé avec une fréquence de coupure de 100 à 2000 Hz, pour récupérer un niveau de tension continu proportionnel au champ magnétique. La sortie du filtre passe-bas est ensuite injectée dans des buffers analogiques et directement injectée dans un convertisseur analogique-numérique (CAN). Pour les mêmes raisons que pour le filtre passe-haut, le filtre passe-bas est implémenté sous forme de structure RC passive. La fréquence de coupure du filtre passe-bas étant conçue pour être comprise entre 100 et 2 kHz, cela permet de faire le moyennage de quelques centaines (100 à 1000) de retournements pour minimiser l'impact de la stochasticité et diminuer le bruit rms en sortie du capteur.

Ainsi, l'utilisation de jonctions tunnel magnétiques à couple de transfert de spin perpendiculaire nanométrique comme éléments sensibles magnétiques à l'échelle nanométrique à travers deux architectures de lecture différentes et spécifiques est démontrée, basées sur des composants microélectroniques CMOS standard et des méthodes de lecture simples. Grâce à une manière unique d'utiliser les STT-MTJs, relativement similaire au principe de fonctionnement du fluxgate, une preuve de concept réussie a été réalisée. De tels éléments sensibles, représentant les plus petits éléments sensibles rapportés à ce jour, avec un diamètre nominal de 20 à 100 nm, sont intrinsèquement adaptés à l'intégration monolithique, grâce à l'utilisation de pMTJs, développés à l'origine pour les MRAMs. Deux approches différentes sont démontrées. La première, basée sur des signaux PWM filtrés, offre un meilleur bruit rms et une architecture plus standard avec une sortie numérique classique, basée sur un CAN, au détriment d'une plus grande surface de silicium et d'une bande passante plus faible. Cette méthode, produisant une tension proportionnelle à $\vec{B}$, a un plus fort potentiel d'intégration future dans les circuits monolithiques et la production de masse en raison de sa possibilité de mise en œuvre facile dans des systèmes plus larges comme avec les capteurs Hall ou MR existants. En revanche, la deuxième approche, basée sur les convertisseurs temps-numérique et émettant un signal temporel proportionnel à $\vec{B}$, offre une bande passante plus large, avec une capacité de détection d'événement de commutation unique, au prix d'un bruit rms accru et d'exigences de traitement du signal différé, car les mesures à large bande passante nécessitent une puissance de calcul importante et rapide. De telles méthodes basées sur un convertisseur temps-numérique représentent une méthode plus prometteuse pour des applications spécifiques, par exemple des applications industrielles ou physiques, où la bande passante doit être maximisée ou si l'élément sensible et l'électronique peuvent être séparés, ce qui permet d'utiliser une électronique existante plus complexe mais dédiée ou d'effectuer un meilleur traitement du signal. Cependant, pour améliorer les performances de bruit d'un tel capteur magnétique à base de STT-MTJs, principalement limitées par l'élément sensible lui-même, l'utilisation de MTJs à coercivité plus faible, nouvellement développées et utilisées de manière similaire, présente des performances prometteuses.

Jonctions à basse coercivité

Pour améliorer les performances du capteur présenté, principalement en termes de bruit, des MTJs à faible coercivité ont été fabriqués et évalués. Le principe du capteur basé sur ces MTJs à faible coercivité reste exactement le même que celui décrit précédemment, dans la mesure où un signal de tension triangulaire est appliqué, permettant aux événements APP et PAP de se produire. Les seuils auxquels ces retournements se produisent sont également directement liés au champ magnétique externe, et la mesure d'un tel seuil permet de mesurer $\vec{B}$. Cependant, une nouvelle électronique doit être développée pour surmonter certains problèmes et respecter certaines spécificités des MTJs à faible coercivité.

En effet, malgré un TMR important allant jusqu'à 40 à 60 %, ces MTJs à faible coercivité présentent un changement entre les états P et AP beaucoup plus doux que les MTJs à haute coercivité, ce qui rend la détection des retournements avec un filtre passe-haut impossible. Pour faire fonctionner ces dispositifs comme des éléments sensibles, d'autres approches ont donc été développées, basées sur des amplificateurs opérationnels et des composants microélectroniques standards. Pour faire fonctionner les MTJs dans leur dynamique maximale tout en les gardant intactes, un signal d'entrée triangulaire avec une amplitude de crête de 300 mV (soit ± 300 mV) a été utilisé, à une fréquence de 100 kHz. Cela crée des changements périodiques entre les états AP et P, permettant au principe de mesure présenté de se produire.

Dans la première approche testée, la MTJ a été implémenté comme une résistance variable dans un montage intégrateur standard. La MTJ a été connecté entre le signal d'entrée, provenant d'un générateur de signal, et la masse virtuelle de l'amplificateur opérationnel, garantissant, pour un comportement correct, que la tension appliquée entre les deux électrodes de la MTJ soit toujours référencée à un potentiel constant, la masse. Ainsi, la méthode initiale présentée démontre le principe de fonctionnement avec cependant deux problèmes principaux. Le premier est une symétrie dans les tensions de sortie, rendant impossible la différenciation des champs magnétiques positifs ou négatifs centrés autour du champ d'offset. Le deuxième problème observé est une zone morte, située autour du champ d'offset, où une sensibilité nulle est observée. Par conséquent, une deuxième approche décrite par la suite vise à surmonter ces problèmes métrologiques. Pour surmonter ces inconvénients, le circuit décrit ci-dessus doit être légèrement modifié. Dans cette deuxième approche, la MTJ est placé comme résistance d'entrée d'un montage amplificateur inverseur. Dans les mêmes conditions que dans la première méthode, le gain G du circuit change sur une période, car la MTJ alterne entre les états P et AP, et par conséquent, le signal de sortie correspond au signal d'entrée amplifié avec un gain variable proportionnel au champ magnétique externe. L'utilisation d'un circuit redresseur permet ensuite de corriger ce signal, et de supprimer la symétrisation de la sortie. Il en résulte dans les deux cas un signal de sortie proportionnel au champ magnétique externe qui peut être injecté dans un CAN.

Ainsi, l'utilisation de STT-MTJs à faible coercivité comme éléments sensibles, d'une manière similaire aux MTJ à haute coercivité présentés précédemment, est également démontrée. De telles modifications du stack des MTJs permettent d'améliorer la sensibilité et les performances en matière de bruit tout en conservant la plupart des avantages des approches à base de STT-MTJs à haute coercivité, notamment une dynamique plus élevée ou une consommation d'énergie plus faible que la plupart des technologies MR et/ou Hall existantes. Bien que les circuits conçus pour les MTJs à haute coercivité basés sur des filtres passe-haut soient inutilisables avec de telles nouvelles approches, en raison de renversements APP/PAP plus doux, d'autres solutions simples basées sur des amplificateurs opérationnels ont été proposées avec succès et démontrées par des mesures expérimentales. Trois circuits différents ont été proposés et validés expérimentalement. Le premier basé sur un intégrateur simple permet une mise en œuvre simple du principe de mesure à base de STT-MTJs proposé. Cela permet des systèmes de mesure très compacts grâce à un amplificateur opérationnel unique. Le second, basé sur un redresseur de précision basé sur un amplificateur opérationnel, permet de

supprimer le problème de sortie symétrique en ajoutant quelques composants supplémentaires et deux diodes. Dans les deux cas, comme ces MTJs présentent des tensions de commutation proches autour de 0 V, cela crée une zone de sensibilité réduite voire une zone morte, et une situation complexe à résoudre, car l'électronique fonctionnant à très basse tension devient très difficile à concevoir. Ainsi, si des solutions et des circuits électroniques pourraient éventuellement être mis en œuvre pour minimiser cet effet, la solution la plus efficace serait de décaler toute la réponse des MTJs dans une seule polarité, positive ou négative, permettant aux tensions de commutation de rester loin de 0 V, au prix d'une consommation d'énergie plus élevée. Cependant, des études approfondies n'ont pas encore été réalisées sur la faisabilité physique de telles solutions, mais dans tous les cas, cela nécessiterait un effort important de la part de la conception et de la fabrication des dispositifs. Enfin, une autre approche, basée sur une version modifiée de ces circuits, permet des mesures de renversement unique sans ajouter de complexité significative, et maximise la bande passante au détriment d'un bruit rms plus important, permettant d'atteindre une bande passante encore plus large que les MTJs à haute coercivité, jusqu'à plusieurs centaines de kHz (100 à 1000 kHz), couvrant des applications plus spécifiques nécessitant des mesures à haute fréquences. Des améliorations supplémentaires du stack sont également encore nécessaires pour atteindre des champs d'offset nuls et augmenter encore la sensibilité. Une analyse dédiée de la stochasticité permettra également de mieux comprendre l'origine et les solutions de tels phénomènes, permettant d'obtenir un bruit plus faible grâce à l'optimisation du stack et à un meilleur contrôle des MTJs.

Position du capteur avec l'état de l'art

Si de nombreuses technologies de capteurs magnétiques existent, seules quelques-unes d'entre elles sont disponibles sous forme de circuits intégrés, et représentent les technologies concurrentes typiquement ciblées par le nouveau principe de mesure présenté. Cela inclut presque exclusivement les capteurs à effet Hall, TMR et AMR, à l'exception de quelques GMR, MEMS ou technologies propriétaires.

Pour évaluer les performances des éléments sensibles présentés dans ces travaux par rapport aux capteurs existants, une comparaison des performances entre les résultats obtenus avec ces capteurs est donc effectuée. Cependant, parmi les produits commerciaux, les éléments sensibles sont souvent des secrets industriels et seules quelques références avec des dimensions disponibles peuvent être analysées. De plus, il existe peu de travaux expérimentaux ciblant le développement de capteurs magnétiques à l'échelle nanométrique, avec moins de 10 approches de recherche trouvées. Cela est dû à plusieurs facteurs, notamment des défis technologiques, des limitations d'applications, des limitations de coût ou simplement physiques (par exemple, relation bruit vs dimensions dans certaines technologies MR). Les différents capteurs et travaux trouvés sont donc comparés aux capteurs magnétiques à base de STT-MTJs proposés. Ainsi, les dimensions des MTJs utilisés dans ces travaux sont parmi les plus petits éléments sensibles jamais rapportés, avec des performances de bruit comparables à celles des dispositifs expérimentaux TMR à l'échelle nanométrique. Cela montre que la technologie présentée basée

sur les STT-MTJs offre de bonnes performances par rapport aux technologies existantes lorsque la taille est prise en compte, suivant la même tendance linéaire, qui, dans le cas du fluxgate standard, est très probablement liée au bruit de Barkhausen, représentant les limites de bruit. Cependant, les dimensions des capteurs et la densité spectrale de bruit ne sont pas les seuls paramètres importants dans les capteurs magnétiques. Par conséquent, parmi d'autres paramètres, on peut également s'intéresser aux suivants. Cela inclut également la compatibilité CMOS, car les MTJs pour cellules MRAMs sont, ou deviendront nativement compatibles avec les processus de production de masse avec le développement de la technologie.

- **Dynamique :** les capteurs à effet Hall offrent une dynamique pouvant atteindre plusieurs Tesla. Cependant, pour offrir les meilleures performances de rapport signal/bruit (SNR), la dynamique peut également être réduite, ce qui permet d'obtenir une sensibilité et un SNR plus élevés. Par conséquent, les capteurs à effet Hall à faible bruit présentent souvent une dynamique allant jusqu'à ± 10 à 100 mT avec des densités spectral de bruit de 200 à 500 nT/$\sqrt{Hz}$. D'autre part, les capteurs MR sont généralement beaucoup plus restreints dans leur dynamique, avec généralement quelques mT pour un SNR plus élevé. En comparaison, le capteur STT-MTJ présenté offre une dynamique pouvant atteindre 100 mT, malgré un bruit plus fort, ce qui représente un avantage intéressant pour les applications à fort champ.

- **Linéarité :** les capteurs à effet Hall sont parmi les capteurs les plus linéaires disponibles, avec une erreur de non-linéarité fréquente aussi faible que ± 0.1 % FS. Cependant, les capteurs MR sont beaucoup moins linéaires et les capteurs existants présentent généralement une erreur de linéarité inférieure à ± 2 % FS. Dans le cas des méthodes de mesure présentées par l'approche à haute coercivité, l'erreur de non-linéarité obtenue est similaire à ces valeurs (± 1 à 2 % FS), et, selon la zone de fonctionnement choisie pour les approches à faible coercivité, du même ordre de grandeur, ce qui rend le principe de mesure présenté également compétitif dans ce domaine.

- **Consommation :** les capteurs à effet Hall et MR intégrés consomment généralement quelques mA de courant pour une tension de 1.8 à 5 V (généralement 1.8, 2.5, 3.3 ou 5 V), alimentant soit l'ensemble des circuits analogiques et numériques (par exemple, un CAN ou la communication numérique avec un microcontrôleur) soit uniquement l'élément sensible (dans le cas de dispositifs avec sortie analogique). Cependant, ces valeurs de consommation de courant peuvent être beaucoup plus élevées, par exemple dans le cas d'une architecture à polarisation élevée ou à courant rotatif, dans les capteurs à effet Hall (10 à 25 mA), ou dans le cas des opérations de set-reset dans les capteurs AMR (jusqu'à quelques A pendant une courte durée). De plus, comme ces capteurs sont basés sur les variations de résistance d'un dispositif physique, des résistances plus élevées s'accompagnent également d'un bruit thermique plus fort ($\propto 4k_BT°R$) et sont donc souvent évitées, ce qui entraîne une consommation de courant plus élevée. Le capteur magnétique STT-MTJ présenté est actuellement basé sur des composants discrets, par conséquent, la consommation d'énergie est difficile à comparer équitablement. Cependant, l'ensemble des circuits imprimés utilisés dans ces travaux consomment généralement 10 à 20 mA, avec jusqu'à 90 à 95 % utilisés

par le CAN. La MTJ (élément sensible) elle-même consomme généralement moins de 200 à 100 μA pour une tension de 0.3 à 1 V (résultant en une dissipation de puissance aussi faible que 10 μW), selon le type de MTJ (coercivité élevée ou faible) et le diamètre de la MTJ (proportionnel à la résistance), ce qui rend la méthode présentée très peu énergivore par rapport aux technologies existantes.

- **Axe sensible :** les capteurs à effet Hall sont aujourd'hui disponibles avec trois possibilités d'axes sensible (X, Y ou Z). Cependant, les capteurs AMR, GMR et TMR sont très souvent disponibles uniquement sensibles au plan du wafer, X ou Y, en raison des défis techniques et des difficultés pour la mesure de l'axe Z, en particulier pour les capteurs TMR et GMR. Par conséquent, la plupart de ces technologies MR ne restent disponibles que sensible aux axes X ou Y. En revanche, le capteur STT-MTJ présenté est sensible au plan perpendiculaire du wafer, Z, ce qui le rend complémentaire aux technologies MR existantes.

- **Champ maximal :** alors que les capteurs à effet Hall peuvent être pratiquement exposés à un champ magnétique illimité sans aucun dommage, les capteurs AMR nécessitent une fonctionnalité de set-reset pour être exposés à des champs plus forts, et l'absence d'une telle architecture réduit considérablement l'exposition maximale possible au champ sans affecter les performances du capteur. Les capteurs TMR et GMR sont souvent basés sur une couche de référence, et l'exposition maximale au champ peut aussi être élevée en fonction du champ coercitif de la couche de référence ou de la conception du SAF. Par conséquent, les capteurs basés sur des STT-MTJs présentés entrent dans cette dernière catégorie, ce qui leur permet de résister sans problème à une exposition à champ fort, jusqu'à des centaines de mT ($>$ 200 à 500 mT) dans le cas de MTJs à haute coercivité.

- **Bande passante :** enfin, le principe de mesure présenté, basé sur les retournements d'états résistifs, permet d'effectuer des mesures à haute fréquence, puisque les MTJs pour cellules MRAMs ont une capacité parasite intrinsèquement faible (nF à pF) et une vitesse élevée compatible avec des retournements de l'ordre de la nanoseconde. Ainsi, en utilisant de telles propriétés associées à l'électronique appropriée, des bandes passantes allant jusqu'à des centaines de kHz (100 à 1000 kHz) ont été obtenues. Les technologies existantes présentent généralement certaines limitations, telles que celles induites par la constante de temps RC des éléments sensibles. Dans le cas des capteurs à effet Hall, l'utilisation du spinning current, utilisé pour améliorer les performances du capteur, fait également partie des limitations de la fréquence maximale atteignable en raison des difficultés techniques de l'électronique (coût, taille, etc.). Cela rend les approches présentées également très intéressantes pour les mesures à haute fréquences et à faible bruit, souvent mal adressé par les technologies standard existantes, car l'utilisation de multiples éléments sensibles nanométriques à haute fréquences (pour un moyennage synchrone) permet de traiter les deux problèmes en même temps.

Conclusion

Cette thèse a démontré avec succès l'utilisation de STT-MTJs perpendiculaires à l'échelle nanométrique, utilisées à l'origine pour les MRAMs, comme éléments sensibles magnétiques grâce à des méthodes innovantes. Avec des diamètres allant de 20 nm à 100 nm, ces dispositifs représentent les plus petits éléments sensibles magnétiques jamais décrits à ce jour. De plus, en utilisant des circuits électroniques simples, basés sur des composants microélectroniques standards, les performances et le principe de fonctionnement ont été démontrés. Cependant, la stochasticité, observée dans les retournements dans les STT-MTJ et induisant un bruit important, reste l'un des plus gros inconvénients de cette technologie, nécessitant des travaux supplémentaires pour réduire son impact.

Après l'introduction de toutes les notions nécessaires à cette thèse, concernant les grands principes de physique, les capteurs magnétiques et les mémoires magnétiques, présentées au Chapitre 1, le Chapitre 2 a présenté le principe général de fonctionnement du capteur magnétique, à travers d'une dépendance physique entre les tensions de commutation APP et PAP, et le champ magnétique externe $\vec{B}$ selon la direction perpendiculaire du wafer. Le principe clé du capteur repose sur l'application d'une tension alternative triangulaire (c'est-à-dire linéaire) à une fréquence de plusieurs dizaines à plusieurs centaines de kHz (100 à 200 kHz) et avec une amplitude de crête de 1 V, permettant de couvrir l'ensemble des possibilités de tension de commutation APP et PAP sans endommager la MTJ. Lorsque la tension atteint le seuil critique de commutation (soit APP soit PAP), la résistance de la MTJ change rapidement en quelques nanosecondes. Au travers de la loi d'Ohm, cela induit une discontinuité de courant au moment du retournement. Le balayage en tension étant linéaire, le temps entre deux retournements consécutifs est directement proportionnel au champ magnétique externe. Ainsi, l'utilisation de circuits dédiés, décrits dans ce chapitre et basés sur la détection de ces discontinuités avec des filtres passe-haut, permet d'exploiter cette dépendance et d'extraire les événements de retournement. Cela permet de convertir ces événements en signaux mesurables (signaux de tension ou temporels) qui sont ensuite proportionnels à $\vec{B}$ et qui peuvent être numérisés. Enfin, l'adaptation du mécanisme de conversion décrit permet d'échantillonner des événements de retournement uniques, ce qui permet d'effectuer des mesures à haute fréquence, jusqu'à 100 à 200 kHz avec un spectre fréquentiel plat. Grâce à ces mécanismes, des densités spectrales de bruit de 10 à 20 $\mu\mathrm{T}/\sqrt{Hz}$ ont été obtenues.

Dans une optique d'améliorer les performances obtenues avec des MTJs à haute coercivité, le Chapitre 3 présente l'utilisation de STT-MTJs dédiés, présentant des champs coercitifs aussi faibles que 1 mT, conçus pour des applications de capteurs, permettant d'atteindre une sensibilité plus élevée, et qui ne diffèrent des MTJs à haute coercivité que par leurs stacks. Cependant, cela s'accompagne de changements plus doux entre les états P et AP, rendant inutilisables les approches initiales proposées avec des filtres passe-haut, décrites avec des MTJs à haute coercivité. Par conséquent, une nouvelle électronique est démontrée, basée sur des circuits à base d'amplificateurs opérationnels simples, permettant de mettre en œuvre le

principe basé sur STT présenté avec ces MTJs à faible coercivité, avec des tensions de commutation allant jusqu'à ± 350 mV et à des fréquences de centaines de kHz jusqu'au MHz. Grâce à ces nouvelles approches, des mesures ont été réalisées, démontrant le principe de fonctionnement et permettant d'atteindre des densités spectrales de bruit aussi faibles que 2 à 3 $\mu\mathrm{T}/\sqrt{Hz}$ sur une large gamme dynamique de plusieurs dizaines de mT. De plus, l'utilisation de quelques composants supplémentaires associés avec des séquences de contrôle dédiées permet des mesures de périodes uniques, rendant possibles les mesures à haute fréquence, avec une bande passante allant jusqu'au MHz.

Enfin, le Chapitre 4 compare les performances du capteur proposé avec des dispositifs commerciaux et expérimentaux existants, à différents niveaux. Les capteurs existants (basés sur l'effet Hall ou l'effet MR) sont souvent fabriqués avec des dimensions de l'ordre du μm, soit pour permettre aux phénomènes physiques de se produire (par exemple, les plaques Hall), soit pour réduire le bruit (par exemple, les capteurs MR). Par conséquent, en comparaison avec les technologies existantes, disponibles dans le commerce ou avec des travaux expérimentaux, on peut observer les dimensions extrêmes atteintes au cours de ces travaux. De plus, malgré un bruit supérieur aux technologies standards, ce capteur offre des performances de pointe en termes de bruit lorsqu'il est normalisé avec ses dimensions. D'autres paramètres métrologiques restent également significativement proches ou meilleurs que les valeurs des technologies standards (par exemple, la linéarité, la consommation d'énergie, la bande passante ou la dynamique), ce qui rend le capteur proposé également compétitif dans ces domaines. Pour finir, l'évaluation de l'impact des paramètres du signal d'entrée (par exemple, l'offset, l'amplitude ou la fréquence) ainsi que la dépendance à la température, permet de mieux comprendre la meilleure configuration possible à utiliser pour des travaux futurs et permet de valider la capacité du capteur à fonctionner en situation réelle (par exemple, température non contrôlée) ainsi que la compatibilité avec la production de masse grâce à l'évaluation de la variabilité sur une partie des plaques.

Ainsi, cette thèse a démontré avec succès plusieurs aspects de cette preuve de concept d'une nouvelle génération de capteurs magnétiques intégrés basés sur des STT-MTJs perpendiculaires. Cependant, pour améliorer encore le capteur magnétique à base de STT-MTJs proposé, deux aspects doivent être étudiés plus en détail : l'électronique, principalement décrite dans ces travaux, et les MTJs.

Sur la base des wafers existants et évalués dans ces travaux, l'utilisation des wedges fabriquées, au travers de l'évaluation et comparaison des performances métrologiques sur chaque MTJ, permettra d'obtenir les meilleures épaisseurs de couches, en trouvant les meilleures régions dans le wafer présentant le rapport SNR le plus élevé. Cela permettra de démarrer d'éventuelles optimisations (MTJs à faible coercivité ou à haute coercivité) des stacks, en jouant avec différentes épaisseurs de couches. De plus, des stacks entièrement nouveaux, avec l'introduction de couches différentes, d'ordres de couches différents, de matériaux différents ou d'autres architectures de MTJ (par exemple, double barrière MgO, différents SAF, etc.), tout en essayant de rester proche des MTJs dédiés aux MRAMs, permettront peut-être d'atteindre une sensibilité plus élevée et potentiellement d'obtenir une

stochasticité plus faible ainsi qu'un champ d'offset réduit, deux des principales préoccupations des MTJs à faible coercivité et/ou à haute coercivité. De plus, l'analyse de l'impact des diamètres des MTJs (20, 50, 80 ou 100 nm dans ces travaux) nous permettra éventuellement de conclure sur les meilleures dimensions à utiliser. Enfin, la mise en œuvre de concentrateurs de flux "perpendiculaire" ou l'évaluation de MTJ en parallèles (soit en tant qu'éléments sensibles individuels, soit en tant qu'unité globale plus grande) aidera également à évaluer ce qui pourrait être réalisé en termes de meilleur rapport signal/bruit possible grâce à une telle approche basée sur le STT et à évaluer les applications possibles.

L'intégration future de l'électronique sous forme de circuit intégré monolithique, l'intégration de la MTJ avec le circuit, avec un design optimisé, un choix de composants ou de meilleures simulations contribueront également à réduire le bruit global (bien que cela soit moins pertinent en raison du bruit beaucoup plus élevé induit par la MTJ par rapport à l'électronique, en particulier pour les MTJs à haute coercivité). De nouvelles architectures possibles pourraient également potentiellement aider à réduire le problème principal présenté avec les MTJs à faible coercivité (zone morte/région de sensibilité inférieure autour du champ d'offset) même si ce problème peut déjà être minimisé en utilisant des MTJs avec de faibles champs coercitifs. De plus, l'évaluation d'une électronique plus complexe peut potentiellement aider à améliorer les performances des capteurs. Cela comprend, par exemple, l'utilisation d'électronique non linéaire (par exemple, un diviseur analogique) ou d'amplificateurs à détection synchrone dédiés pour se verrouiller la fréquence de commutation, minimisant ainsi le bruit rms du capteur, ainsi que des circuits de compensation avec des bobines pour l'annulation du champ d'offset ou une meilleure linéarité. Avec l'intégration de l'électronique et de la MTJ au sein d'une seule puce, une première évaluation des applications en situation réelle deviendra également possible.

Avec de telles améliorations et optimisations, cette technologie de mesure de champ magnétique intégrée, innovante et basée sur les STT-MTJs offrira de nouvelles possibilités métrologiques, que ce soit implémentées sous forme de capteur unique, soit sous forme de réseau d'éléments sensibles à haute densité, ouvrant la voie à différentes applications, allant du domaine médical aux applications industrielles ou physiques, le tout avec une faible consommation énergétique. Cela comprend de véritables mesures ponctuelles à l'échelle nanométrique, requises dans des applications spécifiques telles que l'alignement de masques photolithographiques ou la détection de particules magnétiques, dans les domaines de la biologie aux domaines industriels, avec des applications nécessitant des larges bandes passantes tels que les mesures de courant, nécessaires pour répondre aux nouvelles exigences industrielles.

Publications

Published journals and conferences

- **H. Nicolas**, J. Pascal, L. Hebrard, J.-B. Kammerer, R. C. Sousa, A. Mora-Hernández, and I.-L. Prejbeanu, "A Magnetic Sensor Based on a Nanometric Spin Transfer Torque Magnetic Tunnel Junction Suitable for Monolithic Integration," 2022 IEEE Sensors, Dallas, TX, USA, 2022, pp. 1-4, 10.1109/SENSORS52175.2022.9967227
- **H. Nicolas**, R. C. Sousa, A. Mora-Hernández, I.-L. Prejbeanu, L. Hebrard, J.-B. Kammerer, and J. Pascal, "Conditioning Circuits for Nanoscale Perpendicular Spin Transfer Torque Magnetic Tunnel Junctions as Magnetic Sensors," in IEEE Sensors Journal, vol. 23, no. 6, pp. 5670-5680, March, 2023, 10.1109/JSEN.2023.3241967
- **H. Nicolas**, R. C. Sousa, A. Mora-Hernández, I.-L. Prejbeanu, L. Hebrard, J.-B. Kammerer, and J. Pascal, "Low-Coercivity Perpendicular Spin Transfer Torque Magnetic Tunnel Junctions as Nanoscale Magnetic Sensors," 2023 IEEE Intermag, Sendai, Japan, 2023, 10.1109/INTERMAGShortPapers58606.2023.10228290
- T. Quirin, C. Vergne, C. Féry, P. Badertscher, **H. Nicolas**, D. Mannhart, S. Osswald, M. Kuhne, C. Sticherling, M. Madec, L. Hebrard, S. Knecht, and J. Pascal, "A magnetic camera to assess the risk of magnetic interaction between portable electronics and cardiac implantable electronic devices," 2022 IEEE MeMeA, Messina, Italy, 2022, pp. 1-6, 10.1109/MeMeA54994.2022.9856580
- C. Vergne, C. Féry, T. Quirin, **H. Nicolas**, M. Madec, S. Hemm, and J. Pascal, "Low-Field Electromagnetic Tracking Using 3-D Magnetometer for Assisted Surgery," in IEEE Transactions on Magnetics, vol. 59, no. 2, pp. 1-5, February 2023, 10.1109/TMAG.2022.3204918
- C. Vergne, **H. Nicolas**, and J. Pascal, "Experimental assessment of the performances of an anisotropic magnetoresistive sensor after exposure to strong magnetic fields," 2023 IEEE Intermag, Sendai, Japan, 2023, 10.1109/INTERMAGShortPapers58606.2023.10228508
- **H. Nicolas**, T. Quirin, and J. Pascal, "FPGA-Based Magnetic Field Camera for Dynamic Magnetic Field Mapping," in IEEE Sensors Letters, vol. 8, no. 5, pp. 1-4, May 2024, Art no. 2501004, 10.1109/LSENS.2024.3389099
- **H. Nicolas**, C. Vergne, and J. Pascal, "Iron detection method based on high-resolution magnetic field camera," 2024 IEEE Sensors, Kobe, Japan, 2024, pp. 1-4, 10.1109/SENSORS60989.2024.10784707
- C. Vergne, **H. Nicolas**, and J. Pascal, "Flexible coils localization using optically pumped magnetometers for biomedical applications," 2024 IEEE Sensors, Kobe, Japan, 2024, pp. 1-4, 10.1109/SENSORS60989.2024.10784888

- K. Komuro, **H. Nicolas**, B. Dieny, D. Oshima, T. Kato, and R. C. Sousa, "Noise Characterization of Spin-Transfer-Torque-based Magnetic Field Sensor," 2025 IEEE Intermag, New Orleans, Louisiana, USA, 2025 (accepted)
- **H. Nicolas**, R. C. Sousa, A. Mora-Hernández, I.-L. Prejbeanu, L. Hebrard, J.-B. Kammerer, and J. Pascal, "Operational Amplifiers Circuits for Magnetic Sensing Using Perpendicular Low Coercivity Nanoscale Spin Transfer Torque Magnetic Tunnel Junctions," in IEEE Sensors Journal, 2024 (accepted)
- **H. Nicolas**, C. Féry, T. Quirin, N. Weber, J. Oster, J. Felblinger, A. Vignaud, and J. Pascal, "Monitoring the head exposure of MRI workers around 3 T, 7 T and 11.7 T scanners using smart goggles equipped with a network of magnetometers," in Magnetic Resonance Medicine, 2025 (submitted)

Conferences (non-published proceedings)

- **H. Nicolas**, R. C. Sousa, A. Mora-Hernández, I.-L. Prejbeanu, L. Hebrard, J.-B. Kammerer, and J. Pascal, "A spin transfer torque magnetic tunnel junction implemented as a magnetic sensor," 2023 IEEE AIM, Moena, Italy, 2023
- **H. Nicolas**, C. Vergne, T. Quirin, and J. Pascal, "Application specific magnetic field cameras for biomedical engineering," 2023 iSIM, Sendai, Japan, 2023
- R. C. Sousa, **H. Nicolas** , A. Mora-Hernández, H. Karaoui, I.-L. Prejbeanu, L. Hebrard, J.-B. Kammerer, and J. Pascal, "Use of Nanoscale Perpendicular Spin Transfer Torque Magnetic Tunnel Junctions as Magnetic Sensors," 2023 IEEE MMM, Dallas, Texas, USA, 2023
- K. Komuro, **H. Nicolas**, B. Dieny, D. Oshima, T. Kato, and R. C. Sousa, "Noise Characterization of STT-based Magnetic Tunnel Junction Sensor," The 48th Annual Conference on Magnetics, Akita, Japan, 2024
- T. Quirin, **H. Nicolas**, C. Féry, and J. Pascal, "A high-speed magnetic field camera to characterize magnetic gradients imperfections of magnetic resonance imaging scanners," ESMRMB 2024, Barcelona, Spain, 2024
- **H. Nicolas**, C. Vergne, and J. Pascal, "Live Demonstration: Iron detection method based on high-resolution magnetic field camera," 2024 IEEE Sensors, Kobe, Japan, 2024

French national conferences

- T. Quirin, C. Vergne, C. Féry, **H. Nicolas**, M. Madec, L. Hebrard, and Joris Pascal, "A magnetic safety scanner to assess the risk of magnetic interaction between portable electronics and cardiac implantable electronic devices," GDR SoC^2 2022, Strasbourg, France, 2022

- **H. Nicolas**, J. Pascal, L. Hebrard, J.-B. Kammerer, R. C. Sousa, A. Mora-Hernández, and I.-L. Prejbeanu, "A Nanometric Magnetic Sensor Based on a Spin Transfer Torque Magnetic Tunnel Junction," GDR SoC² 2022, Strasbourg, France, 2022
- **H. Nicolas**, P. Rotach, G. Baumgarten, N. Weber, J. Oster, and J. Pascal, "Measurements of Clinical MRI Gradients," GDR SoC² 2022, Strasbourg, France, 2022

Swiss national conferences

- **H. Nicolas**, R. C. Sousa, A. Mora-Hernández, I.-L. Prejbeanu, L. Hebrard, J.-B. Kammerer, M. Ulrich, and J. Pascal, "A Nanoscale Magnetic Sensor Based on a Low Coercivity Spin Transfer Torque Magnetic Tunnel Junction," Swiss Nanoconvention 2023, Neuchâtel, Switzerland, 2023
- **H. Nicolas**, S. Gorenflo, M. Ulrich, R. C. Sousa, A. Mora-Hernández, I.-L. Prejbeanu, L. Hebrard, J.-B. Kammerer, and Joris Pascal, "NanoHighSens: Nanoscale and High Bandwidth Current Sensor," 2023 SNI Annual event, Meisterschwanden, Switzerland, 2023
- **H. Nicolas**, A. Graña, S. Gorenflo, M. Ulrich, R. C. Sousa, I.-L. Prejbeanu, L. Hebrard, J.-B. Kammerer, and J. Pascal, "NanoHighSens: Towards Nanoscale and High Bandwidth Current Sensor," 2024 SNI Annual event, Meisterschwanden, Switzerland, 2024
- **H. Nicolas**, S. Gorenflo, M. Ulrich, R. C. Sousa, A. Mora-Hernández, I.-L. Prejbeanu, L. Hebrard, J.-B. Kammerer, and J. Pascal, "NanoHighSens: Nanoscale High Bandwidth Magnetic Field Measurements Using Spin Transfer Torque Magnetic Tunnel Junctions," 2023 SNI Annual event, Meisterschwanden, Switzerland, 2023
- **H. Nicolas**, A. Inderbitzin, J.-B. Kammerer, R. Sousa, S. Gorenflo, M. Ulrich, and J. Pascal, "Nanocompass: Nanoscale Magnetometer with Nanotesla Resolution," SNI Annual Report, 2021
- **H. Nicolas**, A. Inderbitzin, J.-B. Kammerer, R. Sousa, S. Gorenflo, M. Ulrich, and J. Pascal, "Nanocompass: A Nanoscale Magnetometer," SNI Annual report, 2022
- **H. Nicolas**, A. Inderbitzin, S. Gorenflo, T. Keusch, R. C. Sousa, I.-L. Prejbeanu, L. Hebrard, J.-B. Kammerer, and J. Pascal, "Nanocompass – Nanoscale Magnetometer with Nanotesla Resolution," 2021 SNI Annual event, Lenzerheide, Switzerland, 2021
- **H. Nicolas**, A. Inderbitzin, S. Gorenflo, M. Ulrich, R. C. Sousa, A. Mora-Hernández, I.-L. Prejbeanu, L. Hebrard, J.-B. Kammerer, and J. Pascal, "Nanocompass – A Magnetic Sensor Based on a Spin Transfer Torque Magnetic Tunnel Junction," 2022 SNI Annual event, Lenzerheide, Switzerland, 2022
- **H. Nicolas**, A. Graña, J.-B. Kammerer, R. Sousa, S. Gorenflo, M. Ulrich, and J. Pascal, "NanoHighSens: A High Bandwidth And Nanoscale Magnetic Sensor For Current Measurements," SNI Annual report, 2023

Université de Strasbourg

Hugo NICOLAS

Fachhochschule Nordwestschweiz

Développement de magnétomètres intégrés à base de jonctions tunnel magnétiques à couple de transfert de spin

Résumé

Cette thèse présente l'utilisation de STT-MTJs perpendiculaires, développées initialement pour les MRAMs, en tant que capteurs magnétiques intégrés. Les MRAMs basées sur des MTJs utilisent généralement l'effet STT pour modifier l'orientation de l'aimantation d'une couche ferromagnétique douce en appliquant une forte tension aux bornes de la MTJ. Cela conduit à un changement de résistance permettant de placer la MTJ dans deux états distincts, parallèle et antiparallèle. Cependant, la tension nécessaire pour provoquer le retournement de l'aimantation de la couche douce dépend du champ magnétique externe. En utilisant cette propriété, nous explorons une nouvelle application des STT-MTJs qui consiste à les utiliser comme capteurs magnétique présentant des avantages significatifs par rapport aux capteurs à effet Hall et magnétorésistifs. Leurs dimensions nanométriques ainsi que leurs bandes passantes élevées permettent le développement de nouvelles applications.

Mots-clés : STT-MRAM, STT-MTJ, Capteur magnétique, Electronique, Spintronique.

Résumé en anglais

This thesis presents the use of perpendicular STT-MTJs, originally developed for MRAMs, as integrated magnetic sensors. MRAMs based on MTJs are often using the STT effect to change the orientation of the magnetization of a soft ferromagnetic layer by applying a strong voltage across the junction. This leads to a change of resistance allowing the MTJ to be set in two different resistive states called parallel and antiparallel. However, the energy required to flip the magnetization of the free layer from one state to the other is not only related to the voltage applied to the junction but also to the external magnetic field. Using this property, this work investigates a new application of STT-MTJs, which consists of using it as a magnetic sensor. These sensing elements have significant advantages compared to currently available Hall effect and magnetoresistive sensors. Hence, their nanometric dimensions as well as high bandwidth allow the development of new applications.

Key-words: STT-MRAM, STT-MTJ, Magnetic sensor, Electronics, Spintronics.